$\mathbf{J/\psi}$ Production in $\sqrt{s} = 7$ TeV pp Collisions

Dissertation

zur Erlangung des Doktorgrades
der Naturwissenschaften

vorgelegt beim Fachbereich Physik
der Johann Wolfgang Goethe-Universität
in Frankfurt am Main

von

Frederick Kramer
aus Frankfurt am Main

Frankfurt am Main 2012
(D 30)

vom Fachbereich Physik der
Johann Wolfgang Goethe-Universität als Dissertation angenommen.

Dekan:	Prof. Dr. Michael Huth
Gutachter:	Prof. Dr. Christoph Blume
	Prof. Dr. Dr. h. c. Reinhard Stock
Datum der Disputation:	

Zusammenfassung

Normale Materie ist aus Atomen aufgebaut, in deren Zentrum ein Atomkern den Großteil der Masse ausmacht. Dieser Atomkern setzt sich wiederum aus Protonen und Neutronen zusammen. Durch Beschleunigerexperimente kennt man heutzutage hunderte diesen Kernbausteinen ähnliche Teilchen. Sie alle sind aus Quarks aufgebaut. All jene Teilchen, die wie Protonen und Neutronen aus drei Valenzquarks bestehen, nennt man *Baryonen*. Alle Teilchen, die von einem Quark und einem Anti-Quark gebildet werden nennt man *Mesonen*. Das Proton ist das leichteste der Baryonen, alle anderen zerfallen und bilden letztlich ein Proton. Nur das Neutron ist, solange es im Atomkern gebunden ist, ebenfalls stabil. Die beiden Kernbausteine bestehen aus einer unterschiedlichen Kombination von *up* (u) und *down* (d) Quarks. Es existieren schwerere Varianten dieser ersten Quarkfamilie: *charm* (c) und *strange* (s) sowie *top* (t) und *bottom* (b). Diese zwei Familien sind instabil; je höher die Quarkmasse, desto geringer die Lebensdauer. Das schwerste Quark, das top, zerfällt bereits bevor es eine Bindung zu einem anderen Quark aufbauen kann. Von allen anderen Quarks sind gebundene Zustände bekannt.

Freie Quarks konnten hingegen nicht nachgewiesen werden. Der Grund liegt im speziellen Potential der starken Kraft, welche die Wechselwirkung zwischen Quarks durch den Austausch von Gluonen beschreibt. Dieses Potential beinhaltet neben einem Coulomb-artigen Term einen zweiten Term, der zu großen Abständen hin linear ansteigt. Die Kopplungskonstante des Coulomb-Terms der starken Wechselwirkung weist allerdings auch eine starke Abhängigkeit vom Abstand auf, daher wird sie auch als *laufend* bezeichnet. Als Resultat nimmt die Stärke der Bindungen durch die starke Kraft mit kleiner werdendem Abstand stark ab; dieses Phänomen wird *asymptotische Freiheit* genannt.
Bei ansteigender Quarkdichte sollten sich Bindungen daher lösen und einen Zustand quasi-freier Farbladungen – den Ladungen der starken Kraft – aufweisen. Dies gilt auch für einen Anstieg der Temperatur. Dieser Materiezustand wird als *Quark-Gluon-Plasma* bezeichnet. Es wird vermutet, dass er sowohl im Zentrum kompakter Sterne herrscht, als auch dass ihn das entstehende Universum wenige Mikrosekunden nach dem Urknall durchlaufen hat. Der Nachweis und die Vermessung des Quark-Gluon-Plasmas hat daher weitreichende Auswirkungen auf das Verständniss von grundlegenden teilchen- und astrophysikalischen Prozessen.
In der Kollision stark beschleunigter schwerer Ionen vermutet man Drücke und Temperaturen,

die hoch genug sind, um ein Quark-Gluon-Plasma zu erzeugen. Allein die Tatsache, dass ein solcher Feuerball eine extrem kurze Lebensdauer hat erschwert seinen Nachweis, den man nur auf die Rekonstruktion der entstandenen Produkte stützen kann.

Quarkonia, gebundene Zustände schwerer Quark-Antiquark-Paare, sind vielversprechende Sonden für das Studium des Quark-Gluon-Plasmas. Eine wichtige Referenz für Resultate in Schwerionenkollisionen sind Präzisionsmessungen in Proton-Proton-Stößen, in denen kein Quark-Gluon-Plasma erwartet wird. Die grundlegenden Produktionsmechanismen von Quarkonia in Kollisionen zweier Hadronen konnten bislang jedoch nicht abschließend geklärt werden. Trotz ihrer konzeptuellen Unterschiede können die drei gängigsten Modelle – das *Color-Singlet Model* (CSM), das *Color-Evaporation Model* (CEM) und der nicht-relativistische QCD-Ansatz (NRQCD) – allesamt einen Großteil der gemessenen Daten zu Produktionswirkungsquerschnitten beschreiben. Neue Messgrößen, wie beispielsweise die Polarisation, sowie Daten in einem höheren Energiebereich sind notwendig, um die konkurrierenden Modelle zu prüfen.
Das Proton ist ein komplexes Objekt. Es besteht aus einer Vielzahl an Partonen: Valenzquarks, Seequarks und Gluonen. Aktuelle Monte Carlo-Simulationsprogramme, wie Pythia 6.4, behandeln die harte Parton-Streuung, die letztlich zur Bildung eines Quarkoniums führt, weitgehend unabhängig von den umgebenden Prozessen des Ereignisses. Die Untersuchung einer eventuellen Korrelation zwischen diesen beiden Teilen könnte wesentlich zu einem besseren Verständnis der fundamentalen Quarkonia-Produktion und dem Ablauf einer Proton-Proton-Kollision führen.
Die Messung von Quarkonia in Schwerionenkollisionen könnte grundsätzlich zum Verständnis des Quark-Gluon-Plasmas beitragen. Allerdings ist eine Interpretation der Daten komplexer als ursprünglich angenommen. Demnach würde das schwere Quark-Antiquarkpaar, das bereits gebunden ist oder im Begriff ist eine Bindung einzugehen, durch die quasi-freien Farbladungen im Quark-Gluon-Plasma getrennt, analog zu dem aus der Elektrodynamik bekannten Prozess der Debye-Abschirmung. In der Folge sollte es im Vergleich zu Proton-Proton-Kollisionen zu einer Unterdrückung der gemessenen Raten kommen. Doch anhand verschiedener Messungen stellte sich heraus, dass einige andere Effekte ebenfalls Einfluss auf die Quarkonia-Messraten haben und berücksichtigt werden müssen. Dies sind auf der einen Seite verschiedene Effekte kalter Kernmaterie. Diese treten bereits durch die Präsenz der Kernmaterie auf, selbst wenn kein Übergang zu einem Plasmazustand stattgefunden hat. Durch Messungen von Kollisionen von Protonen mit schweren Ionen, bei denen kein Quark-Gluon-Plasma erwartet wird jedoch Kernmaterie im Spiel ist, versucht man diese Effekte genau zu vermessen. Auf der anderen Seite wird vermutet, dass im Falle eines Plasmazustandes auch Effekte, die der Unterdrückung der Raten von Quarkonia der $c\bar{c}$-Familie entgegenlaufen, auftreten. Erste Blei-Blei-Messungen von ALICE lassen sich mit einem solchen Szenario interpretieren, allerdings nur innerhalb großer Unsicherheiten aufgrund fehlender Kollisionsdaten von Protonen mit schweren Ionen. Bei Quarkonia der $b\bar{b}$-Familie vermutet man kaum Effekte, die der Unterdrückung entgegenwirken. In der Tat zeigen erste Messungen von CMS am LHC eine starke Unterdrückung der Raten dieser Teilchen im Vergleich zu Proton-Proton-Daten.

Der aktuelle Stand der theoretischen Modelle und der Messung von Quarkonia, sowohl in Proton-Proton- als auch in Schwerionenkollisionen, wird in Kapitel 2 der vorliegenden Arbeit besprochen.

ALICE ist das Experiment am CERN-LHC, das insbesondere zur Studie von Schwerionenkollisionen konzipiert wurde. Der technische Aufbau wurde für Präzisionsmessungen in besonders hohen Spurdichten und für Teilchen mit sehr niedrigem Transversalimpuls optimiert. Das Experiment besteht aus mehreren verschiedenen Detektoren zum Nachweis und zur Vermessung der Teilchenspuren, sowohl bei zentralen als auch bei vorwärtsgerichteten Rapiditäten. Für die vorliegende Studie werden Elektronenspuren bei zentralen Pseudorapiditäten von $|\eta| < 0.9$ analysiert. Die für diese Messung wichtigsten Detektoren sind das *Inner Tracking System* und die *Time Projection Chamber*.
Letztere ist eine zylindrische, gasgefüllte Kammer mit Vieldraht-Proportionalzählern an den Endkappen und einer zentralen Elektrode. Geladene Teilchen ionisieren das Detektorgas und erzeugen so Spuren entlang ihrer Flugbahn. Die Elektronen aus der Ionisation driften im angelegten elektrischen Feld zu den Endkappen und werden dort ausgelesen. Anhand ihrer Position an der Endkappe und der Driftzeit lässt sich die Spur dreidimensional rekonstruieren. Ihre Krümmung im Feld des Magneten, der die Detektoren umschließt, liefert den Impuls des Teilchens. Die Stärke der Ionisation pro zurückgelegter Wegstrecke lässt zudem über den spezifischen Energieverlust auf die Teilchensorte schließen. Mit dieser Methode werden in der vorliegenden Arbeit Elektronen-Kandidaten ausgewählt.
Durch eine besonders genaue Ortsauflösung und die Nähe zum primären Kollisionspunkt verbessert das Inner Tracking System die Bestimmung der Teilchenimpulse. Auch wird mit diesem Detektor der Ort der primären Kollision gemessen. Des Weiteren wird das Inner Tracking System in der vorliegenden Arbeit verwendet, um die Multiplizität der Kollisionen zu bestimmen.
Der *Transition Radiation Detector* (TRD) wurde aufgrund seiner Ausbaustufe im Jahr 2010, also zur Zeit der Aufnahme der in dieser Studie untersuchten Daten, nicht in die Analyse mit einbezogen. In der Zwischenzeit wurde dieser Detektor jedoch deutlich erweitert: In zukünftig aufgenommenen Daten ist daher mit einer deutlichen Verbesserung der Elektronen-Identifikation zu rechnen. Darüber hinaus wird mit dem TRD auch eine explizite Vorab-Selektion von pp-Kollisionen, die zu hoher Wahrscheinlichkeit ein Quarkonium enthalten, möglich.
Für die Rekonstruktion aufgenommener Kollisionsdaten ist eine stetige Kalibration der Detektoren nötig. Im Fall des TRD erfolgt diese anhand verschiedener Parameter wie beispielsweise Druck und Temperatur. Des Weiteren muss auch die Konfiguration und der Status der Elektronik jedes TRD-Moduls einbezogen werden. Im Rahmen der vorliegenden Arbeit wurde eine Methode zur Abfrage, Verarbeitung und Archivierung dieser Konfigurationsparameter entwickelt. Eine Beschreibung findet sich in Anhang A dieser Arbeit.
Beim Durchqueren von Materie emittieren Elektronen mit einer gewissen Wahrscheinlichkeit Bremsstrahlung und verlieren dabei an Bewegungsenergie. Mit den aktuellen Methoden zur

Spurrekonstruktion in ALICE kann dieser Energieverlust nicht bestimmt werden. In der Messung von Quarkonia über deren Zerfall in ein Elektron-Positron-Paar ergibt sich hierdurch eine asymmetrische Massenverteilung, die wiederum einhergeht mit einer verringerten Rekonstruktionseffizienz. Verschiedene Ansätze um den Energieverlust durch Bremsstrahlung einzubeziehen, sowie deren mögliche Anwendung in der ALICE-Spurrekonstruktion, werden in Kapitel 3 besprochen. Dort wird auch der experimentelle Aufbau von ALICE beschrieben.

Das J/ψ-Teilchen ist das zuerst entdeckte Quarkonium und der niedrigste Bindungszustand der c$\bar{\text{c}}$-Familie mit den Quantenzahlen des Photons. In der vorliegenden Arbeit wurde der inklusive Produktions-Wirkungsquerschnitt des J/ψ-Teilchens in inelastischen pp-Kollisionen mit einer Schwerpunktsenergie von $\sqrt{s} = 7$ TeV bestimmt. Die Messung erfolgte über den Zerfallskanal des J/ψ in ein Elektron-Positron-Paar und in einem Rapiditätsintervall von $|y| < 0.9$. Das Ergebnis für den integrierten Wert lautet: $\sigma_{\mathrm{J}/\psi}(|y| < 0.9) = 10.7 \pm 0.8$ (stat.) $\pm$ 1.4 (syst.) $\pm$ 0.4 (lumi.) μb. Gemeinsam mit der ALICE-Messung im $\mu^+\mu^-$-Zerfallskanal bei vorwärtsgerichteten Rapiditäten und Daten von anderen Experimenten gibt das hier gewonnene Resultat des p_{t}-integrierten Wirkungsquerschnittes eine umfassende Messung der J/ψ-Rapiditätsverteilung ab. ALICE ist das einzige Experiment am LHC das bei zentralen Rapiditäten in der Lage ist, J/ψ bis zu $p_{\mathrm{t}} = 0$ nachzuweisen. Daher existieren in diesem Rapiditätsintervall keine Resultate anderer Experimente zum direkten Vergleich, da insbesondere niedrige Transversalimpulse zum gesamten Wirkungsquerschnitt beitragen. Experimente, die ihre Daten an Beschleunigern mit niedrigerer Energie genommen haben, decken jedoch einen ähnlichen kinematischen Bereich ab. Ein Vergleich mit diesen Daten zeigt, dass die Produktion von J/ψ eine starke Kollisionsenergie-Abhängigkeit aufweist. Weiterhin wurde in der vorliegenden Arbeit eine differentielle Analyse der J/ψ-Produktion als Funktion des Transversalimpulses durchgeführt. Ein Vergleich zu verfügbaren Daten anderer LHC-Experimente bei zentraler Rapidität und gleicher Schwerpunktsenergie zeigt in dem Bereich in dem sich die Spektren überlappen eine hervorragende Übereinstimmung.
Die gewonnenen Daten als Funktion der Rapidität, der Schwerpunktsenergie und des Transversalimpulses wurden in Beziehung zu den verfügbaren Vorhersagen der drei Modelle, CSM, CEM und NRQCD, gesetzt. Allerdings beinhalten die Modelle im Gegensatz zu den gezeigten Messresultaten nur den Anteil der inklusiven Produktion, der nicht von Zerfällen von b-Hadronen, also Teilchen, die ein b Valenz-Quark enthalten, stammen. Jedoch liefern erste vorläufige Messungen ungefähre Werte dieses Beitrags. Zieht man diese in Betracht, so lässt sich eine gute Übereinstimmung aller drei Modelle mit den Daten annehmen. Für einen abschließenden Vergleich ist jedoch eine genaue Bestimmung notwendig. Die großen Unsicherheiten der verschiedenen Modellvorhersagen, innerhalb derer sie alle miteinander übereinstimmen, werden jedoch auch dann vermutlich keine klare Aussage zulassen, welches Modell gegenüber den anderen zu bevorzugen sei.
Die vorliegende Studie wurde in Verbindung mit der ALICE-J/$\psi \rightarrow \mathrm{e}^+\mathrm{e}^-$-Analysegruppe durchgeführt. Einige Teile konnten zur gemeinsamen Arbeit dieser Gruppe beitragen, welche

letztlich zur Publikation der ersten J/ψ-Messung mit ALICE geführt hat. Darüber hinaus dienen die vorliegenden Resultate als Gegenprobe der publizierten Werte. Daher wurde ein Vergleich zwischen den beiden Analysen angestellt, sowohl für den integrierten Wert als auch für die differentiellen Messungen. Eine sehr gute Übereinstimmung wurde gefunden, die Resultate konnten bestätigt werden. Durch eine weitergehende Modifikation der Analysemethoden konnte in der vorliegenden Arbeit eine Verringerung der statistischen und systematischen Fehler um 20 % bzw. 5 % gegenüber den publizierten Messwerten erzielt werden.
Die hier zusammengefasste Analyse und ihre Resultate werden in Kapitel 4 ausführlich vorgestellt und diskutiert.

Eine völlig neue Betrachtung der J/ψ-Produktion in Proton-Proton-Kollisionen wurde aufbauend auf den zuvor genannten Ergebnissen vorgenommen. Zum ersten Mal wurden die J/ψ-Messraten als Funktion der Multiplizität geladener Teilchen bestimmt. Die Beschreibung dieser Analyse findet sich in Kapitel 5 der vorliegenden Arbeit. Das Ergebnis dieser Analyse ist ein näherungsweise linearer Anstieg der J/ψ-Produktionsraten mit der Multiplizität. Dies gilt sowohl für die Messung aus der vorliegenden Arbeit bei zentralen Rapiditäten ($|y| < 0.9$) im Zerfallskanal $J/\psi \to e^+e^-$, als auch bei vorwärtsgerichteten Rapiditäten ($2.5 < y < 4.0$) im Zerfallskanal $J/\psi \to \mu^+\mu^-$. In beiden Fällen wurden J/ψ mit $p_t > 0$ rekonstruiert und die Multiplizität im Bereich $|\eta| < 1.0$ bestimmt. Mit der Menge der aktuell verfügbaren Kollisionsdaten ist eine Messung bis zum etwa Vierfachen der mittleren Multiplizität aller analysierten Proton-Proton-Kollisionen möglich. Dort wurde gegenüber dem Durchschnitt aller analysierten Ereignisse eine Erhöhung um das etwa 8-fache bei zentralen und um das etwa 5-fache bei vorwärtsgerichteten Rapiditäten gefunden. Die Resultate der zwei unabhängigen Analysen sind auf dem Weg zur gemeinsamen Publikation.
Ein Grund für diese starke Korrelation könnte sein, dass die Produktion eines J/ψ oder allgemein eines c$\bar{\text{c}}$-Paares von einer starken hadronischen Aktivität begleitet wird. Jedoch ist zweifelhalft ob sich eine solche Korrelation unverändert über etwa drei Einheiten der Rapidität erstrecken könnte. Eine andere Interpretation ist, dass pp-Kollisionen mit dem gleichen Konzept des Stoßparameters wie Schwerionenkollisionen behandelt werden müssen. Je zentraler eine Kollision, desto höher die Wahrscheinlichkeit dafür, dass mehrere primäre partonische Wechselwirkungen in einem Ereignis stattfinden. Wenn dies nun für Streuprozesse mit niedrigem sowie mit hohem Energieübertrag gilt, wobei erstere für den Hauptanteil der produzierten geladenen Spuren verantwortlich sind und letztere unter anderem für die Produktion von schweren Quarks, könnte sich eine Korrelation wie die gemessene ergeben. Dies stünde allerdings im Gegensatz zur aktuellen Implementierung von beispielsweise Pythia 6.4. Simulationen von $2 \to 2$ Streuprozessen mit diesem Monte Carlo-Simulationsprogramm können den Verlauf der Messwerte in der Tat nicht reproduzieren. Weitergehende Studien mit verschiedenen Monte Carlo-Simulationsprogrammen könnten im Hinblick auf deren jeweilige Implementierung von mehrfachen partonischen Wechelwirkungen in einzelnen Ereignissen ein tieferes Verständnis verschaffen. Letztlich werden multiplizitätsabhängige Analysen von D-Mesonen, anderen

Quarkonia und anderen Produkten harter Streuprozesse klären, welcher Natur und insbesondere auch wie grundlegend der beobachtete Effekt ist.
Eine weitere Möglichkeit, die sich aus dem Vergleich der in der vorliegenden Arbeit gezeigten Resultate und der entsprechenden Messung von D-Mesonen ergibt, ist die Frage zu klären, ob bereits in pp-Kollisionen von besonders hoher Multiplizität kollektive Effekte zu beobachten sind. Bislang wurden derartige Effekte nur in Kollisionen schwerer Ionen diskutiert. Erste theoretische Studien werfen diese Fragestellung im Hinblick auf die hohen Multiplizitäten in $\sqrt{s} = 7$ TeV pp-Kollisionen jedoch auf. Da pp-Daten als Referenz für Schwerionenkollisionen verwendet werden, sollte mit einer entsprechenden Messung Klarheit geschaffen werden.

Contents

Chapter 1

Introduction

1.1 The Standard Model of Particle Physics

According to the standard model of particle physics, all matter and forces are built up and mediated by a small set of elementary particles. The theory was formulated in its present form in the 1970s after a variety of experimental findings. Especially the observation of point-like constituents inside protons in deep-inelastic scattering experiments clarified that the quark hypothesis of Murray Gell-Mann [1] and George Zweig [2] from 1964 was indeed justified. At that time no experimental hint for the existence of such particles was given; only the growing number of known "elementary" particles and symmetries among them led to this idea.
In the standard model, all matter consists of so-called *fermions* while all interactions between them is mediated by *bosons.*

1.1.1 Matter

Fermions are particles with half-integer spin. They obey the Fermi-Dirac statistics[1] and the Pauli exclusion principle. The latter states that no two identical fermions can agree in all quantum numbers at the same time. There are two groups of fundamental matter particles: quarks and leptons. As summarized in Table 1.1, both groups are divided into three families of two particles each. Three of the leptons—the electron e, the muon μ and the tau τ—carry one unit of electric charge while the other three, the associated neutrinos, are not electrically charged. Quarks, on the other hand, carry fractional charges: $+3/2$ in case of the up u, charm c and top t and $-1/3$ in case of the down d, strange s and bottom b. The different types of quarks are also called *flavors*. In Table 1.1 the particle masses increase from left to right.

[1] The average number of fermions in a single-particle state r in a system of identical fermions is given by the Fermi-Dirac distribution: $\langle n_\mathrm{r}\rangle = \{\exp[(E_\mathrm{r}-\mu)/k_\mathrm{B}T]+1\}^{-1}$. Here E_r is the energy of the state r, μ the chemical potential, k_B Boltzmann's constant and T the temperature [3].

All of those 12 fundamental fermions have a corresponding anti-fermion, a particle of same mass and lifetime but with opposite sign of charge and magnetic moment. The existence of anti-matter was already predicted by Dirac in 1928 [4] after the derivation of the equation named after him. This is the relativistic quantum mechanical wave equation for spin 1/2 particles assuming positive as well as negative solutions for the particle energies.

	Family			El. Charge
	1	2	3	
Quarks	u	c	t	$+2/3$
	d	s	b	$-1/3$
Leptons	ν_e	ν_μ	ν_τ	0
	e	μ	τ	-1

Table 1.1: The elementary matter particles of the standard model.

Another difference between quarks and leptons is that in contrast to the latter the former exhibit another degree of freedom, the *color*. Of course that is only a figurative description and does not correspond to photon emission or absorption or even visible colors. The word stems from the circumstance that there are different color charges what will be further explained in the next section.
An interesting fact is, that the total charge of the quarks is $3 \times 3 \times 2/3 - 3 \times 3 \times 1/3 = 3$ and of the leptons $-1 \times 3 = -3$. Therefore, the total charge of all fermions (and in the same way of all anti-fermions) is zero. This is interpreted such that the Standard Model does not exhibit any anomalies and is a renormalizable[2] field theory [5].

1.1.2 Interactions

All interactions between the above named matter particles are mediated by bosons belonging to the fundamental forces. In contrast to fermions these particles obey the Bose-Einstein statistics[3] and carry integer spin. Two or more identical bosons can occupy the same quantum state at the same time. There are four different fundamental interactions, summarized in Table 1.2.

[2]Renormalization is a method to remove formal infinities from all experimental predictions of a theory and deals with parameters describing large and small distance scales.

[3]The average number of bosons in a single-particle state r is given by the Bose-Einstein distribution: $\langle n_\mathrm{r} \rangle = \{\exp[(E_\mathrm{r} - \mu)/k_\mathrm{B}T] - 1\}^{-1}$. The difference to the Fermi-Dirac statistics is the minus sign in the denominator. Note that this formula yields the average number of bosons in a quantum state. To calculate this number for an energy level the degeneracy of the state must be multiplied [3].

Interaction	Coupling to	Range (m)	Bosons	Boson Mass (GeV/c^2)	Relative Strength
strong	quarks, gluons	10^{-15}	8 gluons	0	1
weak	quarks, leptons	10^{-18}	$\mathrm{W}^{\pm}, \mathrm{Z}^0$	$\approx 10^2$	10^{-5}
elektromagn.	elektr. charged	∞	γ	0	10^{-2}
gravity	mass	∞	(graviton)	0	10^{-38}

Table 1.2: The gauge bosons of the fundamental forces. The graviton is shown in parenthesis because it has not been observed so far. Relative strengths are approximate and taken from [6].

The *gravitation* keeps us on the ground as well as the moon bound to the earth and the latter to the sun. It is the dominant force at the scale of the universe since it couples to all particles even though it is the by far weakest of the forces, compare the relative strengths of the forces in Table 1.2. On the other hand the gravitation most likely does not play any substantial role in sub-atomic scales due to its weakness. The gravitation has always an attractive potential and is supposedly mediated by the graviton, a spin 2 boson. Nevertheless, so far it was not possible to describe this force within the standard model. Also, the reason why gravity is so much weaker than all the other forces is one of the biggest unsolved questions in physics, the hierarchy problem.

Electromagnetic interactions are mediated by the exchange of photons γ. They couple to all electrically charged particles. By this force all atoms and molecules are bound and an indirect result of it are also all intermolecular forces. The theory of the electromagnetic interaction is the theory of Quantum Electrodynamics (QED). Predictions by QED and measurements are in extremely precise agreement.

The mediators of the *weak* force are the $\mathrm{W}^{\pm}$ and Z^0 bosons with masses of around 100 GeV/c^2. These huge masses result in very short ranges and are the reason why the weak force is the only one that does not exhibit any bound states. However, it is responsible for decay processes such as the β-decay of unstable nuclear isotopes. Within the concept of the electro-weak unification those two forces can be described as different aspects of the same theory. Above a given temperature both forces will merge into a single one. The originators of this theory, Glashow, Salam and Weinberg, were awarded with the Nobel Prize in Physics in 1979.

Finally, the gauge bosons of the *strong* interaction are the gluons. Although their mass is zero the range of the strong interaction is limited to very short distances of the order of a fm. The reason is that—in contrast to all the other forces—the exchange bosons of the strong interaction do themselves carry the charge of the strong force, the color. Thus, also gluons interact by the exchange of gluons.

The color comprises three times two different types: r, b and g, standing for *red*, *blue* and

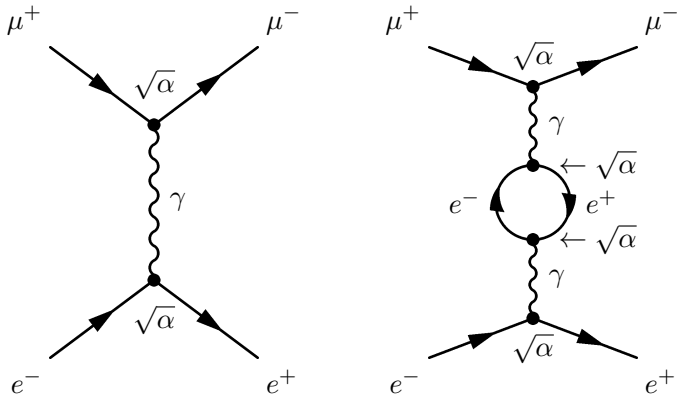

Figure 1.1: Two Feynman diagrams of first (left) and second (right) order electromagnetic $e^+e^- \to \mu^+\mu^-$ scattering processes. Compare to e.g. [7].

green, and the corresponding anti-colors $\bar{r}$, $\bar{b}$ and $\bar{g}$. As already mentioned in the previous section, this property surely does not correspond to any visible color. Merely the properties of this charge led to its descriptive name. All compound quark states are color neutral, no free color charge has ever been found. There are two ways to achieve color neutrality: combine three quarks (qqq), each of a different color and they will add to "white". Or combine a quark of a given color with an antiquark of the corresponding anti-color ($q\bar{q}$). The former system corresponds to a class of particles to which, e. g., the proton (uud) and the neutron (udd) are belonging to, the *baryons*. Bound quark-antiquark states such as the pion are called *mesons*; all compound particles held together by the strong interaction, i. e., baryons and mesons, are further summarized as *hadrons*.

Such observations led to the development of a theory for the strong interaction, called Quantum Chromodynamics (QCD). As the name tells, QCD is conceptually similar to QED, comprising a massless vector boson as mediator.
Gluons carry one color and one anti-color. One would expect $3^2 = 9$ different combinations and thus 9 different gluons. However, according to group theory, the $3 \otimes 3$ color combinations form two multiplets of states, a singlet and an octet: $1 \oplus 8$. The singlet turns out to be colorless: $\sqrt{1/3}(r\bar{r} + g\bar{g} + b\bar{b})$ and is invariant against a rotation of colors. Thus, it cannot be exchanged between color charges. Depending on the used conventions, the remaining eight color-exchanging gluons may be chosen as: $r\bar{g}, r\bar{b}, g\bar{b}, g\bar{r}, b\bar{r}, b\bar{g}, \sqrt{1/2}(r\bar{r} - g\bar{g}), \sqrt{1/6}(r\bar{r} + g\bar{g} - 2b\bar{b})$ [7].

On the one hand the existence and the term scheme of bound heavy quark-antiquark states, called *quarkonia*, immediately suggest a similar potential than that of QED, see Chapter 2. On the other hand a pure Coulomb potential would allow for free color charges, i. e., free quarks or gluons. But no free quarks have ever been observed, in fact, even hard parton scattering processes do not separate a parton from the rest of the hadron. To the contrary *jets*, i. e., sprays of color-neutral particles are created in such reactions. Also, there is always only one type of a

given hadron and not various, each with a different color.
Such observations lead to the conclusion that the quark potential cannot be of a pure Coulomb type. Instead, one assumes the following form:

$$V_s(r) = -\frac{4}{3}\frac{\alpha_s}{r} + kr. \tag{1.1}$$

The first Coulomb-like term corresponds to single-gluon exchange while the factor 4/3 comes from the eight gluon states averaged over three colors. A factor two enters the definition of α_s for historical reasons [5]. The latter is the coupling "constant" of QCD which will be discussed in the next paragraph. The second part of the potential increases linearly with distance and describes the discussed observations: quarks are always confined in bound objects, a phenomenon called *confinement*. If one pulls a quark-antiquark pair apart, the energy stored in the gluon field in between will increase until it is enough to create a new quark-antiquark pair, so again two color-neutral objects are the result. A further discussion of Eq. (1.1) follows in the next chapter, Section 2.2.2.

The coupling constant of QED, α, often called fine-structure constant, is approximately 1/137. Figure 1.1 shows two Feynman graphs of first (left panel) and second (right panel) order $e^+e^- \to \mu^+\mu^-$ scattering processes. In such graphs, the points where three or more particles intersect are called *vertices*. Each vertex corresponds to a term in the transition matrix element containing structure and strength of the interaction. The transition amplitude at each vertex contains a factor proportional to the square root of the corresponding coupling constant. In the examples in Fig. 1.1 this is the fine-structure constant α. Thus, the probability of the first order process shown on the left panel in this figure is proportional to $\sqrt{\alpha} \cdot \sqrt{\alpha} = \alpha$, that of the second order process to α^2. The cross section of the scattering process $e^+e^- \to \mu^+\mu^-$ is therefore dominated by the left diagram while the right one only is a small correction of $\mathcal{O}(1/137)$.

In principle this also holds for processes mediated by the strong interaction provided that $\alpha_s \ll 1$. First, α_s is not really a constant, but it is strongly dependent on the momentum transfer Q^2 of the given process:

$$\alpha_s = \frac{12\pi}{(33 - 2n_f)\ln(Q^2/\Lambda^2)}. \tag{1.2}$$

Where n_f is the number of quark flavors and Λ the QCD scale, a free parameter, $\Lambda \approx 200$ MeV/c [8]. Second, for large ranges of Q^2 α_s is indeed of the order of 1. For soft processes with a low Q^2 and an α_s around 1, higher order terms in ${\alpha_s}^2$, ${\alpha_s}^3$, ... contribute as much as the lowest order term to the cross sections. On the other hand, very hard interactions, where the high Q^2 leads to an $\alpha_s \ll 1$ the picture of a single-gluon exchange analogous to the electromagnetic interactions shown in the diagrams in Fig. 1.1 becomes applicable. Thus perturbation theory in QCD is only calculable for hard processes.

Consequent upon the de Broglie wave length[4] the momentum transfer is equivalent to a distance: the norm of the 4-momentum of the mediating exchange boson is $|\mathbf{P}| = \sqrt{(\Delta E)^2 + Q^2}$. Large distances correspond to small values of Q^2, small distances to large Q^2. Therefore, at decreasing distance the coupling constant vanishes—the tightly packed quarks inside hadrons appear to be quasi-free. This phenomenon is called *asymptotic freedom*. Likewise, the coupling increases with growing distance, the quarks are confined in the hadrons.

1.2 Limitations of the Standard Model

Although the standard model of particle physics provides a very successful description of the fundamental particles and interactions there are several limitations. There are 18 free parameters [7] such as fundamental masses and coupling constants which are not defined by the theory and must be delivered by the experiment. It is also unclear why there are exactly three families of quarks and leptons and why there are six of each. Also, so far it was not possible to include the gravitation to the model. A topic which is currently being heavily investigated is the origin of the mass of the elementary particles. The *Higgs* mechanism provides an explanation, postulating the existence of a new gauge boson, the Higgs particle. The search for this particle is ongoing and one of the main tasks of the LHC accelerator at CERN, see Chapter 3.
Interestingly, the world of the smallest things and that of the biggest—particle physics and astronomy—are closely connected. Fundamental questions in astronomy may be answered by particle physics experiments: the huge matter-antimatter asymmetry in the universe, i. e., the existence of everything that we can see is one of them. Other unsolved problems are the searches for dark matter, needed to explain the rotation velocity of the galaxies, and the dark energy, necessary to explain the expansion of the universe. Also, when trying to understand the evolution of the universe there is no way around particle physics, as will be discussed in the next section.

1.3 Quark-Gluon Plasma

Another possibility to observe quasi-free quarks is by the creation of a *quark-gluon plasma* (QGP) [9]. This is a state of matter in which hadrons are dissolved and their constituting quarks and gluons freely move in a given volume. The phenomenon of asymptotic freedom suggests two possibilities to create such a state: to reach a vanishing coupling constant either the energy must be increased or the distances decreased. The former can be achieved by increasing the temperature, the latter by increasing the density.
Figure 1.2 shows the (μ_B, T) phase diagram of strongly interacting matter. Analogous to phase

[4] All particles can be described by matter waves. The de Broglie equation relates the wave length λ of any

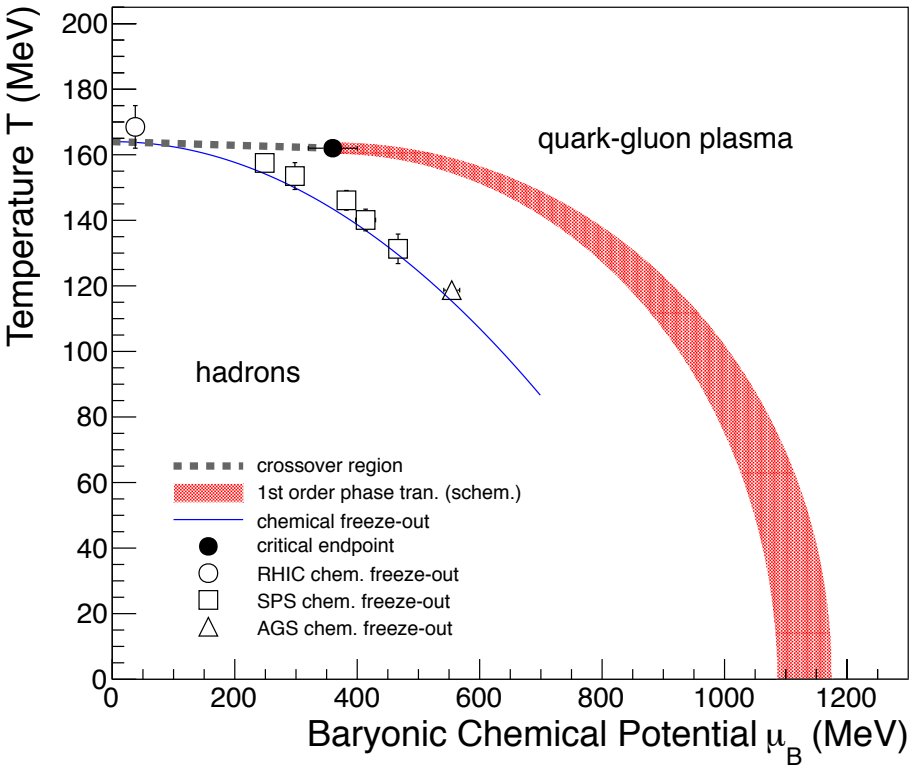

Figure 1.2: The phase diagram of strongly interacting matter. The red band is a sketch of the first order phase transition, the dashed line represents the crossover region. The circle depicts the conjectured critical endpoint separating the two kinds of phase transitions and has been calculated by lattice QCD [10]. The existence and exact position of this point is still unclear, various different predictions exist [11]. T_c at $\mu_B = 0$ is taken from [10], μ_B at $T = 0$ can be estimated with the MIT bag model, see [12]. The blue line corresponds to the chemical freeze-out in heavy-ion collisions and is a fit of a statistical model to the data (open symbols) [13, 14]. The errors of the data points are partially smaller than the markers.

diagrams of ordinary matter there is a phase transition between a hadronic phase and the QGP phase, sketched with the dashed gray line and the red band. Lattice QCD calculations [10] allow to predict the critical temperature T_c at zero baryonic chemical potential[5] by discretization of the four-dimensional space time, putting quarks on the lattice points and the gauge field on the links. Depending on the details of the calculations the results for T_c range from 146 to 170 MeV [10, 15, 16, 17, 18]. Another interesting point, μ_B at $T = 0$ can be roughly estimated with the MIT bag model [12]. The red band in Fig. 1.2 is only a sketch since its actual position is hard to calculate. A critical endpoint separating a first order phase transition from a crossover

particle to its 4-momentum $\mathbf{P}$: $\lambda = h/|\mathbf{P}|$, h is Planck's constant.

[5] The baryonic chemical potential $\mu_B = \left(\frac{\partial U}{\partial N_B}\right)_{S,V}$ is defined as the partial derivative of the total internal energy U with respect to the number of baryons N_B in a given volume V at constant entropy S.

region[6] is suggested by lattice QCD [10, 11]. There are three different places where one could expect a QGP:

- In the early universe: the universe is assumed to be created in a cosmic big bang expanding from a singularity at time zero. Today, measurements of the cosmic microwave background provide the current temperature of the universe of 2.725 K $\approx 2.3 \cdot 10^{-13}$ GeV [19]. It is expected that the QCD critical temperature was passed roughly 10 μs after the big bang. In the phase diagram in Fig. 1.2 this evolution corresponds to a path at low μ_{B}, close to the y-axis, from high to low temperatures. Figure 1.3 sketches the timeline of the universe including several important steps in its evolution.
- In the core of neutron stars: there the gravitational pressure and with it the baryonic chemical potential is believed to exceed the critical value of μ_{B}, pushing the nucleons so tightly into each other that the constituting quarks cannot be assigned to one or another nucleon.
- In high-energy collisions of heavy nuclei: such processes can either happen in the collision of heavy cosmic ray particles with some other heavy particle or in controlled collisions of heavy ions in accelerator experiments. The latter will be introduced in more detail in the next section.

1.4 Heavy-Ion Physics

When two heavy ions[7] collide, their matter is decelerated. This intuitively reasonable effect, called *nuclear stopping*, depends on the actual collision energy. At low collision energies, of the order of a few to a few tens of GeV per nucleon[8], the nuclei tend to stop each other, see the left panel of Fig. 1.4. Moderately high temperatures and very high baryonic densities are the result. On the other hand, at increasing lab energies above about 100 GeV the nuclei more and more pass through each other leaving extremely high temperatures but low baryonic densities behind, see the right panel of Fig. 1.4. Thus, heavy-ion collisions are an excellent method to study the QCD phase diagram shown in Fig. 1.2.

When looking at the space-time evolution of high-energy heavy-ion collisions, depicted in Fig. 1.5, one can distinguish various stages. In that figure on the left-hand side, from bottom to top the Lorentz-contracted nuclei are shown right before the collision, at $\tau = 0$, the moment the collision takes place, at $\tau = \tau_0$, the time when the QGP has been created, and after the

[6] A phase transition is of nth order if the $(n-1)$th derivative of a thermodynamic variable is discontinuous. If variables change rapidly but without an explicit discontinuity the transition is called cross-over.

[7] Here, *heavy* corresponds to atoms heavier than helium, *ion* in the scope of high-energy physics usually refers to fully ionized, *stripped*, nuclei.

[8] See Appendix C for definitions of kinematical variables.

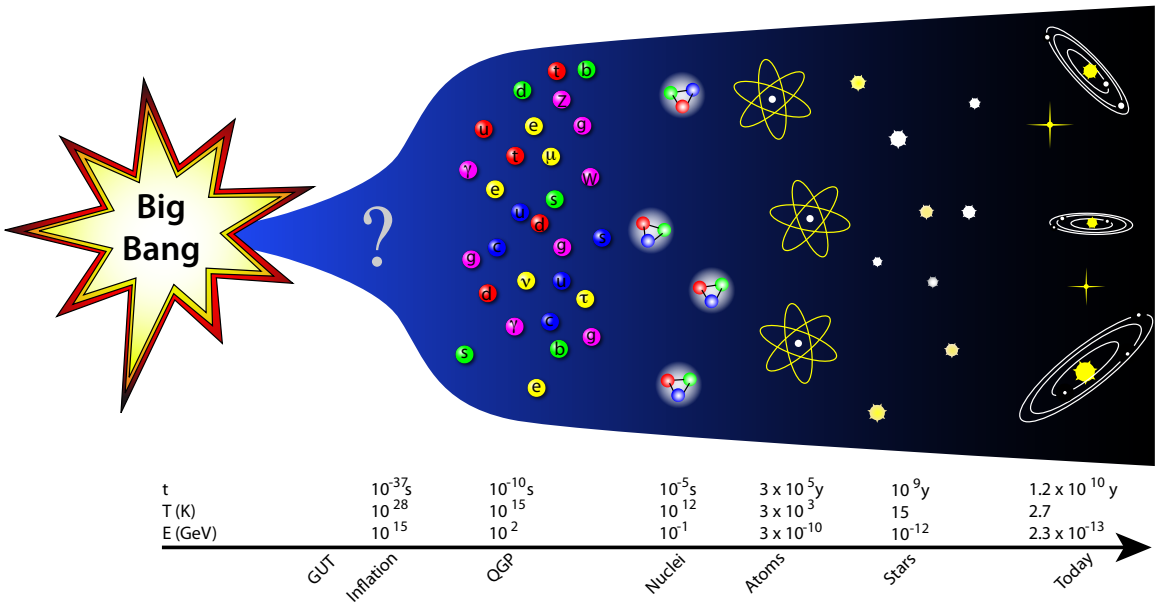

Figure 1.3: Sketch of the timeline of the big bang including several important steps in the evolution of the universe. Rough times with corresponding temperatures in Kelvin as well as in GeV are given. Numbers are taken from [20].

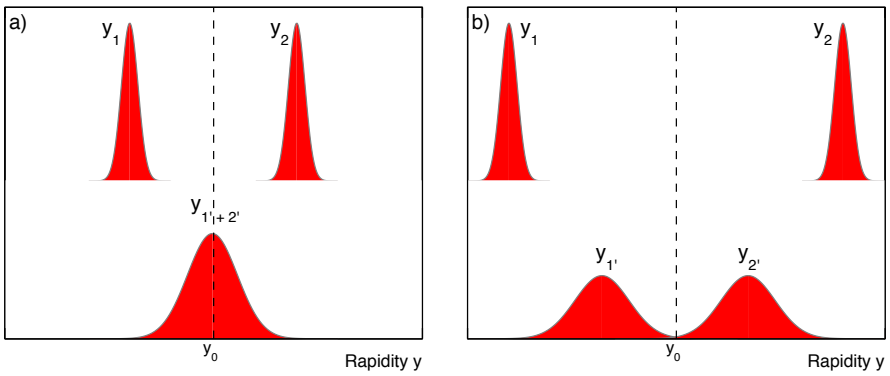

Figure 1.4: Illustration of the nuclear stopping by means of the rapidity distributions of the baryons before (top) and after (bottom) the collision of the nuclei 1 and 2. The left panel corresponds to moderately high collision energies while the right panel corresponds to high energies. Both examples correspond to two colliding nuclei of the same species in the centre-of-mass system.

phase transition back to hadronic matter. These stages are described in more detail on the right-hand side of Fig. 1.5. Here the two incident nuclei travelling with almost speed of light are drawn as the two red lines in a space-time diagram. At the origin of the diagram the nuclei hit and start passing through each other. In this initial stage very hard processes with high momentum transfer occur. These can, as said, be calculated perturbatively. As an example the

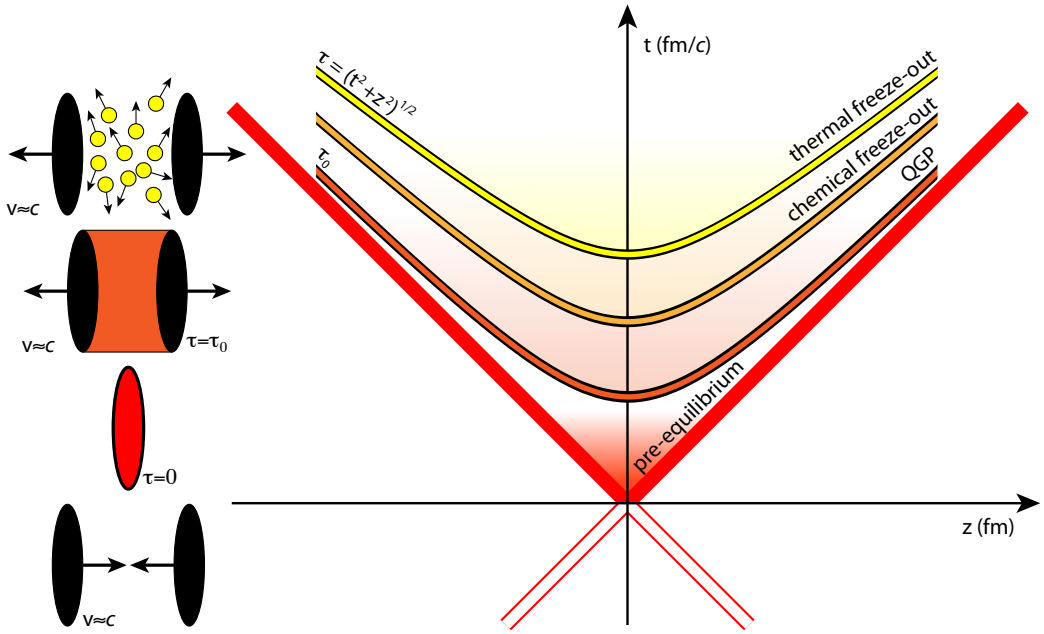

Figure 1.5: The space-time evolution of a heavy-ion collision. Left-hand side: various stages of the collision, right-hand side: schematic space-time diagram depicting the evolution of the collision.

creation of heavy quark-antiquarks such as c plus $\bar{c}$ and b plus $\bar{b}$ is predominantly happening in this moment.

Multiple scattering processes among the nucleons and their constituents as well as of the bulk of produced particles lead to a thermal equilibration of the medium, a *fireball* of strongly interacting matter, the quark-gluon plasma. Being surrounded by the vacuum, the QGP expands and cools down. Hydrodynamic models are very successful in describing the evolution of the medium (see [21]). Therein, the medium is described only with the thermodynamic equation of state, no microscopic description is necessary.

At some point the temperature has dropped so far that the phase boundary is crossed and the medium hadronizes. In the hydrodynamic description the corresponding equations have to be translated into kinetic particle spectra. This part is called *freeze-out*. Theoretical calculations usually apply the so-called Cooper-Frye approach, described in [22].

A little later the kinetic energy of the produced particles is too low to allow for further inelastic collisions. From this moment on all abundances and particle ratios are fixed. This is called the chemical freeze-out. In the phase diagram, Fig. 1.2, the temperature and baryonic chemical potential of this point is shown for various experiments.

Finally the cloud of particles gets so dilute that also elastic collisions cease. This is called the kinetic freeze-out. Thereafter, the kinematical distributions are fixed.

1.5 Signatures of the QGP

With a lifetime of the order of a few fm/c certainly the QGP is not directly observable. Instead, various signatures have been proposed interpreting the final state, i. e., the produced particles and their spectra. As an overview, some of the mostly discussed signatures shall be briefly introduced:

Production rates of quarkonia Various mechanisms are debated that could influence the measured rates of a group of particles called quarkonia. This measurement is the scope of this thesis and will be discussed in more detail in Chapter 2.

Energy loss of particle jets Very hard parton scattering can lead to a back-to-back spray of particles, so-called jets. Such processes occur both in elementary reactions such as proton-proton collisions as well as in heavy-ion collisions. The scattering process happens in the initial stage of the collision. In heavy-ion collisions, depending on its position relative to the fireball it might happen that one jet traverses only little material while the other one has to make its way through a good part of the QGP. By this the jet will be modified, i. e., the scattered parton will suffer from energy loss in the medium which is made up of quasi-free color charges. Extensive studies are ongoing in this field. These started from the observation of suppressed high-p_{t} particles, compared to proton-proton interactions, scaled by the corresponding number of binary nucleon-nucleon collisions. Then, azimuthal angular distributions of charged particles relative to a high-p_{t} trigger particle showed—depending on the p_{t} ranges—various effects on the peak at 180 degrees (the *away-side* peak). Jet broadening, quenching or even cone-like structures have been found [23, 24].
Current investigations include 3-particle correlations as well as $\Delta\eta, \Delta\phi$ 2-dimensional 2-particle correlations.

Electromagnetic signals Photons and dileptons do not interact strongly. Thus they can leave the fireball with much less interactions and carry informations about the initial stages of the collision. Direct photons from the first hard parton collisions can be measured to characterize these processes, thermal photons may serve as a thermometer of the medium. Low-mass dileptons from vector mesons such as the ρ could give hints for the restoration of chiral symmetry[9] [25, 26].

[9] Chiral symmetry is a symmetry of QCD. Its breaking can explain the mass of the pion. It is assumed that in a QGP chiral symmetry may be restored. Hints for chiral symmetry restoration are therefore an indirect measurement of the QGP.

Collective flow Hydrodynamical models deal very well in describing the Fourier coefficients of the charged particles momentum distributions. These coefficients are a measure for directed flow, i. e., a preferred direction, and elliptic flow, i.e. a preferred plane caused by non-central collisions. Recent data analysis [27] reveal that even higher order coefficients have an important impact. Such models may therefore provide informations about the conditions at early stages of the collision, such as the pressure and viscosity of the medium.

Fluctuations Event-by-event fluctuations of various observables such as particle multiplicities or transverse momenta are sensitive to underlying degrees of freedom. They might be characteristic for phase transitions in general and especially for freeze-out close to the critical endpoint in the QCD phase diagram. The goal of the analysis of this signature is therefore also a detailed study of the aspects of the phase diagram [28, 29, 30].

Interferometry Originally developed by Hanbury-Brown and Twiss (HBT) for the measurement of space-time structures in astrophysics via optical intensity interferometry so-called *Bose-Einstein correlations* have become a useful tool also in particle physics. Same bosons are indistinguishable. When two identical bosons are emitted from different parts of a source it cannot be distinguished which of the bosons comes from which of the origins. Therefore the particles interfere with each other. From the resulting correlation function one can extract the spatial dimensions of the source, which is the fireball in this case. Signatures for a QGP phase might be found by analyzing the HBT parameters under varied collision conditions, e. g., the centre-of-mass energy.

1.6 Scheme of this Work

After this short introduction the topical environment of this work is set. The following Chapter 2 assesses the current status of the theoretical understanding as well as the existing experimental data of quarkonia, their properties, and especially their production mechanisms, both in proton-proton (pp) and heavy-ion (A–A) collisions. This will motivate the measurements done for this work, which are carried out with the experiment ALICE. Chapter 3 therefore contains all necessary details of that experiment. In the course of this work a possible improvement of a specific part of the experimental procedure was studied. The outcome is presented in the second half of that chapter.
As the main part of this thesis, Chapter 4 and Chapter 5 describe the analyses carried out for this thesis. Both chapters conclude with the presentation of the results of the analyses. Comparisons to theoretical predictions and to data from other experiments are also given. A summary closes this thesis.

Chapter 2

Quarkonia

Bound hadronic states made of heavy quark-antiquark ($Q\bar{Q}$) pairs are called *quarkonia*. Due to the huge mass of the quarks quarkonium spectroscopy can be described by non-relativistic potential models [31]. While $c\bar{c}$-pairs are further called *charmonia* and $b\bar{b}$-pairs *bottomonia* the life time of the top quark is too small to allow for the formation of bound states; hence, no such state has been measured yet.
Furthermore, again due to their high masses, heavy-quark pairs are expected to be created predominantly in the early stage of hadronic collisions. Thus, quarkonia can be utilized as a very promising probe to study the quark-gluon plasma (QGP). The evolution of this state of matter is expected to take place in later stages of the collision and is therefore believed to modify the measured rates of quarkonia. Before being able to carry out such measurements in A–A, the elementary production processes in hadronic collisions have to be understood.

2.1 Discovery

Heavy quarks and their bound states can only be produced in the laboratory when enough powerful accelerators are available. So the discovery of quarkonia began in the 1970s; it took about two more decades to prove the existence of the top quark.

2.1.1 Charmonia

In 1970 only three quark flavours were known: the u, d and s. But various experimental results, such as the absence of flavour-changing neutral currents, were difficult to interpret theoretically. Glashow, Iliopoulos and Maiani therefore proposed [32] (within the so-called GIM model) the introduction of a new, fourth, quark of charge $+2/3$: the charm quark c. By this idea the experimental constraints could be explained with the interference of decay channels. This

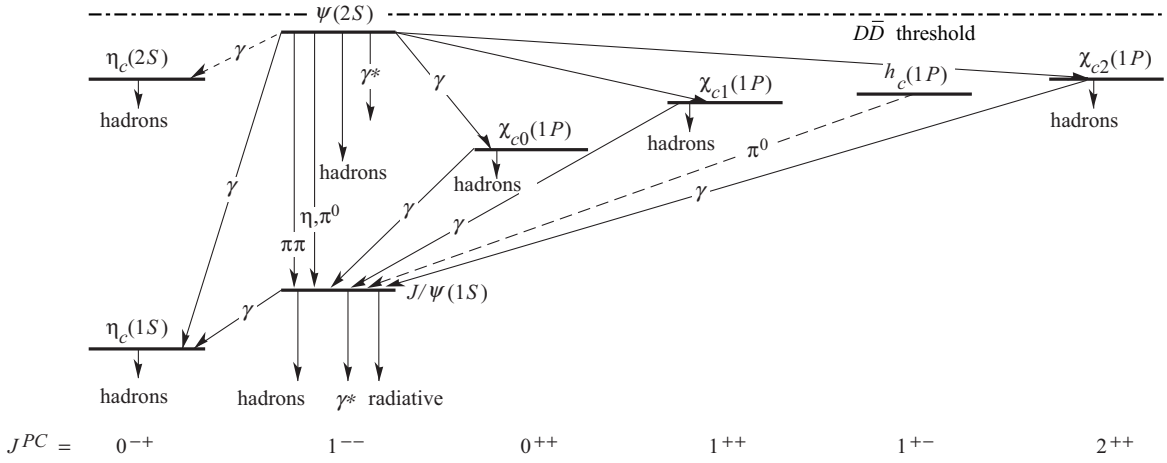

Figure 2.1: Term schema of the charmonium family including transitions. Different spin J and $\mathcal{P}$ and $\mathcal{C}$ symmetry states are drawn horizontally, the mass vertically [36].

fourth quark also increased the symmetry of the schema of elementary particles which then formed two complete lepton and quark doublets.

In early 1974 Gaillard and Lee were able to deduce a first estimate of the—at that time still hypothetical—c quark mass as a consequence of the small $\mathrm{K_L^0} - \mathrm{K_S^0}$ mass difference [33]. The discovery of a bound $\mathrm{c\bar{c}}$ state followed few months later in the same year, almost simultaneously by two groups, suggesting the names J [34] and ψ [35], respectively. Both groups found a narrow resonance at a mass of 3.1 GeV/c^2. At the Brookhaven National Laboratory's (BNL) 30 GeV alternating gradient synchrotron (AGS) the $\mathrm{e^+e^-}$ invariant mass spectrum in $\mathrm{p+Be} \rightarrow \mathrm{e^+e^-}+X$ reactions was studied while at the Stanford Linear Accelerator Center (SLAC) $\mathrm{e^+e^-} \rightarrow \mathrm{e^+e^-}$, *hadrons and* $\mu^+\mu^-$ reactions lead to the observation of a very sharp peak with a width below their experimental resolution.

This particle, further called J/ψ, corresponds to the $1S$ $\mathrm{c\bar{c}}$ state, see Fig. 2.1. The discovery of the c quark was a big success of the standard model of particle physics and honored by the Nobel Prize in 1976 to the representatives of both groups.

2.1.2 Bottomonia and the Top Quark

Only three years after the discovery of the c quark a sharp dimuon resonance at 9.5 GeV/c^2 was observed in 400 GeV proton-nucleus collisions at the Fermi National Accelerator Laboratory [37]. Since in the meantime the τ and by this a third family of leptons was discovered, this resonance was interpreted as evidence for a fifth quark in a third family of such. The broad width of 1.16 GeV/c^2 of the resonance was also quickly interpreted as being, in fact, several narrow resonances of the $\mathrm{b\bar{b}}$ system, analogous to the J/ψ and ψ' states in the charmonium family [38]. This structure was found shortly after as higher statistics data was available [39].

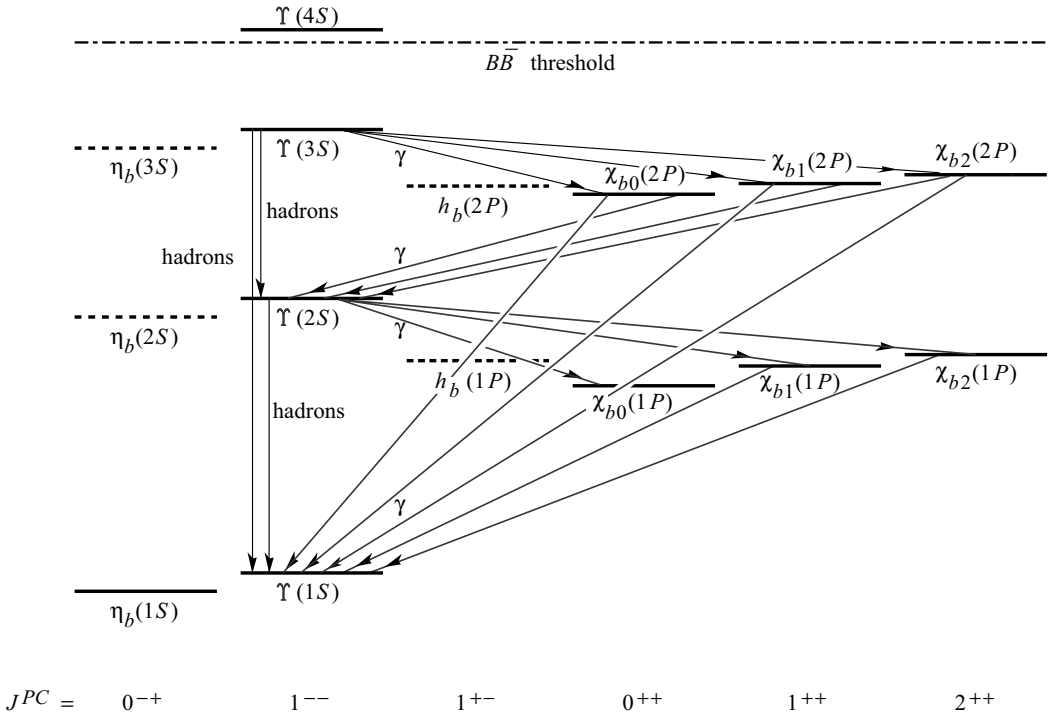

Figure 2.2: Term schema of the bottomonium family including transitions. Different spin J and $\mathcal{P}$ and $\mathcal{C}$ symmetry states are drawn horizontally, the mass vertically. The height of the dashed horizontal line shows the $B\bar{B}$ threshold [36].

The corresponding particles were called Υ, Υ' and Υ'' (see Fig. 2.2).
After the discoveries of the τ lepton and the b quark a sixth quark was expected to complete the quark pair of the third family and to be discovered soon. However, this quark called t (top) was not discovered earlier than in 1995 [40]. Due to its very high mass of around 171.2 GeV/c^2 [36] the first accelerator delivering sufficiently high particle energies was the Tevatron at Fermilab. Another consequence of this huge mass is that the top quark is extremely short lived, with a lifetime of only $0.5 \cdot 10^{-24}$ s [41]. This is shorter than the formation time of hadrons, which is of the order of the QCD timescale $\Lambda_{\mathrm{QCD}}^{-1} \sim 10^{-23}$ s. So top-flavored hadrons or $t\bar{t}$ quarkonium states do not form [42].

2.2 Properties

Before facing the problem of quarkonia production and its measurement—which is the main topic of this thesis—a couple of basic properties of these particles shall be discussed. This is not only necessary for the understanding of the following parts of the discussion but also insightful in itself.

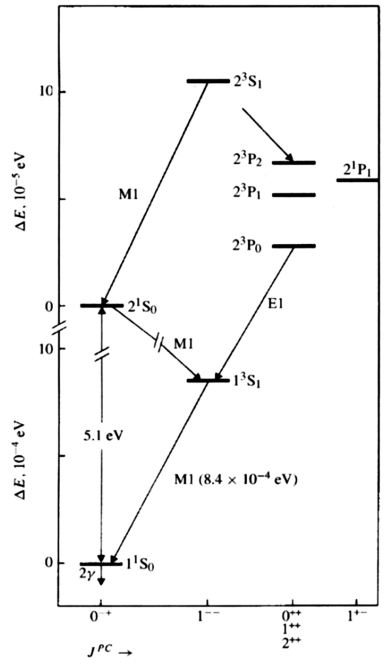

Figure 2.3: The energy level diagram of the positronium system; The lowest level P state is labeled 2P in atomic physics, corresponding to 1P in nuclear physics [5].

2.2.1 Positronium as an Analogon

The simplest bound atomic system is the Hydrogen atom. It consists only of one proton and one electron. In first approximation the non-relativistic Schrödinger equation can be used to calculate the binding energy levels of that system:

$$\left(-\frac{\hbar^2}{2m_{\text{red}}}\Delta - \frac{\alpha\hbar c}{r}\right)\psi(\mathbf{r}) = E\psi(\mathbf{r}). \tag{2.1}$$

The static Coulomb potential has been used in the Hamilton operator, $\hbar = h/2\pi$ is the reduced Planck constant, m_{red} the reduced mass[1] of the system and c the speed of light. The fine-structure constant is labelled as α. The number of nodes in the radial wave function $\psi(\mathbf{r})$ and the orbital angular momentum determine the principle quantum number n, the solutions for the energy levels turn out to be:

$$E_n = -\frac{\alpha^2 m_{\text{red}} c^2}{2n^2}. \tag{2.2}$$

The positronium on the other hand is a bound state of an electron with a positron. Its binding energy levels are calculated analogous to the hydrogen atom but with a different reduced mass

[1] With the concept of the reduced mass $m_{\text{red}} = \frac{m_1 m_2}{m_1+m_2}$ a two-body problem can be solved as a one-body problem of the relative movement and the problem of the movement of the centre of mass.

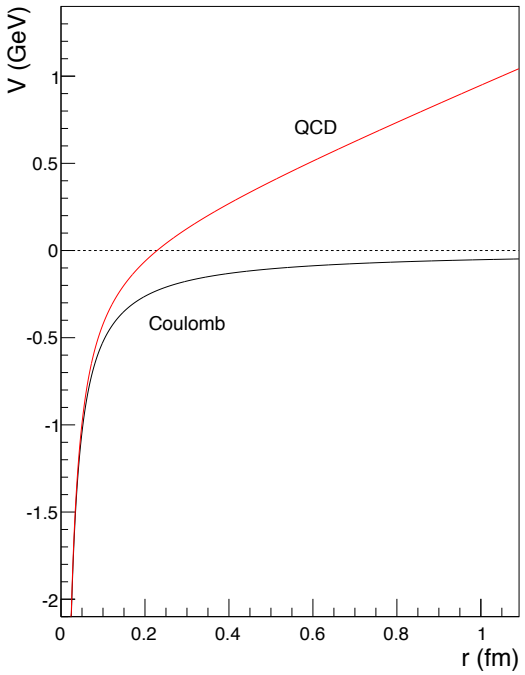

Figure 2.4: The QCD potential (red line), Eq. (1.1), for coupling $\alpha_s = 0.2$ and string tension $k = 1.0$ GeV/fm. The black line shows for comparison the Coulomb part of the potential without the term kr.

m_{red} leading to smaller energy levels:

$$E_n = -\frac{\alpha^2 m_e c^2}{4n^2}. \tag{2.3}$$

In both systems these levels show a fine structure into S, P, etc. states of different orbital angular momentum and a hyper-fine structure into triplet ($^3S_1$) and singlet ($^1S_0$) states. The origin of these structures are first the spin-orbit interaction and second the spin-spin interaction. Because the magnetic moment of the electron is much larger than that of the proton, in the positronium system both relativistic effects are of similar magnitude, see the positronium energy level diagram in Fig. 2.3.

2.2.2 Quarkonium Levels

The positronium is a valuable system to test the QED: both the electromagnetic transitions as well as the lifetime of the system are precisely calculable. Its energy-level diagram is shown in Fig. 2.3, showing the structures discussed above. A comparison of this diagram with the schemas of the charmonium (Fig. 2.1) and bottomonium (Fig. 2.2) systems shows various similarities. This not only supports the interpretation that the J/ψ and Υ families represent

the quantum states of bound fermion-antifermion pairs. Furthermore it provides the possibility to investigate the functional form of the QCD potential and the values of its coefficients. A closer look into the spectra shows good analogy between states of the two lowest principle quantum numbers. Higher states in the quarkonia systems, corresponding to larger binding radii, exhibit large deviations from the $1/n^2$ behavior of the positronium. This circumstance and the phenomenon of the confinement of color charges lead to the assumption that the $q\bar{q}$ potential has a Coulomb-like form at small distances but differs from that at larger distances. Plotting the total angular momentum J of baryons and mesons against the squared particle mass shows a linear dependence, indicating a linear potential at large distance [5].
An ansatz for the quark potential is thus Eq. (1.1) as introduced in Chapter 1.1.2. It is worth noting that the energy level diagrams of the charmonia and bottomonia are very similar; hence, the potential is—as expected—flavor independent. Figure 2.4 shows a plot of a pure Coulomb-like potential and the QCD potential against the distance r. Here, a coupling of $\alpha_\mathrm{s} = 0.2$ and a string tension of $k = 1.0$ GeV/fm have been used (as in [5]). With this potential, the masses of the c and b quarks, and the time-independent Schrödinger equation it is possible to calculate the mean radii of the quarkonium states. These radii, as well as the other discussed properties are summarized in Table 2.1.

The lowest two and three $J^{\mathrm{PC}} = 1^{--}$ states of the J/ψ and Υ families, respectively, exhibit very narrow decay widths and life times ($\tau = \hbar/\Gamma$). Generally, the OZI (Okubo, Zweig and Iizuka) rule favors continuous quark lines and therefore the decay modes into two open heavy flavor mesons. But because the named quarkonium states have lower masses than twice the corresponding D and B mass, this decay channel is not possible. Consequently, the life times are exceptionally long and the decay into a pair of leptons, suppressed by the OZI rule, becomes more probable.

	Mass (MeV/c^2)	Total Decay Width Γ_{tot} (keV/c^2)	Branching Ratio in $\mathrm{e^+e^-}$	Average Radius r_0 (fm)
$\mathrm{c\bar{c}}$ states:				
J/$\psi(1S)$	3096.9	92.9	5.94 %	0.50
$\psi(2S)$	3686.1	304	0.77 %	0.90
$\mathrm{b\bar{b}}$ states:				
$\Upsilon(1S)$	9460.3	54.0	2.48 %	0.28
$\Upsilon(2S)$	10023.3	32.0	1.91 %	0.56
$\Upsilon(3S)$	10355.2	20.3	(seen)	0.78

Table 2.1: Properties of various quarkonia; decay branching ratios are given for $\mathrm{e^+e^-}$ here, those in $\mu^+\mu^-$ are very similar. Sources: [25, 36], the radii are taken from [43].

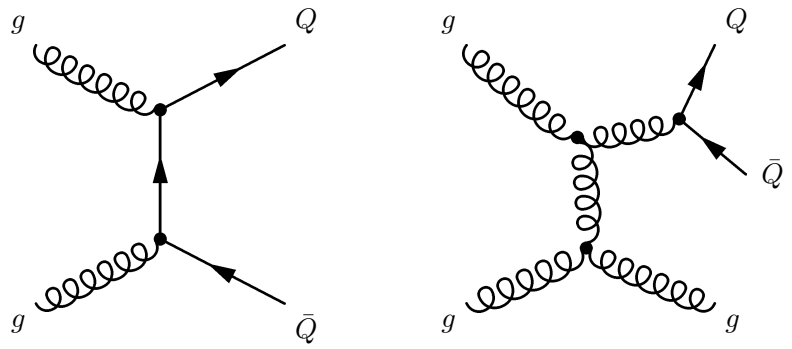

Figure 2.5: Two Feynman diagrams of first (left) and second (right) order $Q\bar{Q}$ production processes. Compare to e. g. [46].

2.3 Production

Quarkonia are highly interesting bound quark systems, both as objects of study themselves and as probes to study heavy-ion collisions (see Chapter 2.4). Yet, the fundamental production mechanisms in elementary proton-proton collisions are still being debated. In the following a brief overview of the current theoretical status shall be given. Based on the QCD factorization theorem [44, 45] the theoretical description of quarkonia production can be separated into two parts. The first one is the creation of a—yet unbound—heavy quark-antiquark pair in a hard scattering process. The second part is the formation of a bound quarkonium state.

One difficulty in the description and also in the measurement of quarkonia production in hadronic collisions is that hadrons, in practice mostly protons, are complex objects. The production of a bound heavy-quark state is thus accompained by a series of other processes, mainly on a soft scale. So far it is mostly unclear whether or not there is any interplay between the two and how this might affect the experimental results. An attempt to address this problem is part of this work and discussed in Section 2.3.3 and Chapter 5.

Finally, quarkonia can also be the decay product of other particles. This issue will be briefly adressed in the last part of this section.

2.3.1 Production of Heavy Quark-Antiquark Pairs

Due to the high c and b quark masses the corresponding production processes can be calculated perturbatively, since $\alpha_{\mathrm{s}}(m^2_{\mathrm{c,b}}) \ll 1$. The most important leading order (LO) process (at RHIC and LHC energies) is gluon fusion [47, 48] as shown with the left diagram in Fig. 2.5. With increasing collision energies the initial parton momentum fraction x necessary to produce a quarkonium decreases and reaches a region of the parton distribution function (PDF) where there are much more gluons than quarks (see Appendix C for details). As stated above, higher

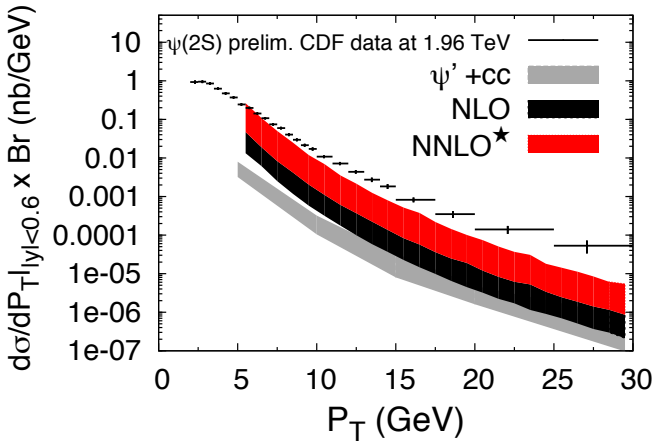

Figure 2.6: Comparison between CDF measurements of the cross sections of ψ' at $\sqrt{s} = 1.96$ TeV and predictions at various accuracies [49].

order diagrams contribute less to the total cross section. Nevertheless, the process gg $\rightarrow$ gg has such a high cross section that the next-to-leading-order (NLO) diagram shown with the right diagram of Fig. 2.5, where the $Q\bar{Q}$ pair is created in an additional gluon splitting contributes significantly [46]. Since the heavy-quark production is governed by gluon interactions the main uncertainty in the calculation of heavy-quark cross sections are the gluon parton distribution functions (PDFs). Other sources of uncertainties are the errors on the values of the c and b quark masses.

2.3.2 Models of Elementary Production

Various competing theoretical models are being developed to describe the production of quarkonia in elementary reactions such as proton-proton collisions. Three of the most popular ones are the Color-Singlet Model (CSM) [50, 47], the Color-Evaporation Model (CEM) [51, 46] and the non-relativistic QCD (NRQCD) effective field theory approach [52] (for a detailed overview of these models, see [53, 47]). One of the main differences between the models is the way the necessity of color neutrality of the final state is dealt with. This is also reflected by the models' names: in the CSM the bound state has the same quantum numbers as the initial $Q\bar{Q}$ pair; hence, only pairs that lead to a color-singlet state are allowed to bind. In the CEM the color is evaporated by a number of soft final-state interactions. In NRQCD, in addition to the conventional term which takes into account the $Q\bar{Q}$ production from color-singlet states, there is a part involving the production from color-octet states. This is often referred to as color-octet mechanism or color-octet model (COM).

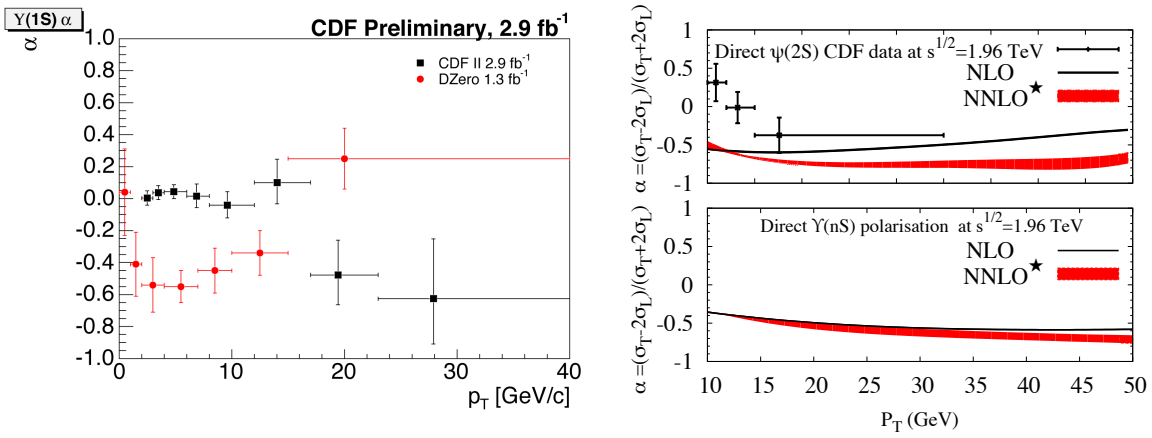

Figure 2.7: Υ polarization measurements as function of p_t from CDF and D0 [54] (left), ψ' (upper right) and $\Upsilon(nS)$ (bottom right) polarization predictions versus p_t of the CSM at various accuracies at Tevatron energies. The ψ' predictions are compared to measurements by CDF (markers), for the bottomonia, the authors do not differntiate between the different nS states [49].

Color-Singlet Model After the production of a $Q\bar{Q}$ the second step is the binding of that pair. This is only possible when the pair has a low relative momentum in its rest frame, compared to the heavy-quark mass. Otherwise the pair will fly apart and produce two open heavy flavor particles, such as D and B mesons. In the CSM it is also assumed that color and spin of the $Q\bar{Q}$ pair does not change during the binding process. Since bound states are colorless, the pair must be produced in a color-singlet state. The calculation of the differential inclusive cross section of a point-like (vanishing relative momentum) $Q\bar{Q}$ pair to form a quarkonium $\mathcal{Q}$ is therefore split into two parts [53]:

$$\mathrm{d}\sigma_{\mathcal{Q}+\mathrm{X}} = \mathrm{d}\hat{\sigma}_{\mathrm{Q\bar{Q}}(\mathbf{1},{}^{L}\mathrm{S}_J)+\mathrm{X}} |R_{\mathcal{Q}}(0)|^2. \tag{2.4}$$

Here $\mathrm{d}\hat{\sigma}$ is the perturbative part defining the probability of the creation of a pre-resonant heavy quark-antiquark pair in a color-singlet state $Q\bar{Q}(\mathbf{1})$ with the correct quantum numbers S, L, J (spin, orbital angular momentum and total angular momentum, respectively) for the quarkonium state $\mathcal{Q}$. All non-perturbative effects are being accounted for in the wave function at the origin $R_{\mathcal{Q}}(0)$. All necessary parameters can be determined from decay widths of quarkonium states. Thus, the CSM gives absolutely normalized predictions for the production rates of quarkonia in high-energy hadron collisions and has therefore strong predictive power.

However, as the first prompt[2] measurements of the differential J/ψ and ψ' cross sections became available [55] dramatic differences to the predictions of the CSM appeared, especially in

[2] One differentiates between three types of quarkonium (especially charmonium) production: *direct* production includes no feed-down at all while *prompt* production refers to the fraction of the charmonium yield coming from $c\bar{c}$. The latter excludes feed-down from b-hadron decay which itself is named *non-prompt* production.

case of the ψ'. It became clear that further mechanisms additional to the pure LO processes cannot be neglected in the calculation of the cross sections. An important contribution is coming from fragmentation processes [56], i. e., the production of a hadron within a high-p_t partonic jet. Higher order terms might also contribute significantly to the cross sections. Recent studies [49, 57] propose various different mechanisms and provide increasing agreement with the existing data.
Figure 2.6, as an example, shows a comparison between measurements by the CDF experiment of the differential ψ' production cross section and predictions of the CSM at various accuracies. The red band corresponds to a calculation including a selection of the most important NNLO processes additional to the set of NLO mechanisms and almost fits the data. The agreement between the corresponding predictions for states of the Υ family are even better [49, 58].

Another important measure to test models for quarkonia production is the polarization. The angular distribution of the quarkonia and their decay products is used to compute the polarization parameter $\alpha = \frac{\sigma_T - 2\sigma_L}{\sigma_T + 2\sigma_L}$. There σ_T and σ_L are the cross sections for transverse and longitudinal polarized quarkonia, respectively. Values of $\alpha = +1$ and $\alpha = -1$ correspond to full transverse and full longitudinal polarization while $\alpha = 0$ means no polarization. Various choices of the reference frame are possible, mostly used are the Collins-Soper frame [59] and the helicity frame [60]. As pointed out recently [61] the choice of the frame may induce a bias. Theory and experiment must be computed for different frames and compared to each other in every frame. So far the results are not yet definitive, both from theory and experiment. Recent CSM calculations predict a mostly longitudinal polarization, see the top (for the Υ family) and bottom (for the ψ') plots on the right side of Fig. 2.7. Yet the authors of the predictions [49] claim that in case of the Υ further necessary corrections are likely to change the trend towards more transverse polarization. In case of the ψ' the total yields are not being reproduced; thus, the comparison between theory and experiment is not yet conclusive. Furthermore, Υ polarization measurements with the D0 and CDF experiments at the Tevatron collider [54] are still inconsistent, see the left panel of Fig. 2.7.
Polarization is a powerful observable for comparison with theoretical predictions, yet high precision and statistics data is necessary.

Color-Evaporation Model One of the basic assumptions of the CEM is that the heavy-quark pair produced in a perturbative interaction does not necessarily have to be in a color-singlet state. Color and spin are *evaporated* by the radiation of a large number of soft gluons; thus, the quantum numbers of the initial $Q\bar{Q}$ and the final $\mathcal{Q}$ states are uncorrelated. Instead, probabilities for color charge states are deduced from SU(3) group algebra which was discussed in Section 1.1.2. One color-singlet state and eight color-octet states being possible with equal weights results in a probability for the $Q\bar{Q}$ of 1/9 to be in a singlet state.
It is furthermore assumed that all color-singlet $Q\bar{Q}$ pairs with masses below the threshold m_{OZI}

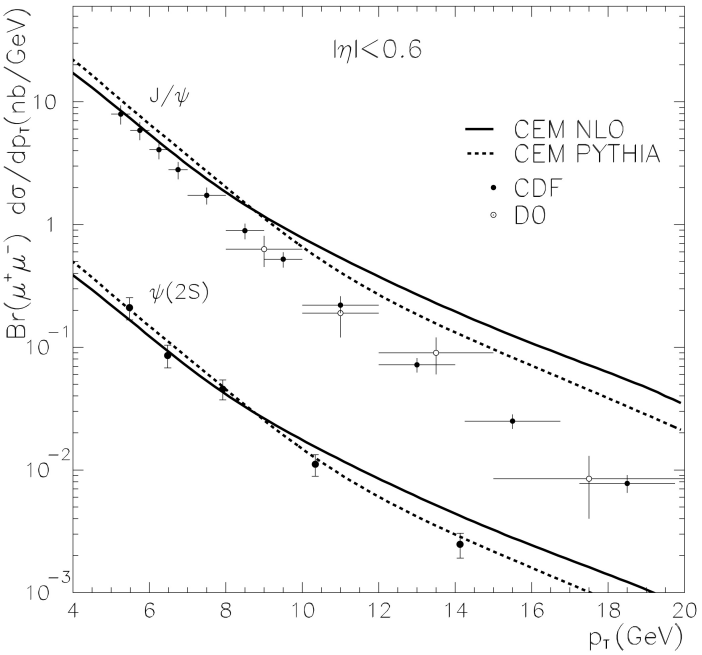

Figure 2.8: Comparison between measurements of prompt J/ψ and ψ' production cross sections versus p_{t} and their predictions from CEM[46]. Two different computations of the CEM predictions are shown: the solid line refers to a calculation using NLO matrix elements, the dashed line to a computation using the Pythia Monte Carlo event generator.

of twice the corresponding open-heavy-flavor meson (see Section 2.2.2) will form a quarkonium state [46]:

$$\sigma_{\mathcal{Q}} = \frac{1}{9} \int_{2m_{\mathrm{Q}}}^{m_{\mathrm{OZI}}} \mathrm{d}m_{\mathrm{Q\bar{Q}}} \frac{\mathrm{d}\sigma_{\mathrm{Q\bar{Q}}}}{\mathrm{d}m_{\mathrm{Q\bar{Q}}}}. \tag{2.5}$$

Where m_{Q} is the heavy quark mass, $m_{\mathrm{Q\bar{Q}}}$ the mass of the heavy quark pair. The term $\frac{\mathrm{d}\sigma_{\mathrm{Q\bar{Q}}}}{\mathrm{d}m_{\mathrm{Q\bar{Q}}}}$ is the differential parton level cross section from perturbative QCD (pQCD) and includes the PDFs of the colliding hadrons. Color-singlet $Q\bar{Q}$ pairs above the threshold m_{OZI} as well as all color-octet pairs will produce open heavy flavor particles. The cross section for their production is [46]:

$$\sigma_{\mathrm{open}} = \frac{8}{9} \int_{2m_{\mathrm{Q}}}^{m_{\mathrm{OZI}}} \mathrm{d}m_{\mathrm{Q\bar{Q}}} \frac{\mathrm{d}\sigma_{\mathrm{Q\bar{Q}}}}{\mathrm{d}m_{\mathrm{Q\bar{Q}}}} + \int_{m_{\mathrm{OZI}}}^{\sqrt{s}} \mathrm{d}m_{\mathrm{Q\bar{Q}}} \frac{\mathrm{d}\sigma_{\mathrm{Q\bar{Q}}}}{\mathrm{d}m_{\mathrm{Q\bar{Q}}}}. \tag{2.6}$$

Finally, the total charmonium and bottomonium cross sections $\sigma_{\mathcal{Q}}$ are split into the cross sections of the different species using weighting parameters. All these parameters have to be

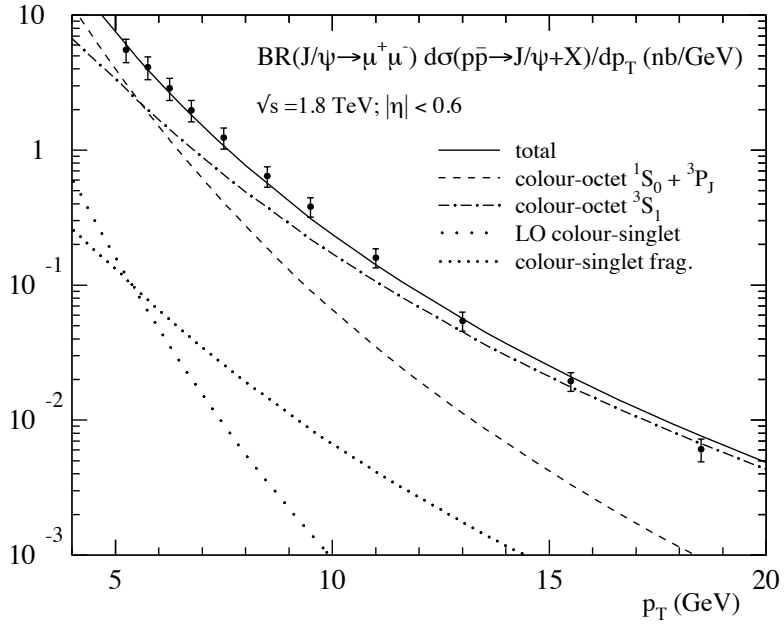

Figure 2.9: Color-singlet and color-octet contributions to direct J/ψ production in p$\bar{\text{p}}$-collisions at Tevatron energies compared to experimental data from CDF [63].

found experimentally and are independent of process and energy. Thus, also ratios of individual quarkonium cross sections such as $\sigma_{\mathrm{J}/\psi}/\sigma_{\chi_c}$ are fixed for all processes. However, measurements of this ratio vary significantly in hadro-production and photo-production. Also, this model is not able to make predictions about the polarization of quarkonia [47] and thus cannot be tested against these measurements. The predictive power of the model is therefore limited. Nevertheless, the CEM can be well tuned to describe the existing data (see Fig. 2.8) and does a reasonable job in predicting cross sections, e. g., at LHC energies [62]. Figure 2.8 shows two different computations of the differential prompt production cross sections both for J/ψ and ψ'. The solid line refers to a calculation using NLO matrix elements, the dashed line to a computation using the Pythia Monte Carlo event generator, see [46] for details. Although the fit to the ψ' data works very well (in case of the J/ψ there is a strong tension between model and data at high p_{t}), the weighting parameters have to be set to rather extreme values [47].

NRQCD factorisation approach After measurements showed that the LO CSM predictions were more than an order of magnitude too low it was realized that mechanisms forming quarkonia out of pre-resonant color-octet $Q\bar{Q}$ pairs might be important. The approach to include these channels is based on a non-relativistic QCD (NRQCD) effective field theory. This is a formulation

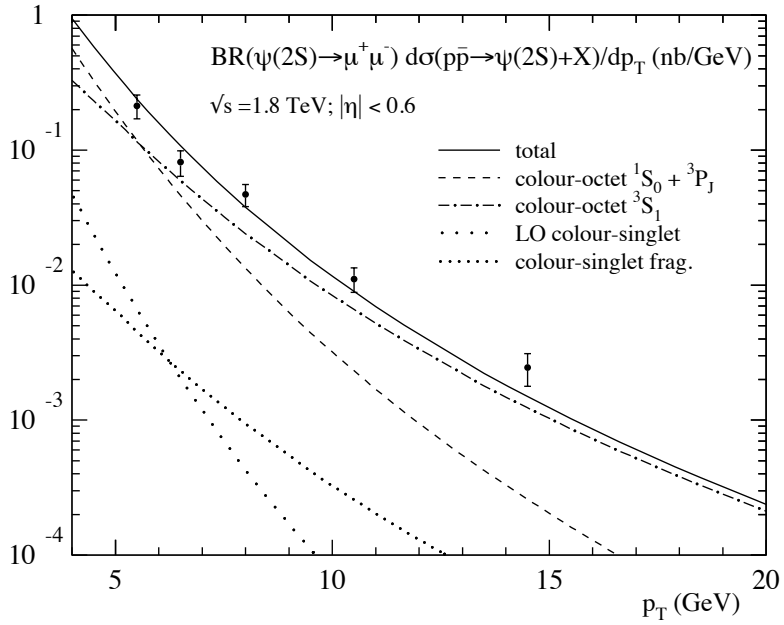

Figure 2.10: Color-singlet and color-octet contributions to direct ψ' production in $p\bar{p}$-collisions at Tevatron energies compared to experimental data from CDF [63].

of QCD in which, due to their huge masses, the heavy quark and antiquark are treated non-relativistically. The gluons and light quarks are described by the relativistic Lagrangian for normal QCD. NRQCD is based on a systematic expansion in α_s and the quark velocity within the bound state. In contrast to the CSM, $Q\bar{Q}$ pairs, produced in hard partonic short-distance interactions, occur both in color-singlet and color-octet states.

Since bound quarkonia can only be in color-neutral singlet states, color has to be radiated from an octet $Q\bar{Q}$. The transition from that pair, with the set of color and angular-momentum quantum numbers n, to the quarkonium state $\mathcal{Q}$ is described by the non-perturbative long-distance matrix element (LDME) $\langle O^{\mathcal{Q}}[n] \rangle$ [64]. In principle, NRQCD predicts an infinite number of LDME, practically one truncates the series at some level. The individual elements are determined by fits to experimental data.

With the cross section of the hard $Q\bar{Q}$ production subprocess, denoted as $\hat{\sigma}$, the cross section for the production of a given quarkonium $\mathcal{Q}$ in NRQCD is then given as [64]:

$$\mathrm{d}\sigma_{\mathcal{Q}} = \sum_n \mathrm{d}\hat{\sigma}_{\mathrm{Q\bar{Q}[n]}} \langle O^{\mathcal{Q}}[n] \rangle . \tag{2.7}$$

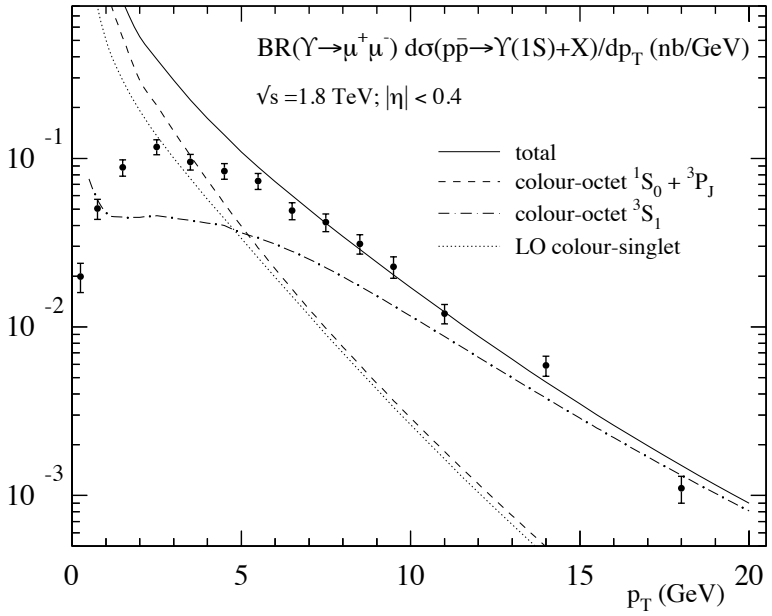

Figure 2.11: Color-singlet and color-octet contributions to direct Υ production in $p\bar{p}$-collisions at Tevatron energies compared to experimental data from CDF [63].

A drawback of NRQCD is that the factorization theorem used in formula Eq. (2.7) is lacking a detailed proof and is expected to break down at low quarkonium p_t [64]. As a result, NRQCD predictions for the total quarkonium production cross sections have to be interpreted with caution. Nevertheless, the predictions for the differential cross sections by NRQCD are very encouraging, see Figs. 2.9, 2.10 and 2.11. Therein, various color-singlet (CS) and color-octet (CO) contributions sum up to the total theoretical prediction which in all cases, i. e. for the J/ψ, the ψ' and the Υ, matches the experimental data points by the CDF experiment very well. The discussed deviation from the experiment at low transverse momenta is visible in Fig. 2.11 where also the low momentum part is shown. A recent work [65, 66] performed a combined fit to the currently available world data for the J/ψ and also found a very good agreement between the model and the data.

NRQCD predicts a strong transverse polarisation of quarkonia, see Fig. 2.12. The CDF data, on the other hand, shows the opposite trend, especially when going to high p_t; so, there are aspects of the production mechanism that are not yet understood. A possibility is that the color-singlet modes have a stronger contribution to the total yield where high-order corrections play an important role.

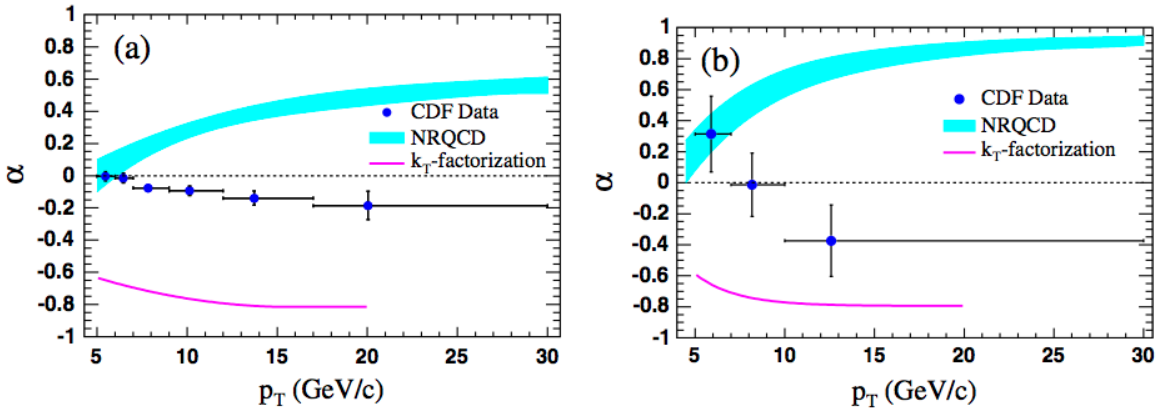

Figure 2.12: Polarization of prompt J/ψ (a) and ψ' (b) as function of p_t. The blue circles are measurements by the CDF experiment, the light blue bands are NLO NRQCD predictions including CS and CO contributions. The purple line corresponds to the model of k_t-factorization which is not further discussed here [67].

Due to the much higher mass of the b quark compared to the c quark the non-relativistic approximation by NRQCD should be more justified, Υ polarization predictions should be a thorough test of this model. Yet, the experimental situation on this is still not clear (see above), high-precision measurements of huge interest.

Recently, ALICE (see Section 3.2) measured the J/ψ polarization at 7 TeV pp collisions for the first time at that energy regime. The polarization parameters λ_θ and λ_ϕ of both helicity and Collins-Soper reference frames were obtained by measuring the azimuthal angle distributions of the decay muons in a kinematic region for the J/ψ of $2.5 < y < 4.0$ and $2.0 < p_t < 8.0$ GeV/c. The results (displayed in Fig. 2.13 which is taken from reference [66]) show a longitudinal polarization at low p_t for λ_θ in the helicity frame, and, within the uncertainties, no polarization at high p_t and all other polarization parameters in both reference frames [68]. While θ and ϕ are the polar and azimuthal angles, respectively, in both reference frames, λ_θ, λ_ϕ and $\lambda_{\theta\phi}$ are the polarization parameters out of which the latter had been implicitly assumed to be zero due to statistics limitations. As for the parameter α, introduced before, values smaller than zero indicate longitudinal, and values larger than zero transverse polarization; parameters which are consistent with zero indicate no polarization.
In [68] it is stated that these results are deemed to be used as a stringent constraint for NRQCD. First predictions are available [66] and can also be seen in Fig. 2.13. A reasonable agreement between the ALICE data and NRQCD is achieved when including color-singlet and color-octet modes at NLO (solid line with yellow uncertainty band). Yet, the contradiction between NRQCD and the CDF data as in Fig. 2.12 is still present in [66]. More data from the LHC, especially at high p_t will help to verify or dismiss the different theoretical approaches.

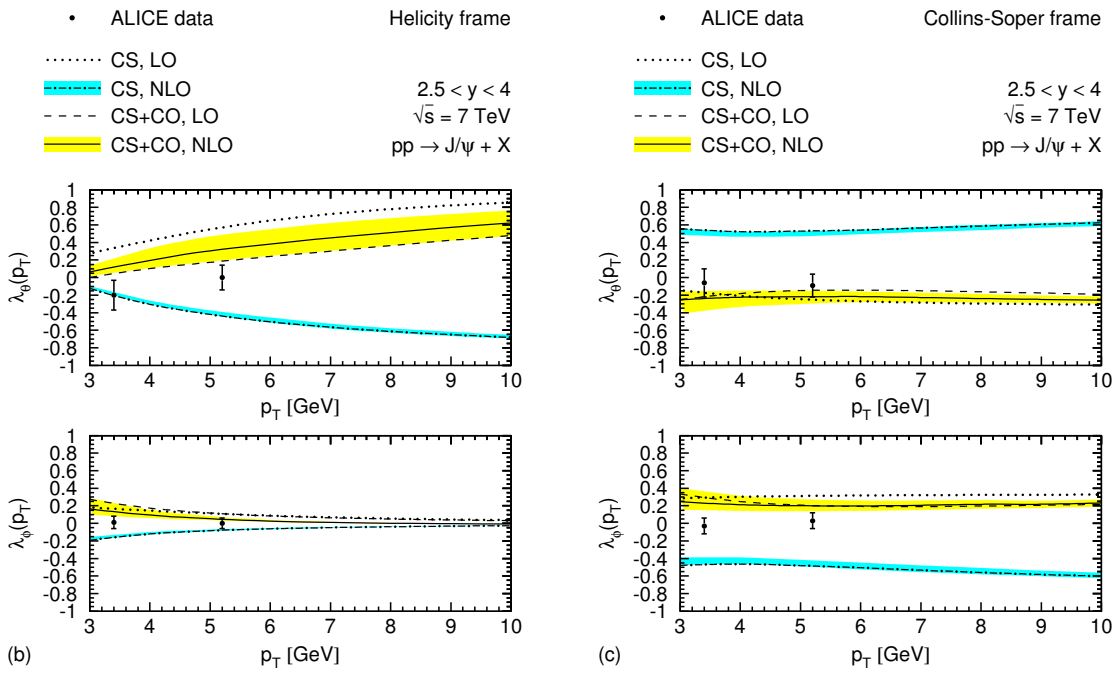

Figure 2.13: The polarization parameters λ_θ and λ_ϕ for inclusive J/ψ, measured in the helicity (left panel) and Collins-Soper (right panel) frames by the ALICE experiment in $\sqrt{s} = 7$ TeV pp collisions [68]. An NRQCD prediction [66] is shown both at LO and at NLO. Additionally the color-singlet contribution is shown individually.

2.3.3 Relation to the Charged-Particle Multiplicity

Unlike in collisions of two accelerated leptons, e. g. e^+e^-, where only one single interaction occurs in the first place, the collision of two protons, i. e. hadrons, is much more complicated since the proton is a complex object made up of valence quarks, sea quarks and gluons. It is assumed that when two hadrons collide the probability exists that several parton pairs interact with each other [69]. These are called multiple partonic interactions (MPI).

Already in the 1980s it became clear that MPI have to be considered in the understanding of observables such as multiplicity distributions and forward-backward correlations [69, 70], and were included in event generators for the simulation of pp events. In the implementation of Pythia 6.4 [71], for example, MPI mainly affect soft processes of light quarks and gluons see [70]. A special type of MPI are double parton scattering (DPS) processes, i. e. the coincidence of two hard parton scatterings in one event. DPS are thus a more direct measurement of MPI and were first observed in 4-jet events [72]. Also more recent measurements show that MPI have to be incorporated for a description of the data. For an example see Fig. 2.14, where the average particle transverse momentum is shown vs. the event charged-particle multiplicity in $\sqrt{s} = 1.96$ TeV $p\bar{p}$ collisions, measured also by the CDF experiment [73]. The shape and

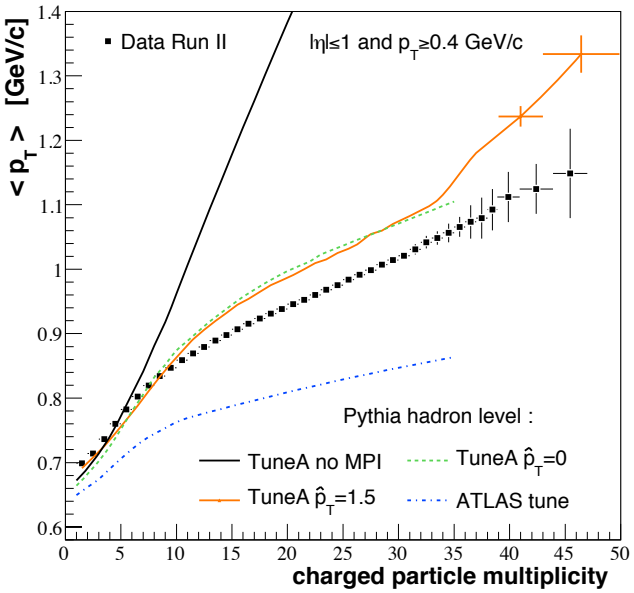

Figure 2.14: The average particle transverse momentum vs. the event charged-particle multiplicity in $\sqrt{s} = 1.96$ TeV $\mathrm{p\bar{p}}$ collisions, measured by the CDF experiment [73] (black squares). The results from different Pythia tunes are shown for comparison. While the tune A without MPI strongly overpredicts the data, two variations of this tune with MPI show a much better agreement.

magnitude of the distribution of the data points is much better resembled by the Pythia tunes (see Section 4.2.2) including multiple partonic interactions than by those without.
The investigation of MPI is a vivid field of research (for a current overview see [74]), but so far no model for an exact description of the underlying event is available and event generators have to be tuned to the existing data.
In the models for J/ψ production introduced above, the creation of heavy-quark pairs is treated strictly perturbatively and mostly independent of the underlying pp (or $\mathrm{p\bar{p}}$) event. If this is true and MPI do not have any impact on hard processes, the production rate of J/ψ should be independent of the event multiplicity. Both for the understanding of the underlying event and the interplay of soft and hard physics it is very interesting to test experimentally whether or not this is indeed the case. This measurement, motivated in [75], is part of this thesis and will be described in Chapter 5; its results are discussed in Section 5.6. It is the first analysis of the multiplicity-dependence of J/ψ production. The only existing measurements pointing in a similar direction that could be found were carried out by the NA27 experiment in $\sqrt{s} = 27.4$ GeV pp collisions [76] and by the LHCb experiment in $\sqrt{s} = 7$ TeV pp collisions [77]. In the former, the multiplicity distributions of all pp events containing charm decays were compared to those not containing charm decays. Here, charm decay products are not counted

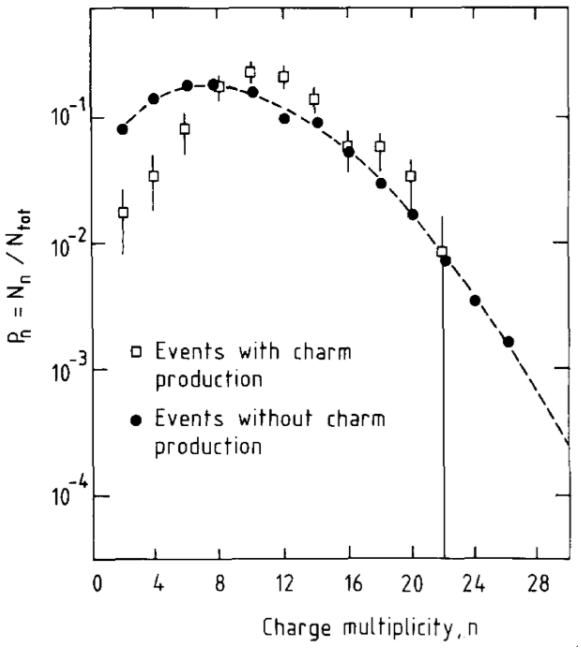

Figure 2.15: Charged-particle multiplicity distributions for $\sqrt{s} = 27.4$ GeV pp collisions with and without charm production, measured by the NA27 experiment [76].

in the multiplicity and only events with two observed charm decays are taken into account. The result is shown in Fig. 2.15: events with charm production have a, on average, $\sim 20\,\%$ larger multiplicity. This increase is mainly due to a depletion of low-multiplicity events in the group of those including charm production. These observations are interpreted by an absence of charm production in diffractive interactions. To emphasize that an increase of 20 % is a strong effect the authors of [76] note that it corresponds to the change of the average charged-particle multiplicity when increasing the collision energy from $\sqrt{s} = 27.4$ GeV to 44.6 GeV.
In 2011, the LHCb experiment reported a first observation of MPI in direct connection with J/ψ production [77]. Their analysis of J/ψ-pair production in $\sqrt{s} = 7$ TeV pp collisions indicate that DPS processes have a significant contribution.

In summary, MPI at the soft scale play an important role in pp collisions. At least at LHC energies, hard MPI, i. e. DPS, have been observed in J/ψ production. The remaining question is if and how soft MPI have any connection with a hard parton scattering producing, e. g., a $c\bar{c}$ and how this would affect the theoretical interpretation of the data.

2.3.4 Feed Down

The models introduced in Section 2.3.2 describe the direct production of quarkonia. However, there are further sources for bound $Q\bar{Q}$ states and especially the J/ψ:

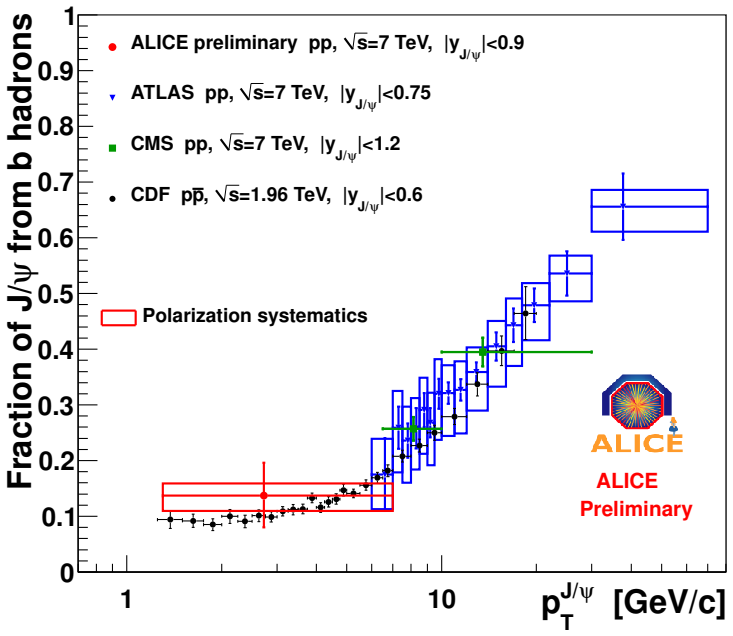

Figure 2.16: J/ψ non-prompt to inclusive fraction as a function of J/ψ transverse momentum. Compilation of results from various measurements around mid-rapidity including a preliminary result from ALICE [78, 79, 80].

- Feed-down from higher mass c$\bar{\text{c}}$ states, such as $\chi_{\text{c}} \rightarrow \text{J}/\psi + \gamma$
- b-hadron decays such as $\text{B} \rightarrow \text{J}/\psi + X$ or $\psi' + X$

The first source might contribute to the inclusive J/ψ yield at the 30–35 % level [81]. First measurements of the fraction of non-prompt to inclusive J/ψ, i. e. the fraction of J/ψ from b-hadrons, at LHC energies are available, see Fig. 2.16 and [82]. Approximately 10–15 % of the inclusive J/ψ are non-prompt. However, this fraction is strongly p_{t} dependent and raises up to about 70 % at transverse J/ψ momenta around 40 GeV/c. For the understanding of quarkonia production, these sources have to be taken into account.

2.4 Quarkonia in Heavy-Ion Collisions

In a collision of two heavy ions a whole bunch of effects can appear that have an influence on the measured quarkonia rates. Various mechanisms are predicted in case of the creation of a quark-gluon plasma. These may serve as an observable to detect the QGP and measure its properties. But also several phenomena have to be taken into account that already appear due to the presence of nuclear matter without the need for a hot phase. These two groups,

cold-nuclear-matter effects (CNM) and QGP-induced effects, are briefly introduced in the following.

2.4.1 Cold-Nuclear-Matter Effects

By the interaction with the cold nuclear matter or even just by its presence around the collision scene or due to interactions with dense material produced in the collisions, various effects with influence on the quarkonia yield may set in. Before drawing any conclusion on the measured rates in collisions of heavy nuclei, CNM effects need to be carefully studied. This is being done by measuring collisions in which no hot matter is created, such as p–A collisions. The two most important cold nuclear matter effects are shadowing and nuclear absorption, additionally, the comover interaction model will be described here.

Shadowing The parton distribution function (PDF) of a free nucleon differs from the one of a nucleon bound in a nucleus. Figure 2.17 shows the prediction of several models of the ratio between the gluon distribution in a nucleon of a Pb nucleus and in a free proton versus Bjorken-x. Depending on whether the PDF is suppressed or enhanced inside the nucleus at a given x this effect is called shadowing or anti-shadowing. Since the cross sections of quarkonia production directly depend on these distributions, such modifications have to be accounted for when comparing different collision systems as pp and A–A. The higher the collision energy, the lower the gluon x sufficient for $Q\bar{Q}$ production (see also Appendix C for details). Thus, the effect of shadowing might increase with the collision energy and become more important at LHC energies. The large spread of the curves in Fig. 2.17 illustrates the current uncertainties in the calculation of parton distribution functions. This is one of the major sources for the large uncertainties in the prediction of quarkonium production.

Nuclear absorption The breakup of pre-resonant $Q\bar{Q}$ pairs due to multiple scattering with nuclear matter surrounding the collision scene is called nuclear absorption. It is a final-state effect. The parameter L is defined as the mean path length of the pre-resonant $c\bar{c}$ through cold nuclear matter. It depends on the colliding species and their centrality. When measuring the J/ψ production cross section as a function of this parameter, the nuclear absorption can be characterized by the cross section σ_{abs}. The latter is determined by an exponential fit to the data: $\sim \exp(-\rho_{\mathrm{nm}}\sigma_{\mathrm{abs}}L)$, where ρ_{nm} is the density of normal nuclear matter. Recent studies [88, 89, 87] show that the absorption cross section σ_{abs} is strongly dependent both on the quarkonium kinematics (Feynman-x or rapidity)[3], see the left panel of Fig. 2.18, as well as on the nucleon-nucleon collision energy. The right panel of Fig. 2.18 shows a compilation of

[3]The scaling variable x_{F} (Feynman-x) is defined as the ratio of the particle's longitudinal momentum p_{L} and its maximal longitudinal momentum, i. e. half of the total centre-of-mass collision energy $\sqrt{s}$: $x_{\mathrm{F}} = 2p_{\mathrm{L}}/\sqrt{s}$. For the definition of the rapidity, see Appendix C

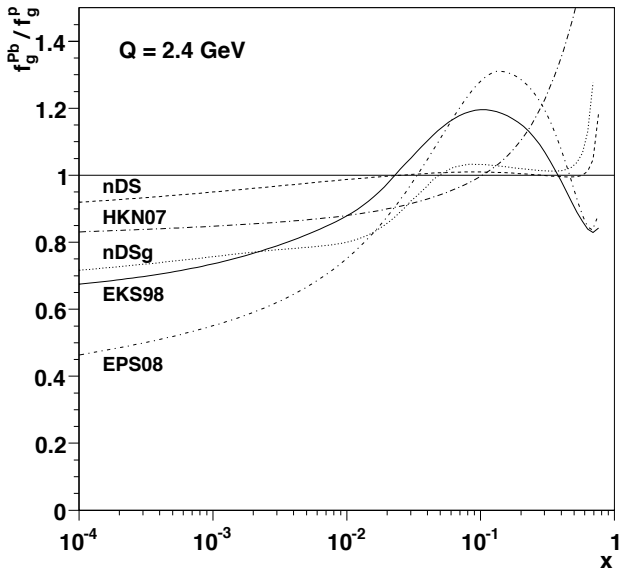

Figure 2.17: Ratio of the gluon distribution function of a nucleon in a Pb nucleus and that of a free nucleon versus x for various models: nDS, nDSg [83], EKS98 [84], HKN07 [85] and EPS08 [86]. Picture taken from [87].

measurements of σ_{abs} at mid-rapidity in the centre-of-mass system at various collision energies. The effect of absorption decreases with collision energy and might have a smaller impact at LHC energies. This observation holds regardless of the specific shadowing parameterization (see previous paragraph) used to obtain the remaining absorption cross section.

Comover interaction The authors of the comover interaction model [90, 91, 92] claim that the data from SPS and RHIC experiments (summarized in Section 2.4.3) can be fully described by inelastic collisions of $c\bar{c}$ or bound J/ψ with the comoving medium. Since in this approach, hot medium effects discussed in the next Section 2.4.2 are not necessary to explain the data, it belongs to the group of cold effects. In contrast to nuclear absorption here the interaction not with the nuclear matter but with the dense pions produced in the collision is considered. The J/ψ survival probability is given by [90]:

$$S_{\text{co}}(b,s) = \exp\left\{-\sigma_{co} N_{\text{co}}^{\text{y}}(b,s) \ln\left[\frac{N_{\text{co}}^{\text{y}}(b,s)}{N_{\text{fo}}}\right] \theta\left[N_{\text{co}}^{\text{y}}(b,s) - N_{\text{fo}}\right]\right\}. \tag{2.8}$$

Here, $N_{\text{co}}^{\text{y}}(b,s)$ labels the initial comover density per unit of transverse area $\mathrm{d}^2 s$ and per unit of rapidity at an impact parameter b. The corresponding freeze-out density is denoted by N_{fo}. The logarithmic factor in Eq. (2.8) is a result of the decrease in density from initial to freeze-out time.

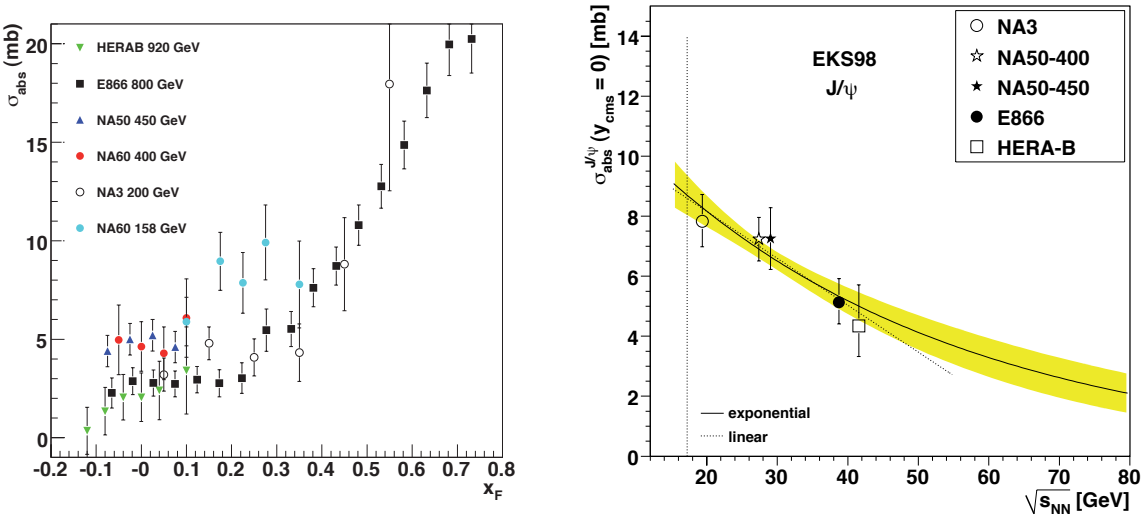

Figure 2.18: Left: compilation of various measurements of the J/ψ absorption cross section σ_{abs} versus x_{F} [89]. Note that measurements from fixed target experiments at different energies are compared. Right: compilation of data from various experiments for σ_{abs} around y_{cms} versus $\sqrt{s_{\mathrm{NN}}}$ [87]. The curves correspond to linear (dotted line) and exponential (solid line with yellow error band) fits to the data.

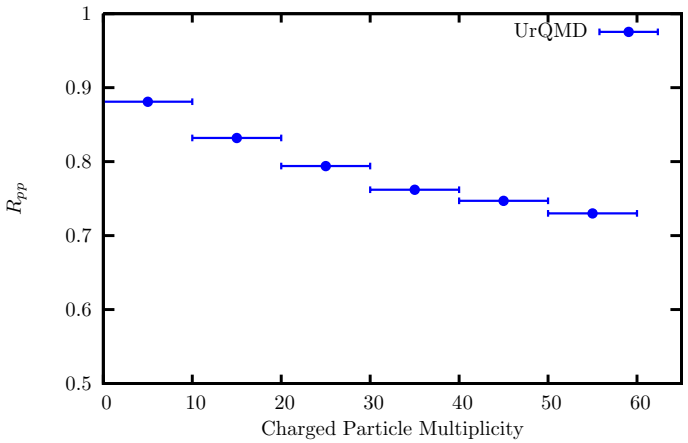

Figure 2.19: Prediction for the J/ψ survival probability in 7 TeV pp collisions as a function of the charged-particle multiplicity using the UrQMD hadronic transport model [94, 95].

While $N_{\mathrm{co}}^{\mathrm{y}}(b,s)$ is the main parameter of the model, the cross section of J/ψ dissociation due to comover interactions can be estimated from fits to low-energy experimental data: $\sigma_{\mathrm{co}} = 0.65$ mb [93].

Inspired by the very high charged-particle multiplicities reached in pp collisions at LHC

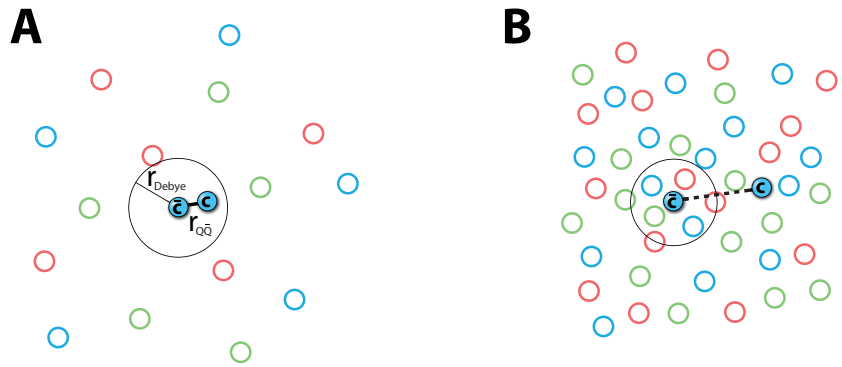

Figure 2.20: Debye screening in a medium of quasi-free color charges. Left: the Debye radius is larger than the binding radius of the Quarkonium state, the state survives. Right: the Debye radius becomes much smaller than the $Q\bar{Q}$ binding radius, the state may melt.

energies (see Section 5), recently, a possible comover interaction was studied with the UrQMD hadronic transport model in this collision system [94, 95]. As shown in Fig. 2.19, due to comover interaction, the J/ψ survival probability R_{pp} might decrease at increasing multiplities, even in pp. A test of this prediction is in preparation, see discussion in Section 5.6.

2.4.2 QGP-Induced Effects

When the elementary production of quarkonia and the effects of cold nuclear matter are well understood the yields and kinetic properties can be used to probe and study the quark-gluon plasma. During the last decades the original straight-forward idea of a melting scenario and its limitations were highly debated. The current status on the theoretical understanding of hot-medium effects shall be briefly discussed in the following.

Melting due to Debye screening The first prediction of a modification of J/ψ yields in heavy-ion collisions was put forward by T. Matsui and H. Satz [96]. The basic idea is the breakup of $Q\bar{Q}$ pairs in the hot environment of a quark-gluon plasma via Debye screening by free color charges, analogous to the well-known QED process in electro-dynamic plasmas. There the QED potential of two charges q of opposite sign gets screened exponentially with their distance r:

$$V(r) = -\frac{q^2}{4\pi r} e^{-r/\lambda_{\mathrm{D}}}. \tag{2.9}$$

The parameter λ_D is called Debye length and is dependent on the temperature T_e and density ρ_e of the electrons in the electromagnetic plasma:

$$\lambda_D = \sqrt{\frac{\epsilon_0 k_B T_e}{\rho_e e^2}}. \tag{2.10}$$

Here, e is the electron charge magnitude, ϵ_0 the permittivity of free space and k_B the Boltzmann constant. Analogously, one can expect a corresponding effect in plasmas of quasi-free color charges. The effective QCD potential becomes [25]:

$$V_{Q\bar{Q}}(r,T) \sim -\frac{4}{3}\frac{\alpha_s}{r} e^{-r/\lambda_D(T)}. \tag{2.11}$$

The effect of the screening is depicted in Fig. 2.20. In the left panel (A) the Debye radius is larger than the binding radius of the Quarkonium state, the state survives. The right panel (B) shows the case where the Debye radius becomes much smaller than the $Q\bar{Q}$ binding radius what may lead to a melting of that state. The separated heavy quarks will arbitrarily bind with other nearby quarks when the QGP freezes out. Most likely these will be light quarks making up D or B mesons that will be measured in the experiment instead of quarkonia. This should be indeed the case for collisions where only few heavy-quark pairs are created. When on the other hand a large number of $Q\bar{Q}$ pairs are present in the medium the situation may become more difficult. This subject will be addressed in the next paragraph.

As discussed in Section 2.2.2 and summarized in Table 2.1 the different quarkonium states exhibit different radii between the bound quark and antiquark. Depending on the temperature of the quark-gluon plasma and the corresponding Debye length λ_D the formation of such a state of matter would lead to a suppression of quarkonia rates in heavy-ion collisions. Due to their varying radii the yields of different quarkonia states might even reflect the temperature of the quark-gluon plasma [97, 43].
A suppression of J/ψ yields has indeed been found at SPS and RHIC, see Section 2.4.3. But so far the interpretation of the results is not as unambiguous as theoretically predicted, mainly because the CNM effects have not been fully understood yet [89]. Another drawback of the idea of Debye screening, especially the part of temperature-dependent melting of different species, is that exact values of the formation time of the QGP and of the bound quarkonium states are still unknown. A recent review [98] states that while the time to create an unbound $c\bar{c}$ pair is of the order of $t_{c\bar{c}} = \frac{1}{2m_c} \leq 0.1$ fm/c, the time to build up a color neutral bound state including its wave function is expected to take one order of magnitude longer.
The formation time of a quark-gluon plasma depends on the energy of the collision. At SPS energies one expects roughly 1 fm/c, at RHIC and especially the LHC this might happen even ten times faster [98]. As a consequence, especially at highest-energy colliders, there might be no bound states with defined radii yet but only pre-resonant pairs when the de-confined medium is created, leading to completely different predictions for quarkonia yields.

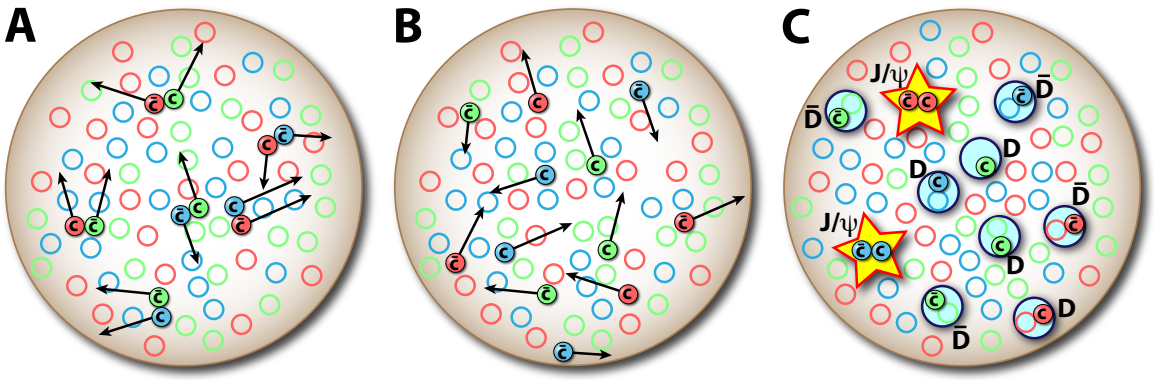

Figure 2.21: Sketch of the dissociation of correlated $c\bar{c}$ pairs (A), their diffusion (B) and the statistical production (C) of uncorrelated $c\bar{c}$ pairs in the quark-gluon plasma in heavy-ion collisions.

	$\sqrt{s_{NN}}$ (GeV)	$N_{c\bar{c}}$/central A–A event
SPS	17.3	$\sim 10^{-1}$
RHIC	200	$\sim 10^{1}$
LHC	5500	$\sim 10^{2}$

Table 2.2: Approximate average numbers of produced $c\bar{c}$ pairs per central A–A collision for different accelerator energies (centre of mass) [99, 100, 62].

Combination of uncorrelated $c\bar{c}$ Moreover, when going to higher accelerator energies, where many $c\bar{c}$ pairs are created in one collision (see average values in Table 2.2 and Fig. 2.21 for illustration), an additional effect may set in. After the diffusion of the c and $\bar{c}$ through the medium (Fig. 2.21, panel B), uncorrelated c and $\bar{c}$ may create bound states at some stage of the medium evolution (Fig. 2.21, panel C). This effect might lead to an enhancement of the yields, especially of the J/ψ, as depicted in panel C, Fig. 2.21. The sketch drawn in that latter panel is inspired by a statistical model [98, 101] assuming that all hadrons including the quarkonia are created almost simultaneously during the chemical freeze-out at the QGP phase boundary. A key prediction of this model is the scaling of charmonium yields with the squared number of $c\bar{c}$ pairs. As this number increases dramatically towards LHC energies, see the numbers in Table 2.2 and the corresponding cross sections in Fig. 2.22, most recent and LHC results provide an important test for the statistical model, see Section 2.4.3.
Another model [102, 103, 104] assumes competing reactions of dissociation in the medium and kinetic combination of c and $\bar{c}$. The simplest dissociation process is the absorption of a single gluon resulting in an unbound $c\bar{c}$ pair in a color-octet state but also any other dissociation process, e. g., the melting process discussed above, is possible.

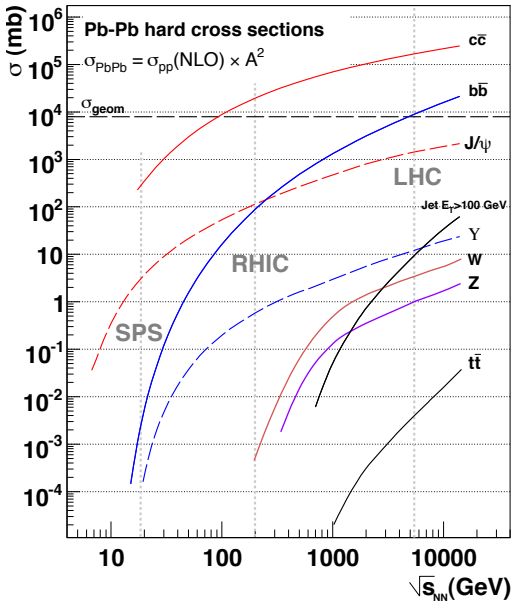

Figure 2.22: Cross sections for various hard probes, including those for $c\bar{c}$ (red line) and $b\bar{b}$ (blue line) as well as for J/ψ (red dashed line) and Υ (blue dashed line) production in Pb–Pb minimum bias collisions ($\sigma^{\text{hard}}_{\text{Pb-Pb}} = A^2\sigma^{hard}_{\text{pp}}$) [105, 106].

All such models predict distinct signatures in the measured rates or phase space distributions of the quarkonia and especially the J/ψ. High precision measurement data is needed to test these predictions.

Thermal production Studies of thermal production of charm quarks in an equilibrated quark-gluon plasma phase [107, 108, 109] suggest that this might be an additional substantial contribution to the overall charmonium yield in heavy-ion collisions at LHC energies. A recent work [107] predicts between 10 and 60 charm pairs, depending of the initial conditions. A main source of uncertainty is the exact choice of the charm-quark mass which is currently believed to be $m_c = 1.27^{+0.07}_{-0.09}$ GeV [36]. At RHIC on the other hand, the charm production in the QGP phase is expected to be negligible because the time scale of chemical equilibration of charm quarks in the medium produced at RHIC energies is much longer than the lifetime of the QGP itself. Due to its mass, thermal bottom production is negligible in any case.

2.4.3 Experimental Status of Anomalous J/ψ Suppression

Anomalous suppression names the suppression of the J/ψ yield that can not be explained by CNM effects and summarizes the above described in-medium effects. The NA50 [110] and NA60 [111] experiments at CERN measured both p–A and A–A collisions at the same incident

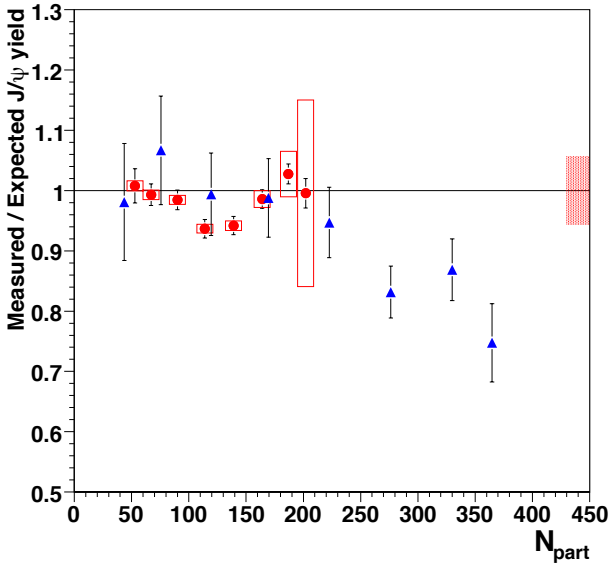

Figure 2.23: The ratio of the measured and the expected J/ψ yield as a function of centrality (N_{part}). Red circles correspond to In–In collisions measured by the NA60 experiment, blue triangles depict Pb–Pb data from NA50, both at 158A GeV. Boxes around the points are systematic errors. The height of the red box on the right corresponds the uncertainty on the absolute normalization of the In–In points, a global error of 12 % due to the uncertainty on the J/ψ absorption cross section is not shown [89].

energy of 158A GeV and in the same x_{F} range. The results in p–A can be used to calculate the J/ψ suppression from CNM effects in A–A, and by this, calculate an expected J/ψ yield without consideration of hot-medium effects. Figure 2.23 shows the ratio of the measured and the expected J/ψ yield as a function of N_{part}, the number of participating nucleons: due to their finite size, two colliding nuclei can hit each other with a varying overlap, according to the impact parameter. The nucleons in the overlap region will participate in the interaction and stop each other, see Section 1.4. While these nucleons are called *participants* the others will just be torn apart from the nucleus and continue flying along their trajectory. These *spectators* can be measured via the energy deposited in zero-degree calorimeters. The collision centrality, and likewise the impact parameter, is extracted from that measurements by a model-dependent estimation. A common approach to calculate N_{part} is the Glauber model [112]. Red circles in Fig. 2.23 correspond to In–In collisions measured by the NA60 experiment, blue triangles depict Pb–Pb data from NA50. Although the amount of anomalous suppression is significantly smaller compared to previous studies [113] that did not take the effect of shadowing into account, above $N_{\mathrm{part}} \sim 200$ there is still a significant suppression of around 20–30 %.

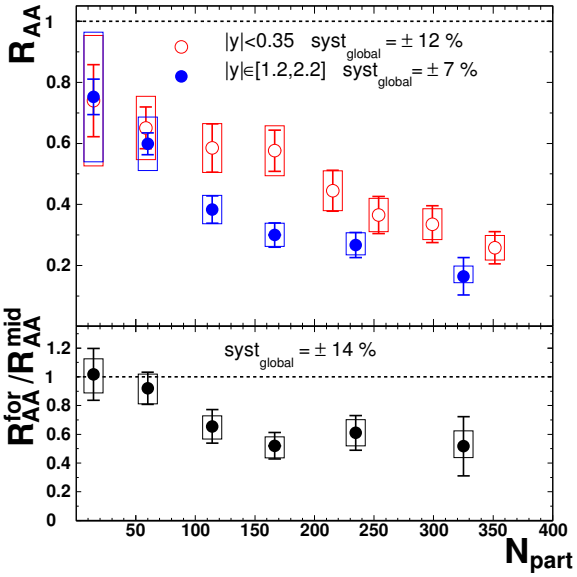

Figure 2.24: Upper panel: the PHENIX J/ψ $R_{\rm AA}$ in $\sqrt{s_{\rm NN}}$ = 200 GeV Au–Au collisions versus centrality in measures of $N_{\rm part}$ for central ($|y| < 0.35$, red circles) and forward ($1.2 < y < 2.2$, blue dots) rapidity regions. Lower panel: the ratio of forward and mid-rapidity J/ψ $R_{\rm AA}$ [115].

The PHENIX [114] experiment at RHIC[4] has measured [115] the J/ψ nuclear modification factor:

$$R_{\rm AA} = \frac{Y_{\rm A-A}}{\langle N_{\rm coll}\rangle\, Y_{\rm pp}} \tag{2.12}$$

allowing to compare nucleus-nucleus to nucleon-nucleon collisions. It unveils the effects that occur in A–A collisions but not in pp collisions. Here, $Y_{\rm A-A}$ and $Y_{\rm pp}$ are the yields in A–A and pp collisions, respectively, $\langle N_{\rm coll}\rangle$ is the mean number of binary nucleon-nucleon collisions. The latter is calculated using the Glauber model.

Figure 2.24 shows the results for $\sqrt{s_{\rm NN}}$ = 200 GeV Au–Au collisions, both for the central ($|y| < 0.35$, red circles) and forward ($1.2 < y < 2.2$, blue dots) rapidity regions.
Both at central and forward rapidity a strong suppression (from CNM effects plus hot-medium effects) of the yield in A–A collisions with respect to pp collisions can be seen. The suppression is increasing with the centrality of the collision (measured as $N_{\rm part}$). It is also significantly stronger at forward rapidity compared to mid-rapidity as can be seen in the lower panel of Fig. 2.24 showing the ratio between the two.

To estimate the contribution of CNM effects to the suppression seen in Fig. 2.24, PHENIX analyzed d-Au collisions to extract an expected cold-nuclear-matter $R_{\rm AA}$. This is further used

[4] **R**elativistic **H**eavy **I**on **C**ollider at Brookhaven National Laboratory

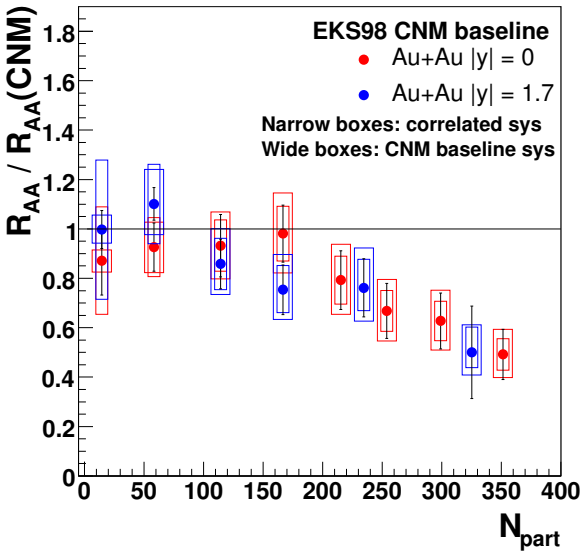

Figure 2.25: Ratio of the measured R_{AA} and the R_{AA} as expected for cold-nuclear-matter effects in $\sqrt{s_{\mathrm{NN}}} = 200$ GeV Au–Au collisions. The effect of shadowing has been taken into account with the EKS98 parameterization. Other parameterizations have been applied leading to almost identical results. Red dots correspond central rapidities, blue dots to forward rapidities. Systematic errors are represented by the boxes [81].

to normalize the two distributions of the nuclear modification factor versus the number of participants from Fig. 2.24 to extract the anomalous suppression pattern. The result is shown in Fig. 2.25. Here, the difference between the two rapidity regions vanishes. The PHENIX d-Au analysis referenced in [81] is preliminary. If the final version confirms this result, the highly debated difference in suppression at mid and forward rapidities might be due to CNM effects. Similar as in the SPS results discussed above a substantial suppression can be seen above $N_{\mathrm{part}} \sim 200$.

Figure 2.26 finally compares the SPS and RHIC data. Anomalous suppression patterns from Pb–Pb data from NA50, In–In data from NA60 and Au–Au data from PHENIX (at mid-rapidity) are presented as a function of the number of charged particles per unit of rapidity $\mathrm{d}N_{\mathrm{ch}}/d\eta$ at $\eta = 0$. It should be emphasized that the magnitude of anomalous suppression as function of the charged-particle multiplicity is almost independent of system size and collision energy.

At the end of 2010 the LHC (see Section 3.1) accelerated Pb beams for the first time, at an energy of $\sqrt{s_{\mathrm{NN}}} = 2.76$ TeV. In March 2011, proton beams were collided at the same energy, allowing for a direct comparison of the data. Only two months later the CMS collaboration was able to find first indications for a suppression of excited Υ states in Pb–Pb with respect to pp collisions [116]. Figure 2.27 shows the dimuon invariant-mass spectra from the pp and the

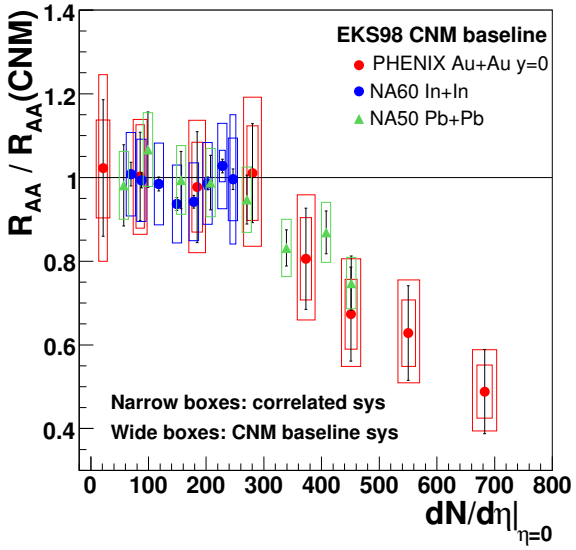

Figure 2.26: Comparison of the anomalous suppression patterns: PHENIX data at $\sqrt{s_{\mathrm{NN}}} = 200$ GeV Au–Au collisions, and NA60 and NA50 data at 158A GeV as function of the number of charged particles per unit of rapidity $\mathrm{d}N_{\mathrm{ch}}/\mathrm{d}\eta$ at $\eta = 0$ [81].

Pb–Pb data on the left (a) and the right (b) panels, respectively. Already by eye one can see a clear reduction of the Υ' and Υ'' peaks, compared to the Υ in the spectrum from Pb–Pb. Both distributions are fit with a combination of three Crystal Ball functions [117], one for each Υ state, and a second-order polynomial for the background. The fit results are drawn as the solid lines. The Crystal Ball function (named after the Crystal Ball Collaboration) is a probability density function composed of Gaussian core and a power-law tail at its lower end (see Appendix E for details). It gives a good description of mass spectra that are affected by asymmetric losses. The yields are then extracted from the fit results and used to calculate the double ratio $\left[\left(Y_{\Upsilon'} + Y_{\Upsilon''}\right)/Y_{\Upsilon}\right]_{\mathrm{Pb-Pb}} / \left[\left(Y_{\Upsilon'} + Y_{\Upsilon''}\right)/Y_{\Upsilon}\right]_{\mathrm{pp}}$ to quantify the suppression. It is found to be 0.31, a suppression of more than a factor of three. The authors of [116] claim that the probability to obtain this value or a lower one is below 1 % for the case that the double ratio was indeed unity. This observation gives new support to the melting scenario described in Section 2.4.2.

The same LHC $\sqrt{s_{\mathrm{NN}}} = 2.76$ TeV Pb–Pb data has been analyzed by ALICE to measure the J/ψ R_{AA} as a function of rapidity (Fig. 2.28, left panel) and N_{part} (right panel). No significant y dependence of the inclusive J/ψ R_{AA} at $p_{\mathrm{t}} \geq 0$ GeV/c can be seen. At above $p_{\mathrm{t}} \geq 3$ GeV/c the R_{AA} is decreased at the highest y bin. Two different shadowing predictions for both p_{t} ranges do not show a strong y dependence, their magnitude cannot solely account for the suppression seen in the data. Furthermore, in contrast to the experimental results, the predicted suppression due to shadowing is stronger for the p_{t} range starting at zero.

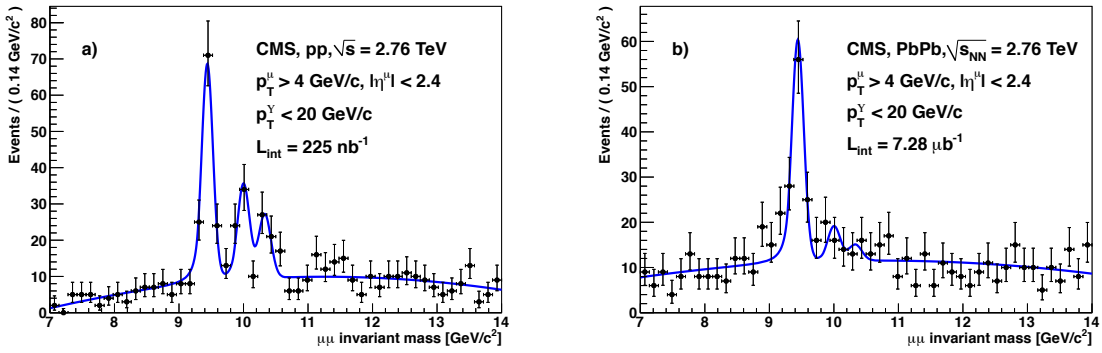

Figure 2.27: The dimuon invariant-mass spectra of the CMS experiment for pp (left) and Pb–Pb (right) collisions, both at $\sqrt{s_{\mathrm{NN}}} = 2.76$ TeV. The same reconstruction algorithm has been used for both data sets [116].

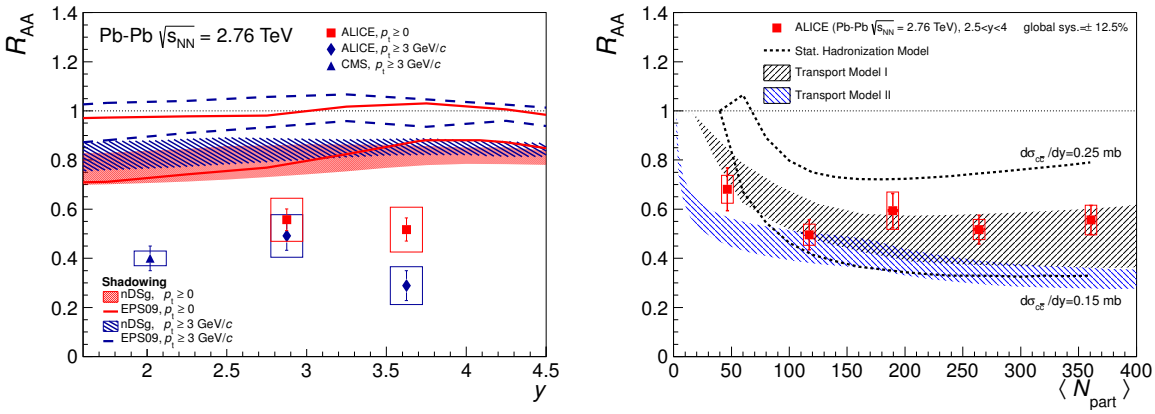

Figure 2.28: Centrality integrated (0 %–80 %) inclusive J/ψ R_{AA} [118]. Left: as a function of rapidity. Data from ALICE for two different p_{t} ranges (red squares: $p_{\mathrm{t}} \geq 0$ GeV/c, blue diamonds: $p_{\mathrm{t}} \geq 3$ GeV/c) are compared to the result from CMS (blue triangles: $p_{\mathrm{t}} \geq 3$ GeV/c) [119]. For both p_{t} ranges, the expected suppression due to shadowing is represented for two models by lines and areas. Right: as a function of N_{part}, compared to various model predictions [120, 121, 122].

The R_{AA} at $\sqrt{s_{\mathrm{NN}}} = 2.76$ TeV does not show a significant dependence on N_{part} (right panel of Fig. 2.28). When it is compared to the results at $\sqrt{s_{\mathrm{NN}}} = 200$ GeV (Fig. 2.24), the observed suppression is much weaker, especially at central events. Three different model predictions including J/ψ generation in a QGP phase are compared to the data in the right panel of Fig. 2.28. The statistical model [120] is given for two values of the yet unknown $\mathrm{d}\sigma_{c\bar{c}}/\mathrm{d}y$. Apart from the most peripheral bin the model describes the trend of the data. The two transport models [121, 122] shown in the figure are given with (lower bounds) and without (upper bounds) shadowing contribution. Especially the prediction of [121] gives a good description of the data.

In [118] it is stated that in both transport models about 50 % of the measured J/ψ yield in most central collisions is due to combination of uncorrelated $c\bar{c}$ pairs in the medium.

2.5 Experimental Outlook

So far, the understanding of quarkonia production mechanisms in elementary hadronic collisions is still a challenge for theory. Two of the main sources for uncertainties of the predictions are the precise value of the charm quark mass and the gluon distribution functions inside the nucleons. Due to these limitations of the predictions it is difficult to decide which of the competing models is preferred by the data. Differential production cross sections of higher precision from the experiments at SPS and RHIC cannot substantially improve this situation. Figure 2.22 shows the dependence of the cross section of various hard probes on the collision energy. Going towards higher collision energies significantly increases the statistics of all quarkonia measurements. Also, at higher collision energies, the full bottomonia family becomes accessible for analysis; first results at LHC energies are already available. The polarization of quarkonia turned out to be a powerful observable to provide constraints on the different models. As mentioned above, especially the polarization measurement of bottomonia is a strong test for theoretical models; moreover, this family suffers much less from feed-down than the charmonia and is thus more accurate. The strategy will be to look at the full picture and find out which of the models can reproduce the whole set of available data in a consistent way.

The interpretation of quarkonia measurements in heavy-ion collisions is relying on the understanding of quarkonium hadro-production as well as on the results from elementary collisions as a baseline, and on p–A measurements for the extraction of CNM effects. Also, detailed analyses of various observables just started and may lead to a much better understanding of the interaction with the medium soon, such as polarization and collective flow of quarkonia in heavy-ion collisions. As it is the case for pp collisions, also the analysis of A–A collisions highly benefits from increased collision energies. With the higher heavy-quark production cross sections the full set of quarkonia (J/ψ, ψ', Υ, Υ', Υ'') will be accessible within the statistics of a few run periods.

The LHC, will provide all these measurements, a few that have also been discussed here are already available. Three experiments at the LHC, ALICE, CMS and ATLAS, are well-suited and partially even designed for this type of analysis. The next chapter will introduce the collider machine and especially the experiment ALICE, at which the present work is affiliated. The analysis carried out in this study is intended to contribute to the understanding of quarkonia production and provides a measurement at the new energy regime of the LHC and a new observable calling for theoretical interpretations.

Chapter 3

ALICE at the LHC

The first part of this chapter briefly introduces the accelerator LHC. Thereafter, the experiment ALICE is discussed with a focus on those parts which are mainly relevant for this work. The second half of this chapter addresses the methods for the reconstruction of particle trajectories, tracks, in the detector and a possible improvement of a part of this procedure.

3.1 The Large Hadron Collider

The Large Hadron Collider (LHC) at CERN[1] has been built in the circular tunnel of 27 km length previously used by the Large Electron Positron collider (LEP). Having delivered the first proton-proton collisions on November 23rd in 2009 it is now the most powerful accelerator ever constructed. As all colliders the LHC consists of acceleration cavities, bending magnets and two beam lines plus a huge set of beam optics and diagnostics instruments. At the LHC both beam tubes are installed in the same super-conducting bending dipole magnets. Their field provides a Lorentz force $F_{\mathrm{L}} = qvB$ matching the centrifugal force $F_{\mathrm{C}} = mv^2/r$ of the accelerated particles. The nominal field of 8.3 T and the collider radius of about 4.3 km leads to a nominal proton-proton centre-of-mass collision energy of 14 TeV.
An important part of the LHC program are annual heavy-ion runs. In that case also neutrons have to be carried in the nuclei; thus, the maximum beam energy per nucleon is reduced by the factor of Z/A, see Table 3.1.

For a measurement cycle in a collider experiment the accelerator is filled with particles of given injection energy which are then accelerated. In this process both the operation frequency of the accelerating cavities and the magnetic field of the bending dipoles have to be increased synchronously, what led to the name *synchrotron* to such types of accelerators.

[1] CERN, the European Organization for Nuclear Research was founded in 1951 as a council named Conseil Européen pour la Recherche Nucléaire.

Figure 3.1: Aerial view of the CERN accelerator complex and the surrounding region of France and Switzerland; The LHC (large ring) and the SPS (smaller ring) cross each other close to the CERN main site. Following the LHC to the left, a bright spot on the LHC marks the ALICE experimental area [123].

The bending magnets have a minimum current at which they can be operated. The resulting magnetic field corresponds to a minimal particle energy at which they have to be injected into the collider; thus, pre-accelerators are necessary. In Fig. 3.1 the LHC is drawn as the big circle. The smaller one, the Super Proton Synchrotron (SPS), is used as pre-accelerator for the LHC, being itself filled by the Proton Synchrotron (PS). The latter is still small enough to fit on the CERN main site.
When the nominal or desired beam energy is reached the beams are being collided at several interaction points around which the experiments are constructed. The beam intensity is slowly decreasing, after several hours the interaction rates are becoming too low and a new fill is prepared. A measure for the beam intensity is the luminosity:

$$\mathcal{L} = \frac{N_{\mathrm{a}} N_{\mathrm{b}} n f_{\mathrm{r}}}{4\pi\sigma_{\mathrm{x}}\sigma_{\mathrm{y}}}. \tag{3.1}$$

For technical reasons the beam is not continuous but the particles are packed together in bunches. $N_{\mathrm{a,b}}$ are the numbers of particles per bunch in the two beams a and b, n is the number of bunches per beam and f_{r} the revolution frequency. Assuming a Gaussian particle distribution in the bunches in the plane orthogonal to the beam axis, $\sigma_{x,y}$ are the standard deviations in

the two transverse directions. The luminosity is of unit $\mathrm{cm}^{-2}\mathrm{s}^{-1}$. When multiplied with a cross section of a given process it yields the rate of that process, see Fig. 2.22 and Table 3.1. Also noted in that table is a value for the reduced luminosity at the ALICE interaction point. This is necessary because of the rather long TPC drift time (see Section 3.2.4). A pile-up of too many events would render the data unusable for analysis.

	$\mathcal{L}$ ($\mathrm{cm}^{-2}\mathrm{s}^{-1}$)	$\sqrt{s_{\mathrm{NN}}}$ (TeV)	σ_{inel}
Anticipated			
pp, ALICE	$3 \cdot 10^{30}$	14	70
pp, nominal	$1 \cdot 10^{34}$	-"-	-"-
Pb–Pb	$1 \cdot 10^{27}$	5.5	7745
Delivered			
pp, ALICE	$\approx \cdot 10^{30}$	2.76	62.1 ± 1.6 (model) ± 4.3 (luminosity)
pp, ALICE	$\approx 2 \cdot 10^{30}$	7	72.7 ± 1.1 (model) ± 5.1 (luminosity)
pp, nominal	$\approx 3.5 \cdot 10^{32}$	-"-	-"-
Pb–Pb	$\approx 4 \cdot 10^{26}$	2.76	n/a

Table 3.1: Envisaged luminosities, nominal collision energies and expected total inelastic cross sections at the LHC [124, 125, 62] as well as the delivered beams (as of fall 2011) [126, 127].

3.2 A Large Ion Collider Experiment

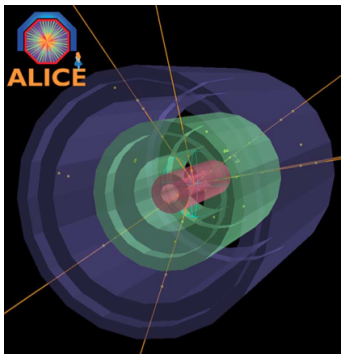

Figure 3.3: The first pp collision candidate [129].

ALICE [128] is the only dedicated heavy-ion experiment at LHC. In contrast to the other big experiments, ATLAS [130], CMS [131] and LHCb [132], its design has been optimized for high precision measurements in very high track densities and down to very low transverse momenta (of the order of 100 MeV/c).

Well before the LHC start-up ALICE was continuously running and taking cosmic data for preparation and calibration. As the very first LHC collisions took place, ALICE was taking data and directly able to reconstruct the events [129]. Figure 3.3 shows a 3D event display of the very first proton-proton collision candidate, recorded with the ALICE experiment. In

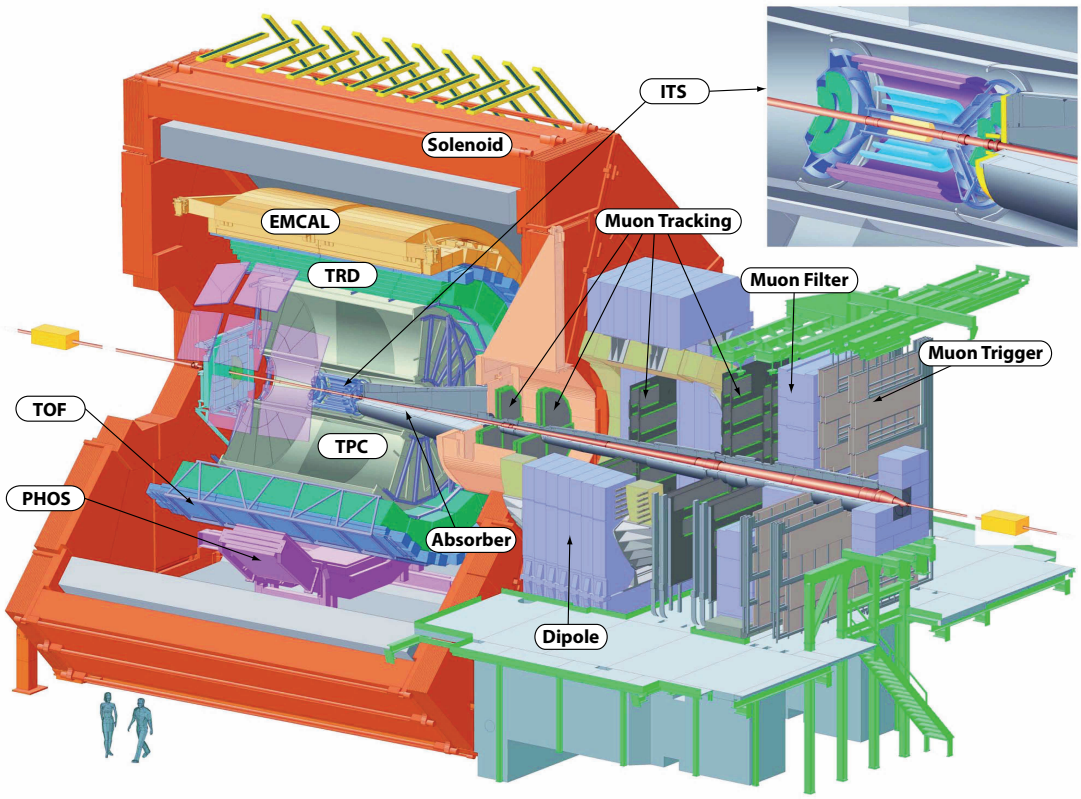

Figure 3.2: Schematic overview of the ALICE setup; the left part of the figure shows in red the L3 magnet and inside, symmetric and barrel shaped around the interaction spot, the central detectors. The main detectors used for quarkonia measurements are the ITS, the TPC and the TRD. The right part of the figure shows the forward muon arm including an absorber and a muon filter, a large dipole magnet and various tracking and triggering stations [128].

that phase the LHC only circulated both beams without further acceleration; thus, the energy of that collision is the injection energy of $\sqrt{s} = 900$ GeV, i. e., twice the top SPS energy. The dots correspond to hits in the ITS, the lines correspond to reconstructed tracks.

A sketch of the ALICE setup is illustrated in Fig. 3.2. One can divide the various detectors in three parts: the *forward detectors*, the *the muon spectrometer* and the *central barrel*. These will be introduced in more detail in the following sections of this chapter.

3.2.1 The ALICE Coordinate System

A right-handed orthogonal cartesian system has been defined [133] as the ALICE global coordinate system. Its origin $x, y, z = 0$ is the beam interaction point (IP). The three axes are

defined as follows: The x axis is perpendicular to the mean beam direction at the IP, aligned with the local horizontal accelerator plane and pointing with positive values of x to the LHC ring center. The y axis is perpendicular to the x axis and the mean beam direction at the IP, pointing upwards. The z axis is parallel to the mean beam direction, with negative values of z in direction of the muon spectrometer.
Most of the central barrel detectors are designed in cylinder geometry. The corresponding spherical coordinates are defined as: The radius $r = \sqrt{x^2 + y^2 + z^2}$ is the distance to the IP, the polar angle $\theta = \arccos\frac{z}{r}$ increases from the z axis ($\theta = 0$) to the x, y plane ($\theta = \pi/2$) up to the negative z axis ($\theta = \pi$). The azimuthal angle ϕ increases counter-clockwise starting from the x axis ($\phi = 0$). An illustration of the global coordinate system is given in the left panel of Fig. 3.4.

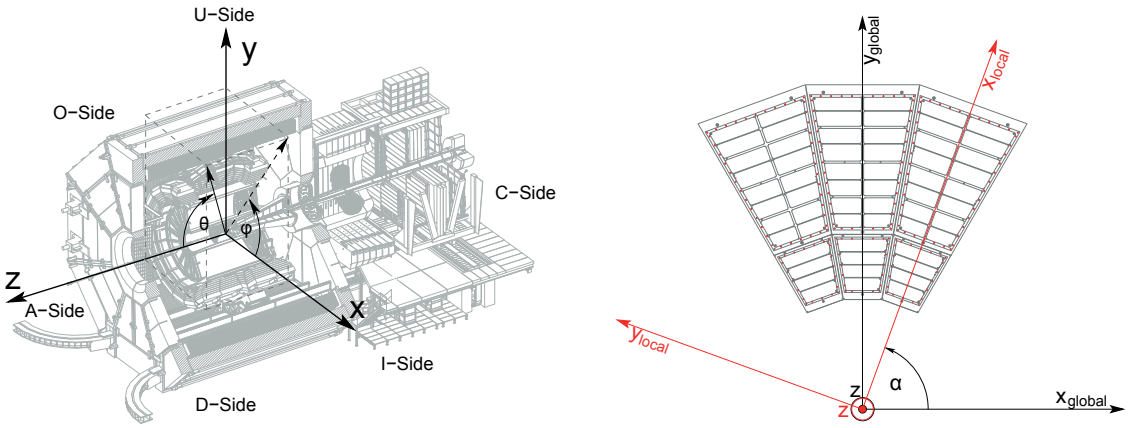

Figure 3.4: The ALICE global (left) and local (right) coordinate systems [134].

Furthermore, the directions from the IP, i. e. detector sides, have been named A, C for positive and negative z, I and O at positive (inside the accelerator ring) and at negative x (outside the accelerator ring) and U and D at positive (upwards) and negative y (downwards).

Additionally to the global ALICE coordinate system a local coordinate system has been defined. As the global one it is a right-handed cartesian system and has the same origin and z axis. The difference is, that the local system is rotated such that its x axis is perpendicular to the given detectors sensitive plane. This can be, e. g., the pad row in case of the TPC and the pad plane in case of the TRD (see Section 3.2.4).
The global and the local coordinate systems can be transformed into each other by the rotation of an angle α around the z axis, see the right panel of Fig. 3.4. This local coordinate system is used during the ALICE track reconstruction (see Section 3.3). Its choice simplifies the reconstruction equations and allows for a fast transformation to the global coordinate system.

3.2.2 Forward Detectors

Various detectors at forward rapidities are used for triggering decisions and the measurement of global event properties. But also detectors for specific analyses are installed in forward rapidity regions.
The T0 detector measures the event time with high precision and generates a start time for the time of flight detector (TOF, see Section 3.2.4). It can also be used to measure the vertex position and to provide trigger signals, either a L0 (for the ALICE trigger setup, see Section 3.2.5) or a wake-up signal to the TRD (see Section 3.2.4). Furthermore, it can serve as a multiplicity trigger. The main purpose of the V0 detector is to generate minimum bias trigger decisions and the rejection of beam-gas events. It can also be used for luminosity measurements and serves as an indicator of the centrality of the collision.
The latter is obtained with high precision also with the Zero Degree Calorimeter (ZDC) by measuring the energy of the spectator nucleons. Likewise, the impact parameter in heavy-ion collisions is extracted from that measurement.
At pseudo-rapidities larger than $|\eta| = 1.7$ the multiplicity is measured with the Forward Multiplicity Detector (FMD). Also far from mid-rapidity, the Photon Multiplicity Detector (PMD) measures the multiplicity and spatial distribution of photons.

3.2.3 Muon Spectrometer

The muon spectrometer is, as the name already indicates, designed to provide muon measurements for specific analyses, especially that of quarkonia. It consists of a 10 plane tracking system with high granularity, partially inside a large area dipole magnet for momentum determination. Four planes of trigger chambers behind a filter wall provide a fast trigger decision on events with one or more opposite sign muon pairs with high p_{t}. The muon system is protected from hadrons and photons by a large front absorber and a beam shield [135, 136]. The longitudinal acceptance of the system is $-4.0 < \eta < -2.5$. One of the main objectives are to measure quarkonia states in their dimuon decay channel over the whole range of transverse momenta down to $p_{\mathrm{t}} = 0$.
Advantages of the muon spectrometer are that it can be operated with dedicated triggers at very high rates compared to the central barrel detectors. Also, since behind the absorber there is only very little contamination by other particles than muons, the purity of the measurements is very high.
Disadvantages of the absorber are a slightly reduced momentum resolution due to multiple scattering in the absorber. Furthermore, secondary vertices as those from $\mathrm{B} \rightarrow \mathrm{J}/\psi + X$ decays cannot be detected in the muon channel.

3.2.4 The Central Barrel

The central barrel of the ALICE experimental setup is used for a broad variety of measurements including the reconstruction of quarkonia in their dielectronic decay channel. Detectors belonging to this part of the experiment are used for this study; thus, those parts will be discussed in more detail in the following.

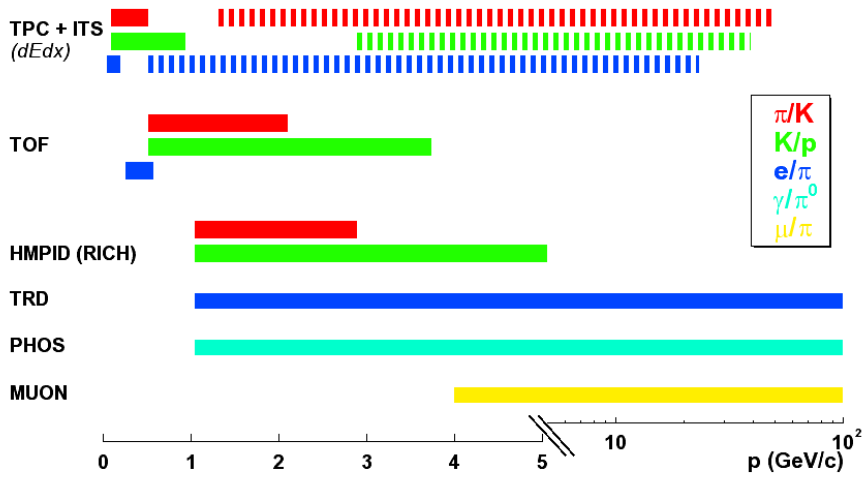

Figure 3.5: The PID performance of the different ALICE detectors providing PID information in terms of particle ratios as a function of momentum [137]. Solid lines represent a separation of the particle species better than 3σ, dashed lines better than 2σ [134].

Detector	Acceptance $\lvert\eta\rvert$	Radial Position
SPD (ITS layer 1)	1.98	3.9 cm
SPD (ITS layer 2)	1.4	7.6 cm
SDD (ITS layer 3, 4)	0.9	15.0 cm - 23.9 cm
SSD (ITS layer 5, 6)	0.97	37.8 cm - 43.3 cm
TPC	0.9 (full track length)	0.85 m - 2.47 m (active volume)
TRD	0.84	2.90 m - 3.68 m

Table 3.2: Summary of the longitudinal acceptances and radial positions of the central detectors which are most important for the measurement of quarkonia [128].

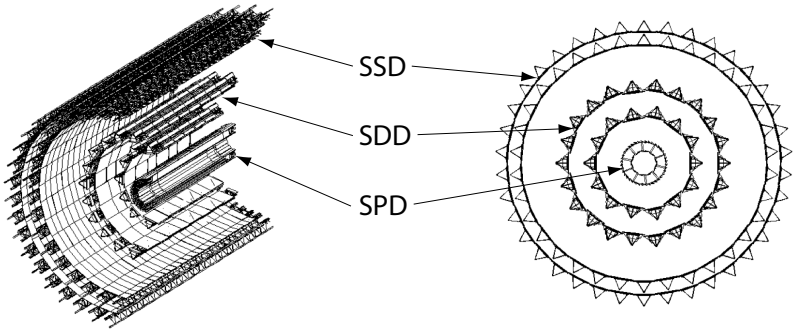

Figure 3.6: Layout of the ITS, comprising the SPD, the SDD and the SSD [138].

Inner Tracking System The Inner Tracking System (ITS) is a very important detector of ALICE. Its main tasks are a precise measurement of the primary vertex with a resolution of less than 100 μm in $r\phi$ and the reconstruction of secondary vertices, for example from B and D decays. Furthermore, the ITS does track finding and particle identification for tracks below p_{t}= 100 MeV/c that do not reach the TPC. Also, it improves the momentum measurement for tracks reconstructed with the other detectors.
Being the detector closest to the interaction vertex and surrounding the beam pipe, the ITS is built up of six cylindrical layers of silicon detectors. Three different technologies are used with two layers each: Silicon Pixel Detectors (SPD), Silicon Drift Detectors (SDD) and Silicon Strip Detectors (SSD). All six layers have a cylindric shape, as illustrated in Fig. 3.6. Pixel and drift technologies have been applied for the four innermost layers in order to achieve the anticipated impact parameter resolution and to cope with the high track densities expected in heavy-ion collisions at the LHC.
Both SDD and SSD are providing an analog signal and can thus be used for particle identification via the specific energy loss (see Section 3.3.2 and Fig. 3.5) of charged particles traversing the detector material. As summarized in Table 3.2 the ITS is located at a radial position of about 4 cm to 43 cm.

Time Projection Chamber The main tracking detector of the ALICE experiment is a cylindrical Time Projection Chamber (TPC). With a total gas volume of about 90 m^3 the ALICE TPC is the largest TPC ever built. This device further provides particle identification and a two-track resolution separating tracks with relative momentum differences of below 5 MeV/c.
Being symmetric around the azimuth, the longitudinal acceptance is $|\eta| < 0.9$ for tracks reaching the outermost part of the TPC; tracks with a smaller angle to the z-axis and thus with a reduced length can be measured up to $|\eta| < 1.5$. Table 3.2 lists the radial dimension of the TPC. In transverse particle momentum, the detector covers a very large range: from about 100 MeV/c up to 100 GeV/c. The granularity of the detector was chosen such that the occupancy does not

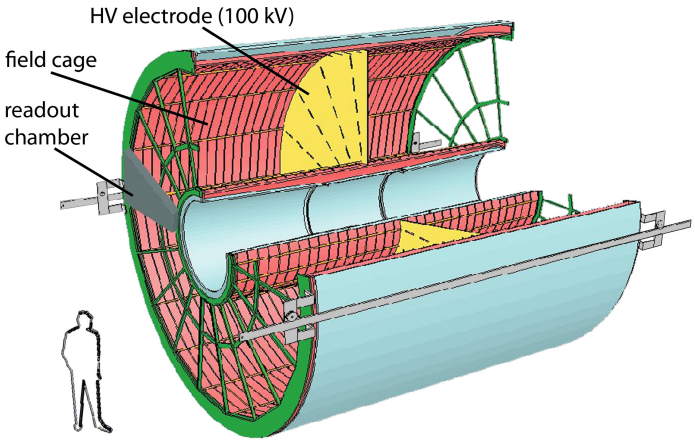

Figure 3.7: Schematic sketch of the TPC setup [139].

exceed 40 % in any part of the detector, even for events with extremely high charged particle densities of up to $\mathrm{d}N_{ch}/\mathrm{d}\eta = 8000$ (around mid-rapidity).

The general layout of the TPC is shown in Fig. 3.7. Its cylindrical gas volume is divided in two drift regions by the central electrode. From there the electric field lines are guided homogeneously along the field cage until the end-caps where all readout chambers and front-end electronics (FEE) are installed. The total high voltage of the central electrode is 100 kV leading to a field gradient of 400 V/cm and a maximum drift time of 92 μs (for the nominal gas mixture) [128].

A charged particle traversing the sensitive volume ionizes the Ne-CO_2-N_2 gas mixture. The track of ionized gas and electrons drifts along the electric field. As sketched in Fig. 3.8 the electrons from the primary ionization are drifting towards the readout plane which is made up of multi-wire proportional chambers (MWPC). As soon as the drifting electrons pass the cathode wire plane they get accelerated in the high potential difference between cathode and anode plane. The original charge is amplified by creating ionization avalanches with a gain of around $2 \cdot 10^4$. While the electrons from this process are quickly drained away in the anode wires the much heavier gas ions drift back to the cathode wires. These moving space charges induce clusters of mirror charges in the segmented pad plane which is in the end read out by the front-end electronics. By finding the weights between adjacent pads the track position can be determined with a precision of about 0.8-1.1 mm, much smaller than the actual pad size. The third spatial dimension is calculated out of the drift time. This lead to the name *Time Projection Chamber* of that detector type. The resolution of the z coordinate is around 1.1 to 1.25 mm, depending on the drift time: the longer the drift time the more the ionization cluster grows by diffusion.
The third wire plane, the gating grid, is separating the MWPCs from the drift region. By setting its voltage to corresponding potential at its position or $\pm$ a certain additional voltage

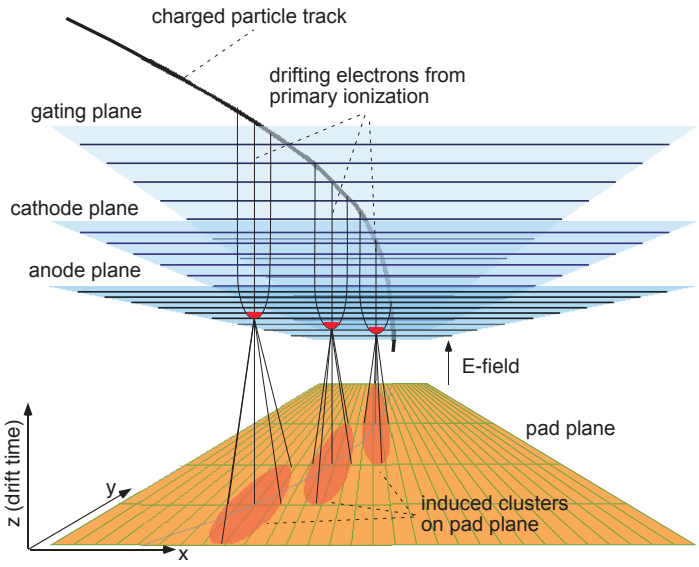

Figure 3.8: Sketch of a TPC with segmented readout pads [134]; the ionization electrons of a charged particle's track drift to the amplification region. If opened, they pass the gating grid and the cathode wire plane after which they create an ionization avalanche in the strong electric field around the anode wires. A mirror charge is induced in the segmented pad plane. By finding the weights between adjacent pads the track position can be determined with a resolution much better than the actual pad width [140].

it can be opened or closed. Only when an interesting event is triggered this grid is opened to enable the gas amplification. This is to prevent un-triggered ionizing events from being amplified and from accumulating ions in the drift region what would lead to field distortions.

About 560,000 pads have to be read out by the front-end electronics. Therein, the analog pad signals have to be processed such that they can be stored and analyzed digitally. This is mainly done in the ALTRO[2] chip [141] and illustrated in Fig. 3.9. The analog pulse coming from the TPC pad is first fed into a preamplifier and shaper amplifier (PASA) which is integrating the charge. Next, inside the ALTRO chip, the pulse is digitized and digitally processed: tail cancellation minimizes the pile-up effect in subsequent signals, pedestal subtraction and zero suppression extract the plain signals and reject samples that do not carry information. Upon reception of an L1 trigger (for the ALICE trigger setup, see Section 3.2.5) several hundreds of time samples are temporarily stored in a multi-event buffer. When also a L2 trigger arrives the event is kept, otherwise it is overwritten by the next one.

Each PASA and ALTRO contain 16 individual channels, 8 of each are put together on one Front-End Card (FEC). One row of up to 25 FECs is controlled by a Readout Control Unit

[2] **AL**ICE **T**PC **R**eado**u**t

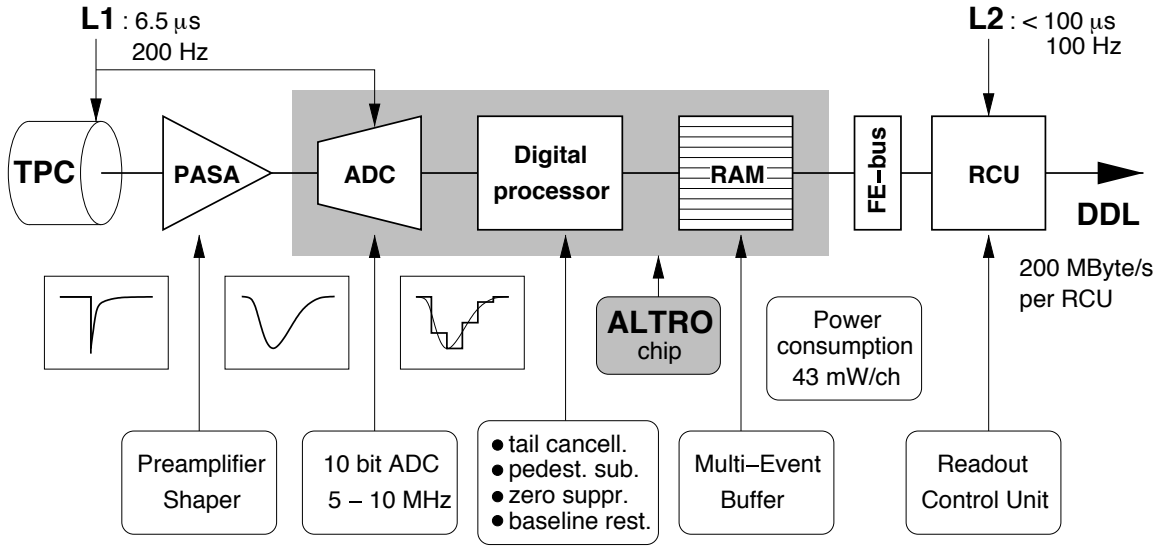

Figure 3.9: Schematic overview of the TPC front-end electronics; each TPC readout pad is connected to a preamplifier and shaper amplifier and one of the 16 channels of an ALTRO chip. The output of each channel is read out by the RCU [128]. See text for details.

(RCU). Finally, the data is sent to the data acquisition (DAQ) via Detector Data Links (DDL).

After the tracking procedure (see Section 3.3) has assigned a set of signal clusters to a track, the specific energy loss (see Section 3.3.2) is determined and used for particle identification. The TPC provides PID information over a very broad momentum range and for a good number of particle species, see Section 3.5.

Transition Radiation Detector The Transition Radiation Detector (TRD) has been added to the ALICE experimental setup to substantially improve the electron measurement. With a longitudinal and azimuthal acceptance of $|\eta| < 0.84$ and 2π respectively, the TRD covers almost the same phase space as the TPC and can contribute to the PID of most of the tracks reconstructed in the central barrel. As depicted in Fig. 3.10 the detector is segmented in 18 azimuthal segments, the so-called super modules. Each super module is divided into five stacks of six chambers each. In spring 2012, 13 of the total 18 super modules were installed.

The main goals of the TRD are the study of light and heavy vector-meson resonances and semi-leptonic open heavy flavor decays as well as a significant enhancement of the corresponding yields by providing a fast trigger. Such a trigger can also be applied to high transverse-energy jets by requiring several close high-p_{t} tracks. These physics objectives implicate the design parameters of the TRD:
A pion rejection capability of a factor of 100 for transverse momenta above 3 GeV/c is mainly

dictated by the J/ψ measurement and its p_t dependence. Also light vector mesons and the dielectron continuum between the J/ψ and the Υ are only accessible with this level of rejection. Good momentum resolution and a high pointing accuracy is of vital importance to match the TPC track with the reconstructed TRD clusters. The better the momentum resolution the sharper the trigger threshold in p_t and the smaller the rate of fake tracks [142].
The material budget has to be kept as small as possible to minimize photon conversions resulting in additional background and pixel occupancy. Also, electron bremsstrahlung, leading to loss of electrons, must be kept at a minimum. This is an important issue for all types of detectors and addressed in detail in Section 3.3.
The granularity of the detector is being defined in bending direction by the envisaged momentum resolution and in longitudinal direction by the need to fulfill the above requirements still at the highest assumed charged particle multiplicities at central Pb-Pb collisions.
The occupancy of the TRD reaches 34 % at $\mathrm{d}N_{ch}/\mathrm{d}\eta = 8000$ what was the maximum estimation during the TRD design phase [142]. The detector is designed to cope with these occupancies.

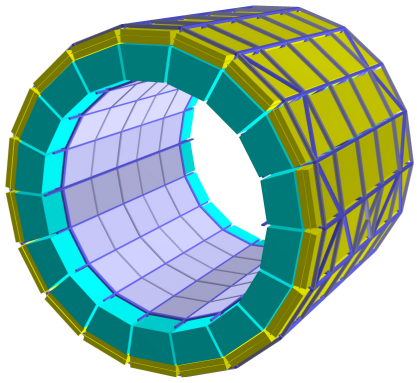

Figure 3.10: Illustration of the space frame holding 18 TRD super modules (green), surrounded by the TOF detector super modules (yellow).

Each individual chamber consists of a radiator, built up as a sandwich of Rohacell plates and polypropylene fibre mats, a drift region of 3.0 cm and a MWPC of 0.7 cm thickness with cathode pad readout. The pad plane is supported by a honeycomb carbon fibre sandwich back panel which also gives stability to the chamber structure. Like this an overall thickness of the TRD in terms of radiation lengths of 23.4 % is reached [128].

This setup as well as the working principle of the Transition Radiation Detector is shown in Fig. 3.11. Charged particles traversing the detector's sensitive volume ionize the gas mixture along their trajectory. In contrast to the TPC the particles traverse also the amplification region and the pad plane. The electrons from the primary ionization clusters drift with a constant velocity of around 1.5 cm/μs [128] to the cathode wire plane, become accelerated in the strong electric field around the thin (20 μm [142]) anode wires resulting in an ionization avalanche. In the same way as explained for the TPC a signal is deduced and read out from the pads.
The average of such signals from pions against the drift time is shown with blue triangles in Fig. 3.12. At short drift times electrons from the primary ionization drift towards the anode wires from both sides of the plane. Therefore the signal is peaked in this region. Thereafter, the signal stays roughly constant until the complete track has drifted into the amplification

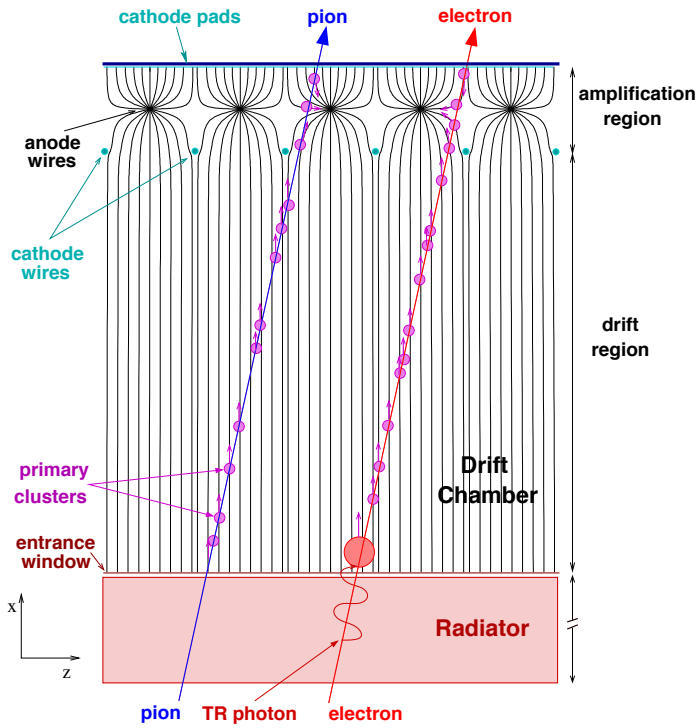

Figure 3.11: Schematic setup and working principle of a TRD readout chamber; Charged particles ionize the detector gas as they traverse the chamber. High velocity particles are likely to emit transition radiation which leads to an extra electron cluster in the drift region close to the radiator [142].

region. Compared to the TPC, the distance between anode plane and radiator is very short. Backward drifting ions are neutralized quickly at the radiator and cannot accumulate in the drift region; thus, there is no need for a gating grid in case of the TRD.

When an electron passes a TRD chamber as in Fig. 3.11, it is likely that inside the radiator a transition radiation (TR) photon is created. This process, further described in Section 3.3.2, sets in at electron momenta around 0.5 GeV/c. To obtain reasonable amounts of TR the electrons have to traverse many material surfaces. Extensive studies have been performed [142] to identify the optimal solution for the TRD in terms of TR yield, mechanical stability and radiation thickness. As a result the TRD radiators are built in a sandwich structure. A box of Rohacell foam panels contains polypropylene fibre mats. Above the threshold for the production of transition radiation ($\gamma \approx 1000$) on average 1.45 TR photons in the range of 1 to 30 keV (part of the X-ray spectrum) are produced [128]. In order to measure the large part of the TR photons a detector gas with a very short absorption length[3] is necessary. Here Xe is the only possible choice which is used together with 15 % CO_2 as quencher [142]. The additional ionization cluster from the absorbed TR photon leads to an enhancement of the electron signal

[3]The absorption length λ is defined as the path length after which the intensity of the incident radiation has been reduced from I_0 to I_0/e: $I(x) = I_0 \cdot e^{-x/\lambda}$.

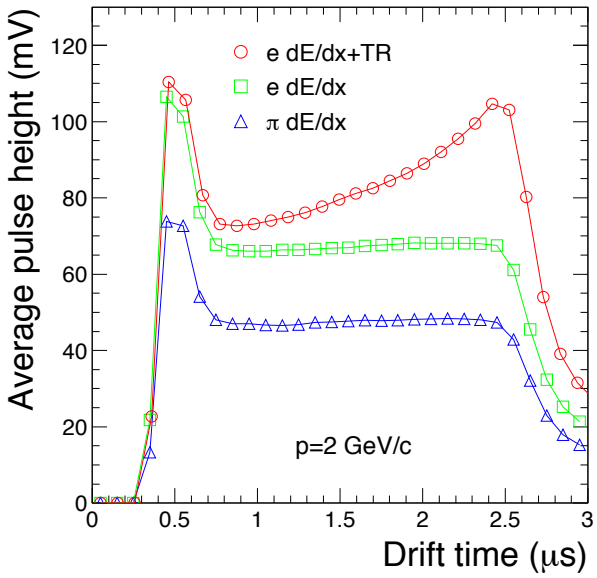

Figure 3.12: Average pulse height as a function of the drift time for electrons with (red circles) and without radiator (green squares) and for pions (blue triangles) [143].

at late drift times, i. e., close to the radiator.
The red circles in Fig. 3.12 are corresponding to the average signal of electrons of $p = 2$ GeV/c. The green squares show average electron signals without radiator; thus, without additional TR signal. By comparing the red and the green curves one can see the exponential absorption of the TR photons close to the radiator. The difference between the blue and the green curve is the different specific energy loss of pions and electrons at same momenta, see Section 3.3.2.

Various algorithms using Bayes' theorem of conditional probabilities or neural networks analyze the signal of each track to decide whether it might be from an electron or not. Combining the six TRD layers provides the target pion rejection at a given electron efficiency of 90 %. By this, the electron PID is dramatically improved over a broad range of particle momenta, see Fig. 3.5.

Large parts of the TRD readout chain are installed as front-end electronics directly on the chambers. As illustrated in Fig. 3.13 the total of around 1.18 M readout channels are connected to the so-called Multi-Chip Modules (MCM). Each MCM comprises an 18 channel PASA and a 21 channel[4] Tracklet Processor (TRAP) chip performing digital data processing: After the

[4]The charge of tracks is distributed over neighboring pads. To allow for a precise position resolution in the tracklet reconstruction of tracks crossing MCM boundaries 3 adjacent channels are shared with neighboring MCMs.

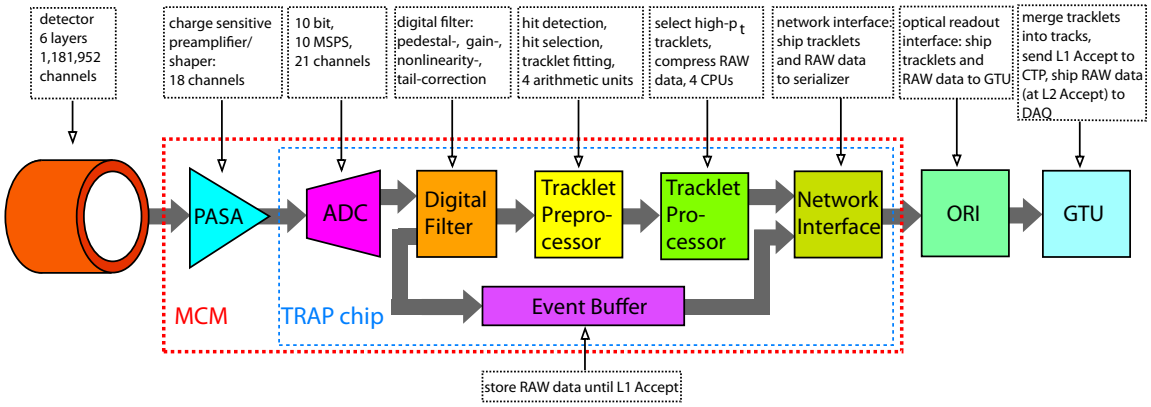

Figure 3.13: Overview of the TRD readout electronics [128].

digitization of the signals by an ADC the pedestal, gain, nonlinearity and tail corrections are done in digital filters. Processing units perform track fitting and a buffer stores events until a trigger has been received.

Always 16 MCMs with connection to the pads are installed on one readout board (ROB), each chamber is equipped with six or eight of those, depending on the chamber's size. In Fig. 3.14 the eight columns of MCMs can be easily identified. A 17th MCM on each ROB, the board merger, receives the data from the other MCMs. Two boards on each chamber are equipped with yet another MCM, the half-chamber merger. From there the data is shipped via optical readout interface cards (ORI) to the Global Tracking Unit (GTU). In Fig. 3.14 the two ORIs are located in the upper part of the chamber, connected with black cables.

The last part of the TRD FEE is the DCS board. In Fig. 3.14 this is installed on the left part of the chamber, on top of the green readout boards. The DCS boards control and monitor the chamber's FEE. The configuration of the chambers, e. g. settings of filter and gain parameters, are done by sending it to the DCS boards which are then configuring the MCMs.

TOF The detector surrounding the TRD, the time of flight detector (TOF), is the outermost one having a full azimuthal coverage and a longitudinal acceptance of $|\eta| < 0.9$. Being segmented in 18 super modules in ϕ and 5 segments in z direction the TOF measures the flight time of particles with an overall resolution of better than 80 ps [128]. By the combination of this information with the particle momenta one can determine their masses. The TOF provides particle identification in the intermediate momentum region: below about 2.5 GeV/c for pions and kaons and below 4 GeV/c for kaons and protons a separation of better than 3 σ can be achieved [128], see Fig. 3.5.

The detector has been realized using Multi-gap Resistive-Plate Chambers (MRPC). These are gaseous detectors with high and uniform electric fields where ionizations immediately start avalanches without any drift times. Some main advantages of MRPC are: they can be operated

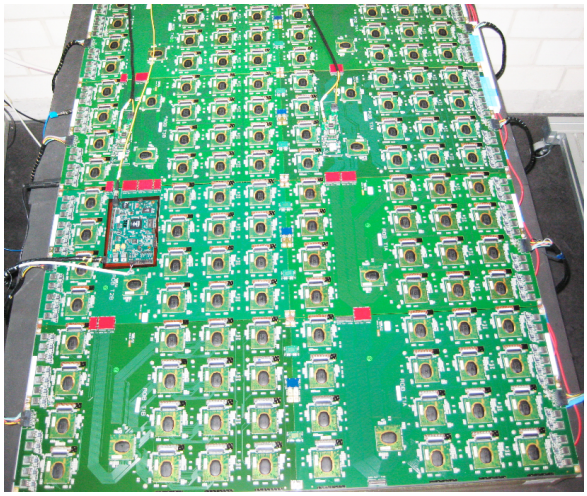

Figure 3.14: Picture of a TRD chamber equipped with front-end electronics.

at atmospheric pressure and with high gain due to the internal quenching capabilities of the resistive plates. Also, the signals do not have any late tails. Finally, the construction of MRPC is rather simple and does not require cost-intensive materials.

Another important purpose of the TOF detector is to create trigger signals. On the one hand it provides Level 0 (L0) triggers to select ultra-peripheral collisions, minimum bias events in proton-proton collisions and cosmic muons for the calibration of central detectors and cosmic-ray physics. On the other hand the trigger signal is fast enough to be used as a pretrigger for the TRD.

HMPID The High Momentum Particle Identification Detector (HMPID) is a Ring Imaging Cherenkov detector (RICH) dedicated to identify hadrons at transverse momenta above 1 GeV/c. The setup of the HMPID is a single arm array of seven modules of about 1.5×1.5 m^2 each. In total the acceptance is about 5 % of the central barrel phase space [128].

PHOS The Photon Spectrometer is a high-resolution electromagnetic spectrometer covering 100 degrees in azimuth and ± 0.12 units around mid-pseudorapidity. It is divided into five independent modules of a segmented electromagnetic calorimeter and a Charged-Particle Veto (CPV) detector. Each calorimeter consists of 56 rows of 64 cells of lead-tungstate crystals $PbWO_4$; the CPV is a MWPC with a charged-particle detection efficiency better than 99 %[128]. The main task of the PHOS is the measurement of photons. In spring 2012, three out of five modules are installed.

EMCal In 2008, the construction of the huge electromagnetic calorimeter (EMCal) was started, in spring 2011 the last modules were installed. It is a Pb-scintillator sampling calorimeter read out with Avalanche Photo Diodes (APD). Being the outermost detector inside the ALICE L3 solenoidal magnet at a distance to the IP of about 4.5 m it covers $|\eta| < 0.7$ in longitudinal direction and 107° in the azimuth [128]. The main reason for the addition of the EMCal to ALICE was to significantly improve the capabilities of jet quenching studies in heavy-ion collisions. By providing a fast and efficient (L0 and L1) trigger on hard jets, photons and electrons the EMCal allows ALICE to better exploit the LHC luminosity.

3.2.5 Trigger Setup

Triggers are necessary to start the detector read-out whenever an interesting event occurs. Moreover, at LHC design luminosities, more collisions take place than can be recorded. Thus, a trigger system has to be able to enhance rare signals by selecting events exhibiting various features. The ALICE trigger system comprises four different levels. The lower the level, the faster the decision, the higher the level, the more complex the analysis of the event.
The trigger signal of the lowest level (level 0, L0) reaches the detectors after a delay of only 1.2 μs [144] and can provide simple information as whether there was a collision or what its multiplicity was. This information is retrieved from detectors such as the V0 and the T0. After 6.5 μs [144] the inputs of all other fast detectors are available, including the TRD. In this stage the TRD can already make information available on identified high transverse momentum electron tracks. Another special trigger signal, the so-called pre-trigger, has to wake-up the TRD electronics a few hundred ns after the collision so that the TRD is able to receive L0 trigger signals. Copies of the V0, T0 and TOF trigger signals are used for this dedicated pre-trigger. The subsequent trigger level L2 waits for the end of the so-called *past-future protection interval* of to reject pile-up events. The length of this interval is essentially defined by the TPC readout time. As at nominal LHC luminosities a pile-up of events is frequent the L2 trigger logic has to take care that its degree is still tolerable and the event has not been spoiled. The L2 delay time can also be used to apply more complex trigger algorithms. The final stage of the trigger system, the High Level Trigger (HLT), provides full online data reconstruction and analysis. By rejecting events based on this analysis and by applying compression algorithms without the loss of physics information the HLT reduces the data volume significantly. Like this, the available data acquisition throughput rate can be used most efficiently.

3.2.6 Control System

The ALICE experiment is centrally controlled by the Experiment Control System (ECS). It operates the different online systems which are the Data Acquisition (DAQ), the Trigger System (TRG), the High Level Trigger (HLT), and the Detector Control System (DCS).

The DCS provides remote control and monitoring of all experimental equipment. It is organized in a tree-like structure as illustrated in Fig. 3.15. The central DCS top control unit is itself steered by the ECS or an operator and commands the DCS control units of all detectors. All units in the control tree are monitored by the above units while their status is represented using finite-state machines (FSM). Each unit is in one of a finite set of predefined states. Transitions between states are possible by executing actions. Such actions can be performed by an operator, another unit or by events as state changes of other components. The hierarchy can have as many levels as necessary, the lowest control unit steers the actual device.
A method to acquire and store the DCS configuration data of the TRD has been developed and implemented throughout this thesis and is presented in the Appendix A.

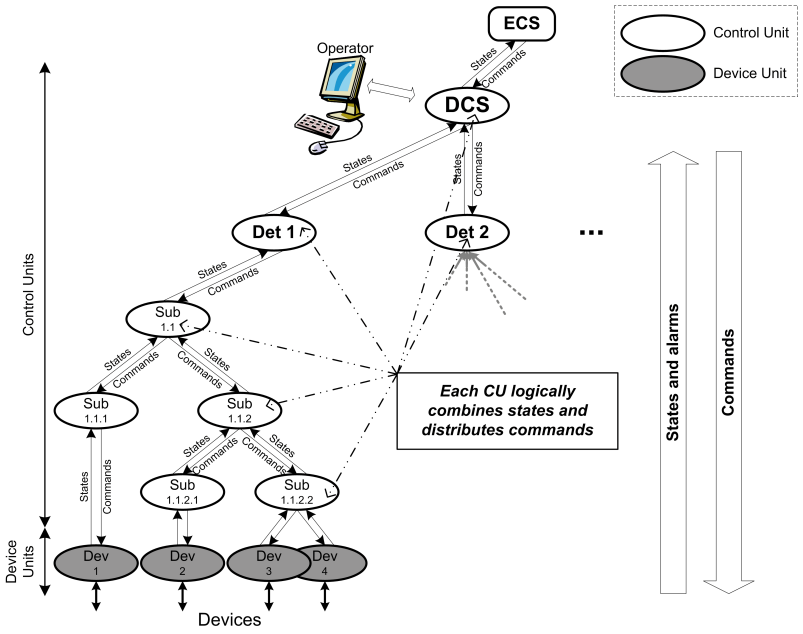

Figure 3.15: The DCS control structure [128].

3.3 ALICE Central-Barrel Track Reconstruction

Charged particles in motion interact with traversed material. The different processes that are creating signals in the detectors along the path of the particles are briefly described in this section. Thereafter, general methods for the reconstruction of such tracks are introduced, followed by an overview of the ALICE tracking procedure.

3.3.1 Charged-Particle Tracking in Magnetic Fields

Charged particles traversing a static uniform magnetic field $\mathbf{B}(\mathbf{r})$ describe a helix. Given the momentum p and charge q of a particle its trajectory is given by the equation [145]:

$$\frac{\mathrm{d}^2\mathbf{r}}{\mathrm{d}s^2} = \frac{q}{p}\frac{\mathrm{d}\mathbf{r}}{\mathrm{d}s} \times \mathbf{B}(\mathbf{r}). \tag{3.2}$$

Here $\mathrm{d}s = v\mathrm{d}t$ is the distance along the trajectory and $\mathrm{d}^2\mathbf{r}/\mathrm{d}s^2$ a vector perpendicular to it. The length of the latter is $C = 1/R(s)$, i. e., the inverse curvature radius of the helix.

3.3.2 Passage of Charged Particles Through Matter

When charged particles traverse a medium various effects can play a role, depending on the mass and velocity of the particle. Those effects that have an impact on the measurement of charged particle tracks in the detector, with special focus on electron tracks, are discussed in the following.

Multiple scattering through small angles Charged particles traversing matter are deflected by many small angle scatters, mostly due to Coulomb scattering from nuclei. The angular distribution is roughly Gaussian around zero with a width of [36]:

$$\theta = \frac{13.6\ \mathrm{MeV}}{\beta cp} z\sqrt{x/X_0}\left[1 + 0.038\ \ln(x/X_0)\right], \tag{3.3}$$

where x/X_0 is the thickness of the scattering medium in units of radiation lengths X_0 and βc, p and z are the particle's velocity, momentum and charge number. The above approximation covers 98 % of the angular distribution at small deflection angles. At larger angles the Coulomb scattering distribution behaves like Rutherford scattering with larger tails than those of a pure Gaussian.
In practice, layers of material, traversed by the particles, are not perfectly homogenous. This can result in a further enhancement of the tails of the scattering angular distribution [36].

Electronic energy loss Ionization and atomic excitation are the most dominant mechanisms for energy loss of moderately relativistic charged particles in a medium. The mean energy loss on the particle's way through a material is given by the Bethe-Bloch equation [36]:

$$-\frac{\mathrm{d}E}{\mathrm{d}x} = Kz^2\frac{Z}{A}\frac{1}{\beta^2}\left[\frac{1}{2}\ln\frac{2m_\mathrm{e}c^2\beta^2\gamma^2 T_\mathrm{max}}{I^2} - \beta^2 - \frac{\delta(\beta\gamma)}{2}\right] \tag{3.4}$$

Here $T_{\max}$ is the maximum energy that can be transferred to a free electron in one collision and I the mean excitation potential which can be typically approximated by $16\ \mathrm{eV} \cdot Z^{0.9}$ [36]. Z and A are the atomic number and mass of the traversed material, z the electric charge of the incident particle. While m_e is the electron mass, K a constant and β and γ the usual relativistic variables, $\delta(\beta\gamma)$ is the correction for a density effect setting in at very high particle energies due to polarization of the medium. In the above form, the Bethe-Bloch formula describes the mean energy loss, e. g. of pions with energies between 6 MeV and 6 GeV traversing copper with an accuracy of about 1 % [36]. Both at lower and higher energies further corrections must be made. Figure 3.16 shows the energy loss per unit length against the momentum for various particle species, each point corresponds to one measured particle. The solid lines correspond to the calculations using the Bethe-Bloch formula, Eq. (3.4).

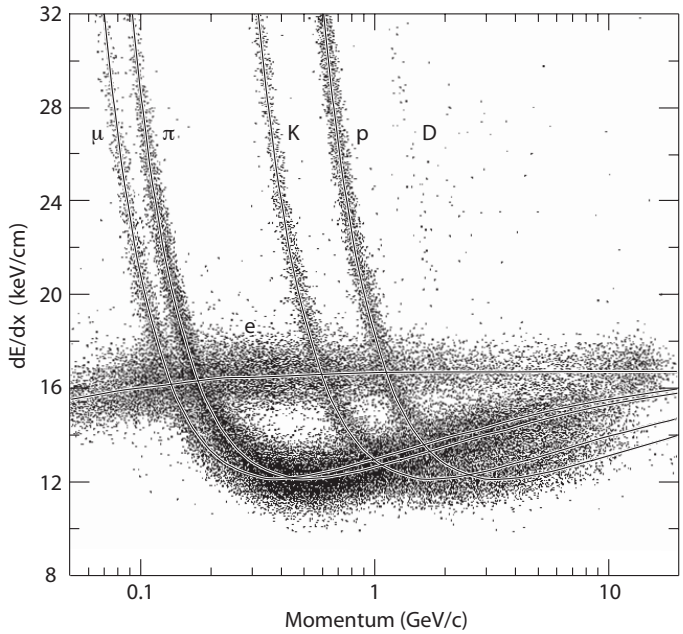

Figure 3.16: Energy loss of various particle species versus their momentum. The solid lines correspond to the specific energy loss of the different particle species calculated with the Bethe-Bloch equation [36].

Transition radiation When charged particles cross the boundary of two media with different dielectric constants there is a finite probability to create electromagnetic radiation. This so-called transition radiation has been predicted in 1946 [146] and first observed in 1959 [147]. For a given relativistic[5] particle of charge $1e$ that traverses one single border orthogonally the

[5] With a $\gamma = E/mc^2$ much larger than one.

differential photon emission intensity is [148, 149]:

$$\frac{\mathrm{d}^2 I_0}{\mathrm{d}\theta \mathrm{d}\nu} = \frac{2\alpha\hbar\theta^3}{\pi}\left(\frac{1}{1/\gamma^2+\theta^2+\omega_1^2/\nu^2} - \frac{1}{1/\gamma^2+\theta^2+\omega_2^2/\nu^2}\right)^2. \tag{3.5}$$

Here α is the electromagnetic coupling constant. The plasma frequencies $\omega_{1,2}$ of the two adjacent media are calculated from the dielectric constants $\epsilon_{1,2}$:

$$\omega_{1,2} = \sqrt{(1-\epsilon_{1,2})\nu^2}. \tag{3.6}$$

The photons are emitted at small angles $\theta \sim 1/\gamma$ in forward direction. This is an important circumstance for the technical application in high-energy physics detectors. Integrating the differential intensity, Eq. (3.5), over all emission angles and photon frequencies yields the total intensity:

$$I_0 = \iint \left(\frac{\mathrm{d}^2 I_0}{\mathrm{d}\theta \mathrm{d}\nu}\right) \mathrm{d}\theta \mathrm{d}\nu = \frac{\alpha\hbar}{3}\frac{(\omega_1-\omega_2)^2}{\omega_1+\omega_2}\gamma, \tag{3.7}$$

which is directly dependent on the particle's velocity: $I_0 \sim \gamma$. Only particles with a γ exceeding 1000 produce significant amounts of transition radiation. Over a large momentum range between 1 and 100 GeV/c only the light electrons fulfill this requirement. Thus, electrons can be separated from all other particles by measuring transition radiation.
Another property of the TR emission process is that the energy of the TR photons is in the range of the X-ray spectrum—high enough to be detected in proportional counters. A technical difficulty is that the average TR emission intensity per material boundary is only of the order of $10^{-2}\gamma eV$. Many transitions are necessary to produce a measurable amount of TR. This can be realized by stacks of foils, foams or fibers.

Bremsstrahlung At very high particle velocities another effect becomes dominant, namely radiative energy loss by bremsstrahlung. While the energy loss by ionization rises logarithmically with the particle energy, bremsstrahlung increases almost linearly and becomes the dominant effect at a few tens of MeV for electrons in most materials. All other charged particles have much higher masses and are thus much slower as electrons at the same energies; consequently bremsstrahlung is only relevant for electrons (further reasons are discussed in [36]).

Energy loss by radiation of bremsstrahlung can be described by the model of Bethe and Heitler [150, 151]. Bremsstrahlung can diminish the energy of electrons suddenly by a large fraction of its initial value, an effect which is called *straggling* [150]. The assumption that the probability of emitting a light quantum with the energy $h\nu$ is described by the equation [150]:

$$\sigma(\nu)d\nu = a\frac{d\nu}{E_0 \ln(E_0/E)} \tag{3.8}$$

is used as an ansatz to calculate the effect of straggling. This provides a good representation of measured photon energy distributions. Here $\sigma(\nu)$ denotes the cross section, E_0 and E are the electron energies before and after the radiation and a is a constant. The probability density function[6] (PDF) for an electron, traversing material of thickness t (in units of radiation lengths[7]) as a function of the remaining fraction $z = E/E_0$ of its initial energy can then be described by [152, 150]:

$$f(z) = \frac{-\ln z^{t/\ln 2 - 1}}{\Gamma(t/\ln 2)}, \tag{3.9}$$

which is known as the Bethe-Heitler distribution. Figure 3.17 shows this distribution for various values of t.

It can be seen that the shape of the Bethe-Heitler distribution is very different from that of a Gaussian. In the next section the track finding algorithm used in ALICE will be explained. After that the reason will be given why the non-Gaussian shape of the bremsstrahlung PDF does not allow to be directly accounted for in that procedure.

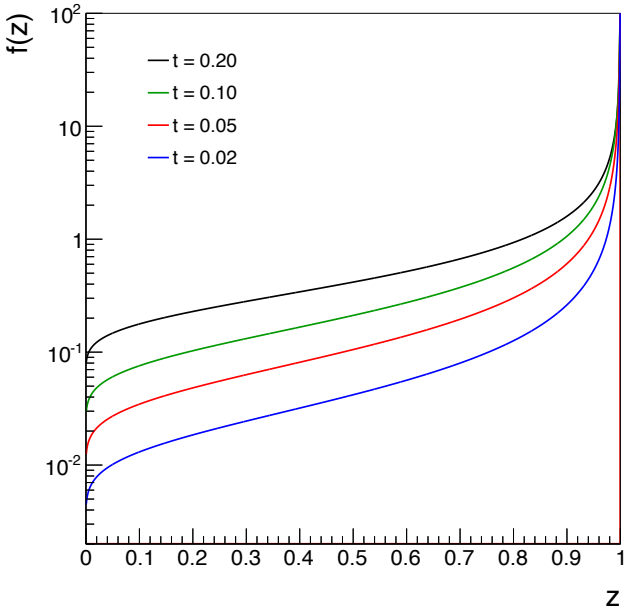

Figure 3.17: The Bethe-Heitler distribution $f(z)$ for different typical material thicknesses t in units of radiation lengths. The fraction of the remaining energy of the particle is denoted as z.

[6]Unlike the probability distribution the probability density function can exhibit values above 1.0. The probability of z to lie in a given interval equals the fraction of the integral over the interval and the full integral of the function. Not to be confused with the portable data format or the parton distribution function that both are referred to using the same abbreviation.

[7]The radiation length of electrons is defined as the length through a material after which an high-energy electron has lost all but $1/e$ of its energy by bremsstrahlung.

3.3.3 Kalman Filter

In many situations the goal is to estimate the state of a dynamic system from a series of incomplete and noisy measurements. Such situations are for example automotive navigation systems, weather forecasting, radar tracking, satellite navigation and charged particle track finding in high-energy physics experiments as ALICE. For all measurements with linear[8] processes, white[9] and Gaussian noise a recursive algorithm called the Kalman filter [153, 154] is the optimal approach. It incorporates all information that is provided to it and minimizes the error covariances. Unlike other recursive data processing concepts it does not require all previous data to be kept in storage. The Kalman filter has been used successfully in high-energy experiments [155, 156] and will be briefly introduced in the following.

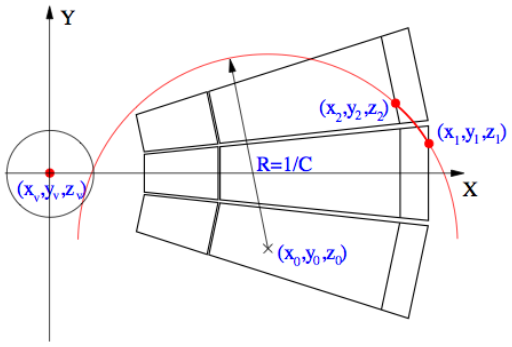

Figure 3.18: Illustration of the ALICE track-finding coordinate system and track parameters [62].

The state vector The state of the system is represented by a vector of real numbers $x \in \mathbb{R}^n$. In case of the automotive navigation system these numbers can be the x,y,z-components of position and speed of the vehicle. In case of the ALICE experiment the state vector

$$x_{\text{Track}} = (y, z, C, \tan\lambda, Cx_0) \tag{3.10}$$

makes use of the local ALICE coordinate system as defined in Section 3.2.1. The state vector consists of the y and z coordinates, the curvature of the track C, the angle λ between track and xy-plane and Cx_0, where (x_0, y_0, z_0) is the centre of the curvature of the track, see Fig. 3.18. The choice of the vector components has been optimized for high computational processing speed: only two—the coordinates y and z—of the five components change as the track is propagated from one propagation layer to the other. The accuracy of the state vector is represented by a covariance matrix P.

[8] Additivity: $f(x+y) = f(x) + f(y)$ and homogeneity: $f(ax) = af(x)$ are fulfilled.
[9] No dependence on time or frequency in a certain frequency bandwidth.

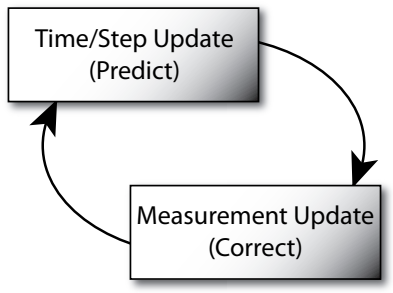

Figure 3.19: The discrete Kalman filter cycle.

Iterative state estimation The discrete Kalman filter cycle consists of two parts (Fig. 3.19). For each iteration the current state vector is used for an a priori estimate to predict the state at the next step; afterwards, the feedback in form of noisy measurements is used for the a posteriori estimate of the current state.

For the actual computation of the first part of the cycle, the time update, all knowledge about the influences on the system has to be taken into account. Technically, to calculate the next step k, this is done by the multiplication of the state vector at the previous step $(k-1)$ with a matrix F as depicted in Fig. 3.20. In ALICE for example the magnetic field along the path and the position of the next measurement (the propagation layer) have to be incorporated in that matrix F. The prediction of the next step is then calculated by:

$$\tilde{\mathbf{x}}_{\mathrm{k}} = F_{\mathrm{k}}\mathbf{x}_{\mathrm{k}-1} + B_{\mathrm{k}}\mathbf{u}_{\mathrm{k}} + \mathbf{w}_{\mathrm{k}-1}. \tag{3.11}$$

Here the tilde represents an a priori quantity, the estimated state vector before the measurement. An optional additional control input $\mathbf{u}$ gets related to the current state by a matrix B. In satellite navigation this could be, e. g., commands to accelerate, at the ALICE experiment a change in the magnetic field due to inhomogeneities could be accounted for via the control input. This is also illustrated in Fig. 3.20: $\mathbf{u}$ is an input and thus known, so it is drawn on the upper, the visible, part. Furthermore, $\mathbf{w}$ is a random variable, representing the process noise, assumed to have a normal probability distribution with mean at zero and covariance Q. The accuracy of the state vector, the covariance matrix P, is propagated in the same manner, also the process noise Q_{k} has to be accounted for:

$$\tilde{P}_{\mathrm{k}} = F_{\mathrm{k}}P_{\mathrm{k}-1}F_{\mathrm{k}}^{T} + Q_{\mathrm{k}}. \tag{3.12}$$

Examples for process noise are multiple scattering in the crossed material and mean energy loss but also bremsstrahlung.

As drawn in Fig. 3.20 the *true* state $\mathbf{x}$ of the system is not directly accessible - the position of a cluster is measured rather than the curvature of a track. These quantities are related with each other by a matrix H. Of course all measurements are further disturbed by measurement noise $\mathbf{v}$:

$$\mathbf{z}_{\mathrm{k}} = H_{\mathrm{k}}\mathbf{x}_{\mathrm{k}} + \mathbf{v}_{\mathrm{k}}. \tag{3.13}$$

As the process noise, $\mathbf{v}$ is assumed to be a random variable with normal probability distribution

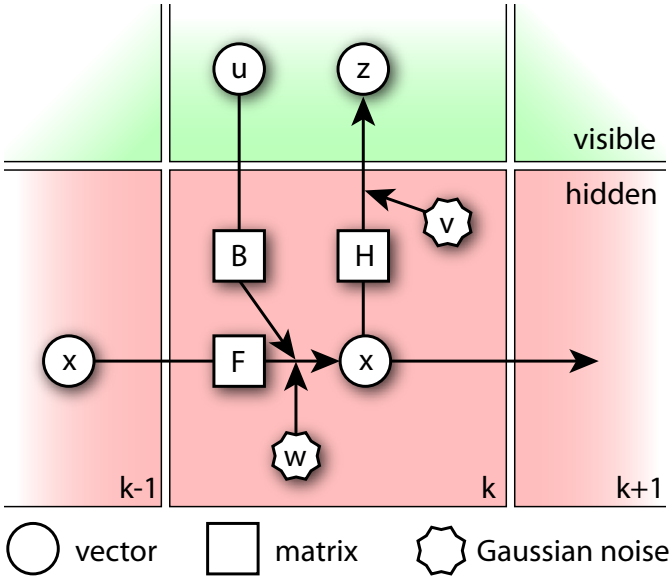

Figure 3.20: The measurement process in the Kalman filter approach at the current measurement step k; see text for further details.

with mean at zero. Its covariance is the matrix R. Finally, the vector $\mathbf{z}$ is the actual (visible) measurement, in ALICE this is the cluster position. The latter is then used for the second step of the filter cycle, the measurement update including the state estimate:

$$\mathbf{x}_\mathrm{k} = \tilde{\mathbf{x}}_\mathrm{k} + K_\mathrm{k}\left(\mathbf{z}_\mathrm{k} - H_\mathrm{k}\tilde{\mathbf{x}}_\mathrm{k}\right) \tag{3.14}$$

and the covariance matrix:

$$P_\mathrm{k} = \left(\mathbb{1} - K_\mathrm{k}H_\mathrm{k}\right)\tilde{P}_\mathrm{k}. \tag{3.15}$$

Here K denotes the so called Kalman gain:

$$K_\mathrm{k} = \frac{\tilde{P}_\mathrm{k}H_\mathrm{k}^\mathrm{T}}{H_\mathrm{k}\tilde{P}_\mathrm{k}H_\mathrm{k}^\mathrm{T} + R_\mathrm{k}} \tag{3.16}$$

where R is the covariance matrix corresponding to the measurement noise. The Kalman gain is derived such that it minimizes the a posteriori error covariance. The above forms are taken from [154].

As R approaches zero $\lim_{R_\mathrm{k}\to 0} K_\mathrm{k} = H_\mathrm{k}^{-1}$, the actual measurement $\mathbf{z}_\mathrm{k}$ is trusted more and more, while the predicted measurement $H_\mathrm{k}\mathbf{x}_{\mathrm{k}-1}$ is trusted less and less. When on the other hand the estimated error covariance approaches zero $\lim_{P_{\mathrm{k}-1}\to 0} K_\mathrm{k} = 0$, the actual measurement is trusted less and less while the predicted measurement is trusted more and more.

In the case of ALICE tracking a cluster to be associated with the track is searched within a window of 4σ around the expected track position in the next propagation layer. While this σ is calculated from track position errors and expected cluster position errors the cluster nearest to the track is taken as the most probable one belonging to the track. This cluster is then used for the above described measurement update of the Kalman filter algorithm.

As said at the beginning of this chapter a prerequisite for the Kalman filter is that all measurement and process noises have Gaussian distributions. This not only makes mathematics tractable. More than that, the Kalman filter which propagates the means and standard deviations of Gaussian distributions includes all contained information. Most other densities require more or even an endless number of parameters to specify their shape entirely. Moreover, according to the central-limit theorem the sum of an increasing number of independent random variables with arbitrary distribution (with finite mean and variance) will tend towards a normal distribution[154]. Since often several random variables contribute to the noise of a measurement, this prerequisite usually is no limitation.
Because of the non-Gaussian shape of the bremsstrahlung PDF on the other hand, this process cannot be accounted for in a standard Kalman Filter such as the ALICE tracking procedure. Therefore, the prediction of the measurement systematically under-estimates the energy loss of electrons. The window in which a cluster is searched for is systematically shifted at positions of correspondingly lower energy loss. The change in the track curvature along the trajectory is larger than estimated by the algorithm. As explained next, the last reconstruction pass at ALICE proceeds inwards; consequently, the electron track momentum is systematically under-predicted.

3.3.4 ALICE Tracking Procedure

The Kalman filter follows a given track and determines its properties iteratively. To start this procedure, the filter needs *seeds*, initial state vectors of the track candidates, as starting points. The seeding is done in the best tracker device and in the area with the lowest track density—at ALICE this is the outermost part of the TPC. Clearly, the output state vectors of the seeding algorithm have too large errors to proceed outwards and extrapolate to the detectors surrounding the TPC right from the beginning. But they are precise enough for the Kalman filter to follow the tracks inwards through the TPC and the six layers of the ITS. These first steps belong to pass one of the reconstruction procedure as depicted in the left part of Fig. 3.21. Tracks with very low p_{t} or those propagating through dead zones may not reach the points where the seeds are created. A stand-alone ITS tracking procedure tries to find these tracks within the clusters that have not been assigned to any tracks before. As the last step in pass one of the tracking procedure a preliminary PID information is generated based on TPC and ITS $\mathrm{d}E/\mathrm{d}x$ information.

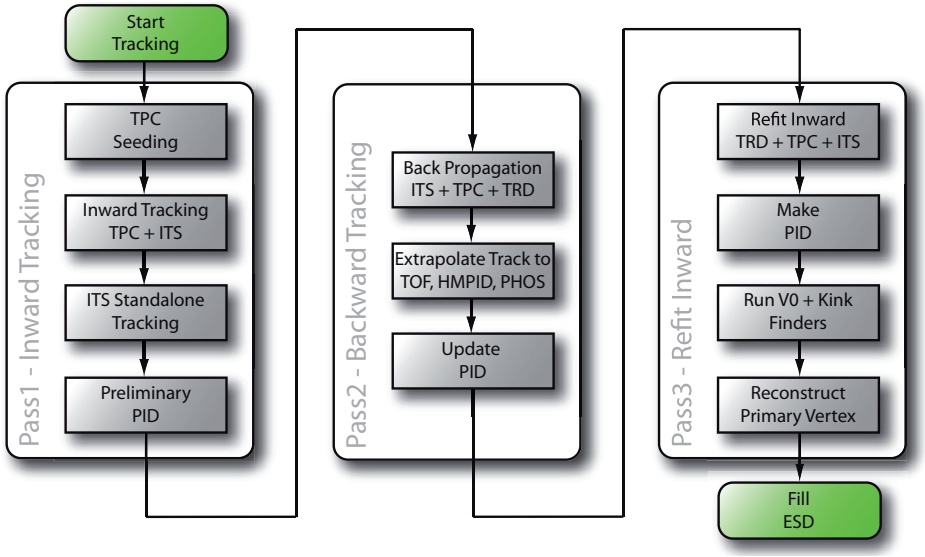

Figure 3.21: The main parts of the ALICE tracking procedure. To acquire the highest precision for all measurements the procedure is divided into three passes which are discussed in detail in the text. All informations are stored in the end in event summary data files, the ESDs.

Pass two of the tracking starts with propagating all tracks from the first ITS layer outwards through the ITS, TPC and TRD. Then the tracks are extrapolated to the outer detectors as TOF, HMPID and PHOS. Using these detectors the PID information of the tracks is updated.

The track parameters at the primary vertex, before the interaction of the particles with detector material are those of interest; therefore, the Kalman filter is used a third time to refit the tracks inwards through TRD, TPC and ITS. The final PID is generated and algorithms searching for special track topologies are run. Finally, after using the tracks to reconstruct the primary vertex, all relevant information is filled in event summary data files, ESDs.

3.4 Electron Bremsstrahlung Recovery

As explained in the beginning of Section 3.3.3, the Kalman filter is optimal as long as the mentioned prerequisites are fulfilled. One of these is that all process and measurement noises have to have Gaussian distributions. In case of the tracking procedure in the ALICE experiment this holds for the main sources of noise: multiple scattering of the particles traversing detector material and the measurement errors on the cluster positions. But unlike the other particles the light electrons emit bremsstrahlung at momenta of around a few GeV/c while traversing material. This is not being accounted for in the current tracking scheme, mainly due to two reasons:

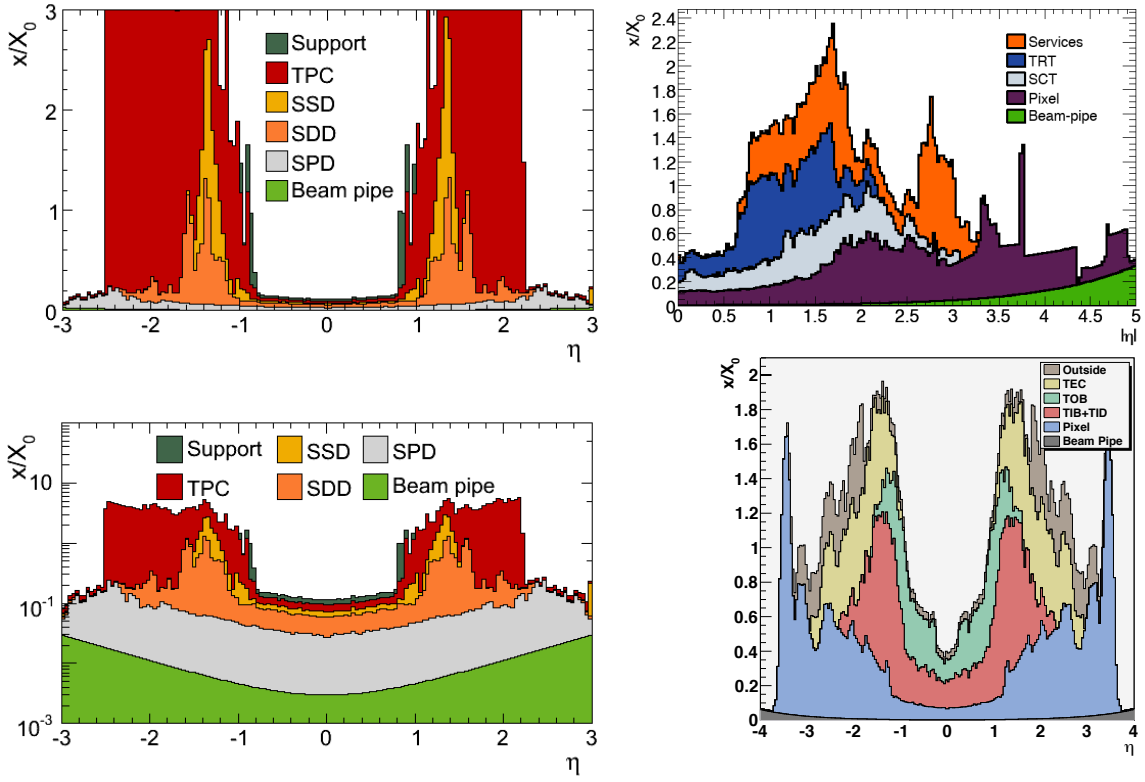

Figure 3.22: The material budget of the experiments ALICE [157] (upper and lower left), ATLAS[130] (upper right) and CMS[131] (lower right) against the pseudo-rapidity. The different detector parts are shown with different colors.

- During tracking there is no particle identification available yet.
- The process of bremsstrahlung is highly non-Gaussian as can be seen in Fig. 3.17 and is explained in Section 3.3.2.

In the calculation of the invariant mass of an e^+e^- pair the underestimated electron momenta result in a too low mass. The $J/\psi \rightarrow e^+e^-$ spectrum thus exhibits a long tail towards lower masses (see Fig. 4.19 in Chapter 4). When extracting the signal and background contributions the integration limits have to be narrow enough for a reasonable signal-to-background ratio. This leads to the loss of a part of the signal, approximately a quarter in the analysis presented in this work (see Section 4.4.4). A recovery of this additional energy loss would be beneficial.

3.4.1 Methods for Electron Bremsstrahlung Recovery

Other experiments are facing the same problem. In contrast to the two largest LHC experiments, ATLAS and CMS, ALICE is a very light detector and does not suffer from this effect as much

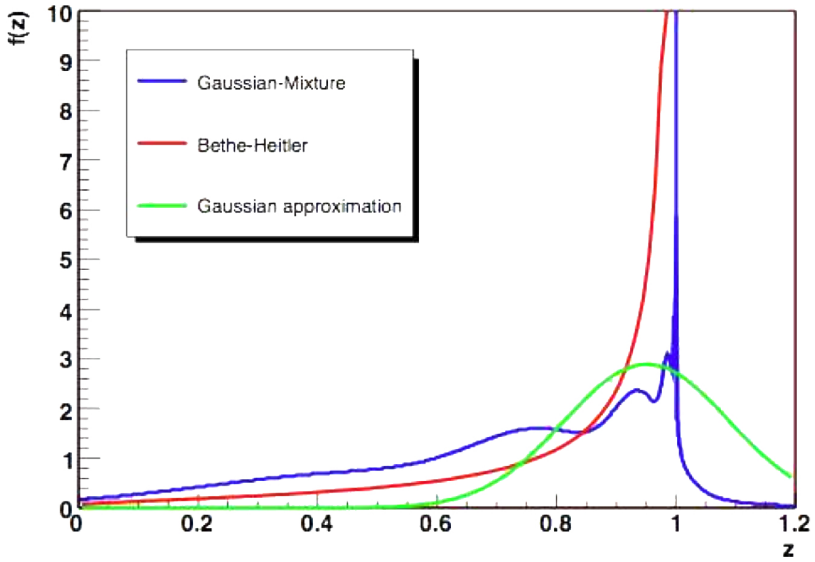

Figure 3.23: Comparison of the Bethe-Heitler distribution (red line) with a single Gaussian (green line) and a sum of several Gaussians used by the Gaussian Sum Filter (blue line) [158].

as these. Figure 3.22 shows the material budget of the ALICE, ATLAS and CMS experiments in units of radiation lengths. In the central barrel part, i. e., in the region of $|\eta| < 0.9$—the acceptance of the ALICE main tracking devices—the material traversed by electrons up to the outside of the TPC is only of the order of 20 % of a radiation length. Nevertheless, the effect is substantial also at ALICE. The current technical possibilities and applications at competing LHC experiments will be reviewed in the following.

Gaussian approximation The first and simplest approach of including the energy loss by bremsstrahlung into an existing Kalman filter based tracking algorithm would be the crude approximation of substituting the Bethe-Heitler distribution Eq. (3.9) with a single Gaussian of same width and mean. This has been studied at the ATLAS experiment [158] as shown in Fig. 3.23.
An implementation of such a solution is rather simple. During the Kalman filter cycle this additional process noise could be added to the covariances of electron candidate tracks. But when comparing the green and red distributions of Fig. 3.23 it is not surprising that this exercise does not yield any substantial improvement in the track reconstruction; the curves are too different from each other [158].

Gaussian Sum Filter The Gaussian Sum Filter (GSF) is a non-linear generalization of the Kalman filter [159, 160]. The basic idea is to model the Bethe-Heitler distribution $f(z)$,

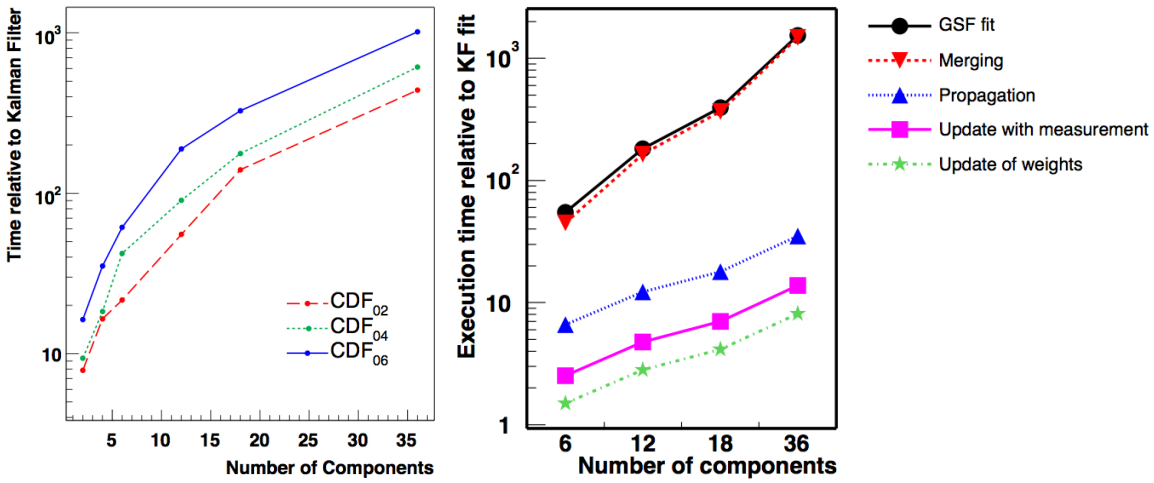

Figure 3.24: The execution time of the Gaussian sum filter relative to the Kalman filter execution time versus the mixture size after component reduction. Three different Gaussian mixtures with two, four and six Gaussians to map the Bethe-Heitler distribution of a given material thickness are shown for the ATLAS GSF implementation (left), the timing for a mixture of six Gaussians (circles) in the CMS implementation is further broken down into the components of the framework (right). Red triangles depict the component merging, blue triangles propagation and estimation of material effects, squares the measurement update and asterisks the calculation of the weights of the updated state [161, 162].

Eq. (3.9), for a given material thickness t with a weighted sum $g(z)$ of a fixed number of Gaussians:

$$f(z) \approx g(z) = \sum_{i=1}^{N_{\mathrm{BH}}} \delta_{\mathrm{i}} \phi(z; z_{\mathrm{i}}, Y_{\mathrm{i}}). \tag{3.17}$$

Here N_{BH} is the number of components which is typically between two and six. The weights δ_{i} of the individual Gaussians, their means z_{i} and variances Y_{i} must be determined [160]. This is illustrated with the blue curve in Fig. 3.23. Each of the N_{BH} individual Gaussians from the sum is then used as additional process noise to compute the a priori estimation of the next cluster position in the detector using one independent Kalman filter. In order to increase the computation speed the Gaussian mixtures can be parameterized as a function of the thickness t so that they do not have to be calculated newly for every step [160].

The number of parallel Kalman filters, N^{k}, in a given step k will therefore increase as $N^{\mathrm{k+1}} = N_{\mathrm{BH}} N^{\mathrm{k}}$ to the next step. Typical numbers of steps in the track reconstruction, i. e., filter cycles, are of the order of a few hundreds. It becomes clear that without reducing the number of components the computing overhead quickly becomes impracticable. Thus, the method of reducing the number of components becomes an essential part of this approach: as

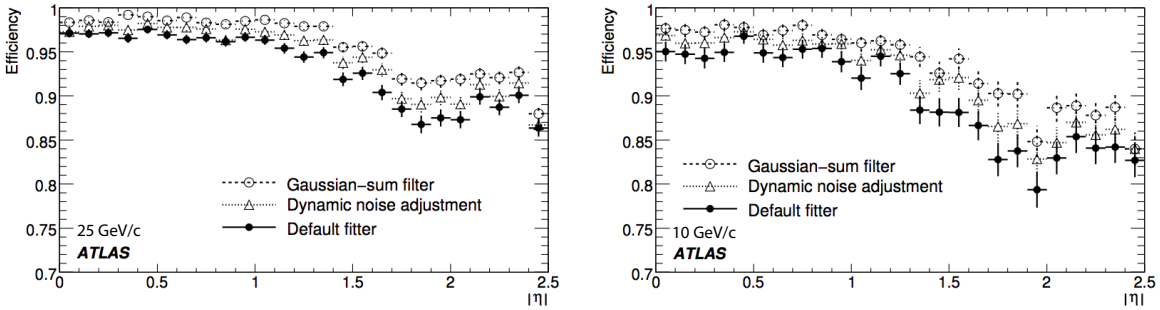

Figure 3.25: Efficiencies of the electron reconstruction versus the absolute pseudo-rapidity for electrons with $p_t = 25$ p_t (left) and $p_t = 10$ GeV/c (right) for different track reconstruction strategies in the ATLAS experiment [163].

little information as possible should be lost hereby.
The number of components is restricted to a certain maximum N. Increasing N improves the quality of the filter but with a significant increase in computing time. Figure 3.24 shows the computing time of the GSF, relative to the standard Kalman filter against the number of components. On the left panel the analysis of the GSF execution time of the ATLAS experiment can be seen for three different Gaussian mixtures with two, four and six Gaussians. The GSF needs between one (very low number of components) and three (relatively high number of components) orders of magnitude longer execution time then the simple Kalman filter. On the right panel of Fig. 3.24 the timing performance is shown for the CMS experiment for a mixture of six Gaussians. The result is comparable to that by ATLAS and further broken down into the different parts of the GSF procedure. The by far most time consuming part is the component merging procedure, described in the following.

Possible ways to reduce the number of components are to select the N components with the largest weights or by merging close components until not more than N remain. The first method is relatively simple but has the disadvantage that the mean and variance of the original distribution is not preserved. To overcome this one can add a new single Gaussian equivalent of the remaining components. In the latter method the so-called *Kullback-Leibler* distance of all components is calculated; the pair with the closest distance is merged into one single component. This reduction is done recursively until only N components remain. The above mentioned is described in detail in [161, 152].
Another advantage of the GSF is that also the small deviations of the multiple scattering angular distribution from a pure Gaussian, as discussed in Section 3.3.2, can be mapped with a Gaussian sum [161]. By this the step update, i. e., the prediction in the Kalman filter cycle, can in principle be improved for all particle species.
The two largest LHC experiments, ATLAS [164] and CMS [165] have carried out extensive studies to incorporate the GSF tracking approach in their track reconstruction scheme (see [166, 158, 167, 161, 168] and [162, 169], respectively).

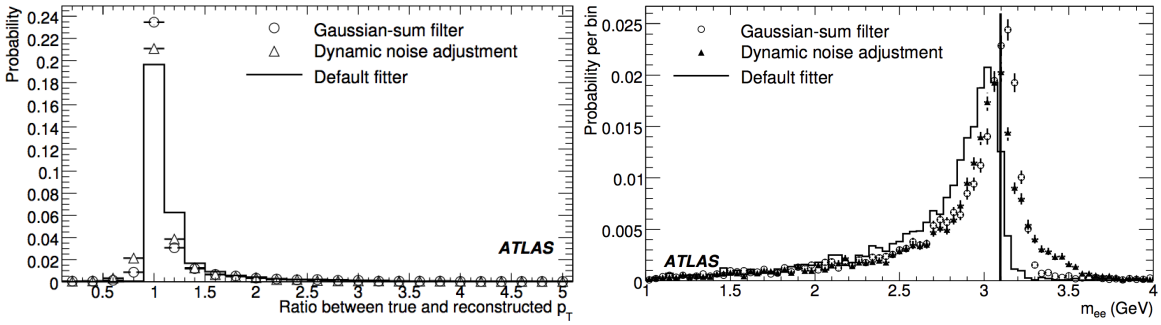

Figure 3.26: Probability distributions for the ratio of the true to reconstructed momentum for electrons with $p_t = 25$ GeV/c in the ATLAS central ($|\eta| < 0.8$) detector for different track reconstruction strategies (left) and probability for the invariant mass of electron pairs from dielectronic J/ψ decays for electrons in $|\eta| < 0.8$ for different track reconstruction strategies (right) [163].

Gaussian sum filters can be quite successful in bremsstrahlung recovery. They allow bigger changes in the track curvature so they can follow the electron tracks better and correctly associate more clusters to them. Such tracks are more likely to fulfill the track quality cut criteria in the data analysis leading to a 2–3 % higher efficiency in the electron reconstruction using the GSF [163]. The latter is illustrated in Fig. 3.25 for electron momenta of 25 (left panel) and 10 GeV/c (right panel). ATLAS also reports an improvement in the electron track momentum resolution from about 9.5 % to 8 %[167]. This is also visible in the distribution of the ratio of the true to reconstructed transverse momentum for 10 GeV/c electrons, see Fig. 3.26. The distribution of the electrons reconstructed with the GSF is more peaked at unity than the one using the standard Kalman filter and the tail from underestimated electron momenta is smaller. On the other hand, GSF tracks show a slightly larger spread to overestimated momenta. A similar behavior is seen in the application of the GSF at CMS, see Fig. 3.27, both for electron momenta of 10 (left) and 30 GeV/c (right).
Of high interest of course is the final impact of the application of the Gaussian sum filter on the J/ψ invariant mass spectrum, shown on the right panel of Fig. 3.26. The peak of the distribution is closer to the real J/ψ mass, illustrated with a vertical line. Also the tail is reduced and the peak more symmetric.

Dynamic Noise Adjustment Another, rather recent method for electron bremsstrahlung recovery is called Dynamic Noise Adjustment (DNA) and has been implemented in the ATLAS reconstruction [167, 158]. Similar to the ALICE experimental setup, the innermost detector of ATLAS is a silicon based detector, the Semiconductor Tracker (SCT). The main idea of the DNA is to find an approach to justly integrate bremsstrahlung as a source of Gaussian noise despite its different functional shape [158]. Like this the standard Kalman Filter can be used for the track reconstruction, just with an additional source of process noise.

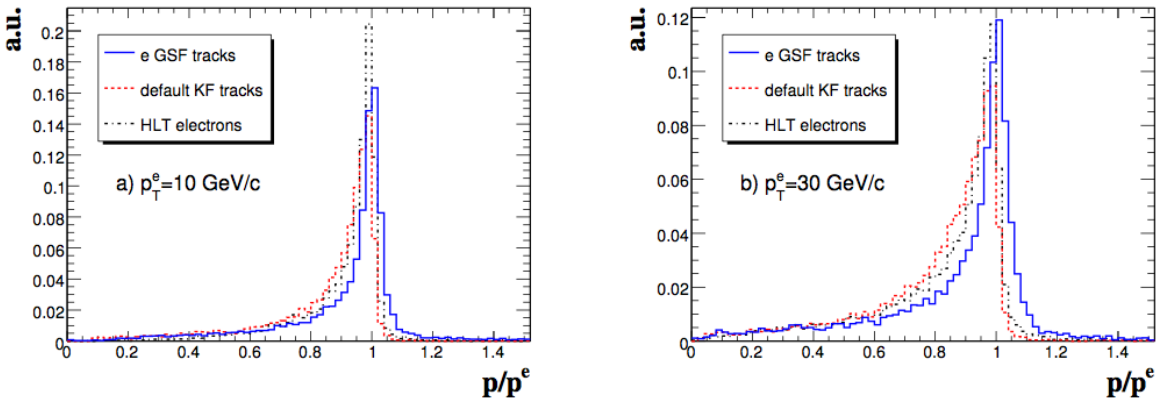

Figure 3.27: Probability distributions for the ratio of the reconstructed (p) to true (p^e) momentum for electrons with $p_t = 10$ GeV/c (left) and $p_t = 30$ GeV/c (right) in the CMS experiment; the distributions are shown for three different reconstruction algorithms: the standard Kalman filter (red dashed lines), GSF (blue lines) and HLT (black dash-dotted lines). The latter is not taken into account in this study [169].

The strategy is as follows: At each layer of the SCT a single parameter fit is performed that tries to find and estimate an increase in the track curvature: When the χ^2 at a given hit is larger than a certain threshold the extrapolation to that layer is done two more times with different assumptions of $z < 1$ (see Eq. (3.9), Section 3.3.2) for bremsstrahlung. The $1/z$-position of the minimum χ^2 is found with a parabolic fit to the three extrapolation results, χ^2 versus $1/z$, and used for the calculation of the additional noise term [170].

In Fig. 3.28 the second part of the procedure is illustrated. The Bethe-Heitler distribution (upper left panel) is mapped onto the Gaussian distribution of zero mean and unit width (upper right panel). This mapping is done via the cumulative distribution functions (CDF, lower two panels) of the two probability distribution functions (PDF). The median z_0 of the Bethe-Heitler PDF—50 % in the corresponding CDFs—points at $x = 0$ in the centered Gaussian PDF. Mapping the fit result z the same way leads to the effective bremsstrahlung process noise as it is estimated in the DNA [158]:

$$\sigma_{\mathrm{DNA}}(z) = \frac{\Delta z}{\Delta x}, \tag{3.18}$$

where $\Delta z = z_0 - z$ and $\Delta x = x_0 - x$. Because the median of the centered Gaussian is at $x_0 = 0$ the above term can be written as:

$$z = z_0 + x\sigma_{\mathrm{DNA}}(z), \tag{3.19}$$

a representation of the Bethe-Heitler distributed z by x, which is a variable of Gaussian distribution.

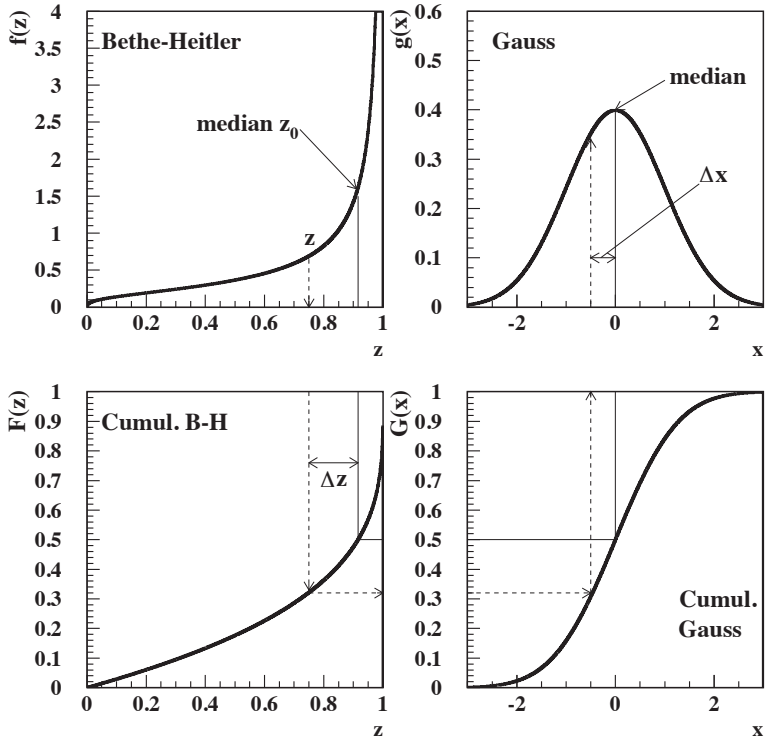

Figure 3.28: Illustration of the mapping of the probability distributions from Bethe-Heitler (upper left panel) onto Gauss (upper right panel) via the respective cumulative distributions (lower two panels). This method is used in dynamic noise adjustment to calculate the variance of the effective noise term [167].

Figure 3.29 shows σ_{DNA} versus z for various material thicknesses. The dynamically estimated variance σ^2_{DNA} of the effective noise, corresponding to the given traversed material thickness and retained fraction of electron energy, is added to the appropriate Kalman covariance matrix (see Section 3.3.3).

Another effect of the increased precision and better error estimation is an improved matching of the track segments between the different detectors. In ATLAS, the SCT is surrounded by the Transition Radiation Tracker (TRT). The percentage of electron tracks from SCT without TRT match drop from 20 % down to 8 % when using DNA [158]. In contrast to the GSF the method of dynamic noise adjustment brings only very low computing overhead, less than additional 10 % of the default global χ^2 fitter [158]. The left panel in Fig. 3.26 shows a reduction of the tail in the ratio of simulated to reconstructed transverse momentum for DNA tracks with respect to tracks from the default fit. Comparing the results of the DNA and GSF procedures, the latter shows a stronger improvement of the momentum reconstruction. A similar conclusion can be drawn when looking at Fig. 3.25. Here the electron track reconstruction efficiencies are shown against $|\eta|$ for $p_{\mathrm{t}} = 25$ GeV/c (left) and $p_{\mathrm{t}} = 10$ GeV/c (right). The DNA fit improves

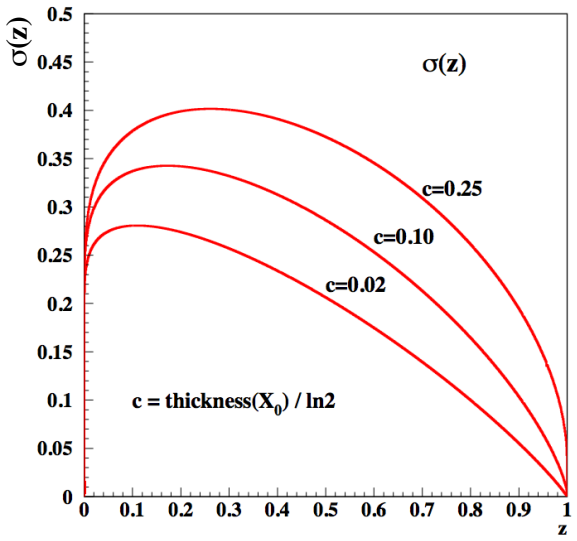

Figure 3.29: The effective $\sigma_{\mathrm{DNA}}(z)$ for three different typical material thicknesses c in units of radiation lengths [167].

the reconstruction efficiency at both momentum samples and over the whole pseudo-rapidity range; though not as much as the GSF does. The right panel in Fig. 3.26 shows the e^+e^- invariant mass spectrum from $J/\psi \rightarrow e^+e^-$ simulations. The true J/ψ mass is drawn as a vertical line, the solid line illustrates the spectrum obtained by using the default filter. As the GSF (open circles), the DNA (full triangles) brings a substantial reduction of the tail and a more symmetrically shaped peak. ATLAS claims [158] an improvement of the invariant mass resolution by 20 % and an increase on 5 % in the J/ψ reconstruction efficiency.

Nevertheless, there are also a couple of disadvantages [158]. Mainly, when applying the DNA to tracks of heavier particles than electrons, some small biases are introduced. Also, not all electron tracks benefit from the procedure: the measurement of small changes of the curvature of very high momentum tracks is not possible. Furthermore only SCT hits are precise enough, so bremsstrahlung in the outer detectors cannot be recovered. Current studies investigate the possibility of including information from electromagnetic calorimeters. In the current ATLAS tracking procedure still the global χ^2 fit is used per default. All other fitting procedures, the plain Kalman filter, the Gaussian sum filter and the Kalman filter plus dynamic noise adjustment are in place and can be selected. Which algorithm is used will depend on individual physics analyses.

3.4.2 Possible Incorporation in the ALICE Tracking Procedure

Both the GSF and the DNA are very promising tools for the recovery of bremsstrahlung and offer substantial improvements in the electron reconstruction. Since the Kalman filter is the

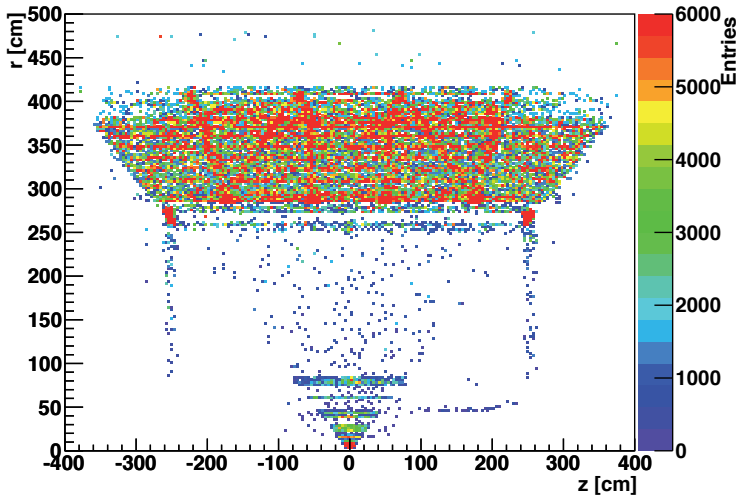

Figure 3.30: Bremsstrahlung vertex positions in the rz plane [171].

default track fitting and finding algorithm at ALICE an implementation of the GSF as well as the DNA has no substantial technical hurdles. Problems with biases in the tracking of heavier particles and especially the huge computing overhead in case of the GSF suggest that the most practical implementation of both strategies would be only on identified electron tracks. This could be realized as an additional reconstruction pass or during the third reconstruction pass.

The question is now whether or not such methods can improve the electron measurements in the special case of the ALICE detector layout. Therefore, a detailed study has been performed [171]. Figure 3.30 and Fig. 3.31 show two-dimensional projections of electron bremsstrahlung vertex positions in Monte Carlo simulations of J/ψ daughter electrons, propagated through the ALICE detector material. The more material electrons have to traverse, the more energy they lose due to bremsstrahlung. In both figures thus several parts of the ALICE geometry become visible. The projection on the rz plane, Fig. 3.30, shows in the lower central part the different layers of the ITS. Above, the TPC field cage can be seen, the upper part of the figure contains the TRD with its supermodules and spaceframe. As expected, in the structures of both TRD and ITS much more bremsstrahlung processes occur than in the TPC, which only consists of gas in its active volume.

Since the last track fitting iteration is starting from the TRD, proceeding towards the primary interaction vertex, one can assume that bremsstrahlung events in the TRD do not have a substantial impact on momentum resolution of electron tracks; there are enough clusters of the track that will correct the distorted track parameters.

Thus, the part of the bremsstrahlung which mainly causes a wrongly reconstructed momentum, occurs in the ITS. Figure 3.31 shows a projection of the bremsstrahlung vertex positions in the xy plane, focussing on the ITS, surrounded by the inner TPC field cage. Comparing

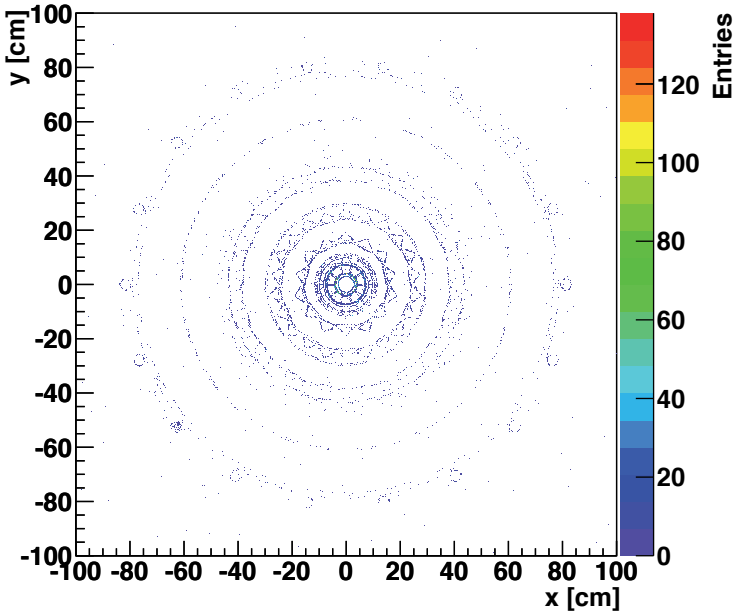

Figure 3.31: Bremsstrahlung vertex positions in the xy plane [171].

to Fig. 3.6, the ITS geometry can be recognized up to very much detail. A large fraction of the entries can be associated to interactions with the SPD material. A more quantitative illustration is given in Fig. 3.32. There, the mean energy loss due to bremsstrahlung is shown vs. the radial distance of the traversed material to the main vertex. In the outer parts, between 2.5 and 4 m, again the high material budget of th TRD is visible, especially at the inner part close to the TPC. In the TPC region, between 0.9 and 2.5 m, only very soft bremsstrahlung is emitted—if at all. In the ITS region, i. e., in the various layers below 0.5 m, the average energy loss of bremsstrahlung processes is almost half a GeV. These are quite hard events leading to a strong kink in the track making it difficult for the tracking algorithm to follow. In all those cases, where the track does not have any further hit before the bremsstrahlung event none of the discussed methods will be able to bring any improvement on the momentum reconstruction.

The remaining question is then whether or not the investigated methods are capable to recover the additional energy loss even if there are only few, i. e. between 1 and 6, clusters left for the fit. Especially with the GSF this might not be the case for most of the events. This algorithm needs a couple of cluster measurements after the bremsstrahlung vertex so that the changed path is recognized. Nevertheless, since the GSF improves the overall tracking performance, an implementation will be beneficial.
The DNA, on the other hand, might find bremsstrahlung events especially in the ITS where a very high spacial resolution is available. Hard processes, as they seem to happen frequently in the ITS, will not be detectable with either of the methods. The largest part of the long tail in the J/ψ invariant mass will not be recovered.

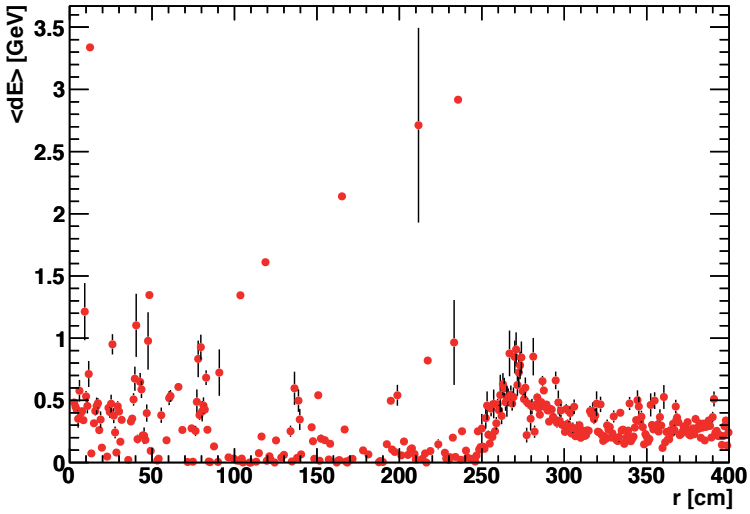

Figure 3.32: The mean energy loss due to bremsstrahlung vs. the radial distance of the traversed material to the main vertex [171].

An implementation of such methods is a substantial modification of a very basic part of the reconstruction. For the J/ψ measurement in ALICE it does not offer a strong gain in the reconstructed signal counts by removing parts of the tail. Due to an overall lower material budget, the mass resolution at ALICE is already very good. Therefore, at the current stage where the first measurements are being performed, no method for bremsstrahlung recovery has been implemented in the ALICE track reconstruction. Still, on a longer time scale an implementation especially of the DNA algorithm might be desirable to further improve the precision of the measurement.

So far, in the currently available data statistics, no Υ signals have been detected with the central barrel detectors (see Chapter 4). As soon as data with the fully installed TRD is available for PID and delivers a trigger on high p_{t} electron candidates significant measurements of the Υ are anticipated. A mass resolution of about 90 MeV/c^2 is expected in the Υ region[172]. The two excited states Υ' and Υ'' have a mass difference of only approx. 350 MeV/c^2. When the resolution of the measurement is only slightly worse than estimated it might become difficult to separate these two states. Due to the high mass of the particles of the Υ family, bremsstrahlung is even more relevant in their measurement.
The improvement of the momentum resolution offered by the two methods might be the key to disentangle the excited states. Again, when an implementation is attempted, the DNA is recommended.

Chapter 4

J/ψ Analysis in Minimum Bias pp Collisions

This chapter presents the analysis of the inclusive J/ψ production cross section in $\sqrt{s} = 7$ TeV minimum bias pp collisions, both as an integrated value and as a differential measurement versus transverse momentum and rapidity. This study has been performed in conjunction with the ALICE J/$\psi \rightarrow e^+e^-$ analysis group. It is serving as a cross check and contributed several of its parts to the combined work leading to the publication of the first J/ψ measurement with ALICE [173].
First the setup and environment of the analysis will be introduced, followed by a list of the analyzed data sets. The strategy to extract J/ψ signal counts out of this data is discussed thereafter; finally, all necessary corrections to the measured rates are presented. In the last part of this chapter the results of this analysis will be shown, followed by a discussion.

4.1 Setup of the Analysis

Data analysis at ALICE takes place in a dedicated environment. The basic tools, methods and frameworks that are especially important for this work are discussed in the following.

4.1.1 The ALICE Analysis Environment

As many other heavy-ion physics experiments and in general many high-energy physics experiments, ALICE makes use of the ROOT framework [174]. ROOT is an object-oriented C++ software package providing large sets of classes for the implementation of detector simulation, event reconstruction, data aquisition and data analysis [175]. Also several event generators are

included as well as interfaces to external ones. Two other important features of ROOT are its input/output (I/O) system allowing to efficiently store and load C++ objects of potentially large size into .root files on the one hand and the CINT C/C++ interpreter on the other. The latter enables the user to execute C/C++ macros and run C/C++ code from the command line without the need of a full compilation. This option speeds up code development.
All ALICE detector-specific code, e. g., for the detector geometry, the reconstruction algorithms and the calibration, is put together in the AliRoot [176] framework. Therein the basic functionalities of ROOT are utilized. AliRoot is used in almost all parts of the experiment, from the data aquisition and the event reconstruction to the analysis of the reconstructed data. Also all necessary interfaces for the application of external event generators, such as Pythia [71] (see Section 4.2.2) or HIJING [177], and tools for the detector simulation, such as GEANT3 and 4 [178, 179] and FLUKA [180] are provided. Such Monte Carlo (MC)[1] tools are important for the generation of simulated events, the subsequent propagation of the tracks through the detector and the simulation of the detector response. Just as real data, this response can be used for the reconstruction of the original particle tracks. Unlike in the real experiment, here a comparison of the Monte Carlo input to the result of the reconstruction is possible. Such studies are essential for the understanding of detector effects as its acceptance and efficiency. Also in this study this is a neccessary step and will be discussed in detail in Section 4.4.

The analysis train framework The amount of recorded data, both simulated and reconstructed, is too large that each user, working on an individual analysis, could process a good fraction or even the full data set on his own. The only possibility to analyze such amounts of data is to implement the individual analysis within the framework of the ALICE analysis train. Such an analysis train can be run centrally on a computing site with large amounts of resources or on the Grid[2] [181]. Instead of, e. g., an analysis macro that loops over the data itself, every user writes an analysis task. The tasks of all users are then put together in the analysis train. Compared to the individual analysis the difference is that the train accesses the same data only once and provides it to all tasks. Like this, the I/O and CPU cost is minimized.
For the present study the full 2010 minimum bias data set is used; thus, this analysis has been implemented within the framework of the ALICE analysis train.

The ALICE Correction Framework Many analyses of the ALICE data sets share a lot of similar techniques. To keep redundant code development at a minimum and provide well-tested tools the Correction Framework (CF) is provided within AliRoot. Its basic features can be divided into two groups: container classes and selection classes. While the first allow efficient

[1] Monte Carlo techniques are stochastic methods to compute mathematical or physical problems. They are based on repeated computation of the simulation algorithm using random numbers or samples.
[2] The Grid is a virtual super computer made up of the connection of a large number of distributed computers or computing facilities. Grid computing is a special sort of parallel computing.

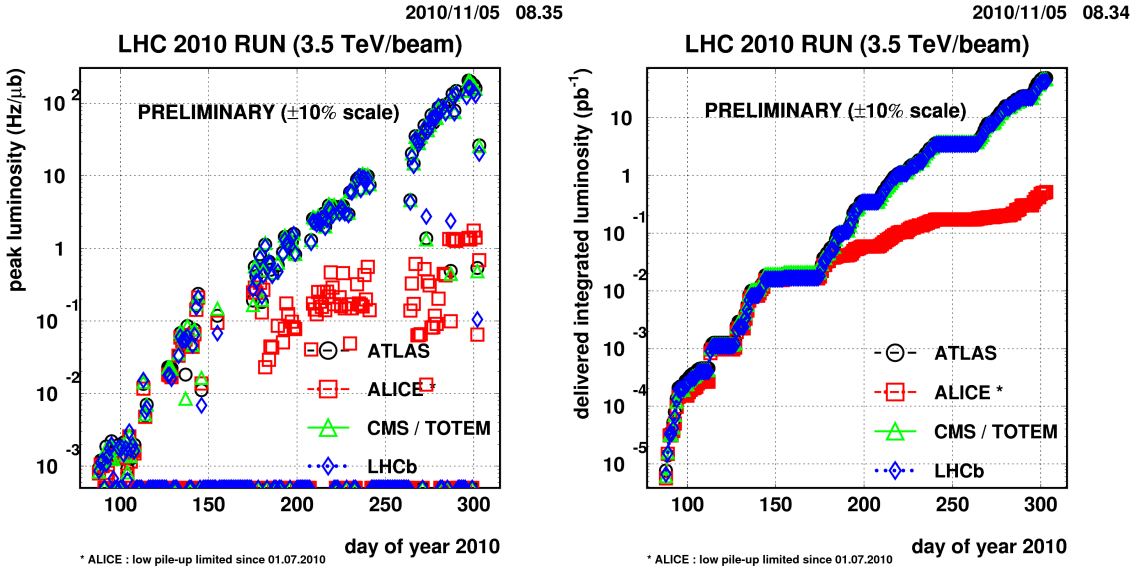

Figure 4.1: Peak (left) and total integrated (right) luminosities delivered to the different LHC experiments [127].

and easy possibilities to store data in n-dimensional grids, the latter combine many configurable selections, both at event and at track level. The container classes can not only be used to store the counts but also to calculate efficiencies of any selection when simulated data has been studied. One of the main advantages of these CF containers is that instead of the normal histogram `TH` they are based on the ROOT `THnSparse` class: only bins filled with data consume memory. Thus, CF containers are not limited to three dimensions and are advantageous for grids with a high number of bins and a low occupancy. In the current analysis the container classes are used both for storing the signals and to calculate the efficiencies.

4.2 Data Sets used for the Analysis

The data sets used for this analysis are listed in the next two sections. Full lists of run numbers are summarized in Appendix F.

The analysis is based on the *event summary data* files, ESDs. ESDs are .root files with a dedicated file structure to store the informations which had been extracted from the raw data by the reconstruction procedure (see Section 3.3.4 for details). Each ESD can contain one or several events. Every stored event contains all necessary informations about itself as well a list of all reconstructed tracks. ESDs carry almost all available informations from the detectors; therefore, the corresponding data size is too large for an analysis on a small computing cluster or even a single workstation.

Another data analysis method is via so-called *analysis object data* files, AODs. AODs are derived from ESDs and contain only the necessary data for a specific analysis. This could be, e. g., all electron candidates. These have to be selected once from the ESDs and stored in the AODs. Like this the amount of data can be strongly reduced. For this analysis the event and track selection is one of the main tasks therefore it has to be based on ESDs. On later stages of the J/ψ analysis, the strategy could be AOD based.

4.2.1 Proton-Proton Data Sets

In 2010, the LHC provided $\sqrt{s} = 7$ TeV pp collisions at steeply increasing luminosities: Fig. 4.1 shows on the left panel the peak and on the right panel the total integrated luminosity. Both luminosities are shown on a logarithmic scale versus the day of the year 2010. Between the 150th and the 200th day, the LHC peak luminosities, see Eq. (3.1), reached values corresponding to the maximum ALICE data taking rate (see Section 3.1). Since the other experiments, ATLAS, CMS and LHCb, are designed for much higher interaction rates, they are running ahead from that time on in both panels of Fig. 4.1. For ALICE, this full run period has been divided into various beam periods in which the data taking conditions were mostly unchanged. For this analysis, the following beam periods are taken into account: LHC10[b,c,d,e]. Table 4.1 shows the event statistics for each of the four beam periods and the full sample. The different values given in the table will be explained in Section 4.2.3.

Beam Period	$N_{\mathrm{MB}} \cdot 10^6$	$f_{\mathrm{z}_{vtx}}$	$N_{\mathrm{MB}}^{\lvert \mathrm{z}_{vtx}\rvert < 10\,\mathrm{cm}} \cdot 10^6$	$N_{\mathrm{MB}}^{\mathrm{ana}} \cdot 10^6$
LHC10b	29.46	0.998	29.40	25.41
LHC10c	74.92	0.993	74.37	63.42
LHC10d	153.11	0.881	134.89	115.59
LHC10e	116.19	0.871	101.18	87.49
Sum	373.68	0.909	339.84	291.91

Table 4.1: The $\sqrt{s} = 7$ TeV pp data used for this analysis. The first column shows the names of the individual beam periods. The number of MB triggered events is given in the second column. In the third column, the ratio of events within $|\mathrm{z}_{vtx}| < 10$ cm and all events, $f_{\mathrm{z}_{vtx}}$, is listed for each beam period. The corresponding number of events $N_{\mathrm{MB}}^{\lvert \mathrm{z}_{vtx}\rvert < 10\,\mathrm{cm}}$ is given in the fourth column while the last column shows the number of analyzed events passing all cuts. The last row contains the same numbers, summed over all beam periods.

MC Sample	Anchor Run for	$N_{\mathrm{MB}}^{\mathrm{ana}} \cdot 10^6$
Min. bias		
LHC10d1	LHC10b	20.14
LHC10d4	LHC10c	24.58
LHC10f6a	LHC10d	107.99
LHC10e20	LHC10e	2.33
Min. bias + heavy flavor		
LHC10f7a_b	LHC10b	1.68
LHC10f7a_c	LHC10c	4.02
LHC10f7a_d	LHC10d	4.78
LHC10f7a_e	LHC10e	10.47

Table 4.2: The different MC data samples used in this analysis. Two different types of samples are listed: pure $\sqrt{s} = 7$ TeV Pythia min. bias pp events and $\sqrt{s} = 7$ TeV Pythia min. bias pp events, enriched with heavy flavour signals, such as $\mathrm{J}/\psi \rightarrow \mathrm{e}^+\mathrm{e}^-$. For these central MC productions Pythia 6.421[71] was used, in the tune Perugia-0[182].

4.2.2 Monte Carlo Data Sets

For the understanding of various detector effects and as a necessity for correction procedures, as described in Section 4.4, reconstructed Monte Carlo simulations of proton-proton events in the ALICE detector are analyzed. Table 4.2 summarizes the data samples that are used in this analysis. Two different types of MC productions are taken into account. While the samples LHC10d1, LHC10d4, LHC10f6a and LHC10e20 are MC productions of $\sqrt{s} = 7$ TeV Pythia 6.421 [71], tune Perugia-0 [182], minimum bias pp collisions, LHC10f7a_[b,c,d,e] also consist of such events, but enriched with heavy flavor signals such as D and B mesons, and J/ψ. For this analysis all events containing one additional J/ψ are taken into account. This sample is used to determine correction factors for acceptance and detector efficiency. Inclusive CDF measurements [80], extrapolated from $\sqrt{s} = 1.96$ TeV to LHC energies, and parameterizations from CEM calculations[183] (see Section 2.3.2) have been used for the input p_{t} and y distributions, respectively.
Since the exact detector setup and the information which modules have been switched on and off has an impact on these correction factors, for each data taking period listed in Table 4.1 a dedicated MC data sample is centrally produced making use of all these informations.
It may be noted here that for this procedure also the detector's configurations are taken into account. The method to acquire and store the configuration data of the TRD (see Section 3.2.4) has been developed and implemented throughout this thesis and is presented in Appendix A.

4.2.3 Trigger Conditions and Event Selection

Trigger conditions All inelastic pp collisions, $\mathrm{pp_{inel}}$, define the group of events used as reference throughout this study. These include non-diffractive, single-diffractive and double-diffractive events [184]. A minimum bias interaction trigger to record these events has been defined for the ALICE experiment. This trigger is fired when at least one of the following conditions is met:

- a hit in the V0A detector,
- a hit in the V0C detector,
- a hit in the SPD detector.

The technical name of this trigger class is CINT1B. Events triggered by this class are further referred to as minimum bias events (MB) throughout this thesis. All results presented in this study correspond to events selected with this trigger scenario. Table 4.1 shows the number of recorded MB events in each of the analyzed beam periods.
For any normalization to the number of inelastic pp events the trigger efficiency must be determined, and the number of events must be corrected accordingly. In case of the MB trigger, this efficiency is defined as $\epsilon_{\mathrm{MB}} = N_{\mathrm{MB}}/N_{\mathrm{pp,inel}}$; it was determined in a MC study [185] with the result:

$$\epsilon_{\mathrm{MB}} = 0.864 \ \pm 1.5\,\% \text{ (syst.)}. \tag{4.1}$$

For the determination of a cross section, another trigger class has to be introduced, V0AND, which is defined as the coincidence of signals in both of the V0 detectors. The cross section of this trigger has been determined in a series of van der Meer scans [186, 187, 188] for different beam energies. For $\sqrt{s} = 7$ TeV pp collisions, this reference cross section is [187]:

$$\sigma_{\mathrm{pp,V0AND}} = 54.1 \text{ mb} \pm 4\,\% \text{ (syst.)}. \tag{4.2}$$

This study uses the MB trigger class for event selection. Since the cross section is only available for V0AND triggered events, in order to acquire the minimum bias cross section, the factor $\sigma_{\mathrm{pp,V0AND}}/\sigma_{\mathrm{pp,MB}} = 0.875$, was determined as the fraction MB events where the V0AND trigger has fired. It has also been checked that this ratio is constant within 1 % over all analyzed beam periods (see Figs. D.1 to D.4 in Appendix D). The result for the cross section is:

$$\sigma_{\mathrm{pp,MB}} = 61.8 \text{ mb} \pm 4\,\% \text{ (syst.)}. \tag{4.3}$$

The systematic errors of the V0AND cross section Eq. (4.2) and of the fraction $\sigma_{\mathrm{pp,V0AND}}/\sigma_{\mathrm{pp,MB}}$ are added in quadrature, resulting in 4 %.

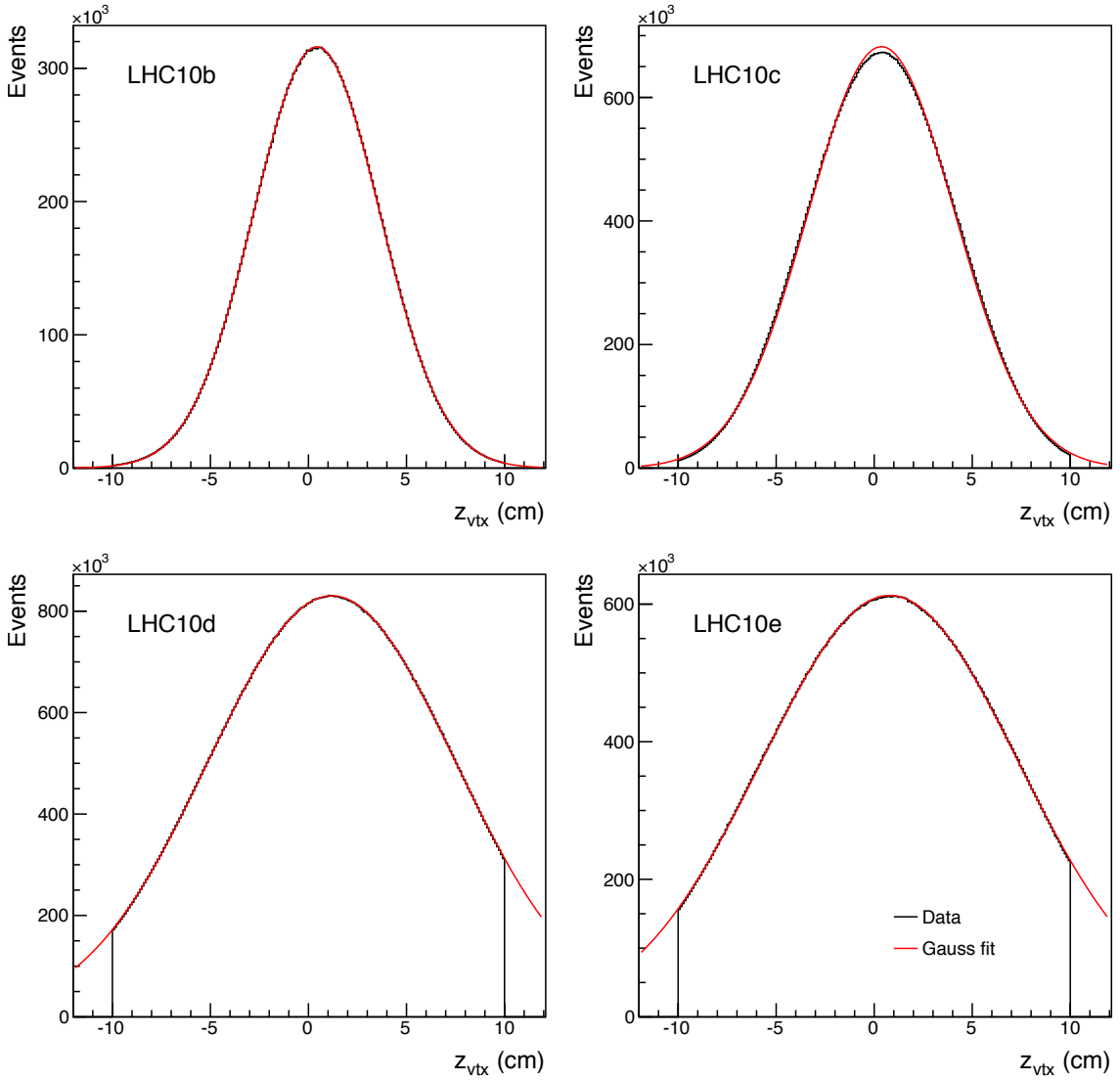

Figure 4.2: The distribution of vertex positions in z direction for the beam periods LHC10[b-e]. The distributions are well described by Gaussian fits (red). While the histogram corresponds to the group C, the area of the Gaussians correspond to $C + A$.

Event selection Both beams cross each other in a very small angle. The primary interaction vertex position of the triggered events is spread a few centimeter around the origin along the z axis in the ALICE coordinate system (see Section 3.2.1). On the other hand, the spread in the transverse plane is negligible. To ensure that the characteristics of the detector are the same for all analyzed events, those with a reconstructed vertex position $|z_{\mathrm{vtx}}| > 10$ cm are rejected. Since the physics processes do not depend on the position of the collision in the experiment no bias is introduced by applying this selection. The distribution of primary interaction vertex positions in z direction changes with the LHC setup and is different for the beam periods

taken into account, see Fig. 4.2. The distribution of vertex positions in z direction is shown for LHC10[b-e]. Later beam periods (LHC10d and -e) exhibit a broader width of the distribution than earlier ones (LHC10b and -c) due to high intensity beams. All data are well described by Gaussian fits. Only for the beam periods LHC10c, in the tail region and for the central part, small differences between data and fit can be seen. A reason for this could be that in the last runs of that period the distribution already started to become broader. Still this is a small effect without impact on the analysis.
Not all MB triggered events do have a reconstructed primary vertex since at least one track in the acceptance of the central barrel detectors is necessary for a successful reconstruction. Nevertheless, all events within $|z_{\mathrm{vtx}}| < 10$ cm belong to the reference $\mathrm{pp_{inel}}$, both those with and those without a detected vertex. Figure 4.3 illustrates this situation: the full area (A+B+C+D) corresponds to all MB triggered events, N_{MB}. The area shaded in red ($A + B$) depicts the number of events which are rejected because of a vertex more than 10 cm away from zero in the z coordinate. These events are excluded from the further analysis where only the group $C + D = N_{\mathrm{MB}}^{\mathrm{ana}}$ is used. While C is just the area in $|z_{\mathrm{vtx}}| < 10$ cm of the distributions in Fig. 4.2, the problem is now to find out the number of events with a vertex inside $|z_{\mathrm{vtx}}| < 10$ cm which had not been reconstructed (D). The area shaded in blue ($B + D$) corresponds to all those events for which no vertex was found in the reconstruction. Using the assumptions that the z_{vtx} distribution is the same for events with and without reconstructed vertex ($C/A = D/B$) and that the vertex reconstruction efficiency is flat over a z range including the largest fraction of the events[3], the number of events D can be estimated:

$$C + D \simeq (A + B + C + D) \cdot \frac{C}{C + A}. \tag{4.4}$$

While the fraction $\frac{C}{C+D} \approx 86\,\%$ does not depend on the beam period, this is indeed the case for $f_{\mathrm{z_{vtx}}} = \frac{C}{C+A}$, see Fig. 4.2. So the number of all MB events within $|z_{\mathrm{vtx}}| < 10$ cm, $N_{\mathrm{MB}}^{|\mathrm{z}_{vtx}|<10\,\mathrm{cm}}$ is determined separately for each beam period. The results for the correction factors $f_{\mathrm{z_{vtx}}}$ as well as the corresponding number of events are summarized in Table 4.1.
An important issue is whether or not a bias on the J/ψ signal is introduced herewith. There are several arguments why this is not the case:

- The electron-positron pair from the J/ψ decay inside the TPC acceptance would lead to the reconstruction of the vertex.
- The fraction of events without reconstructed vertex in the class of V0AND triggered events is only about 7 % compared to about 14 % in MB events. On the other hand the signal is found to be the same within 1.2 %.
- The charged-particle multiplicity dependence of J/ψ production indicates a small J/ψ

[3] In the relevant region, the vertex-reconstruction efficiency is indeed practically independent of the z position of the vertex, see [184].

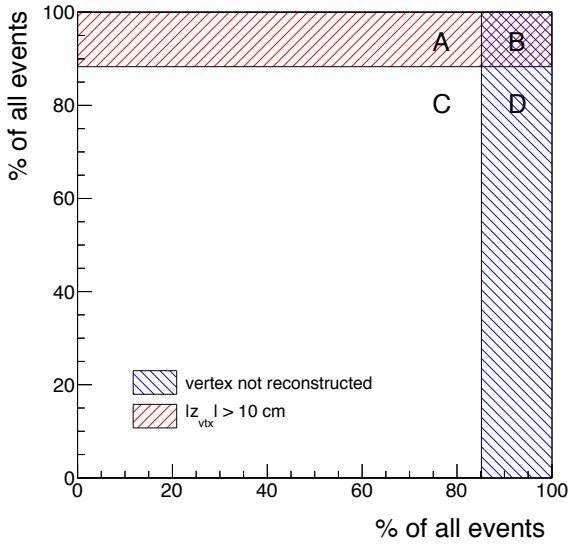

Figure 4.3: Sketch to illustrate which fraction of all triggered events belong to the reference $\mathrm{pp}_{\mathrm{inel}}$. The red area corresponds to all events that have a primary interaction vertex more than 10 cm away from the nominal interaction point in z direction. The blue area corresponds to all events that do not have a reconstructed vertex. The area labeled as D belongs to the reference number of events even though it cannot be directly determined since the vertex position has not been measured. The indirect determination of the area $C + D$ is explained in the text.

yield for low multiplicities, see Section 5.6. Events with high multiplicities will have a reconstructed vertex.

So there is no J/ψ signal lost in the events without reconstructed vertex belonging to the total number of events in the sample. Table 4.1, below the event statistics of the individual beam periods, lists the total number of events analyzed here.

Integrated luminosity The total number of selected triggered events $N_{\mathrm{MB}}^{|z_{vtx}|<10\,\mathrm{cm}}$, listed in Table 4.1, and the cross section of this trigger $\sigma_{\mathrm{pp,MB}}$ the integrated luminosity $L_{\mathrm{int}} = N_{\mathrm{MB}}^{|z_{vtx}|<10\,\mathrm{cm}}/\sigma_{\mathrm{pp,MB}}$ of the analyzed data sample can be given:

$$L_{\mathrm{int}} = 5.50\ \mathrm{nb}^{-1} \pm 4\,\%\ (\mathrm{syst.}). \tag{4.5}$$

The integrated luminosity is a useful number e. g. for comparisons with other experiments. Event numbers depend of the specific trigger thus cannot be compared.

4.3 J/ψ Reconstruction

In all available events J/ψ are reconstructed via their decay into e^+e^-. Various selection cuts as well as a particle identification procedure are applied to select electron candidates and to reduce the background from other sources. These steps are explained in detail in the following. Thereafter, the invariant-mass spectrum, obtained from all remaining electron-positron-candidate pairs is discussed. In this spectrum a clear J/ψ mass peak is found. For the extraction of the J/ψ signal counts an estimation of the background below the peak has to be done. Various approaches to do so are presented.

4.3.1 Track Cuts

The following kinematical selection cuts are applied to all tracks:

- Tracks with a θ angle between 45° and 135° traverse the full volume of the TPC and are measured with the highest possible precision. This corresponds to a pseudo rapidity range of $|\eta^{e^\pm}| < 0.9$, tracks outside of that region are rejected from the further analysis.
- A minimal transverse momentum of $p_t^{e^\pm} > 1.0$ GeV/c is required to reject background from processes as from γ conversions, π^0 decays and misidentified hadrons.

Together with the kinematical selection of the J/ψ these define the geometric acceptance of the measurement, see Section 4.4.
Various quality cuts are applied to all tracks in the acceptance. By these requirements, all those which were not properly reconstructed or do not come from the primary vertex are sorted out. For this analysis, four different cut sets have been defined: the default(1) set and a slight variation of it, default(2), and one set of loose and on set of tight cuts. The latter are used to estimate a possible sytematic uncertainty of the efficiency correction, see Section 4.4 and Section 4.5.
The set default(1) is based on the ALICE standard track quality cuts, defined for the run periods in 2010, for all analyses using both TPC and ITS. Its components are as follows:

- Each track is required to be associated with at least one cluster in one of the two SPD layers. Like this the contribution from secondary electrons, created by primary particles interacting with the material of the ITS, is kept at a minimum. This cut is further referred to as *SPDany*.
  It turned out that this is a very strong selection, increasing the ratio of signal to background counts, but also rejecting approx. a third of the signal counts [171]. As it will be shown later, at high J/ψ p_t there is only very little background in the J/ψ mass region. Therefore,

a variation of the default(1) set is introduced, applying a released version of this selection. In this default(2) set instead of the selection SPDany, a less restrictive ITSany(4) is applied. All other selections are unchanged with respect to default(1). The number in parenthesis of ITSany(4) correspond to the number of innermost ITS layers in which at least one cluster is required. Thus, ITSany(2) would be identical to SPDany. In [171] it was shown that while releasing this cut more and more, until ITSany(4) the signal counts increase. Releasing even further only the background counts increase without a substantial difference in the signal. Therefore, ITSany(4) was taken here as the optimal choice.

- An upper limit on the distance of closest approach (dca) to the primary interaction vertex is defined. The $c\tau$ of the J/ψ of $\approx$ 2.1 pm can be neglected, that of B mesons is of approximately half a millimeter. Within 2 mm thus more than 99 % of all secondary J/ψ vertices are located, so in principle this value could be used for the cuts. Still, the resolution of the *dca* measurement is less precise (see [128]), leading to values of $dca_{\mathrm{XY}} < 1.0$ cm in radial direction and $dca_{\mathrm{Z}} < 3.0$ cm in longitudinal direction.

- The first possibility to define the reconstruction quality of a given track in the TPC is to count the number of clusters in the TPC, divide it by the number of possible clusters and require a minimum fraction. Since in this analysis the acceptance is limited to $|\eta^{\mathrm{e^+e^-}}| < 0.9$, the maximum is always the total number of pad rows: 159 [128]. So it is enough to cut on the total number of clusters $N_{\mathrm{cls}}^{\mathrm{TPC}}$ associated to the track. Here a minimum of 70 is required.

- The second possibility to ensure a good quality of the track reconstruction in the TPC of all used tracks is to limit the $\chi^2/N_{\mathrm{cls}}^{\mathrm{TPC}}$ [62]. For this value an upper limit of 4.0 has been used. Since every TPC cluster has a spacial position, i. e., three coordinates out of which one is fixed to the position of the pad row, the number of degrees of freedom is twice the number of TPC clusters minus 5, the number of parameters of the track fit.

- The refit status bits of ITS and TPC are required. These are enabled when the track fitting procedure successfully followed the track through one or both of the detectors.

- Finally decay tracks, i. e. kink daughters, are rejected using the default kink finder algorithm [62] running during the reconstruction.

A dedicated study of the values of these cuts and the resulting J/ψ reconstruction efficiency can be found in [189]. It concluded with the same set of cuts as listed here, default(1), as the optimal choice for the analysis. Also the analysis in [173] was performed with the set of cuts labeled as default(1) here.
The parameters of all discussed cut sets used in this analysis are listed in Table 4.3 for an overwiew. For an illustration of the effect of the different cuts, the distributions of the

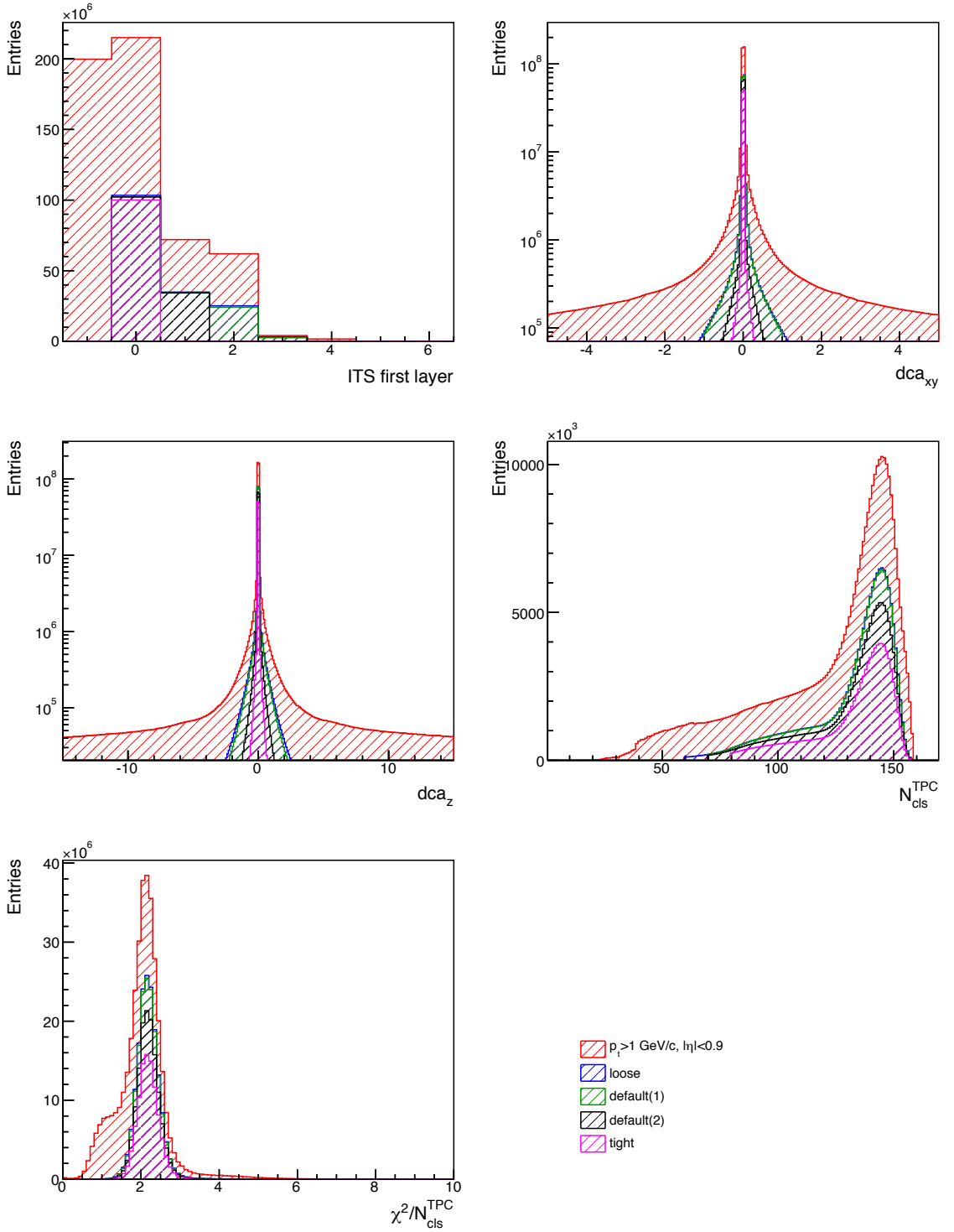

Figure 4.4: The distributions of the track variables discussed in the text (for LHC10d as an example). All tracks that are satisfying the kinematial selections ($p_{\mathrm{t}} > 1$ GeV/c and $|\eta| < 0.9$) are shown in red. The distributions of the tracks remaining after applying the different cut sets listed in Table 4.3 are shown with the other color codes.

cut variables are shown in Fig. 4.4. All tracks that are satisfying the kinematial selections ($p_{\mathrm{t}} > 1$ GeV/c and $|\eta| < 0.9$) are shown in red. The distributions of the tracks remaining after applying the different cut sets listed in Table 4.3 are shown with the other color codes. The top left panel shows the distributions of the number of of the first ITS layer with a hit associated to the track. For the most restrictive setting of the ITS cluster reqiurement, SPDfirst, a hit in the first layer is required. Therefore, the first ITS cluster has to be found in the first layer (counting starts at zero). For SPDany this can either be the first or the second, and so on. A negative value corresponds to no ITS cluster at all. The other cut variables shown in Fig. 4.4 are shown as discussed above.

On top of this set of standard cuts, a couple of analysis specific cuts have been applied to suppress further sources of background tracks. The analysis train is equipped with a pre-filter, running before the analysis tasks and which is searching for V0 daughter[4] candidates[62]. These are flagged and can be sorted out in the analysis. The combinatorial background is decreased by about 20 % by sorting out these tracks. Within the statistical uncertainties no significant difference of the signal counts is found. Still, the loose cut set does not include this selection so that any possible effect is covered by the systematic uncertainties (see Section 4.5).

One last cut is performed after all other selections. The aim is to remove tracks that can be associated with γ conversions or Dalitz decays (of π^0 or η) which are one of the main source of background electron tracks. This selection is done with another pre-filter analyzing the invariant mass of all pairs remaining after all other cuts. All tracks leading to a $\mathrm{e}^+\mathrm{e}^-$ candidate pair with an invariant mass below a certain threshold are rejected from the further analysis. To reject all tracks coming from these background sources, the threshold would have to be set to the η mass of about 547.9 MeV/c^2. But also J/ψ daughter tracks, combined with any other electron candidate, can contribute to the invariant mass spectrum at low values. Thus, the higher the threshold of this cut is set, the more signal counts will be affected. Furthermore, since the exact composition of the background continuum may not be correctly reproduced in MC simulations, an effect of the cut on the J/ψ signal might be estimated incorrectly, i. e., the efficiency correction would be biased. To avoid any improper correction, the threshold in the reconstructed invariant mass, below which the tracks of all $\mathrm{e}^+\mathrm{e}^-$ pairs are rejected, is set to a value which is low enough that no significant loss in the signal counts is found. The resulting value is 50 MeV/c^2. Despite this low threshold, approximately 8 % of the combinatorial background in the J/ψ mass region is removed without any modification of the signal.

	Cut Set			
Cut Variable	Loose	Default(2)	Default(1)	Tight
Track Level				
ITS Cluster Requirement	ITSany(4)	ITSany(4)	SPDany	SPDfirst
dca_{xy}	1.5 cm	1.0 cm		0.5 cm
dca_{z}	5.0 cm	3.0 cm		1.0 cm
$N_{\mathrm{cls}}^{\mathrm{TPC}}$	60	70		80
$\chi^2/N_{\mathrm{cls}}^{\mathrm{TPC}}$	4.5	4.0		3.5
ITS Refit Bit Required	true	true		true
TPC Refit Bit Required	true	true		true
Reject Kink Daughters	true	true		true
Reject V0 Daughters	false	true		true
Pair Level				
γ Cut, $m_{\mathrm{inv}} >$	n/a	50 MeV/c^2		150 MeV/c^2

Table 4.3: The values of all loose default(2), default(1) and tight analysis cuts. Cuts on the track level and on the pair level are shown separately.

4.3.2 Particle Identification

For the selection of electron candidates the TPC signal is used. Particles are identified (PID) via their specific energy loss ($\mathrm{d}E/\mathrm{d}x$) in the detector gas (see Section 3.3.2). Figure 4.5 shows on the left panel the TPC signal versus the total momentum of all particles satisfying the above track selection criteria. For a better visualization, the p_{t} cut is not required for this picture. The selected electron/positron candidates are highlighted by the colored area. Black lines correspond to the expected mean energy loss of the most abundant particle species: pions, muons, kaons, protons and electrons. They are calculated according to a tuned parameterization of Eq. (3.4). A good agreement with the measured spectrum is found for each species. The difference of the measured energy loss $(\mathrm{d}E/\mathrm{d}x)_{\mathrm{meas.}}$ of a given track and the expected one $(\mathrm{d}E/\mathrm{d}x)_{\mathrm{exp.}}$, assuming that the particle is an electron/positron, is shown in the right panel of Fig. 4.5. This value is expressed as multiples of the expected standard deviation of the line:

$$n\sigma = \frac{(\mathrm{d}E/\mathrm{d}x)_{\mathrm{meas.}} - (\mathrm{d}E/\mathrm{d}x)_{\mathrm{exp.}}}{\sigma_{\mathrm{exp.}}} \tag{4.6}$$

[4]The name *V0* stands for particles with zero electrical charge, decaying into two daughter particles of opposite charge. The daughter tracks are looking similar to the letter *V*. Most typical V0 particles are K^0 and Λ; γ conversions into an $\mathrm{e}^+\mathrm{e}^-$ pair also have the same topology.

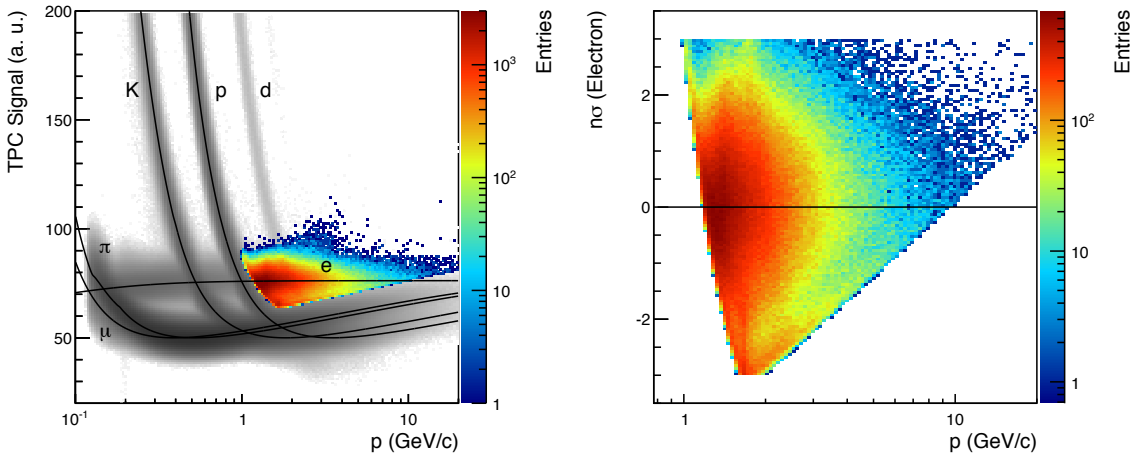

Figure 4.5: Left: the TPC signal in arbitrary units versus the particle momentum for all tracks passing the quality criteria in the beam period LHC10d. The data of all tracks passing loose quality cuts (for a better illustration, also the p_t cut has not applied to these tracks) are shown in a gray scale, the selected e^+e^- candidates are highlighted as the colored area. Black lines correspond to the expected mean energy loss. Right: the difference of the measured energy loss and the expected energy loss, assuming that the particle is an electron/positron. The value is shown in multiples of standard deviations of the Bethe-Bloch lines and versus the particle momentum.

where $\sigma_{\text{exp.}}$ is the expected width of the line as the quadratic sum of the systematic and statistical components, $\sigma^2_{\text{exp.}} = \sigma^2_{\text{syst}} + \sigma^2_{\text{stat}}$. With the number of TPC clusters associated to the track which are used for the $(\mathrm{d}E/\mathrm{d}x)$ measurement, $N^{\text{TPC}}_{\text{cls,PID}}$, and $\sigma_{\text{stat}} \sim 1/\sqrt{N^{\text{TPC}}_{\text{cls,PID}}}$ the width can be calculated as:

$$\sigma^{\text{exp.}} = \Delta_0 \cdot \sqrt{1 + \Delta_{\text{N}}/N^{\text{TPC}}_{\text{cls,PID}}}. \tag{4.7}$$

Here, Δ_0 and Δ_{N} are the $\mathrm{d}E/\mathrm{d}x$ resolution parameters. Their determination by fits to the data is done during the TPC calibration. The average resolution of the $\mathrm{d}E/\mathrm{d}x$ measurement in pp collisions is $\langle\sigma_{\text{exp.}}\rangle = 5\,\%$ [128]. Note that $N^{\text{TPC}}_{\text{cls,PID}}$ is slightly different from $N^{\text{TPC}}_{\text{cls}}$ for two reasons: due to edge effects the gain of the outermost TPC pad rows is not as well defined as of the others. Thus, clusters measured by these pads are not used for the PID where an exact gain calibration is crucial. Secondly, when a cluster is only measured by one single pad, its spacial resolution is only that of the size of the pad. This is not precise enough for tracking and therefore not counted in $N^{\text{TPC}}_{\text{cls}}$. Yet, the charge deposit is a valuable measurement also on a single pad. Since the beam period LHC10d, these 1-pad clusters are used for PID and counted in $N^{\text{TPC}}_{\text{cls,PID}}$.

Because of the preceeding cut on the transverse momentum of the track at 1 GeV/c, the kaon line, which is crossing the electron line at around 0.5 GeV/c (absolute momentum) does

not play a role in this analysis. The deuteron line is crossing that of the electrons in a range where most of the selected particles are. Still, the absolute amount of deuterons, misidentified as electrons, is small enough to be neglected. In this analysis, tracks are accepted as electron candidates if:

- $|n\sigma| < 3.0$, if the track is assigned the electron mass,
- $|n\sigma| > 3.0$, if the track is assigned the proton mass and
- $|n\sigma| > 3.5$, if the track is assigned the pion mass.

These values have been optimized for a high efficiency of the electron selection and a low background contribution. The effect of these selection criteria can be seen on the right panel of Fig. 4.5. The distribution is cut at ± 3 $n\sigma$ (electron) for all momenta, the lower and higher bounds are defined by the proton and pion lines.

Even though the TRD is an excellent detector for the identification of electrons, see Section 3.2.4, it could not be utilized in this analysis. As the collision data available for this analysis was taken only 7 out of the total 18 TRD super modules were installed in the experiment. When requiring TRD information the acceptance is thus reduced by 7/18 for single tracks. For the reconstruction of a e^+e^- pair this effects both tracks, reducing the acceptance for J/ψ by a factor of $49/324 \approx 0.15$. Finally the setup in two arms of 3 and 4 modules at opposite sides of the barrel reduces the J/ψ acceptance significantly. The azimuthal coverage of the arms is about 60° and 80°, respectively; they are separated by about 100° on the one side on by about 120° on the other. The decay products of the J/ψ have a typical opening angle of about 100° (mean value, see Fig. D.5 in Appendix D for the distribution), making it very likely that if one of the electrons enters the TRD acceptance the other does not.

4.3.3 Invariant-Mass Spectra and Background Subtraction

Figure 4.6 shows on two panels the invariant-mass spectrum of all remaining electron-positron candidate pairs after track cuts (Section 4.3.1) and PID (Section 4.3.2) for all events selected by the minimum bias interaction trigger defined in Section 4.2.3 and passing the event cuts listed in that same section. While for the left panel the default(1) analysis cuts are applied, for the right panel the set default(2) is used. The invariant mass (m_{inv}) is calculated with Eq. (C.9), see Appendix C.

In both spectra, a clear peak is visible in the mass region of the J/ψ (3.0969 GeV/c^2) indicated by an arrow. On the other hand, no clear indication for signals of higher-mass quarkonia states, as ψ', Υ, Υ' or Υ'', are visible in the spectra (note the logarithmic scale of the

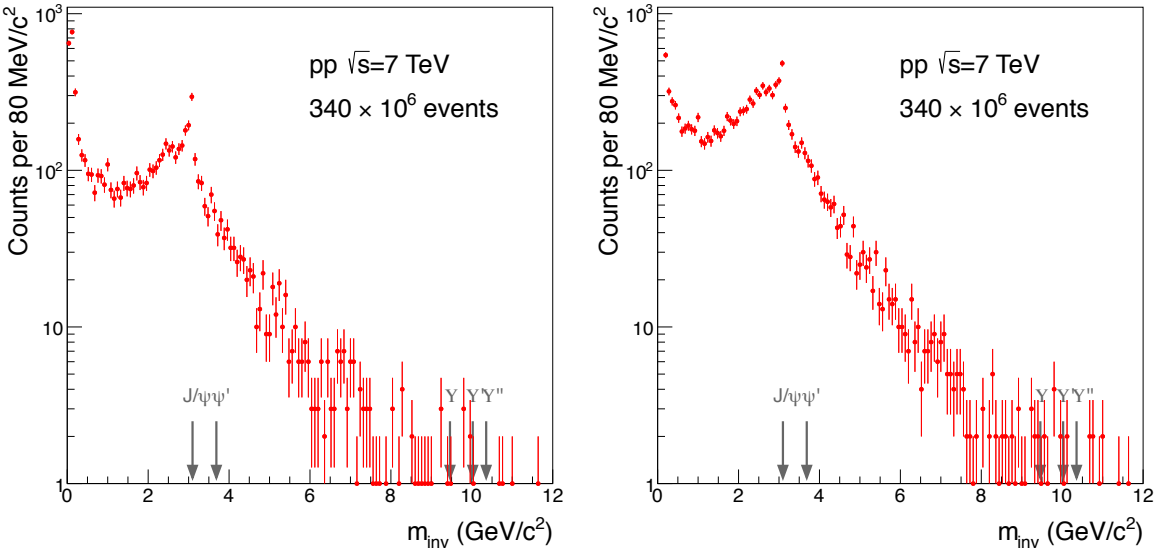

Figure 4.6: The invariant-mass spectrum of all opposite-sign electron candidate pairs using the default(1) cut set on the left panel and with default(2) on the right. In both spectra a clear peak is visible in the mass region of the J/ψ, indicated by the arrow.

figure). Given the total number of events in this analysis this is as expected from a previous simulation [190].

The J/ψ peak is placed on a background continuum. As analyzed in [190], this continuum is mainly composed of electrons from D and B meson and π^0 Dalitz decays, and misidentified pions. Another source of background is due to secondary electrons, e. g., from γ conversions in inner layers of the detector material. Calculating the invariant mass of electron pairs both from Dalitz decays and γ conversions gives entries at very low masses close to zero. The large number of counts in this mass region (Fig. 4.6) shows how abundant these sources are, even after removing all pairs below 50 MeV/c^2. The default(1) set of cuts requires a hit in one of the two innermost detector layers (SPD). Subsequent γ conversion electrons do not have a hit there and are sorted out efficiently. On the other hand also a substantial fraction of J/ψ daughter electrons are rejected due to this selection. For the default(2) set, where a hit in only one of the innermost four detector layers (SPD + SDD) is required, the J/ψ signal is approximately a third larger. The background is increased by almost a factor of 2.4. For an analysis of the total integrated cross section therefore the default(1) set is used since it is offering an excellent signal to background ratio.

The main part of the increased background in the default(2) invariant mass spectrum is due to secondary electrons from interactions with the detector material. Electrons from these sources are likely to have low momenta. For the measurement of the p_{t} differential J/ψ cross section at high J/ψ p_{t} there is no substantial difference in the background contribution as will be shown

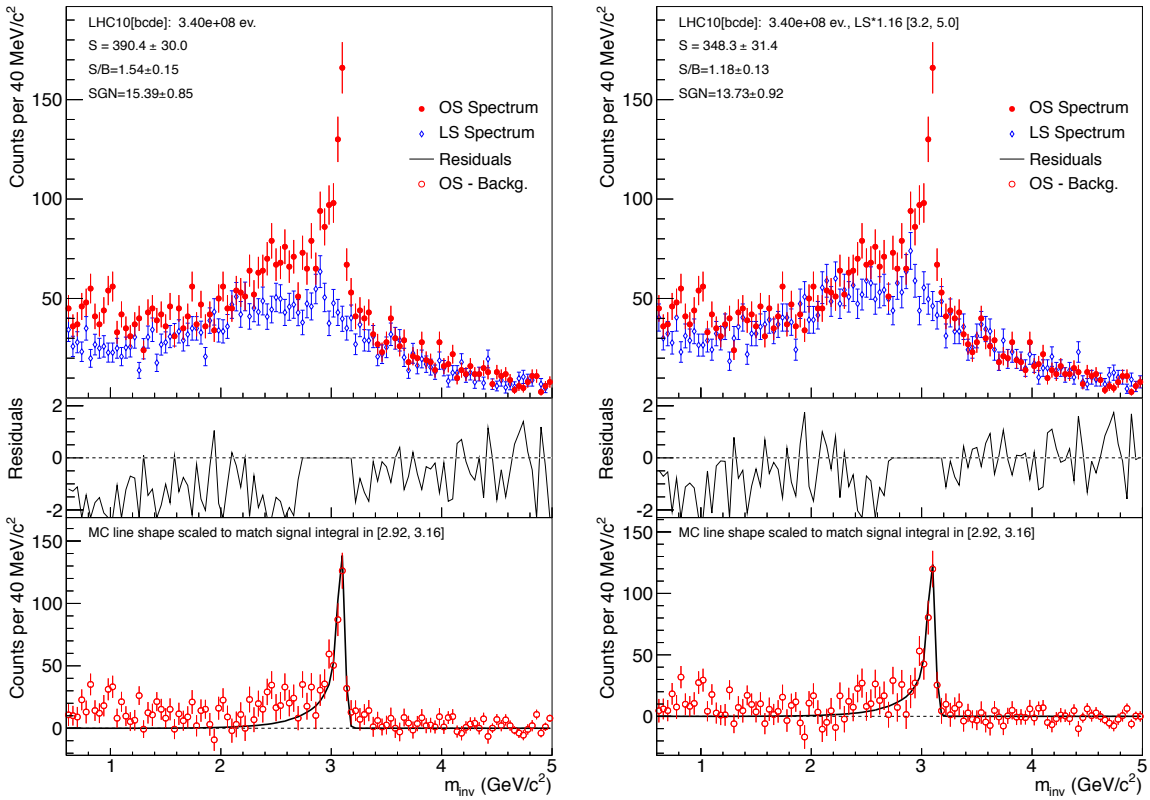

Figure 4.7: Upper panels: the OS (red dots) and LS (blue diamonds) invariant-mass spectra for the $\sqrt{s} = 7$ TeV pp data set LHC10[b-e] using the default(1) analysis cuts. For the left panel the LS spectrum is calculated with Eq. (4.8) while on the right panel the sum of both components $N_{--} + N_{++}$ is scaled to match the integral in the region above the J/ψ mass: [3.2, 5.0] GeV/c^2. The two panels below show with black lines the residuals of the background estimation as defined in Eq. (4.9); the signal region naturally exceeds the scale and is therefore suppressed in this case. Both lower panels show the spectrum after background subtraction. The MC line shape has been scaled to match the integral in the signal region for comparison.

later. Therefore, for low transverse momenta the set default(1) is used while for high transverse momenta the ITS hit requirement is released and default(2) is used.

For the extraction of the signal counts the background spectrum has to be subtracted from the measured opposite-sign (OS) spectrum in Fig. 4.6. In this analysis, two different techniques to estimate the background have been studied: the like-sign method and a fit procedure including various functions. Additionally a combination of the two is investigated.

Background subtraction with the like-sign method The like-sign method (LS) is the most natural way to estimate the background spectrum. All e^+e^+ and e^-e^- pairs in each event

are created and their invariant mass is calculated. Like this, the same spectrum of uncorrelated pairs should be obtained as for OS, without the signals of correlated pairs as that of the J/ψ. The normalization of the LS spectrum should be:

$$N_{+-} = 2 \cdot \sqrt{N_{--}^2 \cdot N_{++}^2}. \tag{4.8}$$

Nevertheless, as the upper left panel of Fig. 4.7 shows, this method clearly underestimates the OS spectrum, even though the overall shapes of the spectra are similar.
The middle panel of this figure shows the residuals $r(m_{\text{inv}})$ of the like-sign spectrum. The residuals are defined as the diffference between the opposite-sign background spectrum $OS(m_{\text{inv}})$ and the background estimator $f_{BG}(m_{\text{inv}})$. Since each bin in the OS spectrum has a different statistical uncertainty, the residuals are normalized to this quantity:

$$\frac{r(m_{\text{inv}})}{\delta OS(m_{\text{inv}})} = \frac{OS(m_{\text{inv}}) - f_{BG}(m_{\text{inv}})}{\delta f_{os}(m_{\text{inv}})}. \tag{4.9}$$

A look at the distribution of these normalized residuals (left middle panel) supports this observation: especially below the signal region the background is more than one standard deviation away from the opposite-sign spectrum in almost all bins. The reason for this difference is assumed to be the contribution from correlated electron-positron pairs from charmed meson decays. In case that a $c\bar{c}$ pair is created in an event which produces two charmed mesons, both have a good probability to decay semi-leptonically—one with an electron as a daughter, the other with a positron. Since there are more decay products involved, a continous spectrum is the result. This is a signal which is not present in the LS spectrum. Thus, the LS spectrum is scaled to match the integral of the OS spectrum in a given mass range.

Besides the scaling factor, another modification of the LS spectrum is done: in the analysis of high p_{t} J/ψ discussed below, many empty invariant-mass bins occur. In the two m_{inv} spectra of e^+e^+ and e^-e^- and therefore with multiplication in Eq. (4.8) the LS spectrum has even twice as many bins with zero entries. Thus, instead of Eq. (4.8), simply the sum of the two spectra is used: $N_{--} + N_{++}$. The difference between the OS and the LS spectra increases towards lower masses; therefore, the choice of the mass region to scale the LS distribution has a direct impact on the extracted signal. Two ranges have been investigated: the first from above the small ϕ signal visible at 1.0 GeV/c^2 up to where the bremsstrahlung tail of the J/ψ signal sets in: [1.5, 2.2] GeV/c^2. The second range is starting just above the J/ψ mass peak: [3.2, 5.0] GeV/c^2. Both scaling factors from the two intervals (1.21 and 1.16 from the low and from the high mass window, respectively), as well as the combination of the two, give a reasonable description of the spectrum. The best description of the OS background continuum has been found for the high mass range, [3.2, 5.0] GeV/c^2 which is thus used for the analysis.
The result is shown in the right panel of Fig. 4.7. A scaling factor of 1.16 is applied to the LS spectrum. The distribution of the residuals now show a much better agreement compared to

the result of the unscaled LS spectrum on the left panel. The resulting raw signal is extracted by summing the bin counts in the signal region [2.92, 3.16] GeV/c^2 (for the optimization of this range, see Section 4.3.4) in the subtracted spectrum, the lower panels in Fig. 4.7. It reads $N_{\mathrm{J}/\psi} = 348.3 \pm 31.4$ with a signal-to-background ratio (S/B) of 1.18 and a significance (SGN) of 13.7.

At masses below approx. 1.5 GeV/c^2 a systematic underestimation is left (upper right panel of Fig. 4.7), but the distance is large enough from the signal region and thus neglected. A simulated MC signal line shape is scaled to match the integral of the subtracted spectrum in the signal extraction integration limits. In the tail region of the J/ψ mass peak, around $\sim$ 2.5 GeV/c^2, the LS seems to underestimate the OS spectrum. If the difference is due to a statistical fluctuation, it is by definition covered by the statistical uncertainty of the measurement. Furthermore, it is located outside of the signal integration limits and has no direct influence on the extracted signal counts. An underestimated width of the MC line could also be the cause for that difference. This should be avoided since it leads to a wrong correction, see Section 4.4.4. Still, the overall good agreement of the main part of the mass peak disfavors such a scenario.

Background subtraction with a fit procedure The second background subtraction method under investigation is a fit procedure using various functions for an estimation of the OS m_{inv} distribution. Three different functions have been studied to describe the background continuum. First, a polynomial of variable order n:

$$f_{\mathrm{BG,pol}}(m_{\mathrm{inv}}) = \sum_{i=0}^{n} a_{\mathrm{i}} \cdot m_{\mathrm{inv}}^{(i)}, \tag{4.10}$$

with the coefficients a_{i} as fit parameters. Second, the Landau distribution with the probability density function defined by the complex integral:

$$\phi(\lambda) = \frac{1}{2\pi i} \int_{c-i\infty}^{c+i\infty} \exp(\lambda s + s \ln s) ds, \tag{4.11}$$

included in the fit procedure as:

$$f_{\mathrm{BG,lan}}(m_{\mathrm{inv}}) = b \cdot \phi\left(\frac{m_{\mathrm{inv}} - c}{d}\right). \tag{4.12}$$

Here, b, c and d are the fit parameters out of which c is the most probable value of the distribution and b and d scaling factors in y and x direction, respectively. The third function

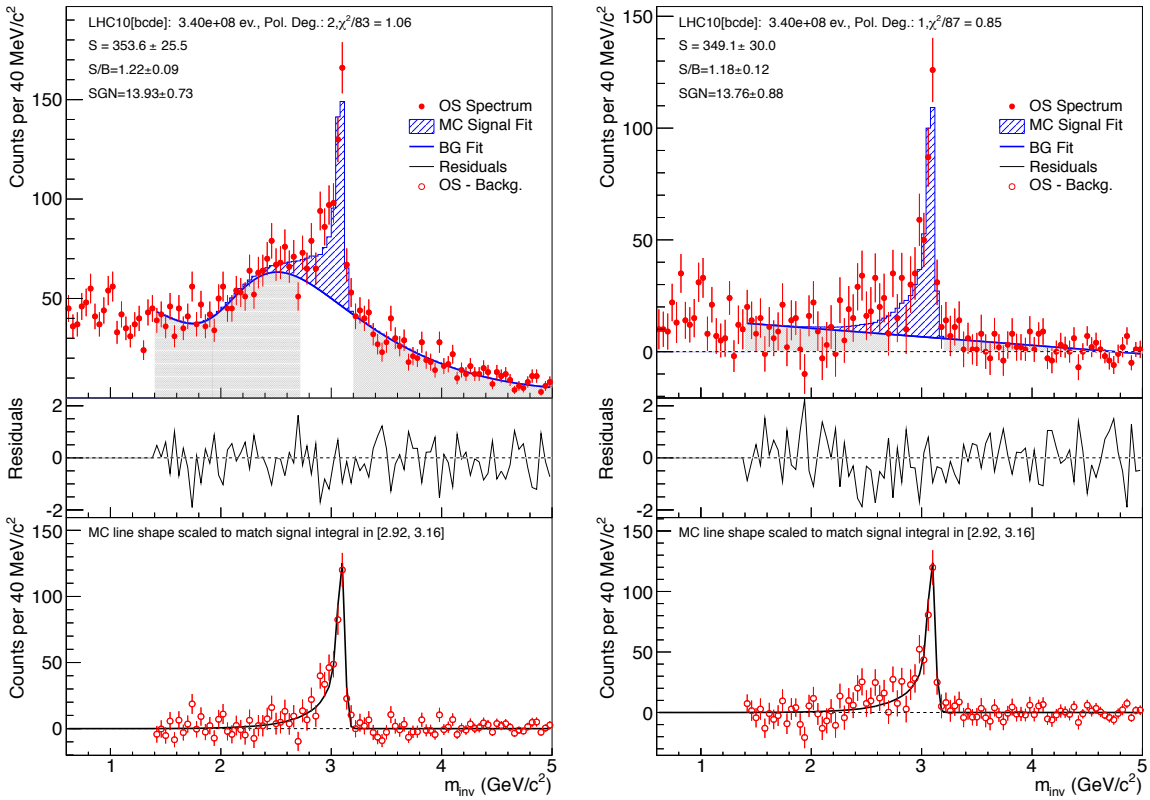

Figure 4.8: As in Fig. 4.7 the invariant-mass spectra for the $\sqrt{s} = 7$ TeV pp data set LHC10[b-e] using the default(1) analysis cuts are shown, only with different background estimations. On the upper left panel a combined fit of a polynomial function, a Landau distribution and the MC signal line shape is performed. On the right side a polynomial fit has been applied to the spectrum after LS background subtraction (scaled as Eq. (4.8)).

used to describe the background continuum is a simple exponential function:

$$f_{\mathrm{BG,exp}}(m_{\mathrm{inv}}) = l \cdot \exp\left(m + n \cdot m_{\mathrm{inv}}\right) \tag{4.13}$$

with again three fit parameters: l, m and n. The procedure has been implemented such that either one of these fuctions can be used to fit the background or any combination of them.
To optimize the desctription of the background in the J/ψ mass region, also a fit to the J/ψ peak is applied. Here, the MC line shape is used, the scaling factor is the only free parameter. The fit range is defined by a lower bound just above the minimum visible in the OS mass spectrum, i. e. at 1.4 GeV/c^2, and an upper bound at 5.0 GeV/c^2.

The implementation of this procedure, derived from previous analyses [191], is done as follows. A first fit iteration is performed only with the background function. Therefore, the signal region, including the part with significant contribution from the bremsstrahlung tail, is

excluded in a range of [2.72, 3.2] GeV/c^2. The results are used as starting parameters for a second iteration, where the combined fit is performed to the whole mass range including the fit to the J/ψ peak.

The best description of the background is found with a combination of a second-order polynomial and a Landau distribution. This decision is based on a goodness-of-fit analysis (see Appendix E) and the distribution of the residuals. The result is shown in Fig. 4.8, upper left panel. The background fit is drawn as a blue line, the scaled MC line shape as the shaded blue area on top of it. Gray areas indicate the fit ranges used for the first fit iteration to the background. The extracted signal is slightly higher but very close to that from the scaled LS subtraction: $N_{\mathrm{J}/\psi} = 353.6 \pm 25.5$, $S/B = 1.22$ and $SGN = 13.9$. Due to the much smaller statistical error of the fit result also the extracted signal count has a higher precision. Over the whole range a very good description of the mass distribution is achieved.

Combination of like-sign method and fit procedure Additionally to the two investigated signal extraction procedures described above, a combination of the two has been implemented. This is motivated by the observation that, after subtraction of the like-sign spectrum according to Eq. (4.8) the disagreement of OS and LS seems to be largest at low masses and decrease towards higher masses. Thus, after subtraction of the LS spectrum, as shown on the left panel of Fig. 4.7, the discussed fit procedure is performed on the subtracted spectrum. Here, the order of the polynomial function is fixed to a straight line with only two coefficients since there is no indication in the spectrum for structures of higher orders.
The result is shown in Fig. 4.8, right panel, and gives a good description of the remaining background. The extracted signal counts are: $N_{\mathrm{J}/\psi} = 349.1 \pm 30.0$ with $S/B = 1.18$ and $SGN = 13.8$, what is in between the results from the other two methods, suggesting that the description of the fit to the full OS spectrum is robust. Compared to the latter the statistical uncertainty by this procedure is in between those of the two individual methods. Indeed, the linear fit does not add a contribution in the first three significant decimals given here, compared to the LS subtraction without additional scaling factor.

The default background estimator In summary, the normal like-sign distribution as shown on the left panel of Fig. 4.7 does not reproduce the opposite-sign mass spectrum. All three other background estimation methods have good results and agree very well in their resulting extracted raw signal counts. The LS subtraction has the advantage that no assumption on the J/ψ signal shape is necessary. On the other hand, a scaling factor has to be applied to account for an underestimation of the background at masses below the J/ψ peak region. This scaling factor, can be determined below or above the J/ψ mass. Since the difference between OS and LS spectra seem to increase towards lower masses, either possibility may introduce a systematic bias.

The fit procedure gives a very good description of the background spectrum. Since the simulated MC J/ψ line shape is used in the fit procedure, a systematic bias might be introduced here. In the comparison of this line shape to the signal after subtraction of the LS spectrum, see Fig. 4.7, a reasonable agreement is observed. Therefore it is expected that if there is any effect, it is small. An advantage of the fit procedure is that the statistical uncertainty of the extracted J/ψ counts is reduced by about 20 %.
The combined LS subtraction and fit procedure gives very similar results as the two other methods. The advantage over the scaled LS distribution is that no bias is introduced by chosing a scaling factor. As in the pure fit procedure a slight dependence on the simulated J/ψ signal shape might introduce a small bias. The results obtained by this method comes with only slightly improved statistical uncertainties compared to the scaled LS method.
Given these arguments, the pure fit procedure is chosen as the default method for the background subtraction. The other two methods are used as a reference and for the estimation of a systematic uncertainty.

Differential analysis The J/ψ cross section is furthermore analyzed differentially versus the J/ψ transverse momentum. To do so, the invariant mass spectra have been recorded in several intervals of this variable. Six bins in p_{t} from 0 to 10 GeV/c are studied. The ranges of these intervals are shown in Table 4.4, the corresponding invariant mass spectra are displayed in Figs. 4.9 and 4.10. Here, following the same arguments from above, the fit procedure has been used to estimate the background spectra. The shape of the background spectrum differs strongly between the analyzed p_{t} intervals. Therefore, for each interval the composition of the fit function is setup individually. For the lowest two intervals, shown on the left and middle panel in Fig. 4.9, a best description of the background spectrum has been found by using the same combination as for the integrated sample discussed above: the sum of a second-order polynomial and a Landau distribution. For the third interval, shown on the right panel in Fig. 4.9, a pure second-order polynomial is used. For all higher intervals, shown in Fig. 4.10, a simple exponential function is found to give the best description of the background shapes.
The invariant-mass spectra of all p_{t} intervals are well described by the fit results. Note that empty bins in the OS spectra are assigned a statistical uncertainty of one to ensure a correct weighting of the fit procedure. As a reference, the results for the other two signal extraction procedures, corresponding to Fig. 4.9 and Fig. 4.10 are shown in Appendix D, Figures D.15 to D.18.

It was found that the increase of the background contribution in the released ITS cluster requirement (default(2) set of cuts compared to default(1)) is largest in the lowest p_{t} interval and becomes smaller with increasing transverse momentum. A direct comparison of the extracted signal and background counts (using the methods bescribed below), as well as the corresponding S/B ratio and significance for the application of the default(1) and default(2) cut sets is shown

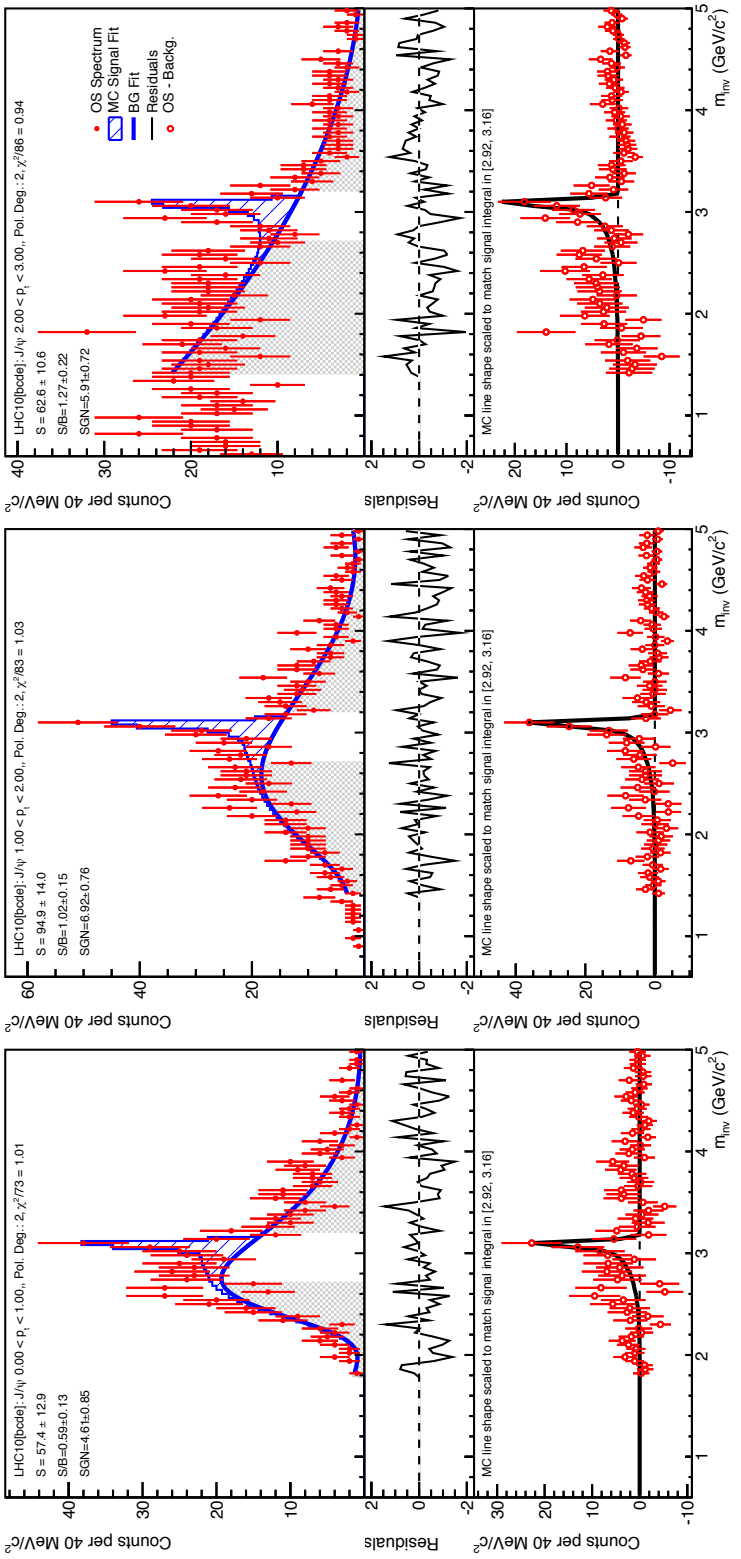

Figure 4.9: The invariant mass spectra for the p_{t} intervals 0 to 1 GeV/c, 1 to 2 GeV/c and 2 to 3 GeV/c. For details, see Fig. 4.8 and Table 4.4.

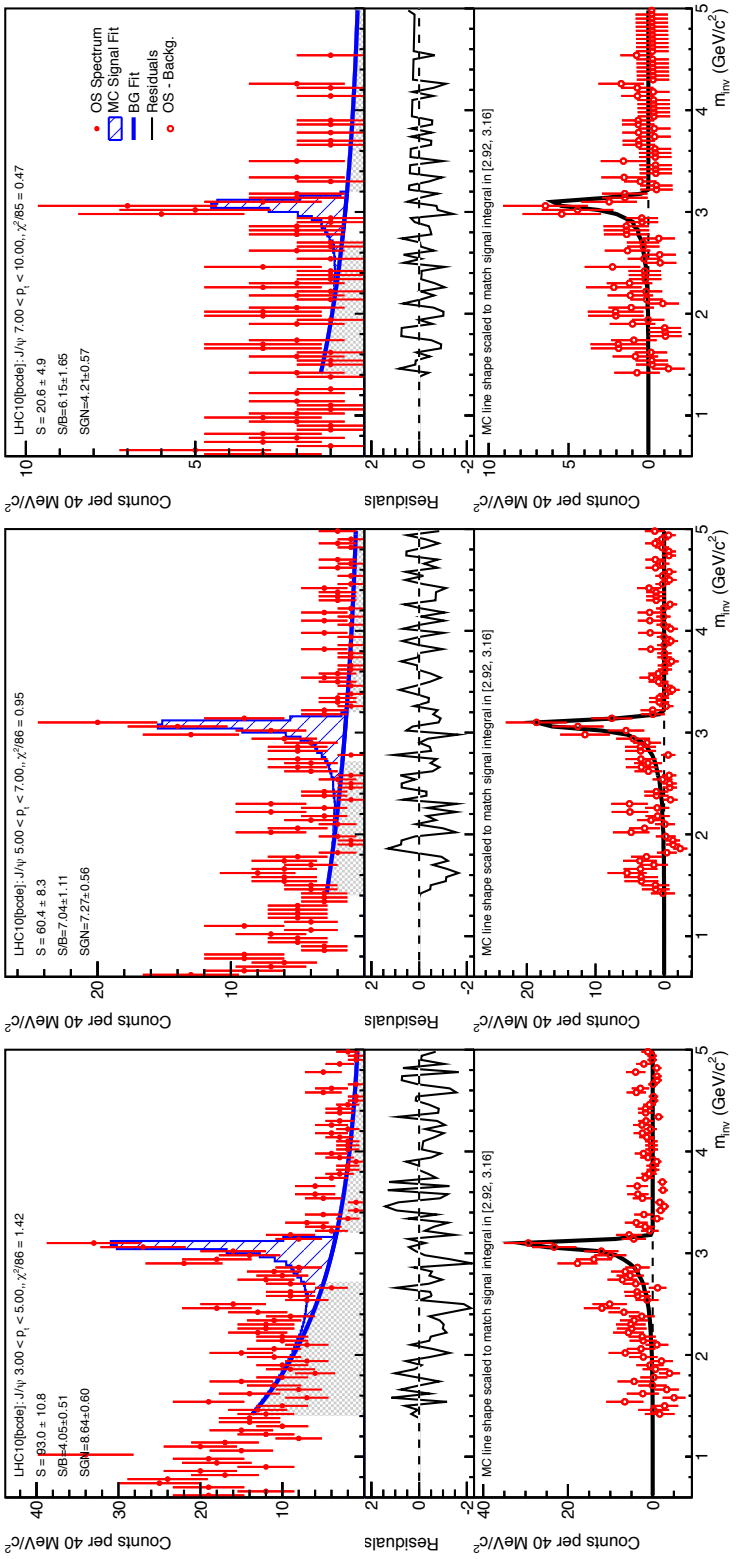

Figure 4.10: The invariant mass spectra for the p_{t} intervals 3 to 4 GeV/c, 4 to 6 GeV/c and 7 to 10 GeV/c. For details, see Fig. 4.8 and Table 4.4.

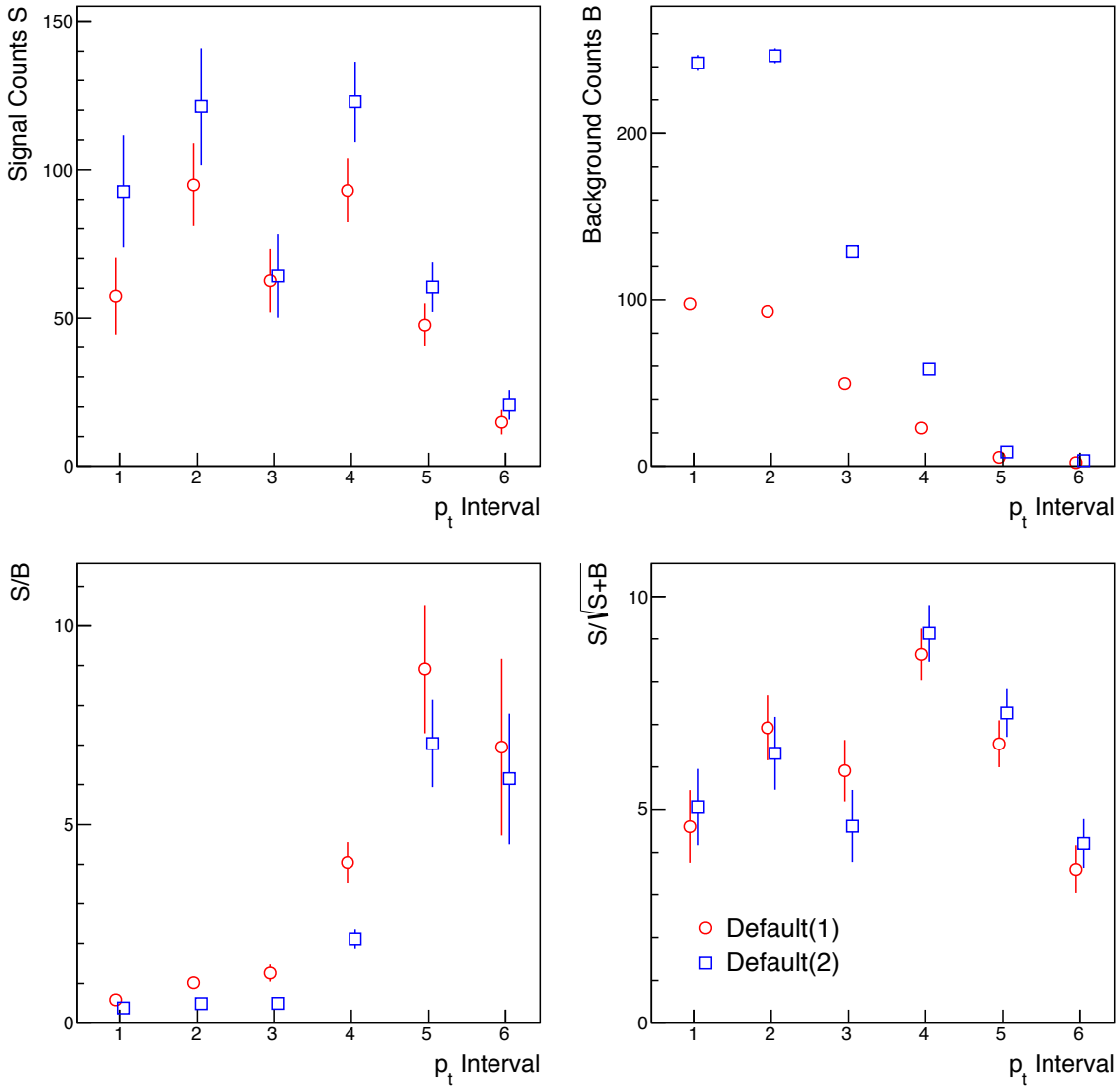

Figure 4.11: Comparison of the extracted J/ψ signal counts S, the background counts B, signal-to-background ratio S/B and significance $S/\sqrt{S+B}$ for the two different sets of analysis cuts default(1) (red circles) and default(2) (blue squares).

in Fig. 4.11. In all intervals more J/ψ signal counts S are extracted for the default(2) cuts, due to the higher efficiency compared to the default(1) cuts (upper left panel). Towards larger transverse momenta the background counts B decrease (upper right panel). In the highest two p_{t} intervals only very little background is left for both cases. The S/B ratio (lower left panel) is substantially higher for default(1) in the lower four p_{t} intervals while it is at a comparable level at the two highest intervals. The significance of the measurements in the different intervals, on the other hand, does not show such a clear difference. In all intervals the values are at a comparable level for the two sets of cuts, with a tendency for higher values for default(2)

towards higher p_{t}.
As a consequence, for the lowest four p_{t} intervals, due to the better S/B ratio, the cut set default(1) is applied. For the remaining two intervals at high p_{t} neither S/B nor significance are substantially higher for one of the cut sets. Therefore, for these intervals the default(2) set is used which is offering higher numbers of signal counts. The extracted J/ψ counts and efficiencies as well as the applied cut set and fit function of each p_{t} interval are summarized in Table 4.4.

p_{t} interval	p_{t} range (GeV/c)	Cut set	Fit function	$A \times \epsilon$	$N_{\mathrm{J}/\psi}$
1	[0.0, 1.0]	default(1)	$f_{\mathrm{BG,pol(2)}} + f_{\mathrm{BG,lan}}$	13.91 ± 0.09	57.4 ± 12.9
2	[1.0, 2.0]	default(1)	$f_{\mathrm{BG,pol(2)}} + f_{\mathrm{BG,lan}}$	9.24 ± 0.05	94.9 ± 14.0
3	[2.0, 3.0]	default(1)	$f_{\mathrm{BG,pol(2)}}$	8.43 ± 0.05	62.6 ± 10.6
4	[3.0, 5.0]	default(1)	$f_{\mathrm{BG,exp}}$	10.36 ± 0.05	93.0 ± 10.8
5	[5.0, 7.0]	default(2)	$f_{\mathrm{BG,exp}}$	15.66 ± 0.10	60.4 ± 8.3
6	[7.0, 10.0]	default(2)	$f_{\mathrm{BG,exp}}$	13.82 ± 0.16	20.6 ± 4.9

Table 4.4: The p_{t} ranges of the six analyzed p_{t} intervals, the applied cut set, the function used for the fit procedure, the value for $A \times \epsilon$ (in percent) and the extracted raw number of J/ψ counts $N_{\mathrm{J}/\psi}$.

4.3.4 Yield Extraction

The number of J/ψ signal counts is extracted by integrating the bin contents of the invariant-mass spectrum after background subtraction in the J/ψ mass region (lower left panel in Fig. 4.8). The limits between which the signal is counted have to be set by optimizing the absolute signal counts, the signal-to-background ratio and the significance. Figure 4.12 shows on four panels the extracted signal counts (upper left), the corresponding background counts (upper right), their ratio (lower left) and the resulting significance (lower right) versus the value of the lower integration limit. Starting from high masses and moving downwards, the signal counts start to increase steeply when traversing the peak region. After that, at around 3.0 GeV/c^2, the gain gets lower for each additional bin towards small masses. The background, on the other hand, does not have such a sharp function. Thus, the ratio peaks at masses between approx. 2.9 and 3.1 GeV/c^2. The significance reaches a maximum between approx. 2.7 and 3.0 GeV/c^2 and constantly decreases towards lower masses. The gain in signal gets smaller for each additional lower bin. On the other hand, the statistical fluctuations of the underlying background increase with a broader range for the integration.

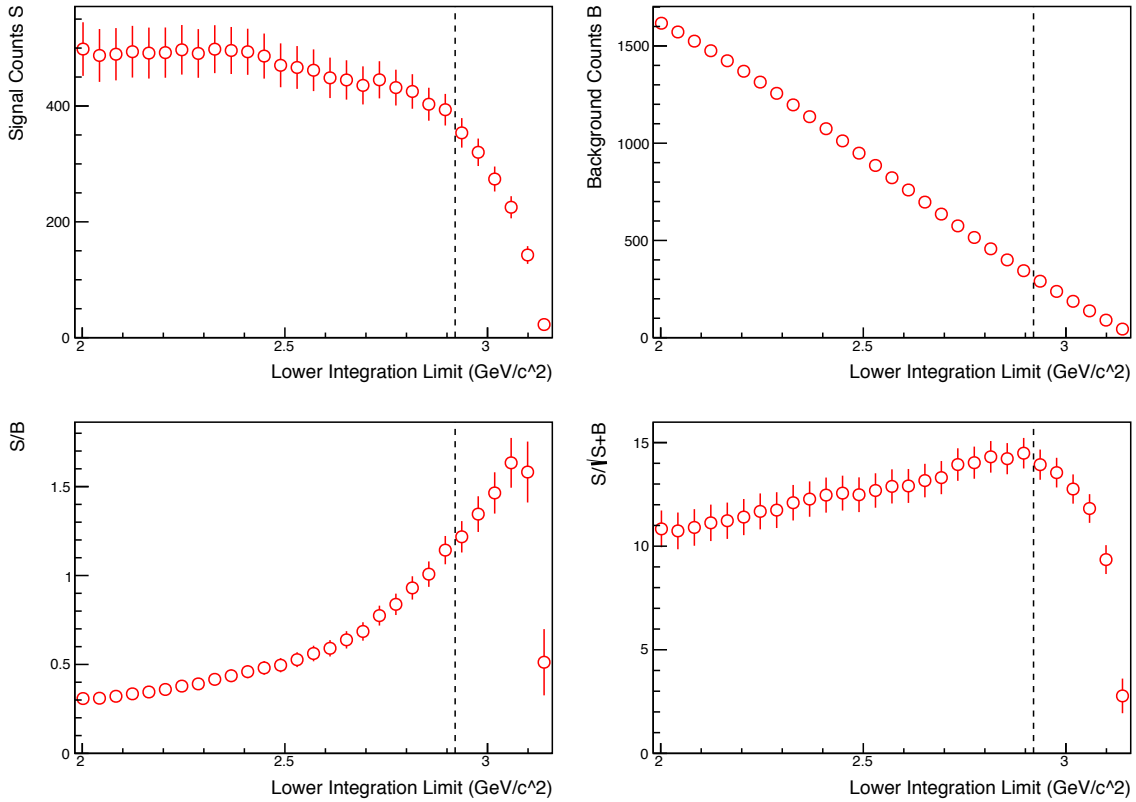

Figure 4.12: The extracted signal counts (upper left), the corresponding background counts (upper right), their ratio (lower left) and the resulting significance (lower right) versus the value of the lower integration limit. Red circles correspond to the invariant-mass spectrum of LHC10[b-e] after subtraction of the background estimated with the fit procedure (lower left panel in Fig. 4.8). The vertical dashed lines show the position of the lower limit that is used for the analysis. Blue circles correspond to the MC J/ψ line shape, scaled to match the integral of the data in these limits.

Therefore, a lower limit of 2.92 GeV/c^2 is used for the analysis. A similar procedure has been performed for the upper edge, leading to a value of 3.16 GeV/c^2.

4.4 Corrections

The measured rates depend on the finite acceptance and measurement efficiency of the detector and its parameters. To extract the physical particle yields these detector effects have to be corrected for. Reconstructed Monte Carlo simulations of events, enriched with J/ψ particles, have been analyzed to obtain the correction factors for the inclusive analysis, as well as the correction tables for the differential analyses. Here, for the four analyzed beam periods the

samples LHC10f7a_[b-e] from Table 4.2 have been used. These are dedicated data sets for efficiency studies, enriched with various quarkonia and heavy flavor signals. For the acceptance and efficiency studies presented here only directly simulated J/ψ are evaluated. Simulated B mesons decaying into J/$\psi + X$ are filtered out since these would distort the results with their different input p_{t} and y spectra.
The reconstruction procedure has been divided into four steps:

- What is called the acceptance of the detector is to some extend matter of definition. Here, the efficiency of the kinematical selection cuts listed in Section 4.3.1 is defined as the *geometrical acceptance* A.
- The probability that both decay products of a J/ψ (which are in the acceptance A) cross the sensitive areas of the detectors, are found by the tracking procedure and pass the track quality cuts (see Section 4.3.1) defines the *reconstruction efficiency* ϵ_{rec}.
- The probability that both reconstructed daughter tracks are selected in the PID as electron candidates is defined as *PID efficiency* ϵ_{PID}.
- The probability that the reconstructed mass of a J/ψ is within the signal integration limits (see Section 4.4.4) is defined as the *signal integration efficiency* ϵ_{int}.

For the correction only the total $A \times \epsilon = A \times \epsilon_{\mathrm{rec}} \times \epsilon_{\mathrm{PID}} \times \epsilon_{\mathrm{int}}$ is necessary. The total value for $A \times \epsilon$, as an average over all four beam periods is:

$$A \times \epsilon = (10.11 \pm 0.02)\,\%. \tag{4.14}$$

With this number the corrected J/ψ yield can be calculated from the measured raw signal counts:

$$N_{\mathrm{J}/\psi}^{\mathrm{corr}} = \frac{N_{\mathrm{J}/\psi}}{A \times \epsilon}. \tag{4.15}$$

The division into several steps is only done for illustrative reasons and to allow more detailed cross checks with other analyses. These efficiencies and also their dependence on p_{t} and y are discussed in more detail in the following. The resulting values are listed in Table 4.5 for each beam period separately and for the average of all periods, weighted with the number of events.

4.4.1 Geometrical Acceptance

In Section 4.3.1 the geometrical acceptance A was defined as $|\eta^{\mathrm{e}^{\pm}}| < 0.9$ in longitudinal direction and $p_{\mathrm{t}}^{\mathrm{e}^{\pm}} > 1.0$ GeV/c in transverse direction. The full azimuthal angle ϕ is covered. In order

Beam Period	A	ϵ_{rec}	ϵ_{PID}	ϵ_{int}	$A \times \epsilon$
LHC10b	33.27 ± 0.12	60.32 ± 0.22	64.39 ± 0.28	72.88 ± 0.77	9.42 ± 0.08
LHC10c	33.07 ± 0.08	57.14 ± 0.15	67.23 ± 0.18	72.98 ± 0.50	9.27 ± 0.05
LHC10d	33.21 ± 0.07	55.84 ± 0.14	81.23 ± 0.14	72.53 ± 0.42	10.93 ± 0.05
LHC10e	33.26 ± 0.05	52.89 ± 0.09	76.71 ± 0.10	72.84 ± 0.29	9.83 ± 0.03
Average	33.20 ± 0.04	55.63 ± 0.07	75.37 ± 0.08	72.75 ± 0.23	10.11 ± 0.02

Table 4.5: The efficiencies (in percent) of the geometrical acceptance A, the reconstruction ϵ_{rec} using the default(1) cuts, the particle identification ϵ_{PID} and the signal integration ϵ_{int}. Also the average total reconstruction efficiency $\langle A \times \epsilon \rangle$ is listed for each beam period. Furthermore, all values are given for the total data sample, as the average, weighted with the number of events $N_{\mathrm{MB}}^{\mathrm{ana}}$.

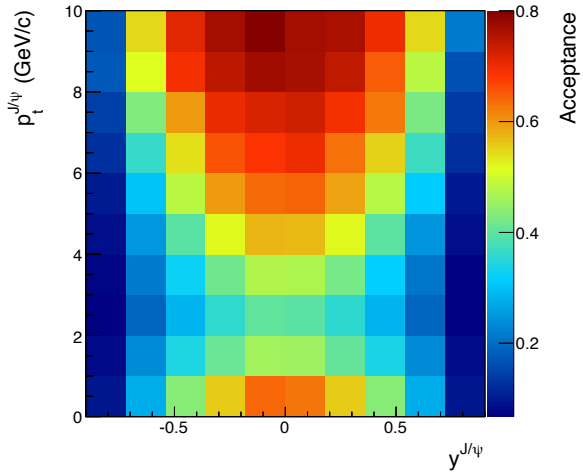

Figure 4.13: The geometrical acceptance for the measurement of J/$\psi \rightarrow \mathrm{e}^+\mathrm{e}^-$ in dependence of transverse momentum and rapidity.

to avoid edge effects in the correction method also the kinematics of the reconstructed pairs is limited to the rapidity region of $|y| < 0.9$. All these limitations lead to an overall correction factor of:

$$A = (33.20 \pm 0.04)\,\%, \tag{4.16}$$

the differential result versus transverse momentum and rapidity of the J/ψ is shown in Fig. 4.13. Figure 4.15 shows in red circles the projection of Fig. 4.13 along p_{t} and y on the left and right panels, respectively.

As visible both in Fig. 4.13 and the right panel of Fig. 4.15 (red circles), the acceptance

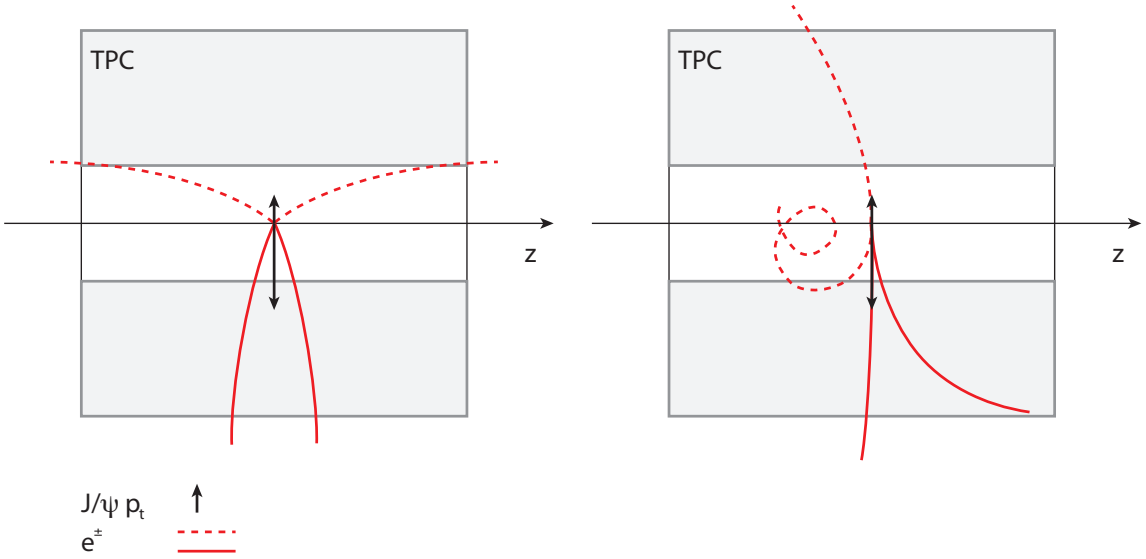

Figure 4.14: Illustration of the effect of the kinematical selections on the J/ψ acceptance A. Left panel: a decay oriented in z direction, right panel: a decay oriented in xy direction. For both orientations one example with a low and one with a high J/ψ p_{t} is shown, their decay electron tracks are shown with red dashed and solid lines, respectively.

is maximal at mid-rapidity and decreases towards larger rapidities where it becomes more probable that one of the daughters has an $|\eta| > 0.9$. At $|y| \approx 0.9$ the acceptance approaches zero.

Versus p_{t} J/ψ are detected starting from zero transverse momentum. Towards intermediate p_{t} the acceptance drops until ≈ 2.5 GeV/c, at higher transverse momenta it increases monotonously. This momentum dependence can be explained as follows. In the rest frame of the J/ψ the daughter particles are flying apart back to back, each with a momentum of around 1.55 GeV/c. Also in the J/ψ rest frame, the angular orientation of the decay is isotropic but one can differentiate between two extreme cases, illustrated in Fig. 4.14. The decay particles can be emitted predominantly in z (left panel) or in xy (right panel) direction. For both cases, the daughter electrons of a high p_{t} (solid red lines) and a low p_{t} (dashed red lines) J/ψ are sketched. For decays oriented in z direction and with very low p_{t}, the daughter tracks are likely to be emitted at low angles such that they escape undetected. With increasing J/ψ p_{t} the opening angle decreases and the tracks are more and more likely to be detected.

For the other case, a decay oriented in xy direction, at p_{t} close to zero both daughter electrons will be emitted to the opposite side of the detector with a p_{t} around 1.55 GeV/c which is more than the p_{t} cut. In this case the J/ψ will be in the acceptance. With an increasing J/ψ p_{t} the p_{t} of the daughter emitted in flight direction is increased while that of the daughter emitted in the opposite direction is decreased and may not anymore pass the p_{t} cut. An even higher

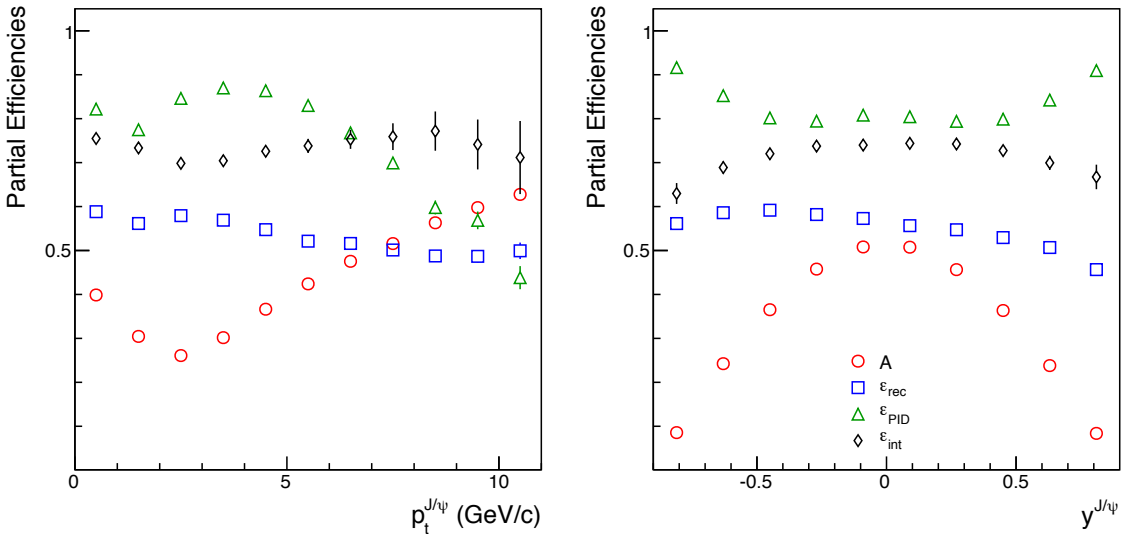

Figure 4.15: The efficiencies of the different steps of the J/ψ reconstruction versus its transverse momentum (left panel) and rapidity (right panel). Red circles correspond to the geometrical acceptance, A, due to the kinematical selections. Blue squares and green triangles show the efficiency of the track quality selection criteria, ϵ_{rec}, and of the paricle identification procedure, ϵ_{PID}, respectively. Black diamonds correspond to the signal integration efficiency, ϵ_{int}. The shown values were obtained by analyzing the data set LHC10f7a_d and correspond to the default(1) set of cuts.

J/ψ p_{t} will overcome the momentum from the decay and also this electron will fly in the same direction. When the J/ψ p_{t} is high enough, the track will then also pass the p_{t} cut.
Like this, an overall increase with p_{t} is seen in Fig. 4.15, with a dip between 1 and 5 GeV/c.

4.4.2 Reconstruction Efficiency

If the kinematics of a J/ψ falls inside the geometrical acceptance, it still might not be reconstructed if one or both of the daughters do not fulfill the above listed selection criteria for track quality. Additional to the geometrical acceptance A discussed above, Figures 4.15 and 4.16 feature the track reconstruction efficiencies ϵ_{rec} as a function of p_{t} (left panels) and of y (right panels). While in both figures the red circles correspond to the geometrical acceptance, in Fig. 4.15 the blue squares show the efficiency of the track quality selection. In Fig. 4.16 the same components are shown multiplicative: blue squares correspond to the product $A \times \epsilon_{\mathrm{rec}}$. Both representations allow a closer look into the p_{t} and y dependence of the different parts. Only a weak p_{t} dependence of ϵ_{rec} is found. The track reconstruction efficiency is highest at low transverse momenta with a decrease of about 15 % until 10 GeV/c. An interpretation of this observation could be that very straight high p_{t} tracks have a slightly larger probability to not achieve the minimum number of associated clusters in the TPC. Low p_{t} tracks have a

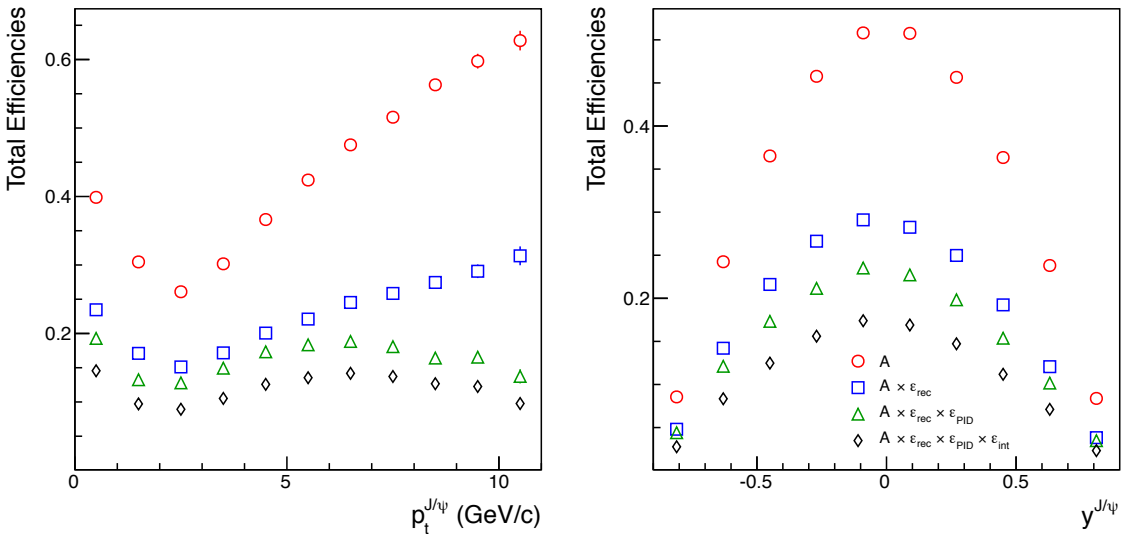

Figure 4.16: As in Fig. 4.15, the acceptance and efficiency are shown as a function of p_t (left) and y (right). In contrast, here the different contributions are cumulated: red circles again show the geometrical acceptance of the measurement, blue squares correspond to the additional application of the track quality cuts. Green triangles are including the above components plus PID. The black diamonds also include the signal integration efficiency and thus schow the total efficiency of the J/ψ reconstruction. The shown values were obtained by analyzing the data set LHC10f7a_d and correspond to the default(1) set of cuts.

shorter bending radius in the magnetic field and thus have a longer path through the sensitive volume of the TPC. Furthermore, the finite resolution of the momentum reconstruction leads to migration between the bins. Thus, the efficiency is reduced in the region of the maximum of the p_t spectrum (at approx. 2 GeV/c^2, see Section 4.6.2), where more entries are shifted into the adjacent bins than in the other direction. Also versus y only a weak variation of the reconstruction efficiency can be seen in Fig. 4.15. The decrease towards positive values of y is due to the limited acceptance of the SPD. More channels of this detector are inactive at that part of the detector.

The figures shown here correspond to the default(1) set of cuts and are extracted by analyzing the MC data set LHC10f7a_d, an anchor run to the beam period LHC10d. Due to small changes in the detector setup the efficiencies slightly vary and have to be taken into account individually, weighted by the respective number of events of the beam periods. The average reconstruction efficiency for the whole data sample and the default(1) set of cuts is found to be:

$$\epsilon_{\mathrm{rec}} = (55.63 \pm 0.07)\,\%. \tag{4.17}$$

For completeness, the partial and total efficiencies determined for the three other periods under investigation, can be found in the appendix, Figs. D.6 to D.11.

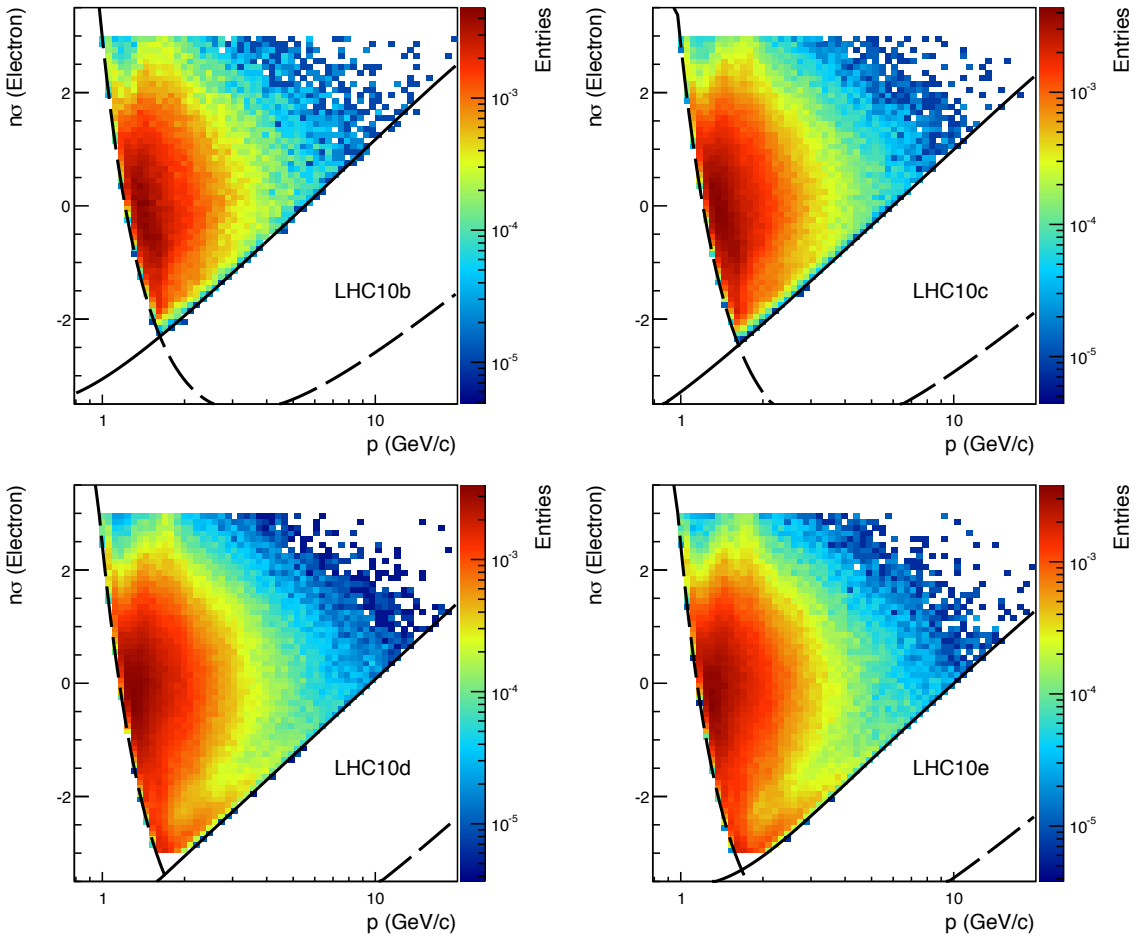

Figure 4.17: The results of the parameterizations Eq. (4.18) used for the PID cuts in MC. Dashed lines correspond to the cut of the proton band, solid lines to that of the pions. The parameters of the functions are tuned to match the edges of the $n\sigma$ distributions of the four beam periods LHC10[b-e] shown as the colored histograms.

An important prerequisite for the validity of the correction procedure is a proper simulation of the detector response, so that the applied selection cuts have the same impact in MC and collisions data. To verify this, the distributions of the different cut variables have been analyzed and compared in data and MC in a previous study [189].

4.4.3 Particle-Identification Efficiency

The simulated energy-loss spectra give a good description of those measured in pp data (for a comparison of the dE/dx spectra in MC and data, see Fig. D.19 in Appendix D). However, the p and π bands are located at slightly lower TPC signals in MC than in pp data. This can lead to an overestimated PID efficiency in the following way: when the exclusion cuts around the

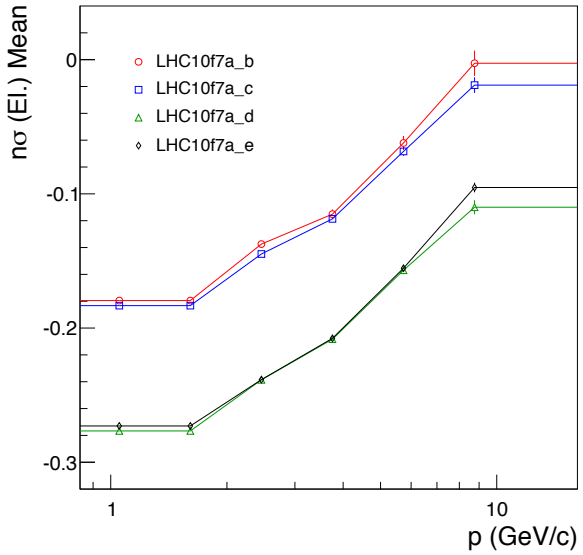

Figure 4.18: The positions of the mean values versus electron momentum (pure MC selected electrons) for the different beam periods LHC10[b-e].

proton and the pion lines are performed, smaller parts of the electron band are removed than it is the case in data (see right panel Fig. 4.5).
For the determination of the PID efficiency thus a different method for the proton and pion exclusion is implemented. Here, analogously to the strategy in [173], an additional cut on the electron line is performed:

$$f_{\mathrm{i}}^{\mathrm{cut}}(p) = \frac{g_{\mathrm{i}}(p) - g_{\mathrm{e}}(p)}{\langle \sigma_{\mathrm{exp.}} \rangle} + n\sigma \tag{4.18}$$

where $i = \mathrm{p}, \pi$ correspond to the lines of the two different particles and g are parameterizations of Eq. (3.4) for the different species p, π and e; $\langle \sigma_{\mathrm{exp.}} \rangle$ is the average $\mathrm{d}E/\mathrm{d}x$ resolution, see Section 4.3.2. Like this, for all momenta, the same probability for accepting or removing an electron is given for data and Monte Carlo allowing for a proper efficiency correction. Figure 4.17 shows the result of the momentum-dependent cuts on the electron line for the four beam periods. Dashed lines correspond to $f_{\mathrm{p}}^{\mathrm{cut}}$, solid lines to f_{π}^{cut}. Using a fit procedure, the parameters have been tuned for an optimal match with the lower edges of the two-dimensional distributions of the four pp data sets LHC10[b-e] shown in Fig. 4.17.
A drawback of this method is that like this only the average resolution is taken into account in MC. The resolution depends on the number of TPC clusters used for PID, $N_{\mathrm{cls,PID}}^{\mathrm{TPC}}$, and this value may be correlated with the particle momentum. Still, on average this method should be correct, any potential bias is expected to be covered by the systematic uncertainties estimated in Section 4.5 where all relevant parameters are varied within reasonable ranges.

Another issue that complicates the efficiency determination is that the $n\sigma$ distributions of

the electron line are not centered at zero. The positions of the mean values versus electron (pure MC selected electrons) momentum are shown in Fig. 4.18. At low p the deviation is strongest, at higher momenta it approaches zero.
In the case of collision data the determination of the mean positions is less precise. On the one hand the asymmetric cuts of the proton and pion lines do not allow for a measurement at broad momentum ranges. On the other hand the contamination of the electron spectrum by particles of these two species limit the precision. Within these uncertainties, no shifts of the mean values were found. Therefore, fixed momentum and beam period dependent shifts of the electron $n\sigma$ values in MC are applied, using the data shown in Fig. 4.18. Since it is not known whether or not there are any systematic shifts in case of the collisions data, the effect of the correction in MC on the extracted PID efficiency is accounted for in the systematic uncertainty of this mechanism.

With these strategies to determine the PID efficiency, as an average over the analyzed beam periods, a value of:

$$\epsilon_{\mathrm{PID}} = (75.37 \pm 0.08)\,\% \tag{4.19}$$

is found. The differential results are presented as green triangles in Fig. 4.15. In Fig. 4.16 the product $A \times \epsilon_{\mathrm{rec}} \times \epsilon_{\mathrm{PID}}$ is shown, again as green triangles. The p_{t} dependence of ϵ_{PID} is a result of the momentum-dependent PID. Versus y an increased efficiency is observed towards larger values. At large rapidities the daughter tracks are likely to traverse a longer path through the sensitive volume of the TPC than close to mid-rapidity. Therefore more $\mathrm{d}E/\mathrm{d}x$ signal is deposited on the same number of TPC pads, resulting in an improved precision.
For completeness, Fig. D.12 in Appendix D shows the resulting $n\sigma$ vs. p spectra for the MC minimum bias data sets. Due to the topological cuts described above the area remaining after the PID selection is the same as for data (see Fig. 4.17). A more detailed comparison (as example for the MC data set LHC10f6a) can be found in Fig. D.13 and Fig. D.14, where the $n\sigma$ distributions from data are compared to MC for various slices in p. A good agreement of the distributions is observed for the electron lines. Due to the stronger separation of the lines of the different particles, the contamination by pions and protons at low momenta and at low $n\sigma$ is not the same. Since this does not affect the determination of the electron efficiency, it can be neglected here.

4.4.4 Signal Integration

For the determination of the J/ψ signal by counting the bin content in the background-subtracted invariant-mass spectrum, integration limits were set. As described in Section 3.3, due to electron bremsstrahlung the J/ψ signal shape exhibits a tail towards smaller invariant masses. This is illustrated in Fig. 4.19, where the pure J/ψ signal from the MC data set LHC10f7a_d is shown,

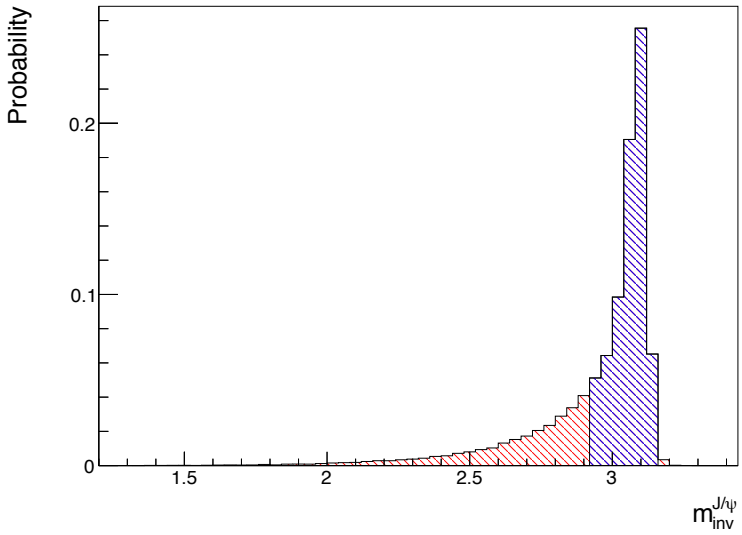

Figure 4.19: The invariant mass of all reconstructed primary J/ψ in the data set LHC10f7a_d, selected via Monte Carlo information. The electrons/positrons in the MC analysis have to pass the exact same set of cuts and PID as those in the pp data.

exhibiting a long tail towards lower masses. Integrating the data over the whole signal area would lead to 100 % efficiency but with a very high background contribution. These limits were optimized as described in Section 4.3.4. In Fig. 4.19 the part of the J/ψ signal within those limits is highlighted with the blue area. The MC J/ψ line shape can then be used to determine the fraction of signal within these limits. This number is needed to correct the measured counts:

$$\epsilon_{\mathrm{int}} = (72.75 \pm 0.23)\,\%. \tag{4.20}$$

This procedure relies on a correct simulation of the interaction of electrons with material and a good description of the detector material. In Figs. 4.7 and 4.8 the invariant-mass spectrum, after subtraction of the background, is compared to the same J/ψ line shape separately shown in Fig. 4.19. Within the statistical uncertainties, the data is well described by the simulation in each of the results, obtained with the different background estimators indicating a reasonable shape of the simulated signal.

In Figs. 4.15 and 4.16 the p_{t} and y dependence of ϵ_{int} is shown as black diamonds. Only a slight dependence on the J/ψ kinematics is observed, still it is significant. Following the discussion in Section 4.4.1, for J/ψ p_{t} around 2.5 GeV/c the transverse momentum of one of the daughter electrons is likely to be low and just above the p_{t} cut of 1.0 GeV/c. These tracks therefore tend to have smaller bending radii compared to the daughter tracks of high p_{t} J/ψ. Small bending radii result in a longer path through the detector, more traversed material and more energy loss due to bremsstrahlung. The same argument holds for the decreased ϵ_{int} at

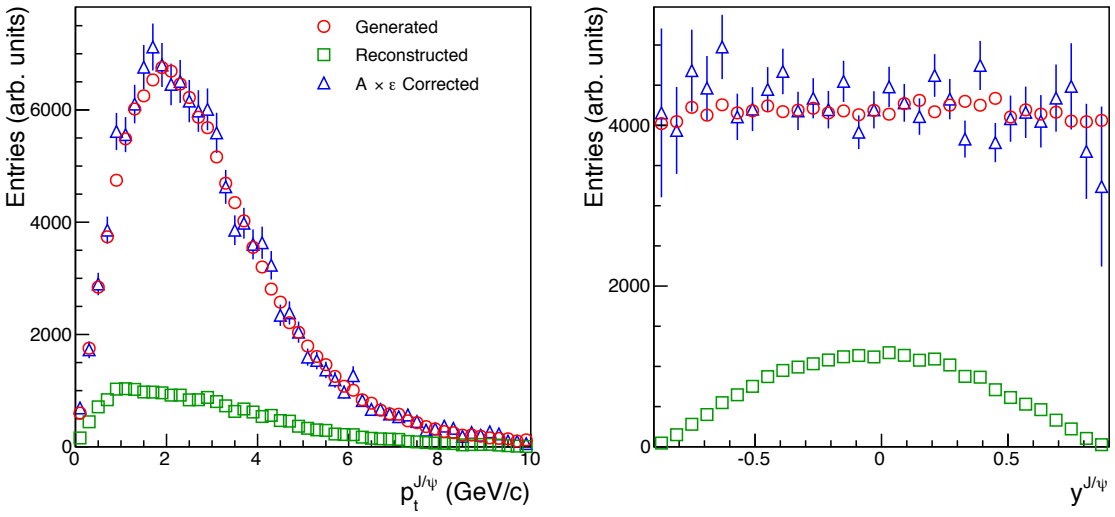

Figure 4.20: A test of the correction procedure. The reconstructed (green squares), corrected (blue triangles) and input (red circles) J/ψ p_t (left panel) and y (right panel) spactra are shown.

high y. Also there the daughter electrons are likely to have a longer path through the detector material then tracks from J/ψ at mid-rapidity.
At the highest p_t a slight indication for a decrease of ϵ_{int} can be seen in Fig. 4.15 (and likewise for the other beam periods Fig. D.6 to Fig. D.8 in Appendix D). This might be due to a decreased momentum resolution for very high p_t tracks which are almost straight.

4.4.5 Selfconsistent Correction Procedure

A test of the correction procedure for acceptance and efficiency is to divide a MC sample in two halfs. The first half is used to calculate the efficiency maps, the second to apply the correction. Result and MC input are then compared. Therefore, the same MC data set LHC10f7a_d is used. This is data enriched with a large number of J/ψ particles, i. e., a large signal and almost no background spectrum, so the normal signal extraction procedure (described in Section 4.3.3) cannot be tested here: reconstructed J/ψ are instead selected via the MC information. Still, the efficiency correction procedure can be tested. The result is shown in Fig. 4.20. Green squares correspond to the reconstruced p_t (left panel) and y (right panel) spectra. After applying the correction for acceptance and efficiency, obtained with the other part of the data sample, the distributions of the blue triangles are obtained. Those can now be compared to the true input spectra (red circles). An excellent agreement proves the validity of the correction procedure.

4.4.6 Comparison to Published Efficiencies

Compared to the efficiencies listed in [173] similar values have been obtained here. The total $A \times \epsilon$ of 10.11 % determined in this analysis is in very good agreement with the 9.8 % quoted in the reference. For the individual components small variations have been found. While the numbers for the acceptance A and the signal integration efficiency ϵ_{int} are in a rather good agreement, for the reconstruction efficiency ϵ_{rec} and the particle-identification efficiency ϵ_{PID} absolute differences of about 5 % with respect to this analysis are found in both cases. These are expected to be a result of differences in the procedures to determine these numbers or due to variations in the track selection. While the quality cuts on the track level are identical, this is not the case on the pair level. Like this, in [173] tracks might be rejected already at this level while in this analysis the same tracks are sorted out in the PID.
For the p_{t} differential analysis the total values for $A \times \epsilon$ are listed in Table 4.4. Also here a good agreement with the published results are found, differences are expected to be due to the independent determinations of ϵ_{PID}. The results for all p_{t} intervals are well within the systematic uncertainties assigned to this procedure (see Section 4.5). For the fifth p_{t} interval which is the highest one in [173] the differences are much larger. This is due to the released ITS cluster requirement in this analysis and a desired effect.

4.5 Systematic Uncertainties

In this section, the different contributions to systematic uncertainties that were identified are discussed. Table 4.6 summarizes the results for all sources. All components are added in quadrature to the total systematic uncertainty which is estimated to be 13.1 %. An uncertainty on the luminosity determination applies equally to all results and is thus given as a separate number.

Signal extraction The systematic uncertainty of the signal extraction procedure is dominated by the maximal differences that are found between the results of the different background estimators. This value can be extracted from the measured J/ψ counts. Fig. 4.21 shows the $A \times \epsilon$ corrected J/ψ yields for the three investigated methods. Here a maximal difference of 1.5 % is found between the results after subtraction of the LS spectrum, the result of the fit procedure and the combined method.
Both the shape of the background and the S/B ratio is very different in the six analyzed p_{t} intervals. Therefore and because different functions are used to describe the background, the systematic uncertainty from the background subtraction has to be estimated separately in each p_{t} interval. The corrected J/ψ yields $N^{\text{corr}}_{\text{J}/\psi}$ for the fit method, the LS method and the combined

Contribution	Uncertainty	
	This analysis	Published results
Signal extraction	6.6 %	8.5 %
Reconstruction efficiency	4.0 %	4 %
PID efficiency	10.4 %	10 %
Acceptance input	1.5 %	
B.R. ($J/\psi \to e^+e^-$)	1.0 %	
Total	13.1 %	13.8 %
Luminosity	4.0 %	

Table 4.6: Contributions to the systematic uncertainty. The values obtained in this analysis are compared to the values published in [173].

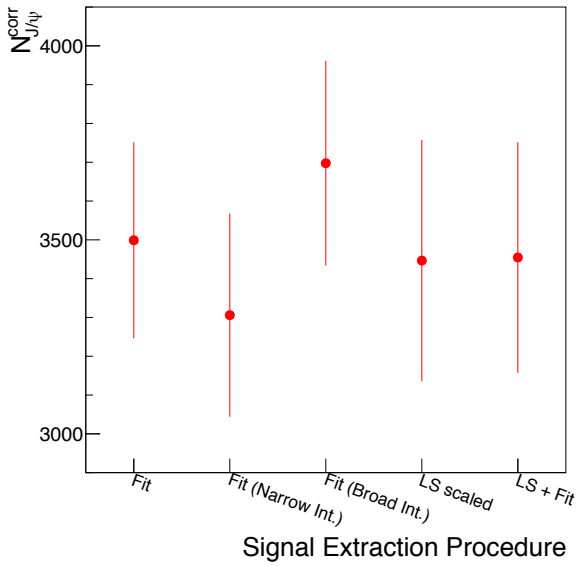

Figure 4.21: The $A \times \epsilon$ corrected J/ψ yield $N^{corr}_{J/\psi}$ for the default background subtraction method (fit) and for a narrow and a broad variation of its integration limits. Also shown in this figure are the results for the two other background estimation procedures (LS scaled, LS+Fit).

one are shown for each p_t interval in Fig. 4.22. The maximal difference between the results from the fit method and the other two are used as a systematic uncertainty, the results for the bins one to six are: 26.4 %, 11.7 %, 15.9 %, 11.2 %, 5.8 % and 12.6 %.

Due to a possibly incorrect description of the background and/or the MC J/ψ signal shape the extracted J/ψ signal might depend on the mass integration limits, even after ϵ_{int} correction.

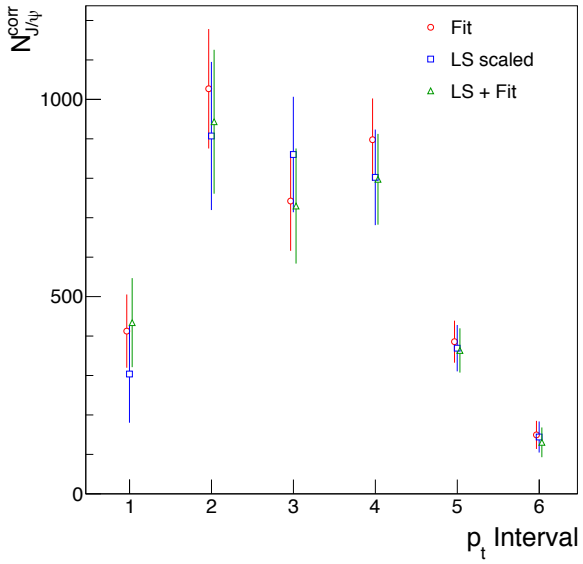

Figure 4.22: The $A \times \epsilon$ corrected J/ψ yield $N^{\mathrm{corr}}_{\mathrm{J}/\psi}$ determined by using the default background subtraction method (fit) and the two other background estimation procedures (LS scaled, LS+Fit) for the six analyzed p_{t} bins.

For an estimation of this effect, two variations of the default integration range of [2.92, 3.16] have been studied: [2.84, 3.20] and [3.00, 3.12]. This is a variation of ± 80 MeV/c^2 of the lower limit and ± 40 MeV/c^2 of the upper limit. The results are also shown in Fig. 4.21. A maximal difference of the $A \times \epsilon$ corrected J/ψ signal from the result of the fit method of 5.7 % is found.

If the material budget of the detector is not properly implemented in the simulation procedure, the MC signal line shape might be too broad or too narrow. This results in a systematic bias in the determination of the signal fraction in the integration limits. Approximately 3 % systematic uncertainty have been estimated in [173]. It had been determined by the analysis of dedicated MC J/ψ productions with variations of the material budget in a reasonable range. This analysis is not repeated here, instead this value is quoted and used. It is added to the contributions from the background subtraction procedure and the variation of the integration limits in quadrature. The resulting uncertainty of the signal extraction is 6.6 %.

It may be noted that the signal extracted with the LS method depends on the range which is used to scale the LS background. Three different ranges have been studied here: [3.2, 5.0] GeV/c^2 which is also the default range, [1.2, 2.0] GeV/c^2, and a combination of both. A maximum difference in the resulting J/ψ signal of 4.7 % is found. Since the LS method is only used as a reference, this value is not propagated to the total systematic uncertainty.

Acceptance input As shown in Section 4.4.1, the acceptance for the reconstruction of a J/ψ depends on its transverse momentum. For the determination of the total inclusive J/ψ cross

section an averaged value for the acceptance and efficiency correction has to be determined which is the weighted average over all transverse momenta. This average therefore depends on the MC input p_t spectrum. For [173] is was studied how much the acceptance may change due to a variation of the $\langle p_t \rangle$ of the input spectrum within a factor 2. The result of 1.5 % is also used in this analysis, the estimation is not repeated here. Furthermore, as will be shown in the next section, the MC input p_t spectrum is in a good agreement with the measured data indicating that the systematic error quoted here is a conservative estimation.
For the J/ψ rapidity such an estimation is not necessary since the y spectrum is expected to be rather flat in the region which is investigated here.

Reconstruction efficiency To estimate the systematic uncertainty of the reconstruction-efficiency correction procedure, additionally to the two default sets of analysis cuts two more sets are defined, see Section 4.3.1 and Table 4.3. This is on the one hand a loose set, wherein most of the applied cuts are changed to a less restrictive value, and a set of tight cuts with more restrictive values on the other hand. Like this, mismatches of the distributions of the cut variables between data and MC simulations are quantified. After the correction procedure, the results for the J/ψ yield $N^{\mathrm{corr}}_{\mathrm{J}/\psi}$ of all three sets are compared to each other, see Fig. 4.23. Within the statistical uncertainties a remarkable agreement of the different results is obtained. Despite the change of the S/B ratio from 0.3 (loose) to 2.1 (tight), a maximal difference of 4.0 % can be seen. Most likely this difference is only due to statistical fluctuations of the strongly changing background magnitude. Nevertheless, for a conservative estimation of the systematic uncertainty this value is used. A more detailed analysis of systematic effects in the $A \times \epsilon$ correction procedure including a study of each individual cut can be found in [189]. That study concluded with comparable results.

PID efficiency For the estimation of the the systematic uncertainty of the PID efficiency correction several variations of the procedure described in Section 4.4.3 have been performed. On the one hand, the exact value of the momentum-dependent cuts might be determined with a systematic bias. Therefore the values of these cuts have been modified by $\pm 0.1\ \sigma$ which is expected to be a reasonable range. Furthermore, the shift of the average $n\sigma$ value in MC might be determined incorrectly. Here, the extreme variations between not performing the correction of the shift at all and an overcorrection of 0.1 σ were investigated. The resulting maximal difference of the efficiency by the above modifications and a combination of them that was observed is 10.4 %. This is a rather extreme scenario, so this is a conservative estimation.

Branching ratio The branching fraction of the J/ψ decay into e^+e^- is known to 1 % precision [36].

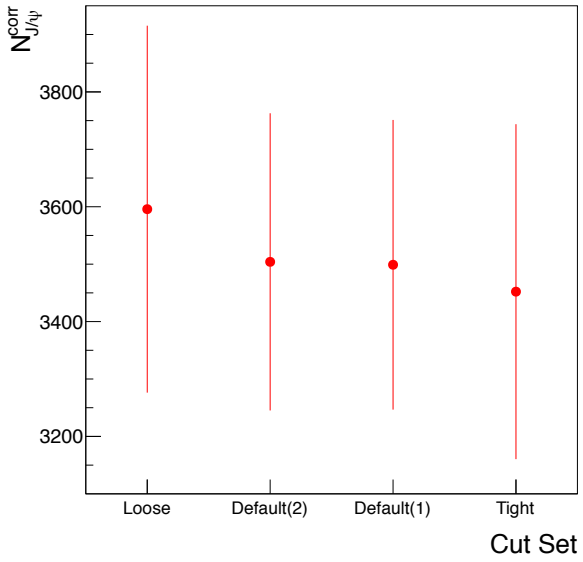

Figure 4.23: The $A \times \epsilon$ corrected J/ψ yield $N^{\mathrm{corr}}_{\mathrm{J}/\psi}$ for the two default cut sets and the loose and tight references.

Luminosity The systematic uncertainty of the V0AND cross section measurement is about 4 % [187]. There, the main contribution stems from the beam intensity determination, known with about 3 % precision. Fluctuations of the ratio $N_{\mathrm{V0AND}}/N_{\mathrm{MB}}$ (see Section 4.2.3) are within about 1 %. Added in quadrature, these two contributions account to 4 % (rounded).

Pile-up events When in one single bunch crossing of the two proton beams more than one pair of protons collide, these pile-up events are treated as if it was only one single event. This might lead to an overestimation of per-event yields. Thus, this study applies the default pile-up rejection technique available in the event analysis. The setup of the algorithm is as follows: all events are rejected if a second vertex with at least three contributors and a minimal distance to the main vertex in z-direction of 0.8 cm is found using SPD tracklets. The fraction of secondary events that have less than three associated tracklets or that are closer to the main vertex than 0.8 cm, and the vertex reconstruction efficiency result in a total pile-up rejection efficiency of approx. 48 % [192]. An average pile-up rate of 4 % leads to a rate of undetected pile-up events of below 2 % out of which the most have less than three tracklets [192]. Events with such a low multiplicity have only a small probability to contain a J/ψ decay (see Section 5.6). And even if, the track cut on the maximal distance in z direction to the main vertex further reduces that contribution strongly. Thus, per-event yields and cross sections are not biased by this effect.

Polarization Any polarization of the J/ψ would have a strong impact on the acceptance. For [173] an estimation had been performed, resulting $^{+21}_{-15}$ % in the helicity and $^{+19}_{-13}$ % in the

Collins-Soper reference frames for full transverse or longitudinal polarization. This is by far the largest contribution to the systematic uncertainty. A first measurement at LHC energies [68] suggests only a slight or no polarization. Thus, these numbers are just quoted here and not included in the total systematic uncertainty.

Comparison to published systematic uncertainties In Table 4.6 the systematic uncertainties estimated in this analysis are compared to those published in [173]. The J/ψ signal counts extracted by subtracting the background with the fit method and the combined LS and fit method are in a very good agreement with the results using the LS method. For [173] the track rotation method (see Section 5.3.1 for an explanation of the method) was investigated in addition to a fit method similar to the one described in this analysis. The results obtained by using the track rotation spectrum for background subtraction are in a slightly worse agreement to the other methods. Possible reasons for this discrepancy are discussed in Section 5.3.1. There, also a way to increase the agreement with the other methods up to the same level found for the other methods investigated here is explained.
The systematic uncertainties estimated in both analyses for the reconstruction and PID efficiencies are in a very good agreement. This is taken as an indication that the obtained values are reasonable. The systematic uncertainty for the acceptance input is not repeated here, the other contributions to the systematic uncertainty are in both analyses quoted from the same sources.

4.6 Integrated and Differential J/ψ Production Cross Sections

In this section the results of the J/ψ analysis in $\sqrt{s} = 7$ TeV minimum bias pp collisions are presented. Inclusive production cross sections are given as an integrated value and as a differential measurement. The results are compared to the ALICE published data, as well as to available data from other experiments. A comparison to model predictions closes this chapter.

4.6.1 Integrated Cross Section

With the corrected yield $N^{\mathrm{corr}}_{\mathrm{J}/\psi}$, Eq. (4.15), the integrated luminosity L_{int}, Eq. (4.5), and the branching ratio in the $\mathrm{e}^+\mathrm{e}^-$ decay channel [36]:

$$BR(\mathrm{J}/\psi \to \mathrm{e}^+\mathrm{e}^-) = 5.94\,\% \tag{4.21}$$

one can calculate the cross section as:

$$\sigma_{\mathrm{J}/\psi} = \frac{N^{\mathrm{corr}}_{\mathrm{J}/\psi}}{BR(\mathrm{J}/\psi \to \mathrm{e}^+\mathrm{e}^-)\, L_{\mathrm{int}}}. \tag{4.22}$$

The result for the inclusive integrated J/ψ production cross section in $\sqrt{s} = 7$ TeV pp collisions for $|y| < 0.9$ is:

$$\sigma_{\mathrm{J}/\psi}(|y| < 0.9) = 10.7 \pm 0.8\ (\mathrm{stat.}) \pm 1.4\ (\mathrm{syst.}) \pm 0.4\ (\mathrm{lumi.})\ \mu\mathrm{b}. \tag{4.23}$$

The systematic uncertainty is given in two components: the total value for all sources except the luminosity is the first, the second corresponds to the uncertainty from the luminosity determination. Compared to [173] ($\sigma_{\mathrm{J}/\psi}(|y| < 0.9) = 10.7 \pm 1.0\ (\mathrm{stat.}) \pm 1.6\ (\mathrm{syst.})$), almost the same result is found here. Indeed, both values for the cross section are identical up to the third significant digit. In a slightly smaller event sample, $L_{\mathrm{int}} = 5.50\ \mathrm{mb}^{-1}$ in this analysis instead of $5.6\ \mathrm{mb}^{-1}$ in [173], approx. the same number of raw signal counts is found, $N_{\mathrm{J}/\psi} = 353.6$ (this analysis) compared to 352 [173], at a slightly higher $A \times \epsilon$, 10.11 % (this analyis) compared to 9.8 %. The agreement of the two analyses indicates that the results are robust.
Due to the choice of the fit procedure to extract the signal the statistical uncertainty is reduced by about 20 %. The systematic error estimation of this analysis concluded with a bit lower value of 13.1 % compared to 13.8 % in [173]. A systematic error on the luminosity determination of 4 % is not included in both values.

A first measurement (see Section 2.3.2 and [68]) indicates no or only a weak J/ψ polarization in $\sqrt{s} = 7$ TeV pp collisions. Therefore, no additional systematic uncertainty on the acceptance determination is quoted here.

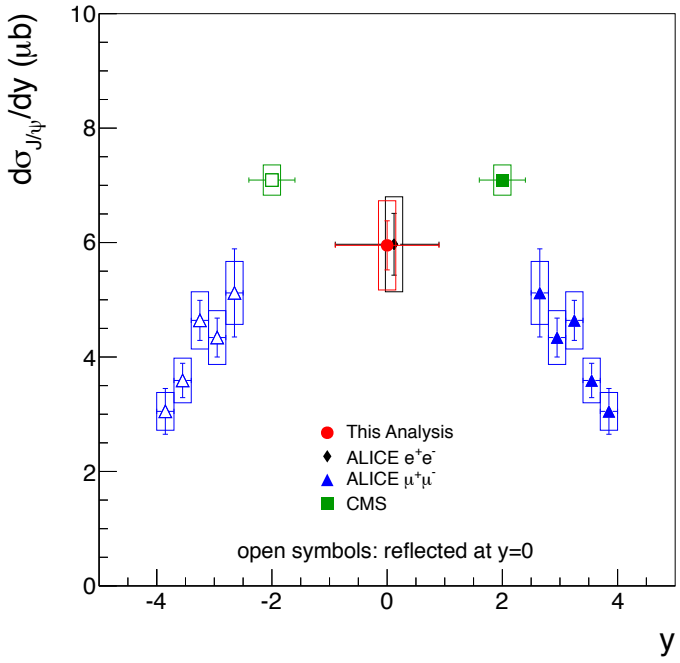

Figure 4.24: The p_{t} integrated inclusive J/ψ production cross section as a function of y. The results of this analysis are compared to the ALICE data at central (black diamond, slightly shifted in y for a better visibility of the error bars) and at forward rapidities (blue triangles) [173] and to the measurement by CMS [79]. The error bars correspond to the statistical uncertainties, the boxes represent the systematic uncertainties. A global uncertainty on the luminosity determination is not shown in the figure. It amounts 4 % for this analysis and the published ALICE measurement at mid-rapidity, 5.5 % for the ALICE measurement at forward rapidities and 11 % for CMS.

4.6.2 Differential Cross Sections

Rapidity dependence To study the shape of the J/ψ y distribution the result of this measurement is shown as the differential value:

$$\frac{\mathrm{d}\sigma_{\mathrm{J}/\psi}}{\mathrm{d}y} = \frac{N^{\mathrm{corr}}_{\mathrm{J}/\psi}}{\Delta y \, BR(\mathrm{J}/\psi \to \mathrm{e}^{+}\mathrm{e}^{-}) \, L_{\mathrm{int}}}, \tag{4.24}$$

together with the published ALICE results at central and forward rapidities [173] and the result of CMS [79] in Fig. 4.24. Data points at forward rapidities are mirrored at $y = 0$ and shown as open symbols. All markers are drawn at the center of the bin, except that of the ALICE measurement at mid-rapidity which is shifted slightly in y for a better visibility of the error bars. The latter correspond to statistical uncertainties only, boxes represent the systematic uncertainties. An additional systematic uncertainty on the luminosity is not shown in the figure, it amounts 4 % for this analysis and the corresponding ALICE measurement at mid-rapidity,

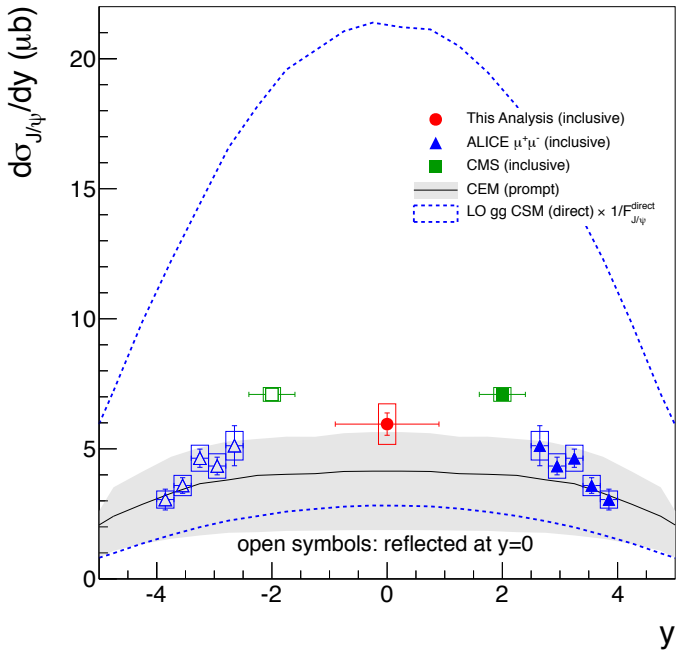

Figure 4.25: The p_{t} integrated J/ψ production cross section as a function of y from this analysis at mid-rapidity and from ALICE [173] and CMS [79] at forward rapidities. The data (inclusive measurements) are compared to predictions from the Color-Evaporation Model [193, 194] (black solid line with gray uncertainty band) and the Color-Singlet Model [195, 196, 197] (upper and lower bounds given as the dashed blue lines) for prompt production. See text for a description of the errors.

5.5 % for the ALICE measurement at forward rapidities and 11 % for CMS. The measurement at mid-rapidity fills the gap between the other results, together a rapidity spectrum spanning over almost eight units is given. Within the uncertainties the cross section rises towards mid-rapidity and reaches a plateau at around 2. Such a plateau has been observed before, e. g. by PHENIX at RHIC [198] in $\sqrt{s} = 0.2$ TeV pp collisions.

The result of this analysis as well as the complementary data at forward rapidities shown in Fig. 4.24 are compared to predictions from the Color-Evaporation Model [193, 194] and the Color-Singlet Model [195, 196, 197] in Fig. 4.25. Note that while the experimental data are corresponding to the inclusive measurement, the fraction of J/ψ from b-hadron decays are not included in the models. The CEM prediction is given as the prompt cross section including feed-down from higher mass c$\bar{\mathrm{c}}$ states. On the other hand the CSM prediction is given as the direct cross section including no feed-down at all. It is therefore scaled by a constant factor $1/F^{\mathrm{direct}}_{\mathrm{J}/\psi}$ where $F^{\mathrm{direct}}_{\mathrm{J}/\psi} = (64 \pm 6)\,\%$ [199] is the fraction of direct to prompt J/ψ cross sections (see Section 2.3.4). First measurements of the fraction of J/ψ from b-hadrons indicate that it is increasing from $\approx 9\,\%$ at $3.5 < y < 4$ [82] to $\approx 15\,\%$ at $|y| < 0.9$ [200]. Within the uncertainties

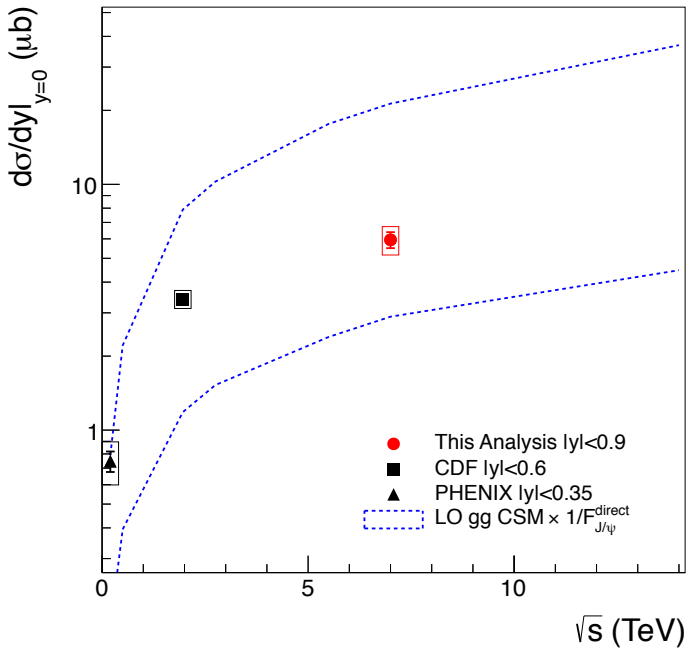

Figure 4.26: The differential cross section $\mathrm{d}\sigma_{\mathrm{J}/\psi}/\mathrm{d}y$ at mid-rapidity vs. collision energy $\sqrt{s}$. Results from PHENIX in 0.2 TeV pp collisions [198] and from CDF in 1.96 TeV $\mathrm{p\bar{p}}$ collisions[80] are shown together with the result of this study and compared to a CSM prediction at LO [195]. While the data correspond to inclusive cross sections, the model is given for prompt J/ψ.

and the fraction of J/ψ from b-hadrons the CEM prediction is compatible with the data. The plateau-like shape at mid-rapidity observed in data is also indicated by the CEM. For a final discussion of the shape a measurement of the prompt J/ψ cross section is necessary. However, taking the approximate values mentioned above into account suggests that after a subtraction of the non-prompt fraction from the data the agreement with the CEM curve will improve. Within the very large uncertaintiy of the CSM, its prediction at leading order (LO) for gluon fusion (gg) is compatible with the data. While this is not the case for the p_{t} differential measurement, the integrated value is reproduced already at LO, as it was already found at lower energies (see [196] and next paragraph). Main sources for these uncertainties are the gluon PDFs, the c quark mass and factorization and renormalization scales [201].

In order to study the energy dependence of the differential cross section $\mathrm{d}\sigma_{\mathrm{J}/\psi}/\mathrm{d}y$ at mid-rapidity, the result of this study is combined with results from other experiments. Figure 4.26 shows the results from PHENIX in $\sqrt{s}$ = 0.2 TeV pp collisions [198] and from CDF in $\sqrt{s}$ = 1.96 TeV $\mathrm{p\bar{p}}$ collisions [80] together with the result of this study. Compared to RHIC energies ($\sqrt{s}$ = 0.2 TeV), the cross section at LHC energies is almost one order of magnitude higher. Compared to Tevatron energies ($\sqrt{s}$ = 1.96 TeV), the increase is nearly a factor of two.

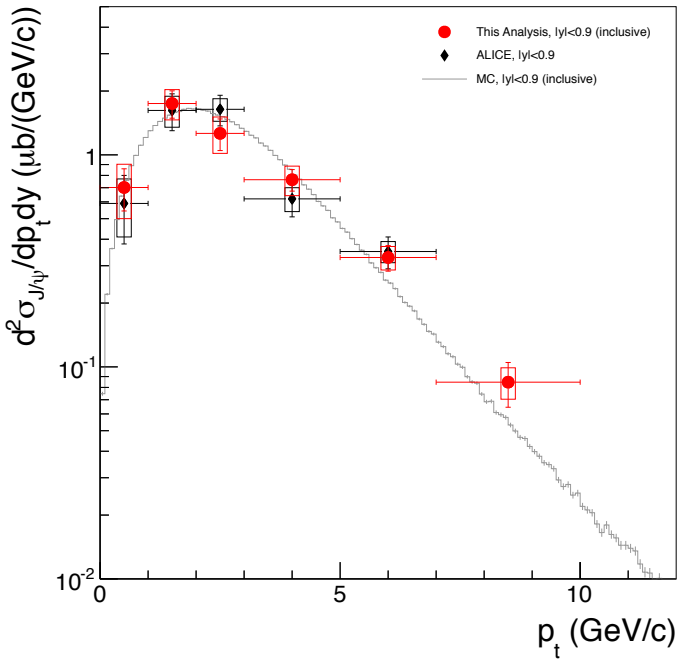

Figure 4.27: Inclusive J/ψ production cross section at mid-rapidity as a function of p_{t}. The results of this analysis (red dots) are compared to the published ALICE result [173] (black diamonds). The error bars correspond to the statistical, the boxes to the systematic uncertainties. A global uncertainty of 4 % on the luminosity determination is fully correlated between the bins and not shown in the figure. The gray line represents the MC input spectrum for the $A \times \epsilon$ determination, scaled to the result of this analysis.

The data in Fig. 4.26 is compared to the prediction from the Color-Singlet Model for gluon fusion at leading order [195]. As before, the prediction is given for direct J/ψ and has been divided by the direct fraction $1/F_{\mathrm{J}/\psi}^{\mathrm{direct}}$ such that it corresponds to the prompt cross section. Within the uncertainties of the model, represented by the upper and lower band in Fig. 4.26, the data is described by the CSM both in absolute amount and in the energy dependence. The increase with the energy seems to be slightly stronger than seen in the data, yet the fraction of b-hadrons might depend on $\sqrt{s}$.

Transverse-momentum dependence To study the transverse-momentum dependence of J/ψ production, the double-differential cross section has to be determined:

$$\frac{\mathrm{d}^2\sigma_{\mathrm{J}/\psi}}{\mathrm{d}p_{\mathrm{t}}\mathrm{d}y} = \frac{N_{\mathrm{J}/\psi}^{\mathrm{corr}}}{\Delta p_{\mathrm{t}} \Delta y \, BR(\mathrm{J}/\psi \to \mathrm{e}^+\mathrm{e}^-) \, L_{\mathrm{int}}}. \tag{4.25}$$

Figure 4.27 shows the result of this study in comparison with the one published in [173]. Within the uncertainties both spectra are in a good agreement. Due to the released ITS cluster

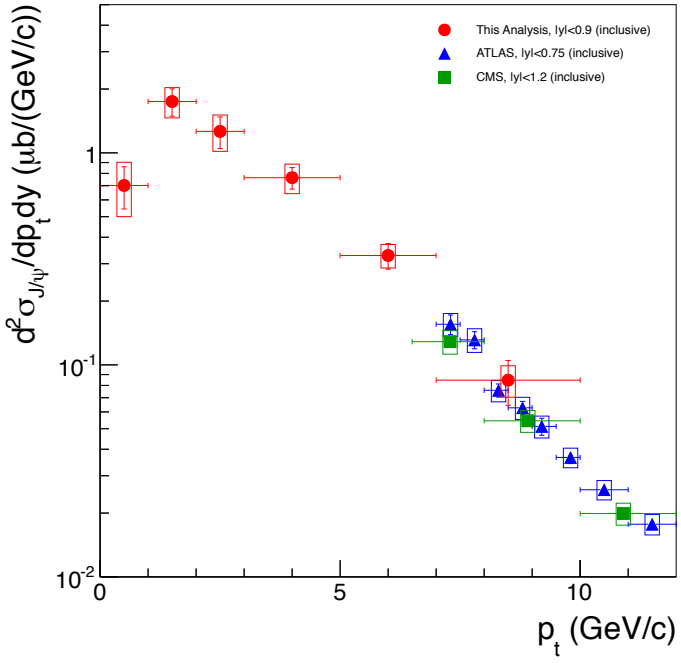

Figure 4.28: Inclusive J/ψ production cross section at mid-rapidity as a function of p_{t}. The results of this analysis (red dots) are compared to the data from ATLAS [78] (blue tringles) and from CMS [79] (green squares). The error bars correspond to the statistical uncertainties, the boxes represent the systematic uncertainties. A global uncertainty on the luminosity determination is fully correlated between the bins and not shown in the figure. It amounts 4 % for this analysis, 3.4 % for ATLAS and 11 % for CMS.

requirement at high p_{t}, this study could be extended to $p_{\mathrm{t}} = 10$ GeV/c.
The MC input p_{t} spectrum, which is used for the acceptance determination, is included in the figure as well (scaled to the result of this analysis). A good agreement with the measurement indicates that a possible bias of the acceptance determination must be small. The 1.5 % systematic uncertainty assigned to this potential bias thus seems to be a conservative estimation. Only the highest two bins are above the MC spectrum by more than one standard deviation, the actual p_{t} spectrum might be harder than expected. Due to the small contribution to the total cross section this has no substantial impact on the determination of the total acceptance.

ALICE is the only experiment at the LHC which is able to measure J/ψ down to $p_{\mathrm{t}} = 0$ at mid-rapidity. At low p_{t} therefore no comparison to other experimental results is possible. Above transverse momenta of 6.5 GeV/c and 7.0 GeV/c mid-rapidity data from CMS [79] ($|y| < 1.2$) and ATLAS [78] ($|y| < 0.75$) are available. Due to the extension of this analysis to 10 GeV/c, there is a region where all three data sets overlap and can be directly compared. This is shown in Fig. 4.28. Note that while the data points of this analysis are drawn at the center of the bins, the data points of CMS and ATLAS are plotted at the average transverse momentum

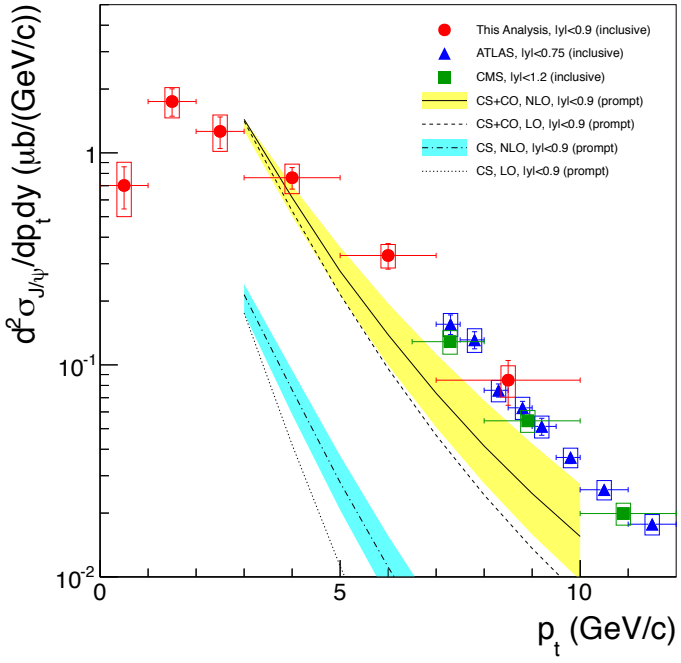

Figure 4.29: The J/ψ production cross section at mid-rapidity as a function of p_{t}. While the experimental data from this study (red dots), ATLAS [78] (blue tringles) and CMS [79] (green squares) are inclusive measurements, NRQCD [65, 202] predictions refer to prompt J/ψ production. The NLO NRQCD result is shown as the solid black line, a calculation to LO is shown as the dashed line. CS contribution at NLO (dot-dashed line) and LO (dotted line) are also shown.

$\langle p_{\mathrm{t}} \rangle$ of the bins. In the p_{t} region where the results of all three measurements overlap a very good agreement is found.

Figures 4.29 and 4.30 both show the same experimental data as Fig. 4.28, additionally various model predictions are included. A NRQCD prediction [65, 202] at next-to-leading order precision (NLO) for prompt J/ψ production is shown as the solid black line in Fig. 4.29, the yellow band corresponds to its uncertainty. For comparison the calculation is also shown at LO (dashed line). NRQCD containes both color-singlet (CS) modes as well as color-octet (CO) modes. The CS contribution is also shown individually at NLO (dot-dashed line) and at LO (dotted line). At the lowest p_{t} for which the prediction is given a good agreement with the data can be seen. Towards higher p_{t} theory and data diverge, the measured data exceeds the prediction by approcimately a factor of two in the region of 7–10 GeV/c.
The CDF experiment measured the fraction of direct to prompt J/ψ and found that it is almost independent of p_{t} in $\sqrt{s} = 1.8$ TeV p$\bar{\mathrm{p}}$ collisions [199]. However, the non-prompt fraction of J/ψ originating from b-hadron decays is of about 10 % at low p_{t} and increases towards higher p_{t} (see Fig. 2.16 in Section 2.3.4). At a transverse momentum of 10 GeV/c approx. 25–30 % of

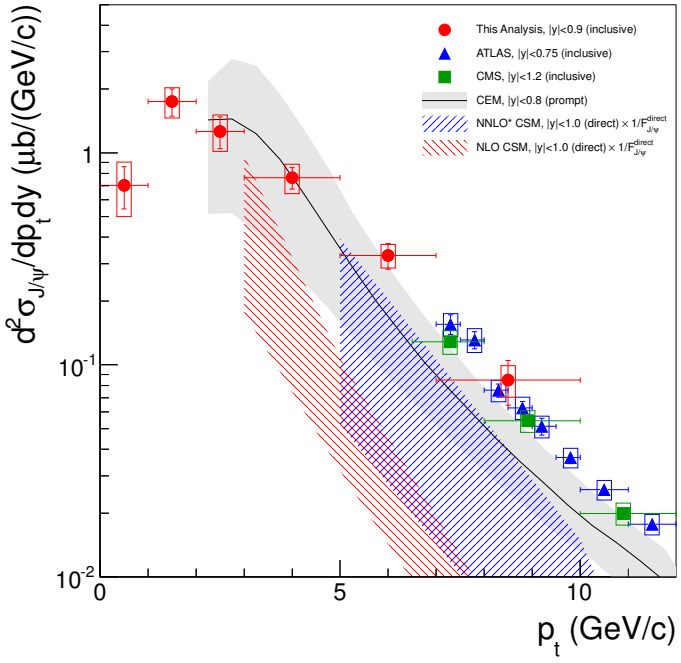

Figure 4.30: The same data as in Fig. 4.29 is compared to CEM [193, 194] and CSM [201, 58, 197] predictions for prompt J/ψ production. The CEM calculation is indicated by the solid black line. The NNLO* CSM result is shown as the shaded blue area, a calculation to NLO is also shown (shaded red area).

the measured J/ψ yield can be expected to be non-prompt. Taking this into account, data and model would be in a good agreement within their errors. This is not the case for leading order accuracy and/or the CS contribution alone.

A prediction of the Color-Evaporation model [193, 194] for the prompt J/ψ cross section ($|y| < 0.8$) is shown as the solid black line in Fig. 4.30, its uncertainty band is represented by the light gray area. The feed-down from higher-mass c$\bar{\text{c}}$ states is included as a factor in the model. Here, the same conclusions as for the NLO NRQCD prediction can be drawn: taking the non-prompt fraction of the J/ψ production and its p_{t} dependence into account, there probably would be a good agreement with the data.

Finally, Fig. 4.30 also features a prediction of the pure Color-Singlet Model [201, 58, 197]. The red shaded area corresponds to NLO accuracy, for the area shaded in blue additionally the most dominant α_{s}^5 contributions are included, referred to as NNLO*. The NLO contributions alone do not describe the measured p_{t} spectrum—the discrepancy can not be explained by the missing b feed-down fraction. Within their errors the two different NLO color-singlet predictions in Fig. 4.29 and Fig. 4.30 are compatible to each other. The NNLO* band tends to lower values for the cross section than the other models. Within its larger uncertainites (same sources as discussed above) it probably is still compatible with the data when taking the discussed b feed-down into account.

4.7 Outlook

Most of the models for J/ψ production present prompt or even only direct J/ψ cross sections. For an accurate comparison with theoretical predictions it is important to determine precisely the fractions of the different sources. The non-prompt fraction of J/ψ, which are decay products of short-lived b hadrons, can be determined via the pseudo-proper decay time [80]. An analysis of this fraction as a function of transverse momentum is performed at ALICE, using the same data sets as this analysis. Results are about to be published, the preliminary data was discussed in Section 2.3.4. Together with results from ATLAS and CMS at higher p_t a similar trend as observed at lower energies measured by CDF is indicated there.
Feed down from higher mass charmonium states has been measured at lower energies where it was found to be about 36 % and almost independent of p_t [199]. This is only true for the sum of the different contributions which are mainly decays of χ_c and ψ'. The individual components indeed show a slight dependence on p_t, though in opposite direction. A measurement at LHC energies will clarify whether or not the fraction of J/ψ from these sources is of the same order and what its dependence on p_t is.
At ALICE, the measurement of the decay $\chi_c \rightarrow J/\psi + \gamma$ is possible at mid-rapidity by reconstructing both the $J/\psi \rightarrow e^+e^-$ decay and the γ via its possible conversion into e^+e^- in the detector material [203, 204]. The conversion probability is expected to be about 8 %, so for this measurement a trigger will be necessary. The same is true for the analysis of the ψ' at mid-rapidity. The TRD (see Section 3.2.4) is an excellent detector for this purpose. It is capable to provide fast trigger decisions on high p_t electron tracks and will be available soon.
The first measurement of the J/ψ polarisation at LHC energies was published by ALICE [68] for forward rapidities. A corresponding analysis at mid-rapidity will further contrain the models.
The proton is an object composed of valence quarks, sea quarks and gluons. A high-energy collision of two protons is thus a complex process. A possible interplay between the hard scattering leading to the production of a quarkonium, and the underlying pp event has been investigated for the first time and is part of this work. This subject will be addressed in the next chapter.

When the LHC has reached its design energy, Pb–Pb collisions will be possible up to $\sqrt{s_{NN}} = 5.5$ TeV. For the determination of the nuclear modification factor (see Eq. (2.12) in Section 2.4.3) a pp reference at the same energy is necessary. Depending on the availability and the quantity of pp measurements at the same collision energy an interpolation between data at $\sqrt{s} = 7$ TeV and at lower energies (as e. g. in [205]) might become relevant. Such an interpolation also serves as a cross check of the data at intermediate collision energies as e. g. the ALICE measurement in $\sqrt{s} = 2.76$ TeV pp collisions [206].

Chapter 5

Multiplicity-Dependent J/ψ Analysis

For the first time, the J/ψ yield has been studied as a function of the charged-particle multiplicity in pp collisions [192]. This measurement has been performed with the ALICE experiment in both dileptonic decay channels of the J/ψ. The analysis in e^+e^- is subject of this thesis and will be addressed in this chapter.
For this part of the analysis, the joint framework of the ALICE J/$\psi \to e^+e^-$ analysis group has been utilized to obtain the results. Therefore, this *dielectron framework* (DF) will be introduced below, followed by a description of the charged-particle multiplicity measurement. The identical data samples are used as in the minimum-bias analysis (see Section 4.2); also, most of the analysis strategy is the same. This chapter will therefore focus on the differences, which are mainly the signal extraction procedure and the neccessary correction procedures.

5.1 The Dielectron Framework

Originally started as a development environment for J/$\psi \to e^+e^-$ analyses, the framework has been generalized to all dielectron studies. It is implemented within the general ALICE analysis environment described in Section 4.1 and especially focussed on data processing with the analysis train. Within the dielectron framework, all technical definitions and routines that are common to the different analyses, are put together in a generic analysis task.
The user, working on a specific analysis, only has to provide a configuration to the DF, including e. g. the cut variables and ranges and the desired output observables. Like this, large parts of the common code development only has to be done once, maintaining a high quality and less redundancy. The DF also makes use of the common correction framework, described in Section 4.1.1. The DF is incorporated and accessible within AliRoot. For the measurement of

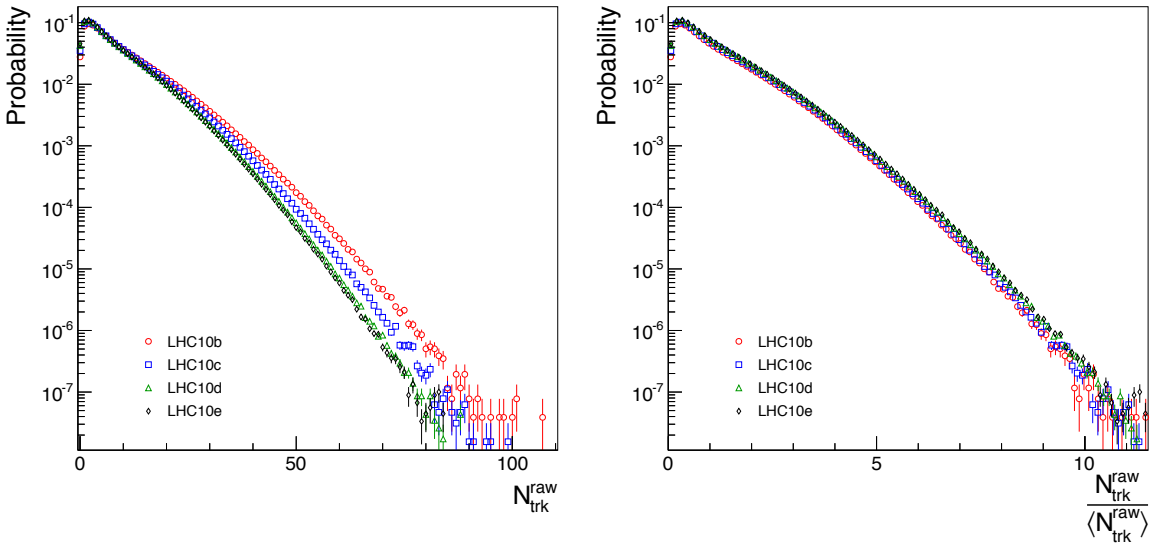

Figure 5.1: Left: the probability distribution for measuring $N_{\mathrm{trk}}^{\mathrm{raw}}$ in the four analyzed beam periods LHC10[b-e] in the range $|\eta| < 1.0$. Right: the probability distribution of $N_{\mathrm{trk}}/\langle N_{\mathrm{trk}} \rangle$, the number of tracklets normalized by the mean number of tracklets per period, for the ame data.

the charged-particle multiplicity dependence of J/ψ production, the DF has been extended by the necessary methods to perform this analysis.

5.2 Determination of the Charged-Particle Multiplicity

The charged-particle multiplicity of each event is measured in terms of the number of accepted SPD tracklets within the pseudorapidity range of $|\eta| < 1.0$. SPD tracklets are created out of all combinations of SPD clusters, one in each of the two detector layers, that are pointing in direction of the primary interaction vertex. Each cluster can only be associated to one single tracklet. See [129, 184] for details of the tracklet algorithm.
Using the SPD for the multiplicity determination has the advantage that this detector is closest to the interaction region, implying a small contamination by secondary particles and a low momentum cut-off (approximately 50 MeV/c due to particle absorption in the material [184]). The measured raw number of SPD tracklets $N_{\mathrm{trk}}^{\mathrm{raw}}$ is evaluated during the reconstruction procedure and is avaliable in the ESDs (`AliESDEvent::EstimateMultiplicity()`).
Figure 5.1, left panel, shows the corresponding multiplicity distributions for the four different beam periods. The variation of the distributions between the different beam periods is due to a decrease of the SPD acceptance with time. Due to limitations in statistics, the analysis cannot be done in each beam period separately but only for the full number of events, i. e., the

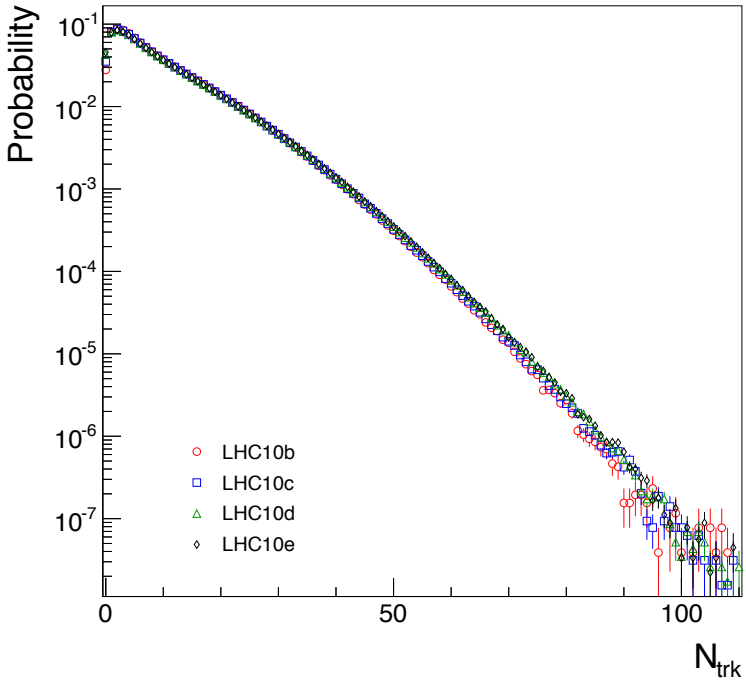

Figure 5.2: As Fig. 5.1, left panel, just after correcting the number of tracklets for the acceptance bias, see text for details.

sum of all periods. To ensure that the same underlying physical number of charged particles N_{ch} of a given event leads to, on average, the same reconstructed multiplicity, a first approach was to normalize each distribution by its mean, $\langle N_{\mathrm{trk}} \rangle$. This is shown in Fig. 5.1, right panel. With this normalization, the agreement between the four beam periods is already quite good. By looking into more detail of the remaining differences of the distributions it was noticed that the SPD acceptance was not only changing with time but is also dependent on the z position of the primary interaction vertex. As it was shown in Chapter 4, Fig. 4.2, the vertex distribution changed within the beam periods. When combining all data together for the analysis, this also has to be corrected for. The procedure for this correction is available in the dielectron framework. The method is to determine the average $N_{\mathrm{trk}}^{\mathrm{raw}}$ as a function of z_{vtx} for each beam period and scale the measured distribution accordingly. See Appendix B for a more detailed description of the procedure. Figure 5.2 shows the result after the correction: the N_{trk} distributions of all four beam periods are in good agreement.

As a cross check, the same procedure has been applied to the MC data sets which have been reconstructed with the same running conditions of the collisions data sets LHC10[b-e] (for details of these MC data sets, see Section 4.2.2 and Table 4.2). In the simulations the inactive SPD modules are accounted for; thus, the according $N_{\mathrm{trk}}^{\mathrm{raw}}$ spectra show the same dependence on

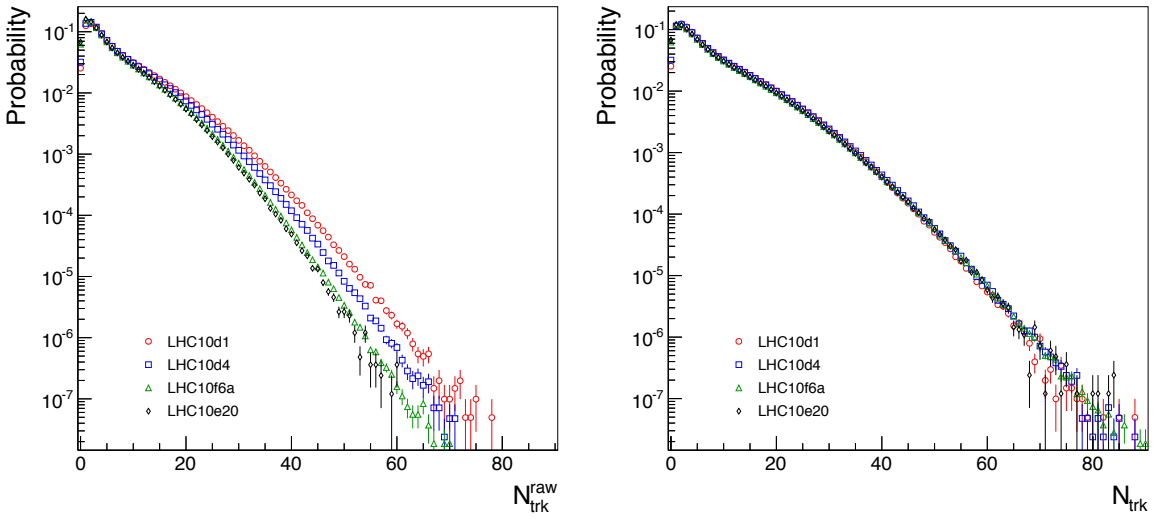

Figure 5.3: Left: as Fig. 5.1, just for the four min. bias MC data sets corresponding to the four analyzed beam periods. Right: as Fig. 5.2, just for the four min. bias MC data sets corresponding to the four analyzed beam periods.

the corresponding run period, see Fig. 5.3, left panel. As for the real data, also in Monte Carlo events the N_{trk} distributions are in very good agreement after the correction procedure, shown in Fig. 5.3, right panel. When comparing Figs. 5.1, left panel and 5.3, left panel, obviously the simulated multiplicity distributions underestimate the measured data. This is strongly dependent on the specific tuning of the MC event generator, see [184, 207] for details.

The multiplicity spectrum is divided into several intervals, for each of these intervals an invariant mass analysis is performed (see the next section). With the requirement of having a similar significance of the J/ψ signal in all intervals, five intervals have been defined for the analysis. Table 5.1 summarizes these multiplicity ranges. Therein, also the average values of the different multiplicity intervals, $\overline{N_{\mathrm{trk}}}$, and the number of analyzed events in each interval are listed. Additional to the intervals 1 to 5, the under- and overflow intervals (0 and 6), are listed as well, for completeness.
Events with zero tracklets are excluded from the first interval. On the one hand there is no J/ψ signal in this bin, on the other hand including it would imply corrections for the number of events, since events with no reconstructed tracklet have a strong contribution from diffractive processes. The corrections and further systematic uncertainties cancel by setting the lower edge of the first multiplicity interval to $N_{\mathrm{trk}} = 1$.
The overflow interval, number 6 in Table 5.1, is excluded from the fifth interval to minimize the systematic uncertainties (see Section 5.5). Moreover, due to limited statistics almost no J/ψ signal is found in that multiplicity range.

Multiplicity interval	N_{trk} range	$\overline{N_{\mathrm{trk}}}$	$\mathrm{d}N_{\mathrm{ch}}/\mathrm{d}\eta$ range	$\langle \mathrm{d}N_{\mathrm{ch}}/\mathrm{d}\eta \rangle$ (bin)	$N_{\mathrm{MB}}^{\mathrm{ana}} \cdot 10^6$
0	[0,1)	0.0			12.23
1	[1,9)	4.056	0.7 – 5.9	2.7	164.64
2	[9,14)	10.796	5.9 – 9.2	7.1	51.05
3	[14,20)	16.216	9.2 – 13.2	10.7	35.72
4	[20,31)	23.949	13.2 – 20.4	15.8	28.52
5	[31,50)	36.481	20.4 – 32.9	24.0	9.69
6	[50,∞)	55.905			0.74

Table 5.1: Statistics of the multiplicity intervals. The N_{trk} range is given together with the average in each interval, $\overline{N_{\mathrm{trk}}}$. Also the corresponding $\mathrm{d}N_{\mathrm{ch}}/\mathrm{d}\eta$ range is given together with the average in each interval, $\langle \mathrm{d}N_{\mathrm{ch}}/\mathrm{d}\eta \rangle$ (bin). Furthermore, the number of analyzed events, $N_{\mathrm{MB}}^{\mathrm{ana}}$, is listed. Bins 0 and 6 are the under- and overflow bins and not used for the analysis.

Since the number of tracklets, no matter if corrected or not, is a detector dependent quantity, results depending on this variable are not comparable to any other experiment or to theory predictions. To allow for such comparisons the measured N_{trk} has to be related to a physical variable, the number of charged particles N_{ch} primarily created in the pp collision.
In the experiment it is not possible to distinguish between particles from the primary interaction and secondary particles which can be created by decays or interaction with detector material. Therefore the following procedure, based on MC informations, has been applied: Monte Carlo productions for all four beam periods have been studied to correlate N_{trk} with N_{ch}, see the left panel of Fig. 5.4. In first approximation, the number of measured tracklets is linearly dependent on the number of primarily created charged particles. The distribution on the right panel of Fig. 5.4 corresponds to the slice of the histogram in the left panel along the red line. The shape is approx. Gaussian as the comparison to a Gaussian fit (red curve) indicates.

Other multiplicity estimators than the number of SPD tracklets, including global tracks have a better resolution and should in principle be favoured. In this analysis these estimators could not be used because their computation was implemented after the reconstruction of the data of the run periods LHC10b and -c. Since in this analysis the whole multiplicity distribution is divided in broad intervals, the resolution of the estimator does not have a big impact on the quality of the result. Furthermore, these two run periods contain approximately one third of the total number of events available in this analysis, leaving the number of SPD tracklets as the only available choice.

Using the assumption of the linear dependence without offset between the measured quantity

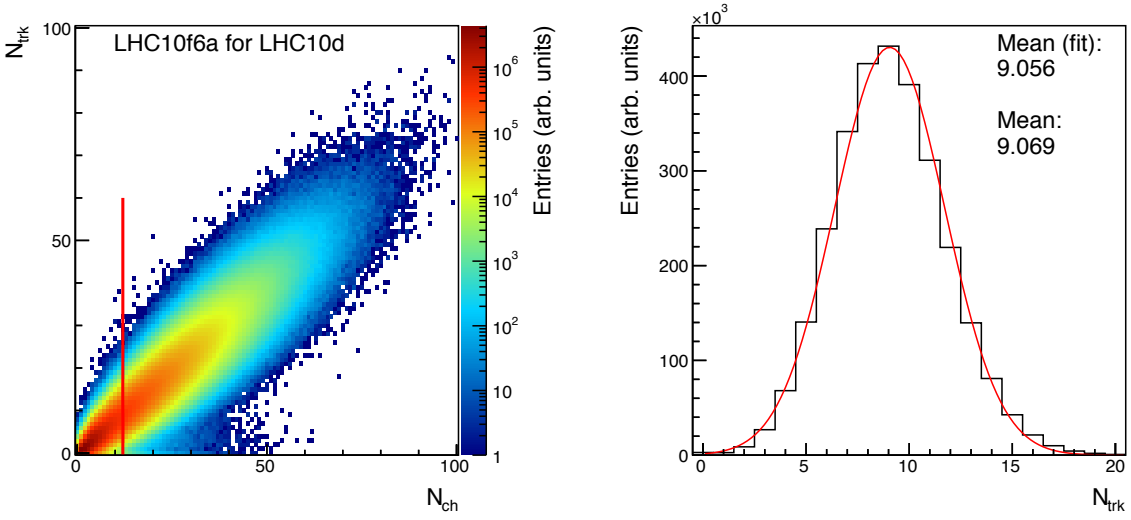

Figure 5.4: Left: the correlation matrix between the simulated physical number of charged particles per event N_{ch} and the measured multiplicity N_{trk}, both counted within a range of $|\eta| < 1.0$. The red line corresponds to the mean charged-particle multiplicity published by ALICE [207]. Right: the distribution of N_{trk} corresponds to the slice along the red line in the matrix on the left panel. The red curve shows a Gaussian fit to the data. The mean values are those of the distribution and the fit. Here, as an example, the results for LHC10d is shown, the corresponding results for the other periods can be found in Appendix D.

and the underlying physical quantity,

$$N_{\mathrm{trk}}\left(N_{\mathrm{ch}}\right) = mN_{\mathrm{ch}}, \tag{5.1}$$

only the slope m has to be determined by chosing one point on the straight line. The most natural choice here is to simply determine the mean N_{trk} corresponding to the mean number of charged particles $\langle N_{\mathrm{ch}}\rangle$. For the latter the ALICE result [207]:

$$\langle \mathrm{d}N_{\mathrm{ch}}/\mathrm{d}\eta\rangle = 6.01 \pm 0.01\ (\mathrm{stat.})\ ^{+0.20}_{-0.12}\ (\mathrm{syst.}) \tag{5.2}$$

is used (multiplied with the width of the η interval). This is illustrated on the right panel of Fig. 5.4. The histogram corresponds to a slice of the two dimensional histogram on the left panel along the vertical red line which is indicating $\langle N_{\mathrm{ch}}\rangle$. Also the result of a Gaussian fit procedure is shown for comparison: the mean of the fit result is in good agreement with the mean of the histogram, $N_{\mathrm{trk}}\left(\langle N_{\mathrm{ch}}\rangle\right)$, which is used in the analysis. This procedure is performed for all analyzed beam periods separately. The average, weighted with the number of events, is used (see Table 5.2). Note that while $\langle N_{\mathrm{ch}}\rangle = 2.0 \cdot \langle \mathrm{d}N_{\mathrm{ch}}/\mathrm{d}\eta\rangle = 12.02$, is a real number, the correlation matrix (Fig. 5.4, left panel) is based on integer values. The result for the

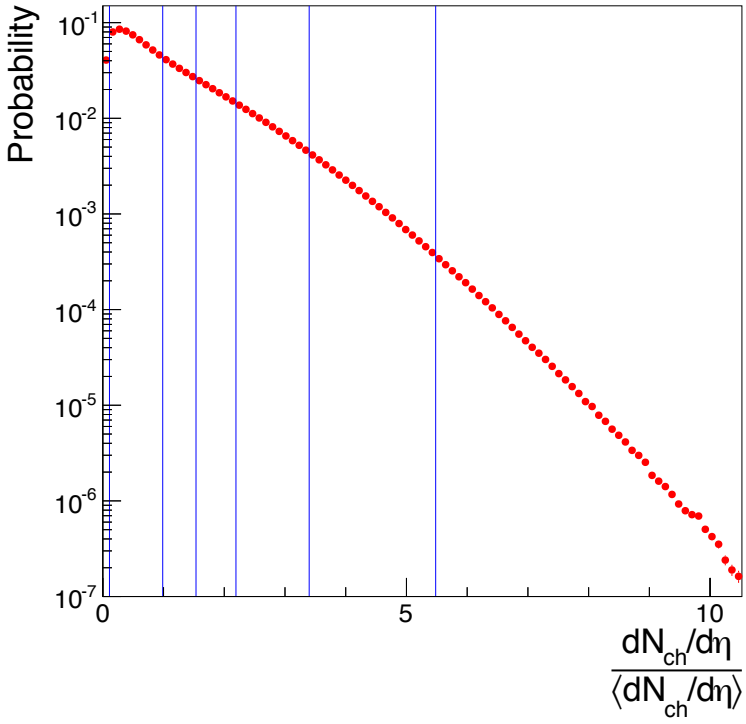

Figure 5.5: The probability distribution of the relative charged-particle density ($\mathrm{d}N_{\mathrm{ch}}/\mathrm{d}\eta / \langle \mathrm{d}N_{\mathrm{ch}}/\mathrm{d}\eta \rangle$). In contrast to the previous figures, here the result after summation over all four analyzed beam periods is shown. The blue lines correspond to the limits of the multiplicity intervals, chosen for the analysis.

corresponding bin of 12 therefore has to be scaled by a factor of 12.02/12.0. If (5.1) is correct, it follows with:

$$\frac{N_{\mathrm{trk}}}{N_{\mathrm{trk}}\left(\langle N_{\mathrm{ch}} \rangle\right)} = \frac{mN_{\mathrm{ch}}}{m\,\langle N_{\mathrm{ch}} \rangle} = \frac{\mathrm{d}N_{\mathrm{ch}}/\mathrm{d}\eta}{\langle \mathrm{d}N_{\mathrm{ch}}/\mathrm{d}\eta \rangle} \tag{5.3}$$

that in this relative multiplicity the slope m cancels out.

The final distribution of the relative charged particle density is shown in Fig. 5.5. The vertical lines indicate the boundaries of the multiplicity intervals used in this analysis. Table 5.2 summarizes the results of $N_{\mathrm{trk}}\left(\langle N_{\mathrm{ch}} \rangle\right)$ for the four beam periods and the total sample, together with $\overline{N_{\mathrm{trk}}}$. Also the number of MB events N_{MB} and all MB events passing the event cuts $N_{\mathrm{MB}}^{\mathrm{ana}}$ are listed. These numbers are identical or almost the same as in Table 4.1, small differences may be due to a failed analysis job in the computation of the output.
Table 5.1 summarizes the resulting ranges in $\mathrm{d}N_{\mathrm{ch}}/\mathrm{d}\eta$ of the multiplicity intervals, corresponding to the ranges in N_{trk}. Also $\langle \mathrm{d}N_{\mathrm{ch}}/\mathrm{d}\eta \rangle$ (bin), corresponding to $\overline{N_{\mathrm{trk}}}$ is given.

Beam Period	$N_{\mathrm{MB}} \cdot 10^6$	$N_{\mathrm{MB}}^{\mathrm{ana}} \cdot 10^6$	$\langle N_{\mathrm{trk}} \rangle$	$N_{\mathrm{trk}}\,(\langle N_{\mathrm{ch}} \rangle)$
LHC10b	27.87	25.79	9.501	9.297
LHC10c	75.75	64.12	9.500	9.259
LHC10d	158.49	119.89	9.501	9.084
LHC10e	122.96	92.88	9.501	9.026
Total	387.08	302.68	9.501	9.122

Table 5.2: Statistics of the beam periods. The number of MB events is given together with the number of analyzed events. Furthermore, the mean values of the corresponding N_{trk} distributions are listed as well as the extracted $N_{\mathrm{trk}}\,(\langle N_{\mathrm{ch}} \rangle)$. All values are given separately for each beam period and for the total sample.

5.3 Yield Extraction

For the multiplicity-dependent analysis the event selection and track reconstruction procedure follows the same procedure as described in the previous chapter. A recent study [171] unveiled that releasing the ITS hit requirement offers an increased reconstruction efficiency and thus an increased number of signal counts with only a moderate decrease of the signal-to-background ratio.
The SPDany condition in the inclusive minimum bias analysis corresponds to requiring at least one hit in one of the two innermost ITS layers, the SPD. The advantage of this cut is a high S/B because a large fraction of the secondary electrons from, e. g., γ conversions happening in subsequent material layers are suppressed. On the other hand, the low SPD acceptance reduces the total number of signal counts. It turned out that releasing the condition to only requiring a hit in at least one of the four innermost ITS layers (SPD + SDD) is the best choice to maximize the signal while keeping the background at a moderate level. This selection, referred to as ITSany(4), had been introduced in Section 4.3.1. As it turned out, the statistical uncertainties of the signal counts after background subtraction (see next section) almost stay the same. The larger signal with reduced uncertainty is extracted after subtraction of a larger background increasing the absolute uncertainty by almost the same amount. The advantage of this released cut is an improvement of the systematic uncertainty of the signal extraction, as will be further discussed in the next sections. Thus, the track cuts used in this analysis are the same as the default(2) set listed in Table 4.3 and discussed in Section 4.3.1.

The yield of J/ψ particles $Y_{\mathrm{J}/\psi}^{\mathrm{i}}$ in a given multiplicity interval i, is given by:

$$Y_{\mathrm{J}/\psi}^{\mathrm{i}} = \frac{N_{\mathrm{J}/\psi}^{\mathrm{i}}}{A \times \epsilon\, BR(\mathrm{J}/\psi \to \mathrm{e}^+\mathrm{e}^-) N_{\mathrm{ev}}^{\mathrm{i}}}, \tag{5.4}$$

where the measured J/ψ counts $N^{\mathrm{i}}_{\mathrm{J}/\psi}$ are corrected for the acceptance A and efficiency ϵ of the detector and the branching ratio $BR(\mathrm{J}/\psi \to \mathrm{e}^+\mathrm{e}^-)$, and normalized by the number of events in the multiplicity interval i, $N^{\mathrm{i}}_{\mathrm{ev}}$.

In the final representation, the J/ψ yields in each multiplicity interval are shown normalized by the average value of all inelastic proton-proton events, $\mathrm{pp}_{\mathrm{inel}}$:

$$\frac{Y^{\mathrm{i}}_{\mathrm{J}/\psi}}{Y^{\mathrm{pp}_{\mathrm{inel}}}_{\mathrm{J}/\psi}} = \frac{\mathrm{d}N_{\mathrm{J}/\psi}/\mathrm{d}y}{\langle \mathrm{d}N_{\mathrm{J}/\psi}/\mathrm{d}y \rangle}. \tag{5.5}$$

In this ratio the correction factors for acceptance and efficiency as well as for the branching ratio cancel out. Without applying these corrections, also their systematic uncertainties cancel, resulting in a more accurate result. Furthermore, the relative yield is more informative than the simple yield since it includes a direct comparison to the inimum bias average.

5.3.1 Background-Subtraction Procedures

Two different procedures for background subtraction are applied in this analysis, their differences are used to estimate a systematic uncertainty inherent to this method. The first one is the like-sign method, which was already described in the previous chapter, Section 4.3.3. There, the sum of both LS invariant-mass spectra $N_{--} + N_{++}$ is scaled to match the integral of the OS spectrum in the mass range [3.2, 5.0] GeV/c^2. Given the available statistics, the main disadvantage of this method are its rather large statistical uncertainty and empty bins in low background mass regions. Therefore, in this analysis this method is only used as a reference for systematic error estimations. The default background estimation method used here is track rotation.
In this method, one track of each opposite-sign pair is rotated around the z axis, i. e. along the azimuthal angle ϕ, by a random value. The other kinematic parameters of the track (η and p_{t}) are kept unchanged. This algorithm is repeated ten times in order to increase the number of pairs. For each iteration randomly one out of the two tracks is selected for the rotation; each iteration starts with the original parameters of both tracks. The resulting invariant-mass spectrum is then scaled to match the integral of the opposite-sign spectrum in the mass region [3.2, 5.0] GeV/c^2 which is the same as for the LS method.

The resulting invariant-mass spectrum of both methods is shown in Fig. 5.6 as blue diamonds (like sign) and green squares (track rotation), together with the opposite-sign spectrum (red dots). While the left panel of Fig. 5.6 corresponds to the result using the default track cuts discussed above (default(2) cut set), the right panel corresponds to the same data, just with the more restrictive cut SPDany, for comparison (default(1) cut set). The lower panels on both sides of the figure show the difference of the opposite-sign and track-rotation invariant-mass spectra. A fit of the MC signal line shape to the data shows a good agreement in both cases.

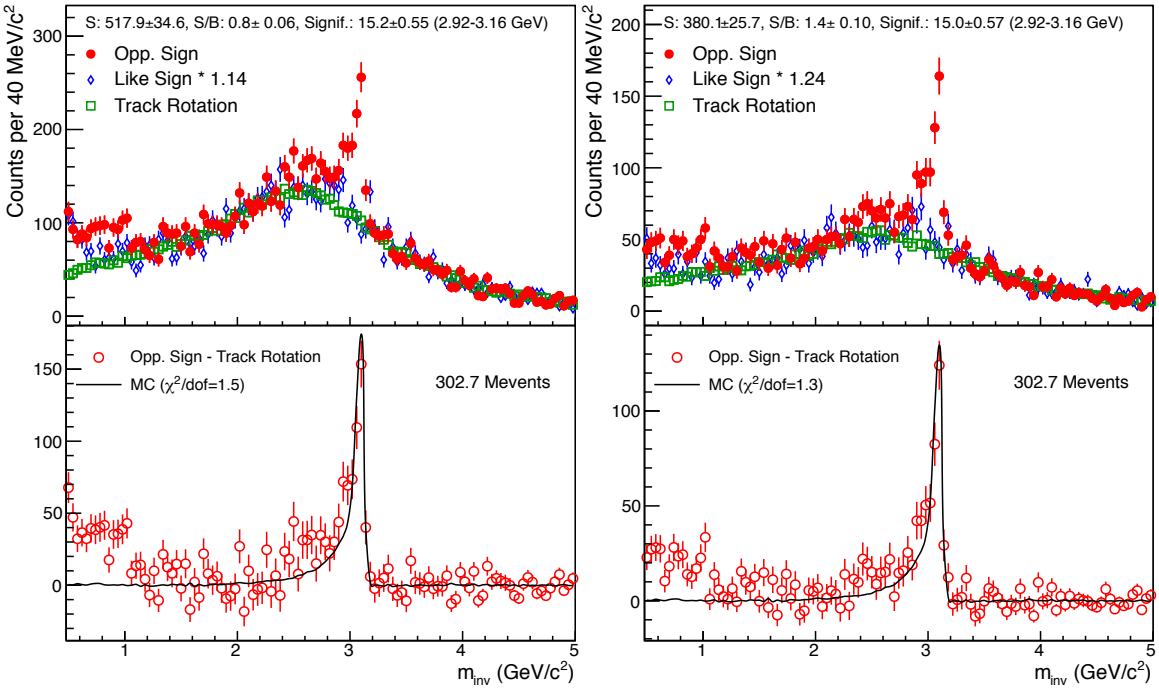

Figure 5.6: Left: invariant mass spectrum of the total available data using the released ITS cluster cut described in the text. Right: the invariant mass spectrum of the same data using the more restrictive cut SPDany. Both panels: red dots correspond to the opposite-sign mass spectra, open blue diamonds correspond to the like-sign spectra. The distribution from the track-rotation method is represented by open green squares. The lower panels show the spectra after subtraction of the track-rotation background from the opposite-sign distribution. The MC signal line shape is fitted to the data, showing a good agreement.

When comparing the agreement of the track-rotation and the opposite-sign spectra for the two cases with the loose and the restrictive ITS cluster cut, for the released cut condition an improvement can be seen. On the right panel of Fig. 5.6 (SPDany) the track-rotation spectrum seems to underestimate the opposite-sign spectrum slightly at invariant masses below that of the J/ψ. Since this may well also be the case in the signal region, leading to an overestimated result, for the analysis in[173] this method was only used as a reference, assigning a conservative systematic error of 8.5 % to the signal extraction procedure. With the selection ITSany(4) the difference in the extracted number of signal counts is much smaller: below 2.5 %.

The higher background magnitude after releasing the ITS selection to ITSany(4) might improve the precision of the background estimation, either just by the increased statistical sample or by the background composition.

Another interpretation is the following: a prerequisite for the track rotation techique is that the reconstruction efficiency should be independent of the azimuthal angle ϕ. Especially for the SPD this is not the case, tracks can be rotated to angles with reduced SPD acceptance.

This might introduce a bias on the J/ψ kinematics and lead to a slightly modified distribution. When the SDD layers are included in the ITS cluster requirement, the acceptance becomes less dependent on ϕ, removing this bias.

The J/ψ yield is studied in the five multiplicity intervals defined above. The corresponding invariant-mass distributions are shown in Fig. 5.7. As in Fig. 5.6, the opposite-sign (red dots), like-sign (blue diamonds) and track-rotation (green squares) invariant-mass spectra are shown for the five multiplicity intervals. Additionally, the overflow interval is shown on the lower right panel, for completeness, which is not containing any substantial signal.
In all intervals a good agreement of the background estimators and the mass distributions outside the J/ψ mass region is found.
It may be noted that the additional scaling factor needed to match the integral of the like-sign distribution to that of the opposite-sign one in the range from 3.2 to 5.0 GeV/c^2 decreases monotonously from 1.45 in the first multiplicity interval to 1.05 in the fifth interval.

The signal and background counts, the S/B ratios and significances of the J/ψ signals are summarized in Fig. 5.8. While the significance is approximately constant, the signal counts increase with multiplicity. But the background increases even faster, leading to a strongly decreasing S/B.

5.4 Corrections

The results of the multiplicity dependent J/ψ analysis are presented with normalization to the result in all inelastic proton-proton events $\mathrm{pp_{inel}}$ (see Eq. (5.5) in Section 5.3 for the normalization and Section 4.2.3 for the definition of $\mathrm{pp_{inel}}$). Therefore, the correction for z_{vtx}, $A \times \epsilon$ and the branching ratio cancel, given that the correction factors do not depend on the multiplicity. It has been studied whether this is indeed the case and will be discussed in the following.

5.4.1 Event Normalization

In order to ensure a constant acceptance for all events the position of the primary vertex is required to be located $\pm$ 10 cm around the origin in z direction. The correction for the number of events due to this selection, as described in Section 4.2.3, should be applicable here. But under the assumption that the correction factor is independent of the event multiplicity, it cancels due to the normalization to $\mathrm{pp_{inel}}$ in this analysis. Figure 5.9 shows the z_{vtx} correction factors determined in each multiplicity interval for all four analyzed beam periods. The horizontal lines correspond to the averaged factors for the different beam periods. There is a good agreement between the values determined in each interval separately and the average results. Only in

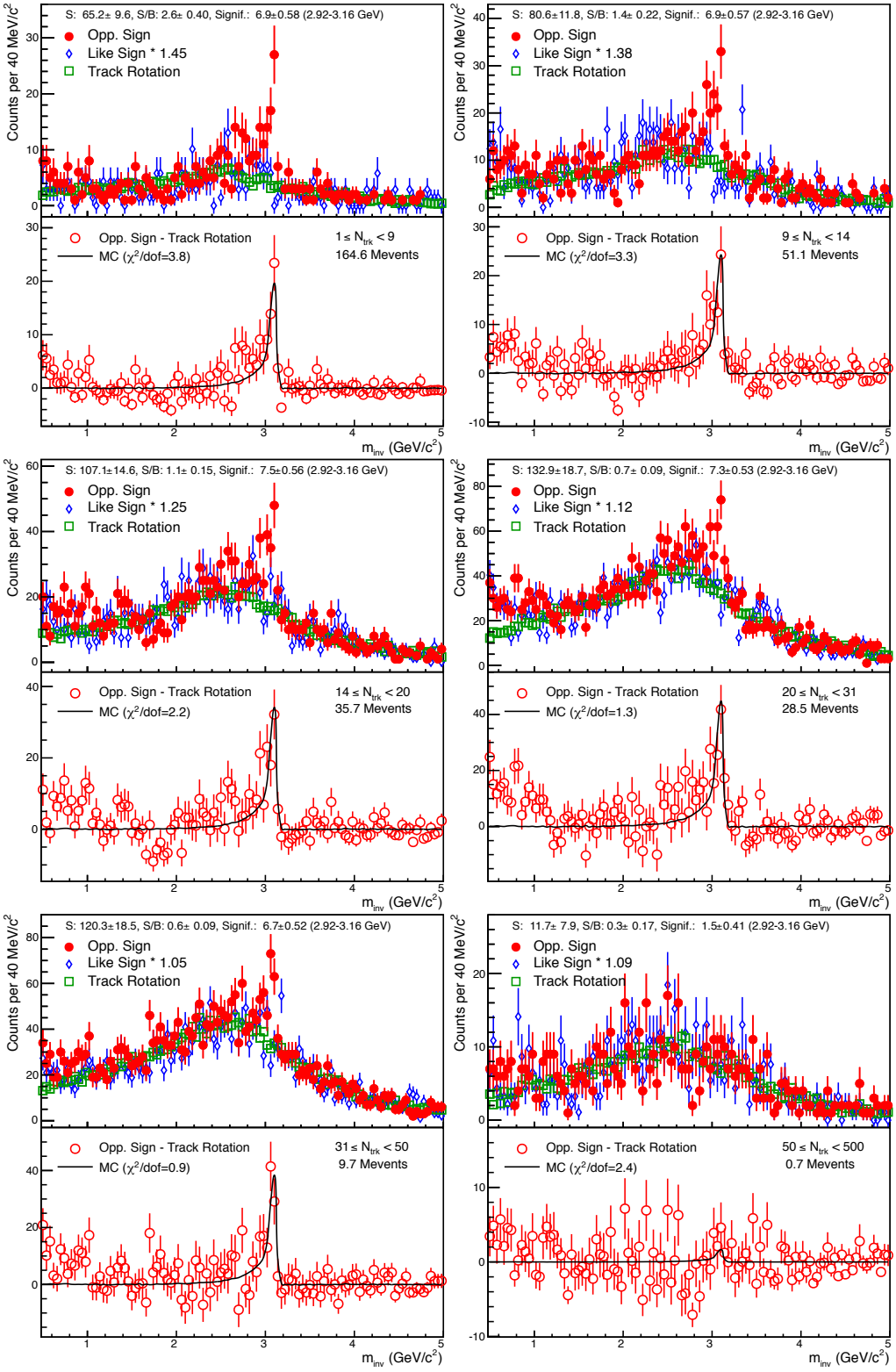

Figure 5.7: The m_{inv} spectra of the multiplicity intervals one to five. Also the overflow interval is shown on the lower right panel. See text and Fig. 5.6 for details.

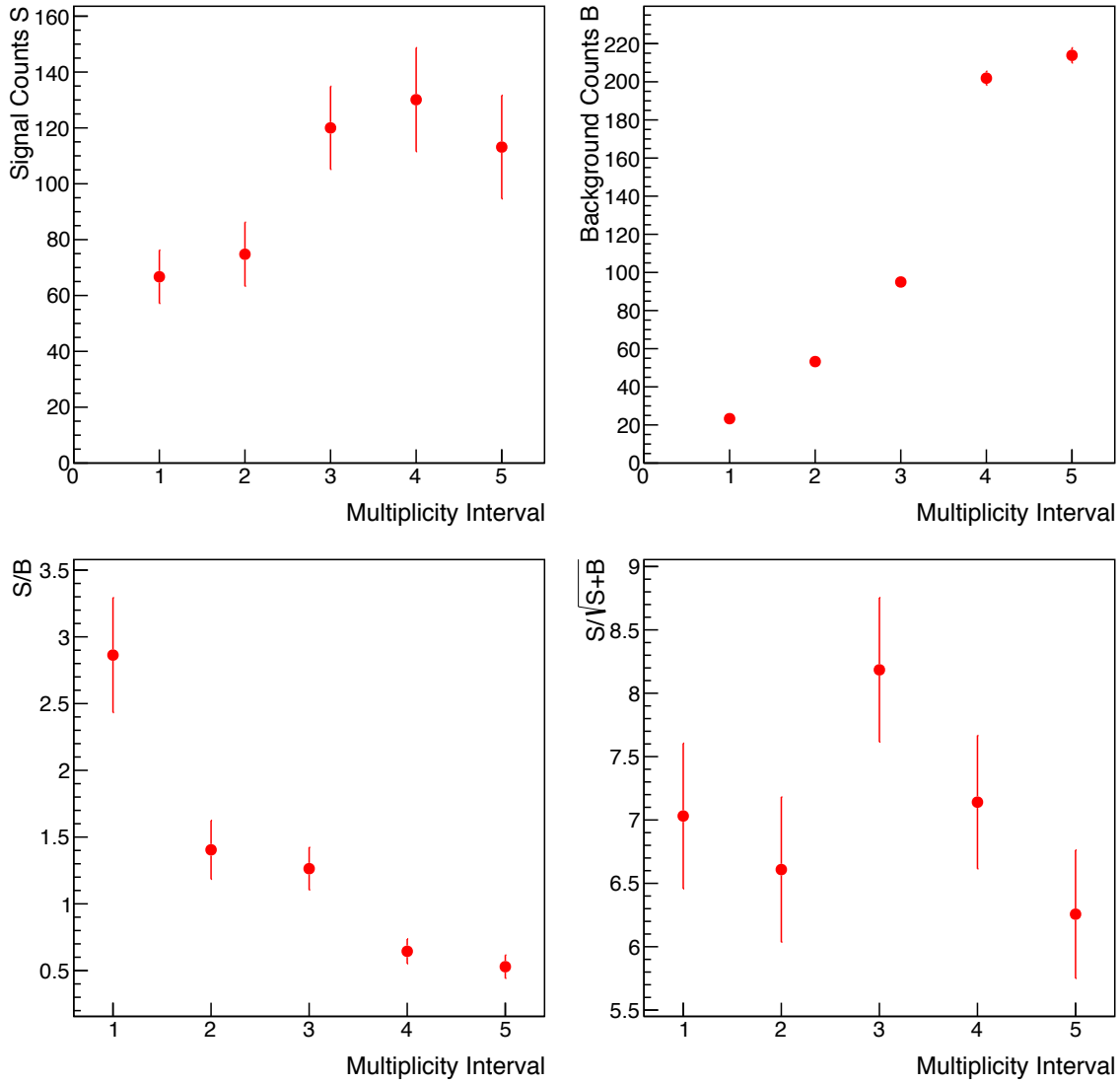

Figure 5.8: The J/ψ signal counts S (top left panel), the background counts B (top right panel), the signal-to-background ratio S/B (lower left panel) and the significance $S/\sqrt{S+B}$ (lower right panel) for all multiplicity intervals.

first and fifth multiplicity interval of the beam periods LHC10d and LHC10e a deviation from the average is found which is not within the statistical errors. This effect is covered by the systematic uncertainties, as described in Section 5.5.

The group of $\mathrm{pp}_{\mathrm{inel}}$ events also includes diffractive events in which, with a large probability, particles are only produced at strongly forward rapidities. In order to obtain the average J/ψ yield for all $\mathrm{pp}_{\mathrm{inel}}$ events, the number of events has to be corrected for the trigger efficiency ϵ_{MB}, introduced in Section 4.2.3. This mainly accounts for diffractive events not seen by the

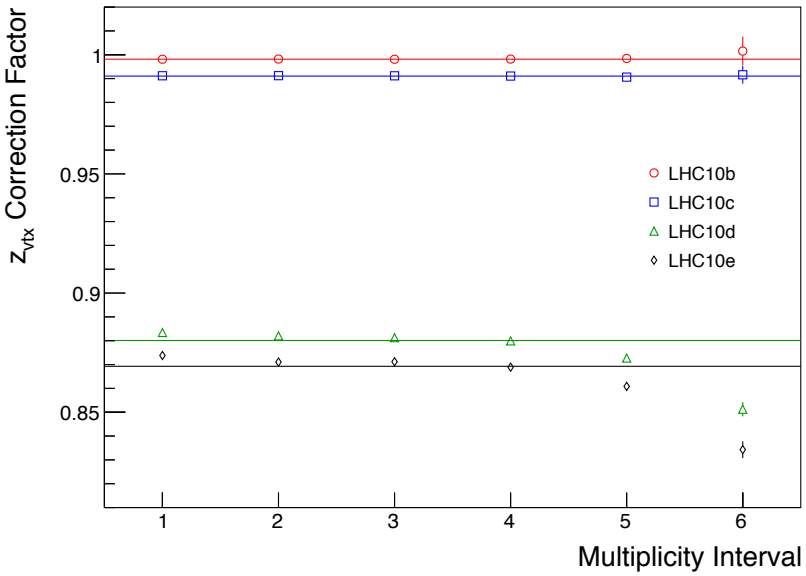

Figure 5.9: The z_{vtx} correction factors, $f_{z_{vtx}}$, determined in each mutiplicity interval for all four analyzed beam periods. The horizontal lines correspond to the factors determined for the whole beam period.

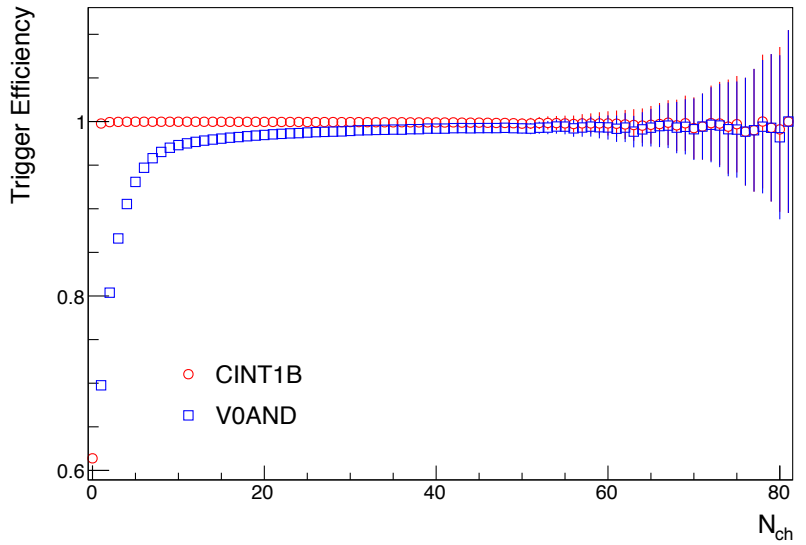

Figure 5.10: The efficiencies of the pp interaction triggers CINT1B (minimum bias) and V0AND vs. N_{ch}. This figure is based on data from [208].

trigger but belonging to $\mathrm{pp}_{\mathrm{inel}}$.

For the different multiplicity intervals, on the other hand, a correction for a trigger efficiency is not necessary. The lowest interval starts at $N_{\mathrm{trk}} = 1$. A reconstructed tracklet is only available when there are at least two SPD clusters. The MB trigger decision is based on the SPD cluster

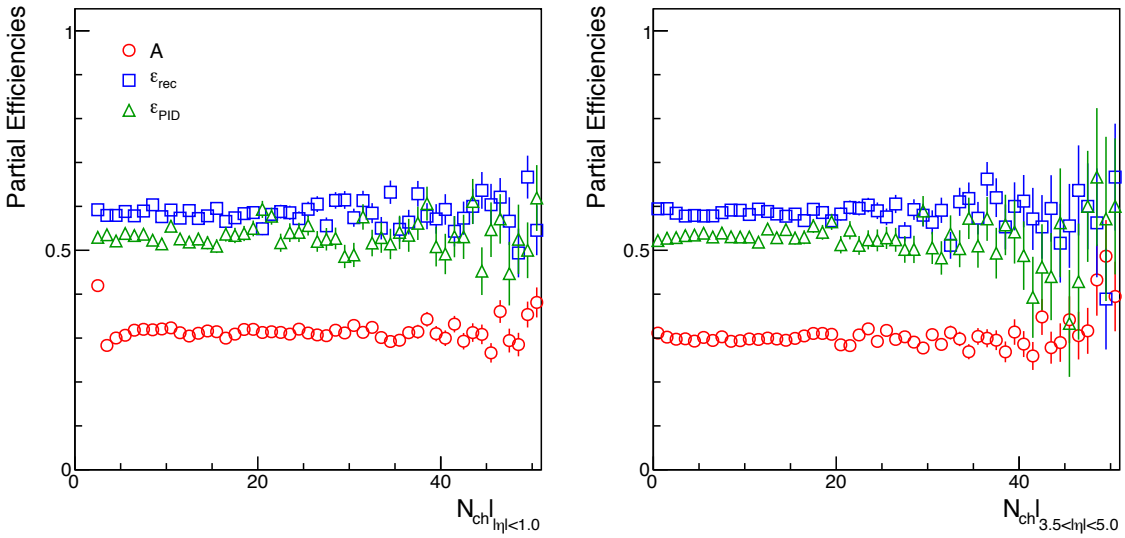

Figure 5.11: The efficiency after the different track selection steps versus the number of primary charged particles N_{ch}. Red circles correspond to the kinematical selection A, blue squares to the track reconstruction ϵ_{rec} and green triangles to the particle identification ϵ_{PID}. The only difference between the left and right panel is the η range used to count N_{ch}.

information (together with the V0 information). Thus its efficiency is above 99,8 % as soon as there is at least one charged particle within $|\eta| < 1.0$ in an event, see Fig. 5.10, in contrast to the V0AND trigger, which is only based on the V0 detectors at forward rapidities. As a result, no correction for the number of events is necessary for $N_{\mathrm{ev}}^{\mathrm{i}}$ in Eq. (5.4).

5.4.2 Acceptance and Efficiency

Even though the multiplicities reached in $\sqrt{s} = 7$ TeV pp collisions are very high compared to measurements at lower beam energies (see [209]), they are small compared to those of central Pb–Pb collisions at LHC energies (see [210]). ALICE had been designed for the extremely high charged-particle densities in Pb–Pb collisions keeping occupancies at moderate levels even in central events. So it is not expected that in the multiplicity range accessible in pp collisions any drop in a detector efficiency is found. Thus, in the ratio to the event average, the correction for acceptance and efficiency should cancel. Of course the assumption that the correction factors are constant over the investigated multiplicity range needs to be proven.

Figure 5.11 shows the efficiency of three selection steps: kinematical acceptance A as red circles, track reconstruction ϵ_{rec} as blue squares and particle identification ϵ_{PID} as green triangles (see Section 4.4) versus the primary-charged-particle multiplicity, determined from MC informations. For the left panel, the same pseudo-rapidity range of $|\eta| < 1.0$ as for the

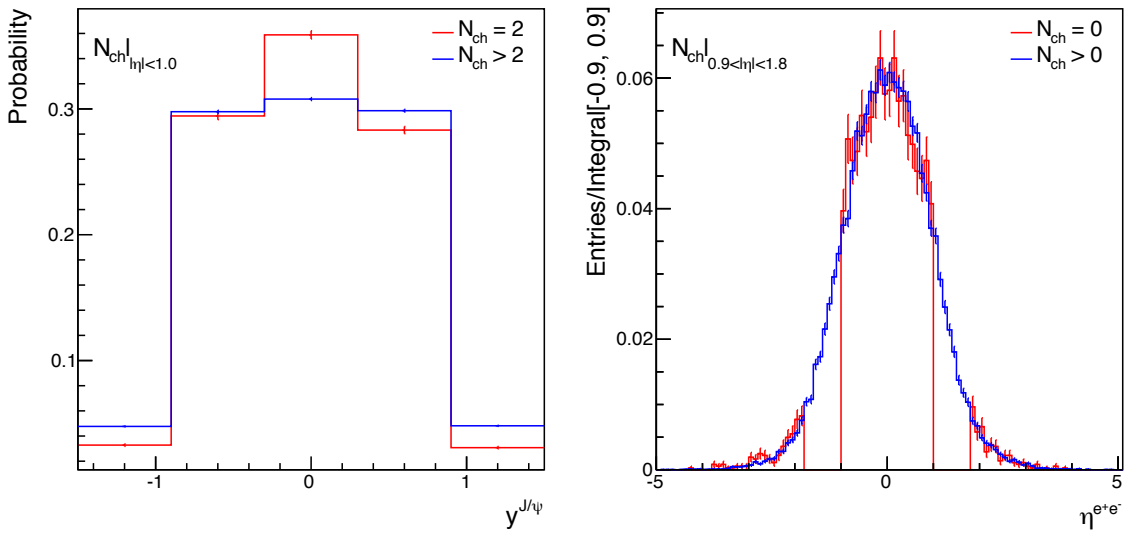

Figure 5.12: Left: the y distribution of J/ψ for events with two primary charged tracks in the range $|\eta| < 1.0$ (red) and for all events with more than two (blue). Right: the η distribution of all J/ψ daughter e^+e^- tracks for events with zero charged particle tracks in the range $0.9 < |\eta| < 1.8$ (red) and for all other events (blue).

N_{trk} determination has been used. Obviously, all selection criteria do not show any dependence on the multiplicity, only the efficiency of the kinematics cuts appears not to be flat at low multiplicities. There is no physical reason why the acceptance shoud depend on the multiplicity, the observed effect is due to a correlation of the J/ψ daughter tracks and N_{ch}.

The reference for the acceptance determination is the sum of all events with a J/ψ within $|y| < 0.9$. This is introducing a strong bias on N_{ch} in the interval $|\eta| < 1.0$, especially at low values. The lowest bin in the left panel of Fig. 5.11 is $N_{\mathrm{ch}} = 2$ which must be the J/ψ daughters. The result is a distortion of the input J/ψ y distribution for that bin what is leading to an enhanced acceptance compared to that of all other events (see the left panel of Fig. 5.12). Figure 5.12 shows on its right panel that it is not enough to choose an interval just outside of that where the measurement of the J/ψ daughter tracks is performed. In that example the range $0.9 < |\eta| < 1.8$ has been used. For $N_{\mathrm{ch}} = 0$ one J/ψ is requested in $|y| < 0.9$, but its decay products are not allowed to propagate in the range $0.9 < |\eta| < 1.8$; otherwise N_{ch} would be greater than zero. With this biased η distribution of the daughter tracks (red line in the right panel of Fig. 5.12) a larger fraction of the J/ψ in this bin will pass the kinematical selections resulting in an enhanced acceptance.

Finally, N_{ch} has to be determined in a range where the input $\eta^{e^+e^-}$ distribution (blue line in the right panel of Fig. 5.12) is depleted. Like this the expected independence of the acceptance on the event multiplicity is found: the right panel of Fig. 5.11 shows the various discussed efficiencies versus N_{ch}, determined in the range $3.5 < |\eta| < 5.0$.

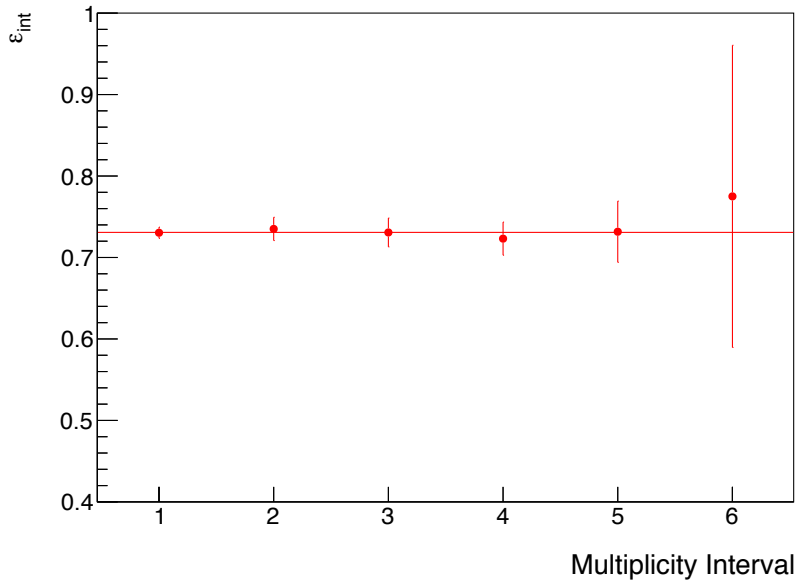

Figure 5.13: The signal fraction within the integration limits, ϵ_{int}, determined separately in each of the five multiplicity intervals. Additionally, the overflow interval is included here. The horizontal line corresponds to the total value for all multiplicities.

To ensure that one can also omit the correction for the signal fraction within the integration limits, ϵ_{int}, in the relative yields, it has to be checked that this value is indeed independent of the event multiplicity. Figure 5.13 shows the corresponding factors for the five analyzed multiplicity intervals, additionally the overflow interval is included here. The values of ϵ_{int} are determined as described in Section 4.4.4. Within the statistical errors, ϵ_{int} is compatible with the total value for all multiplicities, represented by the horizontal line.
Furthermore, the width of the J/ψ mass peak after background subtraction has been analyzed for all multiplicity intervals and for the full minimum bias data sample. For the latter a value of $\sigma = 27.1 \pm 3.4$ MeV/c^2 has been obtained by a fit of the Crystal Ball function (released ITS cluster cut). This is in a good agreement to what is quoted in [173]. Due to the limited statistics in each multiplicity interval the result for the width shows some statistical fluctuations. There is no trend with the multiplicity and the different results are consistent within the uncertainty of the fit result (see Fig. D.23 and Fig. D.24 in Appendix D). Thus, no signifacant multiplicity dependence of the width was found.

5.5 Systematic Uncertainties

Systematic uncertainties in the determination of the relative yield and the relative multiplicity have been estimated. The different contributions are discussed in the following and summarized in Table 5.3.

Contribution	Uncertainty
Signal extraction	2 % to 12 %
Acceptance input	1.5 %
Total uncertainty on relative yield	2.5 % to 12.1 %
Non-linearity in $N_{\mathrm{trk}}(N_{\mathrm{ch}})$	5 %
Syst. uncertainty in $\langle \mathrm{d}N_{\mathrm{ch}}/\mathrm{d}\eta \rangle$	+3.3 % −2.0 %
N_{trk} variations between beam periods	2 %
Total uncertainty on relative multiplicity	+6.3 % −5.7 %
Event normalization	1.5 %

Table 5.3: Contributions to the systematic uncertainties for the measurement of the relative yield and the relative multiplicity and for the event normalization.

5.5.1 Relative Multiplicity

Deviations from a linear dependence of N_{trk} on N_{ch} A linear dependence of N_{trk} on N_{ch} is assumed in Eq. (5.3). Due to detector effects and inefficiencies this is an approximation and a systematic uncertainty has to be attached to it.
In case of a perfect linear dependence the choice of the point where to fix the slope is arbitrary. Chosing $\langle \mathrm{d}N_{\mathrm{ch}}/\mathrm{d}\eta \rangle$ is expected to account best for the largest number of events and is thus used. Figure 5.14 shows for all N_{ch} bins the relative difference between the expected number of tracklets from Eq. (5.1) and the actual mean, determined as in Fig. 5.4.
Since the bin of $N_{\mathrm{ch}} = 12$ is used to calculate the slope, the value is zero by construction at this position. Except for a few statistical fluctuations, all bins above this multiplicity in all data samples are below one percent relative difference. Also no significant dependence on N_{ch} is observed in that region, proving that the assumption of a linear dependence and the choice of the slope are justified.
Below $N_{\mathrm{ch}} = 12$, on the other hand, a slight but significant dependence is found: towards lower N_{ch} the relative difference first decreases, indicating that a smaller slope parameter would be necessary for an ideal description of this region. Still, the maximal deviation here is only abount one percent. Approaching even lower N_{ch}, this behavior is reversed and the measured mean N_{trk} is increasingly underestemated by the linear approximation. The lowest two bins (above $N_{\mathrm{ch}} = 0$ which is zero by construction) are above the expectation by 4 % for $N_{\mathrm{ch}} = 2$ and 20 % for $N_{\mathrm{ch}} = 1$, on average over the four beam periods. Because a good fraction of events with $N_{\mathrm{ch}} = 1$ lead to zero reconstructed tracklets and are thus not analyzed

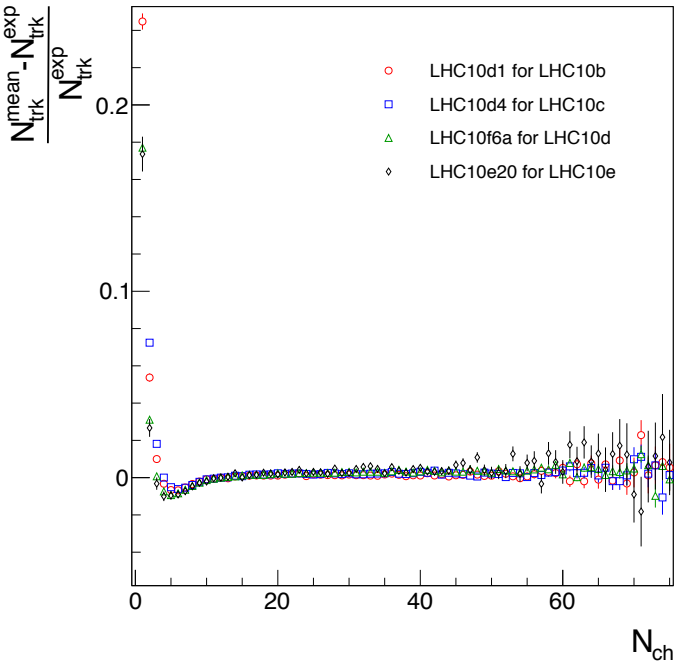

Figure 5.14: The relative difference between the actual mean N_{trk} and the expected one due to the linear assumption, for each N_{ch} bin and for all beam periods. Note that here, the value of N_{trk} ($\langle N_{\mathrm{ch}} \rangle$), determined for each beam period separately has been used. Using the average of all beam periods would mix the systematic uncertainty from possible non-linearities with a systematic error from remaining differences between the beam periods.

anyways and because the lowest multiplicity interval extends from one to (including) eight tracklets, its maximum deviation from the assumed linear dependence is estimated to be less than 4 %.

The extracted relative-multiplicity distribution of Fig. 5.5 is compared to the one published in [207], which had been extracted from the raw distributions using an unfolding procedure described in [184]. The agreement of the two distributions is very good, but only after an additional scaling by 4 % along the x-axis is done. This is shown in Fig. 5.15, upper left panel. The binning of the two distributions is different, therefore the distribution of Fig. 5.5 had been interpolated. Both spectra are normalized to their integral. Remaining systematic effects can be seen in the ratio on the lower left panel. First of all, a wavy structure of the unfolded spectrum can be seen which is due to the unfolding procedure itself, producing a strong correlation between neighboring bins. Furthermore, the spectrum reconstructed for this analysis lies above the other spectrum for almost all multiplicities, only in the lowest bins the unfolded spectrum is above the other. This is likely to be an effect of the different trigger scenarios for the two distributions—while the one of [207] uses all inelastic events with at least

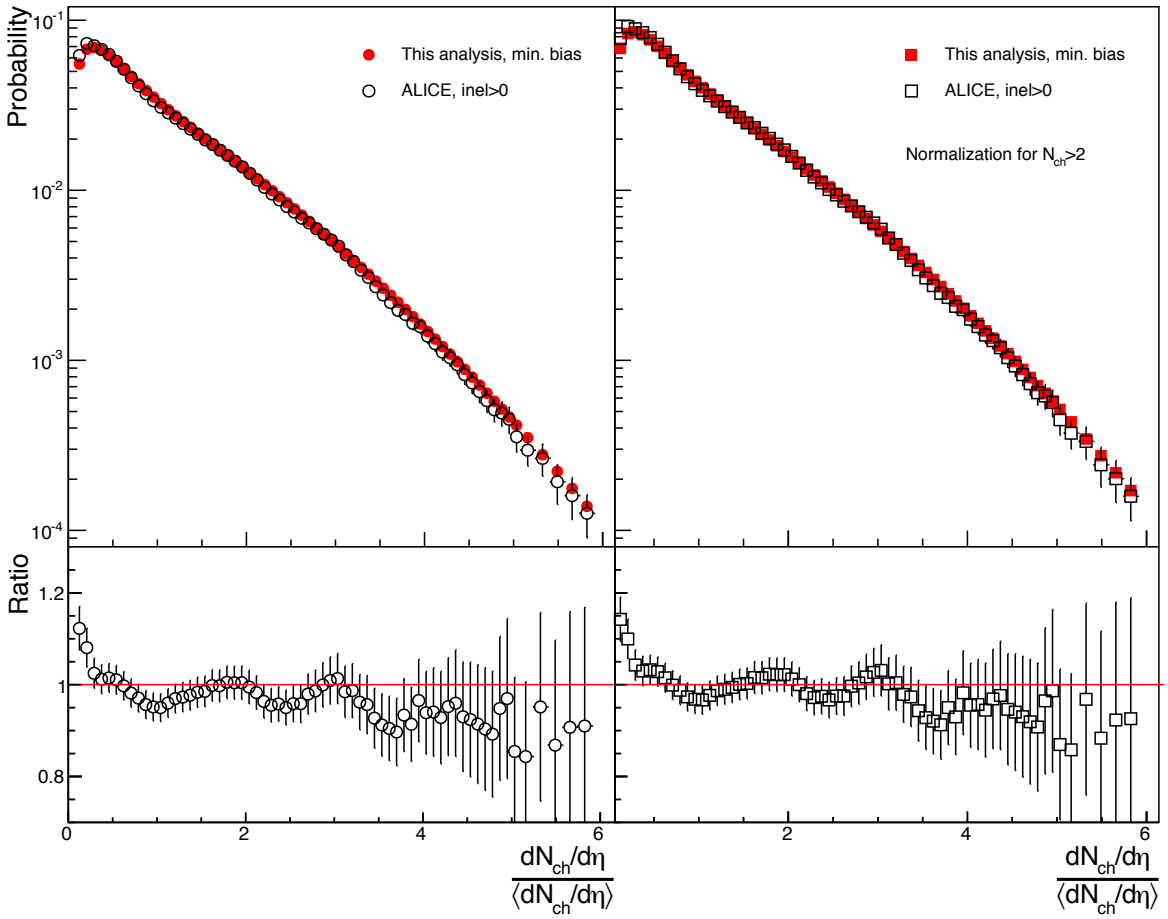

Figure 5.15: Upper left: comparison of the relative charged-particle multiplicity distribution measured in this analysis (red dots) with the one in [207] (black circles), after scaling by 4 % on the x-axis. Both spectra are measured in a range of $|\eta| < 1.0$. The error bars of the latter distribution are the quadratic sum of statistical and systematic untertainties while those of the former are only statistical and smaller than the markers. Lower left: the ratio of both distributions. The two right panels show the same spectra, only with a normalization of the area in the range of $N_{\mathrm{ch}} > 2$.

one charged particle, inel$> 0_{|\eta|<1.0}$, this analysis applies the minimum bias interaction trigger. Especially at low multiplicities this might be relevant. Therefore, for the right panel of Fig. 5.15 both distributions are normalized for $N_{\mathrm{ch}} > 2$. The error bars shown for the ratio correspond to the quadratic sum of statistic and systematic errors from [207]. Due to the unfolding method, the errors of neighboring bins are strongly correlated. Within these errors both distributions are in good agreement.

Thus, the linear approximation of N_{trk} (N_{ch}) is justified, apart from $N_{\mathrm{ch}} = 1$. The slope of the straight line can be fixed at any N_{ch} without introducing a bias larger than 4 %. The resulting multiplicity distribution differs from the published one [207] by 4 %. By using a slope parameter

increased by 4 % all points in Fig. 5.14 are shifted down by this same factor. Then, all values are located within ±5 %. This number is estimated to be the systematic uncertainty on the linear approximation of the dependence of N_{trk} on N_{ch}.

Differences between beam periods The remaining differences of the multiplicity distributions after the correction for the number of tracklets between the analyzed beam periods are estimated to be about 2 %. This value is extracted from the maximal deviations of $\overline{N_{\mathrm{trk}}}$ and $N_{\mathrm{trk}}\left(\langle N_{\mathrm{ch}}\rangle\right)$, listed in Table 5.2, and taken as the systematic uncertainty in the determination of these quantities.

Error propagation The measurement of $\langle \mathrm{d}N_{\mathrm{ch}}/\mathrm{d}\eta\rangle$ is attached with a systematic error of $^{+3.3\,\%}_{-2.0\,\%}$ [207]. This error is included and added to the other contributions quadratically.

Pile-up events Pile-up events that have not been identified with the dedicated rejection mechanism (see Section 4.5) could introduce another bias on the multiplicity. In this mechanism, the minimal distance of a second vertex to be rejected is 0.8 cm. At least three tracklets associated to this second vertex are required. Thus, either events with less than three tracklets are merged with the main event or any second event with a distance of less than 0.8 cm to the main one. The total pile-up rate in the event sample analyzed here is 4 %, the rejection mechanism removes 48 % of those [192]. Out of all pile-up events, those with vertices closer than 0.8 cm account to about 7 % [192]. Thus, even though they can have a strongly biased reconstructed multiplicity, such events occur only with a probability of about 0.3 %. At the highest multiplicities this might still have an effect due to the steeply falling distribution. An estimation [211] showed, that the effect of pile-up on the mulitplicity can be neglected up to approx. $N_{\mathrm{trk}} = 50$. Therefore, as discussed above, the upper edge of the highest multiplicity interval, number five, is limited to that value. A look at the invariant-mass spectrum from all events with higher multiplicities, Fig. 5.7, shows that with this upper limit no substantial signal is lost.
The remaining 45 % of all undetected pile-up events, i. e. 1.8 % of all events, have a vertex displaced more than 0.8 cm from the main one. These most likely contain less than three tracklets and thus have only a small impact on the measured multiplicity. Furthermore, SPD tracklets are only created out of hit combinations with a $\Delta\theta < 25$ mrad using the reconstructed vertex as the origin [184]. Tracklets from displaced vertices are likely to be removed by this cut.

5.5.2 Relative Yield

Signal extraction In the determination of the relative yields the largest possible source of a systematic bias is the choice of the background estimator in the signal extraction procedure. As

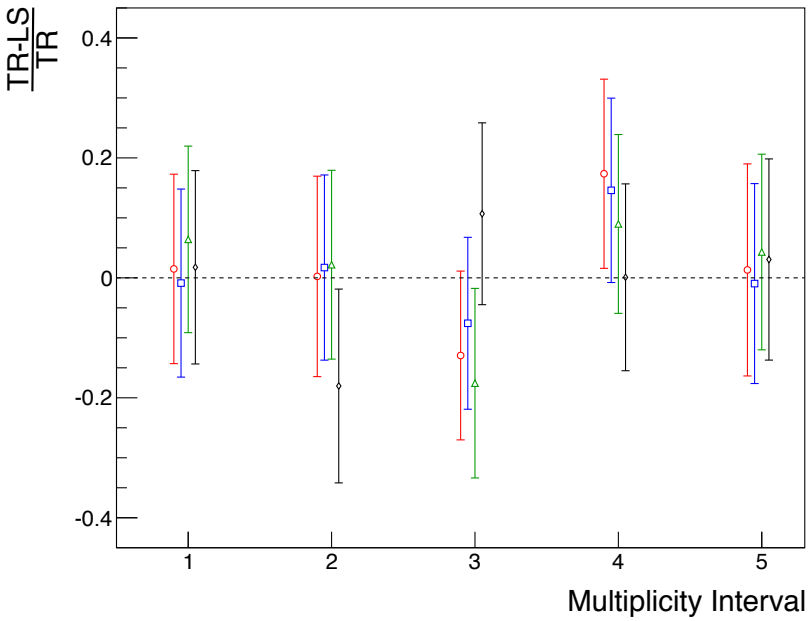

Figure 5.16: The difference of the relative yield in each interval, using track rotation (TR) and like sign (LS) as background estimators. The difference is normalized to the result for track rotation, the error bars correspond to the statistical errors from this method. The four different marker and color codes represent the output of four different runs of the data analysis, including the computation of the track-rotation mass spectra.

discussed above, two different methods have been studied, out of which the track rotation had been defined as the default method. For the inclusive cross section, this uncertainty has already been determined in [173] to be about 8.5 %. But unlike in [173], relative values are calculated here. Nominator and denominator are correlated since the former is a subset of the latter. The systematic uncertainty of the signal extraction procedure is thus estimated separately in each multiplicity interval, as the difference of the relative yields using the track-rotation method and the like-sign method.

Track rotations are calculated with several repetitions for each e^+e^- candidate pair leading to a small statistical error compared to that of the like-sign spectrum. But still, since random numbers are used for the choice of the rotation angle, small statistical fluctuations of the background estimation in the signal region can lead to a higher or lower number of signal counts after subtraction, even when two times the exact same data set is analyzed. Thus, the differences of the relative yields are calculated for several different outputs of the analysis train. The systematic uncertainty in each multiplicity interval is then estimated as the average difference of the relative yields using TR and LS to for the background subtraction in each of the outputs. This is shown in Fig. 5.16, normalized to the results using the TR background estimator. The error bars correspond to the statistical errors of the relative yields using track

rotation, which are about 15 % in each interval. In case of the track-rotation method, the statistical uncertainties of the extracted signals are dominated by those of the opposite-sign mass spectrum. When only taking the statistical errors of the background estimators into account, statisticly significant systematic differences are found between the two methods. That is not the case when the total errors from Fig. 5.16 are taken into account (using the tests described in [212]). The results are 2 % in the first and fifth interval, and 5 %, 12 % and 10 % in the intervals number two, three and four, respectively.

As stated earlier, by releasing the ITS cluster requirement from SPDany to ITSany(4), the agreement between the track-rotation and like-sign methods is improved from 8.5 % to below 2.5 % for the full sample. In some of the the multiplicity intervals, on the other hand, the differences are larger. A possible interpretation is the following: in the lowest intervals, especially the first and, to some extend, also the second, there is only very little background contribution, so differences between the estimators do not have a strong impact on the results. In the intermediate intervals, the differences between the track-rotation and like-sign background become maximal. In the highest interval, the signal is placed on a—compared to the lowest intervals—much higher background spectrum. Similar as when going from SPDany to ISTany(4) in the full sample, by the increase of the statistical sample of the background, its description is improved, reflected in a small systematic uncertainty.

Acceptance input A second source of a systematic uncertainty is the possibility that the J/ψ p_{t} distributions might not be identical in events with low or high multiplicity. If this is the case, then the $A \times \epsilon$ correction is calculated with a wrong p_{t} distribution. At the current stage of the analysis it is not known whether or not there is any dependence of the J/ψ p_{t} distribution on the multiplicity, within the currently available statistics this measurement is not yet possible.
A systematic uncertainty is assigned to this possible bias, introduced by the assumption that the $A \times \epsilon$ corrections cancel out in the ratio of the relative yields. In [173] a similar estimation had already been performed for the $A \times \epsilon$ correction itself. Here, the $\langle p_{\mathrm{t}} \rangle$ of the simulated spectrum had been varied from approximately 2.6 to 3.2 GeV/c, which is a variation of 10 % around the value of the spectrum used for the efficiency determination. It is assumed that this range covers possible modifications of the spectrum, if there are any. By this, a systematic error of 1.5 % had been obtained (see [173]).

Vertex position As already shown in Fig. 5.9 and described in Section 5.4.1, an overall good agreement of the z_{vtx} correction factors determined in each multiplicity interval separately and averaged over all multiplicities has been found. Only in the first and fifth multiplicity interval of the beam periods LHC10d and LHC10e a significant deviation from the average is observed. Still, these deviations are below one percent. Furthermore, such a good agreement is

only visible after the correction of the number of tracklets. For the raw number of tracklets the z_{vtx} distributions of the different multiplicity intervals are distorted by the vertex-dependent SPD acceptance, leading to systematic z-dependent shifts of events to adjacent multiplicity intervals. From general considerations it is not expected that the vertex position should show any correlation with the event multiplicity. Only a slight improvement of the resolution could appear at higher multiplicities, leading to a more narrow distribution and a correction factor closer to unity. Apparently this is not seen in Fig. 5.9. Most likely this effect would only affect events with a very low number of tracks, not visible in the current intervals. It is thus assumed that the remaining deviations are due to small imperfections of the $N_{\mathrm{trk}}^{\mathrm{raw}}$ correction procedure. Therefore, and given the small magnitude of that deviation, this effect is neglected. Such possible imperfections of the $N_{\mathrm{trk}}^{\mathrm{raw}}$ correction procedure and the impact on the determination of the relative multiplicity are covered with separate systematic uncertainties, see above.

Pile-up events For the corresponding analysis of the multiplicity-dependence of J/ψ production in the $\mu^+\mu^-$ decay channel for [192] a conservative estimation of a systematic uncertainty on the relative yield due to pile-up events has been done. Due to the following reasons for this analysis no such systematic uncertainty is given. First, the analysis in $\mu^+\mu^-$ is based only on the beam period LHC10e which is the one with the highest pile-up rate. In this analysis only approximately one third of the total events are belonging to this period. The second reason is that, unlike the measurement of muons with the muon spectrometer, a cut on the DCA of each track to the primary vertex is possible and removes most of the tracks that might come from a second vertex.

5.5.3 Event Normalization

A further uncertainty from the event normalization to $\mathrm{pp}_{\mathrm{inel}}$ has to be taken into account. The minimum bias trigger efficiency had been determined in MC simulations [185], the systematic error of this value is estimated to be 1.5 %. This applies to all multiplicity intervals commonly and is thus given as a separate number.

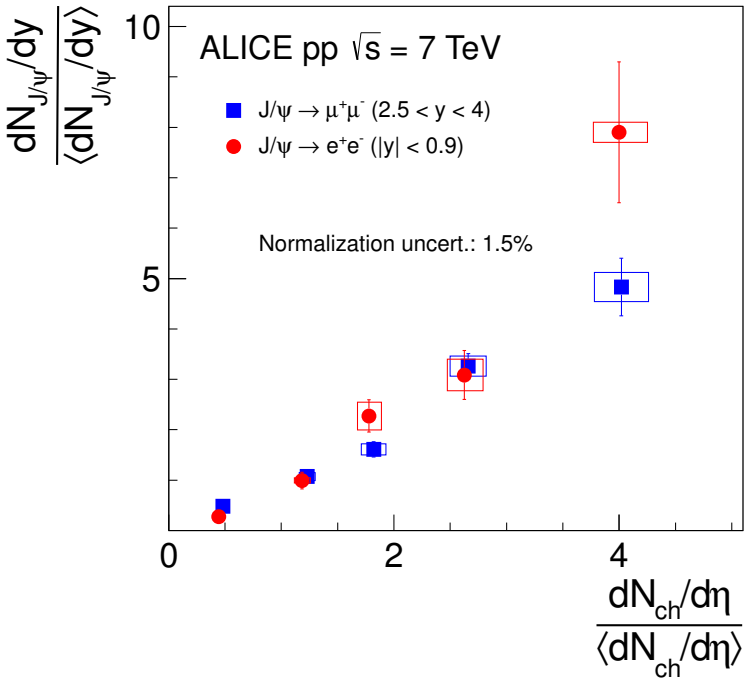

Figure 5.17: The relative J/ψ yield as a function of the relative charged-particle multiplicity in $\sqrt{s} = 7$ TeV minimum bias pp collisions. J/ψ are measured within $|y| < 0.9$ (J/$\psi \to e^+e^-$, red dots) and at $2.5 < y < 4$ (J/$\psi \to \mu^+\mu^-$, blue squares) while the multiplicity is estimated within $|\eta| < 1.0$. The error bars correspond to the statistical error of the measurement in each bin, the boxes show the systematic uncertainty for the relative multiplicity as well as for the relative yield. A global systematic uncertainty of the luminosity measurement of 1.5 % affects all points in the same way and is thus given as a separate number. The data in J/$\psi \to e^+e^-$ shown here are the results of this analysis, the figure is taken from [192].

5.6 Charged-Particle Multiplicity Dependence of J/ψ Production

Figure 5.17 shows the relative J/ψ yield, $\mathrm{d}N_{\mathrm{J}/\psi}/\mathrm{d}y / \langle \mathrm{d}N_{\mathrm{J}/\psi}/\mathrm{d}y \rangle$ Eq. (5.5), as a function of the relative charged-particle multiplicity, $\mathrm{d}N_{\mathrm{ch}}/\mathrm{d}\eta / \langle \mathrm{d}N_{\mathrm{ch}}/\mathrm{d}\eta \rangle$ Eq. (5.3). The results of this analysis (J/$\psi \to e^+e^-$, $|y| < 0.9$, red dots) are shown together with the results of [211] (J/$\psi \to \mu^+\mu^-$, $2.5 < y < 4$, blue squares) as submitted to [192]. The error bars correspond to the statistical error of the measurement in each bin, the boxes show the systematic uncertainty for the relative multiplicity as well as for the relative yield, as discussed in Section 5.5. A global systematic uncertainty of the luminosity measurement of 1.5 % affects all points in the same way and is thus given as a separate number.

A monotonic increase of the relative J/ψ yield with the relative multiplicity is found in both rapidity ranges. At multiplicities of about 4 times the average in minimum bias collisions, the J/ψ yield is found be be approximately a factor 8 higher with respect to the average in MB collisions. For the analysis in the $\mu^+\mu^-$ decay channel [211, 192] an approximate factor of 5 is found. Within the errors, the same correlation of J/ψ yield and multiplicity is observed in both rapidity regions.

A possible interpretation of the observed correlation is that the production of J/ψ, or c$\bar{\text{c}}$ in general, is always accompained by an increased production of charged particles. Yet, it is questionable if a correlation could extend over such a broad range of multiplicities and rapidities. The results from NA27 suggest that also open charm mesons are created predominantly in high multiplicity events (see Section 2.3.3). However, this observation might be due to the absence of charm production in diffractive events and not be the same effect seen here.
Another interpretation is that such a multiplicity dependence is a more general mechanism that affects not only J/ψ production but all hard probes in the same way. Multiple hard partonic interactions happen with probabilities which are strongly increasing with the energy [213, 77]. That DPS (double-parton scattering, see Section 2.3.3) is relevant for J/ψ production at LHC energies has already been indicated by a measurement of LHCb [77]. The transverse structure of the proton, together with the concept of impact parameters in pp collisions [213] could be the reason for a strong correlation between hard (J/ψ yield) and soft (event multiplicity) components of MPI. The more central the pp collision, the larger is the overlap between the colliding nucleons. Also the density of the proton is largest at its center, leading to increased probabilities for scattering processes for head-on collisions than for peripheral collisions. Finally, as argued in [214], partons with $x > 10^{-4}$ are predominantly localized in the central part of the nucleon. Hard processes might therefore be mainly found in central collisions which also feature stronger hadronic activities. Peripheral collisions are on the other hand expected to constitute the dominant part of the inelastic cross section [214]. In [215] the results shown in Fig. 5.17 are interpreted with this concept. Therein, the multiplicity of a given hard process, M, is investigated as a function of a specific trigger, e. g. the overall hardon multiplicity, and compared to the minimum bias average: $R = M_{\text{trigger}}/M_{\text{MB}}$. R is equivalent to $\mathrm{d}N_{\mathrm{J}/\psi}/\mathrm{d}y/\left\langle \mathrm{d}N_{\mathrm{J}/\psi}/\mathrm{d}y \right\rangle$ in this analysis. The impact parameter distribution of pp events with a hard gluon-gluon process is given by the geometric probability for two gluons to collide at the same point [214]:

$$P_2(x_1, x_2, b|Q^2) = \int d^2\rho_1 \int d^2\rho_2 \, \delta^{(2)}(\boldsymbol{b} - \boldsymbol{\rho}_1 + \boldsymbol{\rho}_2) \times F_{\text{g}}(x_1, \rho_1|Q^2) \, F_{\text{g}}(x_2, \rho_2|Q^2), \qquad (5.6)$$

where $b = |\boldsymbol{b}|$ is the impact parameter and $\rho_{1,2} = |\boldsymbol{\rho_{1,2}}|$ are the transverse distances of the two gluons from their proton's centers. $F_{\text{g}}(x_{1,2}, \rho_{1,2}|Q^2)$ are the transverse spacial gluon distributions. The maximum value of R is reached for most central collisions where $b \sim 0$.

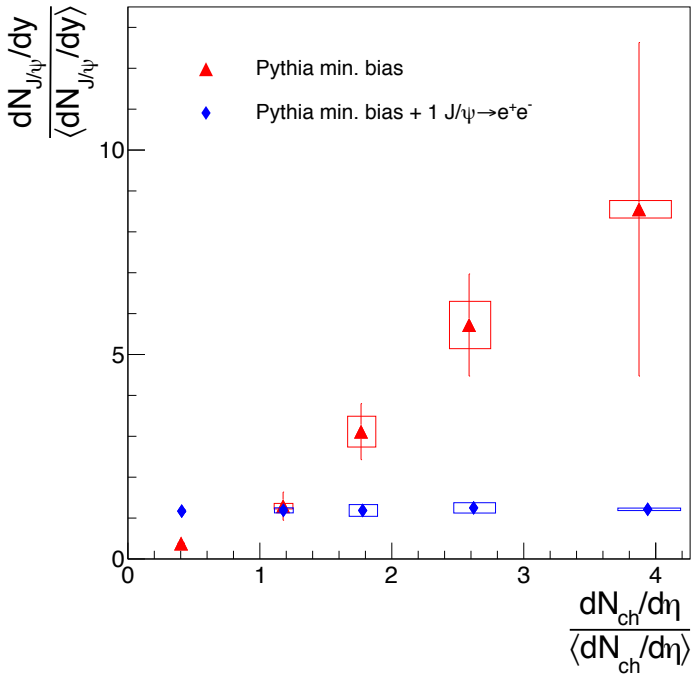

Figure 5.18: The relative J/ψ yield as a function of the relative charged-particle multiplicity in Pythia minimum bias $\sqrt{s} = 7$ TeV pp collisions (red triangles) and in the Pythia sample enriched with one J/$\psi \to e^+e^-$ per event (blue diamonds).

In [215] this has been estimated to be:

$$R = P_2(0)\sigma_{\mathrm{pp,MB}} \approx 4.5. \tag{5.7}$$

Taking the different uncertainties of the measurement in J/$\psi \to e^+e^-$ at the highest multiplicities into account this value might still be compatible with the experimental results shown here. Higher values of R could not be explained only by an increased impact parameter and, according to [215], would in addition require the presence of fluctuations in the transverse gluon density. This idea has been proposed earlier [216] and used to explain the observation of long-range, near-side angular correlations measured by CMS in $\sqrt{s} = 7$ TeV pp collisions [217, 218]. This *ridge* phenomenon, previously known from heavy-ion collisions [219], raised some attention after its observation in pp. More precise predictions will help to draw stronger conclusions.

The decay of b-hardons into J/$\psi + X$ contributes with its products to the total multiplicity and might therefore introduce a bias towards higher values. This might be enforced if the b-hardon production itself depends on the event multiplicity. However, a fraction of about 10 to 15 % (see Section 2.3.4) for the full minimum bias sample could only account for a small part of the observed effect.

A comparison to different event generators might also help in the understanding of the

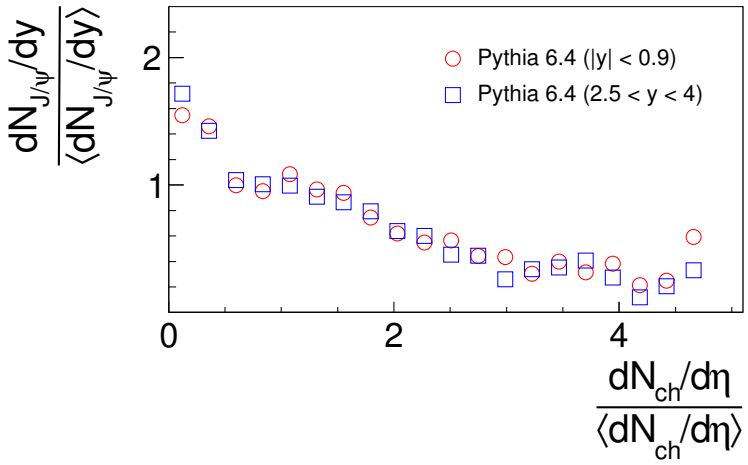

Figure 5.19: The relative J/ψ yield as a function of the relative charged-particle multiplicity as calculated with Pythia 6.4 (Perugia 2011 tune [182]) for hard scatterings both at forward (blue squares) and at mid-rapidity (red circles). The picture is taken from [192].

observed phemonenon. The most simple approach is the analysis of the minimum bias Pythia 6.421 pp event samples listed in Table 4.2 (Perugia-0 tune) just with the same analysis methods used for the collisions data. The result is represented by red triangles in Fig. 5.18. Here, a very similar trend is seen as in data.
In the preparation of [192] a more detailed study has been performed which identified mainly two two sources for J/ψ in the framework of the Pythia event generator. These are on the one hand $2 \rightarrow 2$ hard partonic scatterings and the cluster formation process on the other. The latter is the result of a parton shower evolution with an invariant mass which is too low for the standard Lund string fragmentation procedure [220]. It therefore does not correspond to a well defined hard scattering process. It turned out that in the Perugia-0 tune the dominant part of the produced J/ψ are products of the cluster formation. The results for J/ψ coming only from $2 \rightarrow 2$ hard partonic scatterings in Pythia are shown in Fig. 5.19 [192]. A decrease of the J/ψ yield with the event multiplicity is found in contradiction to the data.

The blue diamonds in Fig. 5.18 are shown as a cross-check. They correspond to the result of the analysis of the MC sample LHC10f7a, i. e. again Pythia minimum bias pp events but enriched with one additional J/$\psi \rightarrow e^+e^-$. In this sample, the J/ψ yield from the underlying MB event is negligible, the total yield should thus be independent of the charged-particle multiplicity. Indeed, for this event sample no dependence of the relative J/ψ yield on the charged-particle multiplicity is found, see Fig. 5.18. This flat result also shows that a possible autocorrelation of the J/ψ daughter tracks with the measured multiplicity does not play a significant role.

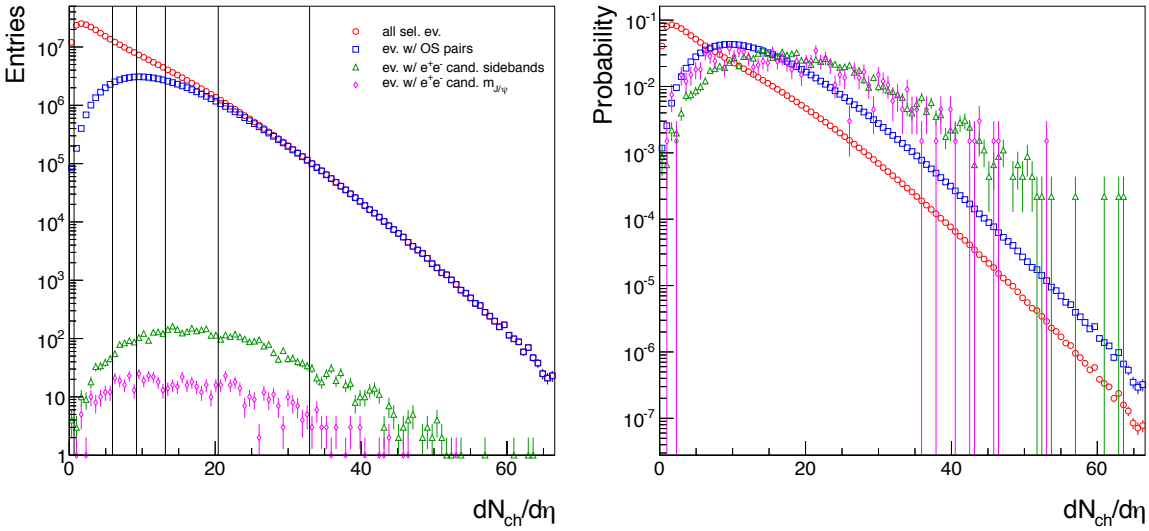

Figure 5.20: The multiplicity distribution $\mathrm{d}N_{\mathrm{ch}}/\mathrm{d}\eta$ for different event classes. Red circles refer to all selected events, blue squares correspond to all events that contain at least one opposite-sign track pair passing the track cuts. The multiplicity distribution of all events that are containing at least one $\mathrm{e}^+\mathrm{e}^-$ candidate pair with an invariant mass in the range [0.25, 2.92] GeV/c^2 or [3.16, 5.0] GeV/c^2 is shown with green triangles. Magenta diamonds correspond to all events with at least one $\mathrm{e}^+\mathrm{e}^-$ pair in the J/ψ mass range [2.92, 3.16] GeV/c^2. The left panel shows the distributions according to the number of entries, the right panel shows the same distributions scaled to their integrals. The vertical lines on the left panel indicate the boundaries of the multiplicity intervals.

A different view on the same effect observed in Fig. 5.17 can be seen in Fig. 5.20 which is showing the multiplicity distribution $\mathrm{d}N_{\mathrm{ch}}/\mathrm{d}\eta$ for different event classes. While the red circles correspond to the min. bias distribution shown in Fig. 5.5, the other spectra are for different selections. Blue squares correspond to all events that contain at least one opposite-sign track pair passing the track cuts. The multiplicity distribution of all events that are containing at least one $\mathrm{e}^+\mathrm{e}^-$ candidate pair with an invariant mass in the range [0.25, 2.92] GeV/c^2 or [3.16, 5.0] GeV/c^2 is shown with green triangles. Magenta diamonds correspond to all events with at least one $\mathrm{e}^+\mathrm{e}^-$ pair in the J/ψ mass range [2.92, 3.16] GeV/c^2.
With an increasing number of $\mathrm{d}N_{\mathrm{ch}}/\mathrm{d}\eta$ the probability to find a reconstructed, oppositely charged track pair approaches one. Therefore the blue squares are on top of the red circles at high $\mathrm{d}N_{\mathrm{ch}}/\mathrm{d}\eta$. The other two distributions refer to all events with $\mathrm{e}^+\mathrm{e}^-$ candidate pairs in outside (green triangles) and inside (magenta diamonds) of the J/ψ mass region. Both seem to have a similar shape at high multiplicities. It is different from that of the other two distributions, as it is expected from the observation that the J/ψ yield increases with the multiplicity. The observation that both events with $\mathrm{e}^+\mathrm{e}^-$ candidates inside the J/ψ mass region as well as in the bands around it have a similar shape might be related to the composition of

the background spectrum in this mass range. Large parts are expected to have charm hadron decays as an origin which could be affected by a similar multiplicity dependence. More detailed conclusions can not be drawn from this representation, since the J/ψ mass range contains about 40 % background which is included in the distribution of the magenta diamonds here. Therefore also a comparison to the similar analysis by NA27, see Section 2.3.3, is not possible.

5.7 Outlook

The observed approximately linear increase of the J/ψ yield with the charged-particle multiplicity could either indicate that the process of J/ψ production is accompained by the production of numerous charged particles or that multi-parton interactions play a significant role in hard scattering processes. These scenarios could be tested with similar analyses of other observables. If open charm mesons show the same trend as the J/ψ, the correlation must be either due to the basic production of the heavy quark pair or due to MPI which affect soft and hard components in the same way. The analysis of the multiplicity-dependence of D meson production is currently ongoing at ALICE, first results are expected soon. If other hard probes, such as particle jets, exhibit the same effect it must be of such a more general nature. By repeating this analysis for the Υ meson the slope of its possible enhancement towards high multiplicities could be compared to that of the J/ψ to find out if the higher b quark mass has any implications. In [215] it is argued that the enhancement observed here could be explained with the concept of impact parameters in pp collisions. Any higher values than observed would require the presence of fluctuations of the transverse gluon density. Therefore a higher reach in multiplicity would be of great value already for the J/ψ measurement.
Further analyses with other models such as Cascade [221] or Pythia 8 [222]—especially with respect to their specific implementations of MPI—might shed more light into the origin of the observed effect.
Furthermore, the data presented here could be extrapolated to higher multiplicities and compared to Pb–Pb results.

Another subject could be investigated with a combination of this analysis with that of open charm mesons. As briefly introduced in Section 2.4.1, collective effects previously known only from heavy-ion collisions may play a role at the highest multiplicities reached in $\sqrt{s} = 7$ TeV pp. The authors of [94] expect a decreased J/ψ survival probability with increasing $\mathrm{d}N_{\mathrm{ch}}/\mathrm{d}\eta$. Such an observation would have consequences on J/ψ cross sections in pp and also on pp collisions used as a baseline for heavy-ion collisions. The ratio of the J/ψ to D meson yield vs. multiplicity could be directly compared to the prediction shown in Fig. 2.19 and unveil whether or not collective effects can already occur in pp collisions.

Chapter 6

Summary

Quarkonia are very promising probes to study the quark-gluon plasma. The essential baseline for measurements in heavy-ion collisions is high-precision data from proton-proton interactions. However, the basic mechanisms of quarkonium hadroproduction are still being debated. The most common models, the Color-Singlet Model, the non-relativistic QCD approach and the Color-Evaporation Model, are able to describe most of the available cross-section data, despite of their conceptual differences. New measures, such as the polarization, and data at a new energy regime are crucial to test the competing models. Another issue is an eventual interplay between the production process of a quarkonium state and the surrounding pp event. Current Monte Carlo event generators treat the hard scattering independently from the rest of the so-called underlying event. The investigation of possible correlations with the pp event might be very valuable for a detailed understanding of the production processes.

ALICE ist the dedicated heavy-ion experiment at the LHC. Its design has been optimized for high-precision measurements in very high track densities and down to low transverse momenta. ALICE is composed of various different detectors at forward and at central rapidities. The most important detectors for this study are the Inner Tracking System and the Time Projection Chamber, allowing to reconstruct and identify electron candidate tracks within $\eta < 0.9$. The Transition Radiation Detector has not been utilized at this stage of the analysis; however, it will strongly improve the particle identification and provide a dedicated trigger in the upcoming beam periods.

In the first part of this work the inclusive cross section for J/ψ production in inelastic $\sqrt{s} = 7$ TeV pp collisions has been determined within $|y| < 0.9$ and in the decay channel J/$\psi \rightarrow e^+e^-$. The result for the integrated value is: $\sigma_{J/\psi}(|y| < 0.9) = 10.7 \pm 0.8$ (stat.) $\pm$ 1.4 (syst.) $\pm$ 0.4 (lumi.) μb. Together with the ALICE measurement in the $\mu^+\mu^-$ decay channel at forward rapidities and data from other experiments this result fills the gap at mid-rapidity for a comprehensive measurement of the J/ψ rapidity distribution. Predictions of the Color-

Singlet Model and the Color-Evaporation Model are in a good agreement with the experimental data; however, the models are attached with large systematic uncertainties and only include the prompt J/ψ production. For a precise comparison the measurement of the non-prompt J/ψ fraction will be necessary; yet, preliminary results of the non-prompt fraction suggest that this is a small factor which will slightly improve the agreement between data and the Color-Evaporation Model. ALICE is the only experiment at the LHC that is able to measure J/ψ down to $p_{\mathrm{t}} = 0$ at mid-rapidity. Therefore, no direct comparison of the total cross section to other experiments is possible in this rapidity region. The result has been compared to other measurements at lower collision energies. A strong increase with $\sqrt{s}$ was found with a similar pattern as a prediction of the Color-Singlet Model.

Furthermore, results of the differential analysis as a function of the J/ψ transverse momentum were presented. A comparison to the available inclusive data at mid-rapidity in $\sqrt{s} = 7$ TeV pp collisions was given. With the statistics currently available for this analysis the p_{t} reach is 10 GeV/c. In the overlap region—the low momentum cut off of CMS and ATLAS is 6.5 and 7.0 GeV/c—a very good agreement with the other experiments is found.

Finally the data are shown together with various theoretical predictions representing the current status of the three most common theoretical approaches for the description of quarkonia production: the Color-Singlet Model, the Color-Evaporation Model and NRQCD. As for the rapidity distribution a direct comparison is not yet possible due to the missing subtraction of the feed-down contribution from b hadron decays. However, first measurements at LHC energies describe the trend of the momentum-dependence of this factor. Taking this into account probably a good description would be found for all three models. Future measurements of the feed-down fractions from b hadrons, χ_{c} and ψ' will allow for more stringent comparisons to the model predictions. Still, the theoretical uncertainties are rather large making it difficult to confirm or dismiss one of the models.

This study has been performed in conjunction with the ALICE J/$\psi \to \mathrm{e}^+\mathrm{e}^-$ analysis group. Several of its parts contributed to the combined work leading to the publication of the first J/ψ measurement with ALICE [173]. It is also serving as a cross check to this data. A comparison between the two analyses was given for the integrated as well as for the differential results. Both are in a very good agreement. Due to a modification of the analysis strategies a reduction of the statistical and systematic uncertainties by 20 % and 5 %, respectively, was achieved in this work.

Proton-proton data is an essential baseline for measurements in heavy-ion collisions. Even though the collision energy to which the results presented in this thesis correspond is higher than the maximum energy for Pb–Pb collisions at the LHC, $\sqrt{s} = 7$ TeV compared to $\sqrt{s_{\mathrm{NN}}} = 5.5$ TeV, the data might be relevant for Pb–Pb. Depending on the availability and the quantity of pp measurements at the collision energy at which Pb–Pb data will be taken in upcoming heavy-ion running periods, an interpolation between data at $\sqrt{s} = 7$ TeV and at lower energies might be necessary. Such an interpolation also serves as a cross check of the

data at intermediate collision energies as e. g. the ALICE measurement in $\sqrt{s} = 2.76$ TeV pp collisions.

A new view on elementary hadronic J/ψ production is discussed in the second part of this work. For the first time, it has been studied as a function of the charged-particle multiplicity in pp collisions. This approach is inspired by the high multiplicities reached in pp collisions at LHC energies. An approximately linear increase of the J/ψ yield with the charged-particle multiplicity is found both at mid-rapidity (this study) and at forward rapidity [192, 211]. With the currently available statistics an investigation is possible up to four times the average multiplicities in minimum bias pp collisions. There, an enhancement relative to the minimum bias yield of approx. 8 is found at mid-rapidity and approx. 5 at forward rapidities.
Possible interpretations are that either J/ψ production is accompained by a strong hadronic activity or that the hard scattering processes forming heavy-quark pairs are affected by multiple partonic interactions just as it is the case for the soft regime. A complementary analysis of J/ψ from $2 \rightarrow 2$ hard partonic scatterings in Pythia 6.4 shows a decrease of the J/ψ yield with the event multiplicity in contradiction to the data. Further analyses with other models such as Cascade or Pythia 8—especially with respect to their specific implementations of MPI—might shed more light into the origin of the observed multiplicity dependence. Multiplicity-dependent analyses of open charm mesons, other quarkonia and other hard probes will clarify how general this effect is.
Collective effects are a phenomenon previously discussed in the context of heavy-ion collisions; recently it was suggested that such effects might also be visible in the highest multiplicities reached in $\sqrt{s} = 7$ TeV pp collisions. Since pp data are used as the baseline for heavy-ion measurements a thorough understanding of all effects in pp is essential. This subject could be adressed by comparing the presented results for the multiplicity dependence of J/ψ production with corresponding results for open charm mesons.

Appendix A

A DCS-Offline Communication Framework

For data reconstruction and quality assurance numerous configuration parameters, counter readings and status informations of the TRD have to be recorded on a run-by-run basis. A framework for the acquisition of this data, its transfer and storage was developed as part of this work. In the following first the information that needs to be stored is discussed, then the general scheme of the framework including the data flow is described. Furthermore, the data structure and tools for monitoring the readout process and the stored data will be introduced. Finally, an outlook will be given about future modifications of the framework.

A.1 Informations to be Stored

Three different components of the TRD have to be monitored by the framework: The Front-End Electronics (FEE) of all detector chambers, the Global Tracking Unit (GTU) and the Pretrigger System. When completed, the TRD will consist of 510 detector modules.

One can divide between time dependent and run dependent information. Examples for the former are temperatures, pressures, voltages or currents. All such data is read out by another framework using the AMANDA protocol [223, 224] and not further mentioned here. The run dependent information currently includes for the FEE:

- All relevant parameters of the chamber's configuration, e. g., the name and version of the configuration scheme, the number of time bins used in the readout process, the type of trigger setup and settings of the pre-amplifiers and shaper amplifiers,
- The status of each TRD chamber as well as the status of each individual MCM (see

Section 3.2.4) on that chamber,

- The readings of the event and pretrigger counters of each MCM and
- Lists of inactive ADC channels, MCMs and interfaces of each chamber.

As long as the FEE is not reset all counter readings are continuously increased. In order to find out the actual numbers of, e. g., events or pretriggers per run the data has to be read out twice per run. First, right before the run was started (start of run, SOR) and second, directly after the run was stopped (end of run EOR). In this way it can also be clarified that no configuration has been changed during the run or if chambers or single MCMs changed their state during the run, due to possible errors.
The GTU delivers the following information:

- Segment, stack and link masks of inactive parts of the TRD,
- Software and hardware versions and
- Configurations.

Finally, the Pretrigger System will publish mainly three sets of data that need to be recorded:

- A main part of the Pretrigger system is implemented with FPGAs[1]. Their functionality is defined by various configuration parameters. The proper configuration needs to be cross-checked and documented,
- The trigger decision is mainly defined by a set of look up tables (LUT). The version tags of the applied LUTs have to be stored and
- Several counter values as the total number of generated triggers and the numbers of the different trigger sources (V0, T0, TOF, bunch crossing) need to be recorded.

A.2 Components of the Framework and Data Flow

The framework can be divided into three parts: first, the online TRD systems that are to be monitored and the central detector systems that trigger the readout process. These are depicted by yellow boxes in Fig. A.1. Second, the infrastructure that actually reads out the data and makes it available for the post-processing, depicted with green boxes in the same figure. And last, the offline part of the framework which, after each run, picks up the data, processes it and stores it in the database. These components are discussed in more detail in the following.

[1] **F**ield **P**rogrammable **G**ate **A**rrays, programmable digital integrated circuits

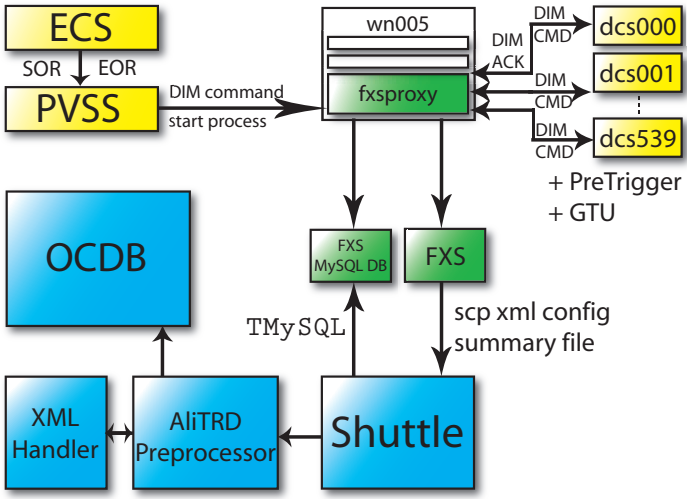

Figure A.1: A general overview of the framework which can be divided into three parts: online (yellow), data acquiring (green) and offline (blue) components. Details are discussed in the text.

A.2.1 Online Systems

The central ALICE experiment control system (ECS) steers the sub-system's detector control systems (DCS) and sends the triggers for all actions that have to be performed at the start (SOR) and end (EOR) of each run. An important part of the TRD DCS is the central control program which is a PVSS[2] implementation. As shown in Fig. A.1 the TRD PVSS program forwards the SOR/EOR triggers of ECS to the fxsproxy (described in Section A.2.2) and by this starts the actual readout processes. The state and the log output of the readout process is permanently monitored with PVSS, eventual errors are published in the PVSS alarm panels. A failure of the readout systems will be immediately communicated to the DCS/ECS shifter of the experiment.

The other part of the online systems are the ones that are actually being read out. These are, as mentioned above, the pretrigger system, the GTU and the FEE of the TRD readout chambers. All communication between the said systems is carried out via the DIM[3] protocol [225]. A DIM server is running on each chamber's DCS board (see Section 3.2.4). When that DIM server receives the command to provide the chamber's configuration and status information several routines are called that create the requested data. Finally this data is published via DIM where it is accessible for the readout program. The implementation is realized in a similar way for the other two systems. The difference in these cases is however that the communication is done via

[2]PVSS (**P**rozess**v**irtualisierungs und **S**teuerungs**s**ystem, process virtualization and control system) is a commercial product by ETM that allows for object oriented implementations for specific requirements, e. g., as control systems for power plants or production sites.

[3]**D**istributed **I**nformation **M**anagement System

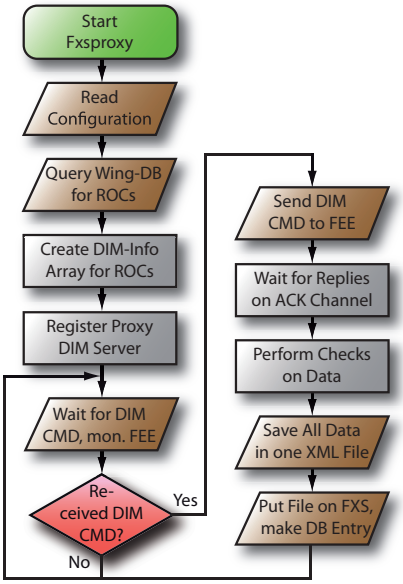

Figure A.2: Flow diagram of the basic features of the fxsproxy program and the readout process.

only one single DIM server per system in contrast to the FEE, where each individual chamber provides its own data.

One of the main advantages of the framework's layout is the flexibility and scalability of the data content. After the implementation of the communication methods and the first creation of output data, additional information can simply be appended by the respective expert of the given software module.

A.2.2 Data Acquisition

The main part of the framework is a proxy program called fxsproxy. It is running permanently on an ALICE Linux PC with access to the DCS network. The program is written in C++ programming language, satisfying the GNU build system [226] and being installable by the RPM package manager [227]. Documentation is available in manual (*man*) files and in the TRD shifter's manual.

A flow diagram of the most important steps in the startup and readout process of the fxsproxy is shown in Fig. A.2. There are many parameters that have to be provided to the fxsproxy as, e. g., the log verbosity level, the place where the output files are temporally being stored or the hostname of the DIM dynamic name server (DIM DNS). All such parameters are defined in a configuration file which is analyzed by the fxsproxy at startup.
A database (wing-db) holds all information about the installed TRD hardware. A query of

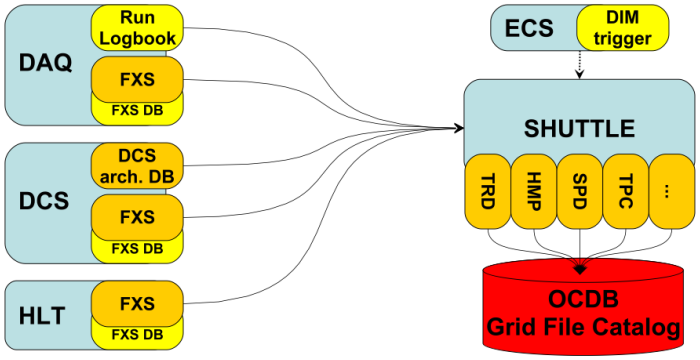

Figure A.3: Schema of the Shuttle framework; The three online systems DAQ, DCS and HLT provide data to the Shuttle system. Triggered by ECS, the Shuttle executes the preprocessors of all detectors. The output of these is stored in the OCDB and later used for the reconstruction of the run [223].

this database finds out which TRD chambers are installed and can be included in the readout processes afterwards. When all this information is gathered the fxsproxy starts a DIM server itself which receives the triggers (from PVSS or any other DIM client) for the readout process. While awaiting such a trigger the state of all DCS boards is continuously monitored. Sending commands to DCS boards not in state *ready* causes an error on that specific chamber. To prevent this from happening such chambers are not sent any commands. Anyhow, storing the above listed information for chambers not participating in data taking is not necessary.
When a trigger command is received by the fxsproxy, the basic procedure is as follows. First, the DIM command with the request to send all configuration and status data is sent to all DCS boards in state ready. The data, which is published on the respective DIM channels, is collected and checked. After the replies of all active FEE are received or the timeout given in the configuration file is exceeded all data are assembled in one file which is stored locally. The last action is to call a bash script which copies the file onto the File Exchange Server (FXS) and makes a corresponding entry in the FXS MySQL database. This script is issued by the ALICE DCS group and can be exchanged, if needed, without any change in the fxsproxy source code. A local copy of the data file is kept for a number of readout cycles, defined also in the configuration file.

A.2.3 Offline Processing and Storage

After each run the Shuttle system [223] gets triggered by ECS, see Fig. A.3. The online conditions data, available via the file exchange servers of the three systems DCS, DAQ and HLT as well as additional information from the run logbook (DAQ) and from the DCS database containing the time-dependent conditions data (DCS) is picked up by the Shuttle and provided

to the preprocessors of the individual sub-detectors. These preprocessors are modules that process the data delivered by the Shuttle, coming from the various sources as shown in Fig. A.3. The output of all these modules is centrally stored and later used for data reconstruction and quality assurance. The preprocessor of the TRD, `AliTRDPreprocessor`, has been added a function to read, parse and digest the two files (one from the start and one from the end of each run, see Section A.2.1) that have been created and put on the DCS FXS by the fxsproxy. As described in more detail in Section A.3.1, XML is used as data format for data transmission within the framework. For this, an XML handler has been developed in which the XML tags are defined. This handler is then given to the ROOT [228] built-in SAX[4] parser which gets called in the TRD preprocessor. In the SAX handler `AliTRDSAXHandler` the data fields of all defined tags are read out and stored in the corresponding data members of object instances of special storage classes (see Section A.3.2). One such class has been developed for each of the systems TRD FEE, Pretrigger and GTU. One mother class `AliTRDCalDCS` holds these objects as data members as well as several global values. The latter values are being obtained by a simple comparison between the numbers of all individual DCS boards that have sent data. If all entries, e. g., for the number of time bins match—as they should—then this number is given as the global one, a corresponding error code is inserted otherwise. In this way all informations are well structured in one place. Two such objects—one for SOR, one for EOR—are put in an array which is stored as a ROOT file. This file is then copied to the central OCDB[5] after each Shuttle processing. The OCDB is the common data base for all conditions data of the experiment. It is a huge catalog of all files containing the data of each run. Being accessible via the grid [229], the OCDB is queried during raw data reconstruction and quality assurance.

A.3 Data Structure

A.3.1 XML File Structure

The Extensible Markup Language (XML [230]) is used as intermediary data format. XML documents are written in clear text, generally in ASCII character scheme [231], and have a tree-like structure composed of markup constructs called tags. As in HTML [232] there are three types of tags: opening tags, closing tags and empty-element tags. All tags begin with "<" and end with ">" and can be freely named. A pair of one opening and one closing tag build up an element, in contrast to the single empty-element tag such a pair may contain child elements or text as the element's content in between. Another important component of XML are attributes. These are pairs of a value and a name. Attributes can be inserted in every opening or empty-element tag. When all XML rules are fulfilled by a given document it is called well-formed. Such rules are, e. g., the existence of one root element. Further every

[4] **S**imple **A**PI for **X**ML
[5] **O**ffline **C**onditions **D**atab**a**se

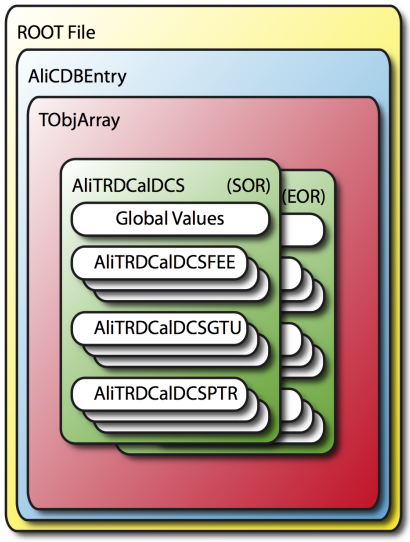

Figure A.4: The OCDB file structure.

tag must be either an empty-element tag or have a corresponding closing tag in the correct tree level. Parsers can test if a document is well-formed. In the given implementation of the framework `TRD` is used as root tag. But each module that creates XML output should itself produce well-formed data.

The choice of XML brings along many advantages: XML is platform independent and human readable. Furthermore, XML is very flexible, the data structure can easily be extended or modified. Since it is a language developed for data exchange and is widely used in modern information technology convenient tools are available that can be easily applied. In particular there are on the one hand the Extensible Stylesheet Language (XSL) for monitoring purposes (see Section A.4) as well as parsers.
It is a huge advantage to be able to make use of well tested parsers since the development of a robust parser is itself a very crucial task. Such a program has to be extremely stable and reliable also in case the data has been corrupted in any way during its generation or transfer. The ROOT [228] analysis framework comes with a built-in XML parser that has been applied here. In case any error occurs with an XML file the parser will detect it and exit safely.

A.3.2 OCDB File Structure

For each run all DCS data (discussed in Section A.1) is put in a ROOT file and stored in the OCDB. This is the final destination for the data. From there and in this format the data is accessible and readable for all analysis purposes. ROOT files are much more efficient in terms of file size: while the XML files have sizes of the order of a couple of MB, the ROOT files

are a factor of about 20 smaller. The structure of these files is depicted in Fig. A.4. The sole content of this file is an `AliCDBEntry` carrying a `TObjArray`. While the latter is a ROOT class for arrays of complex data objects which inherit from the ROOT class `TObject`, the first is the common structure for ALICE CDB entries. The said array holds two objects of the class `AliTRDCalDCS`, one for the start of the run, one for the end of the run. This class has been developed as a container for all relevant data coming from the DCS FXS. It holds arrays of the three classes `AliTRDCalDCSFEE`, `AliTRDCalDCSGTU` and `AliTRDCalDCSPTR`, one for each of the online systems that are being read-out and which are finally storing the data. For access of the data the `AliTRDCalDCS` object can be asked for the corresponding instance of the system or TRD chamber. Also, since mostly global values are of interest, all FEE settings that are common for all chambers are stored in data members of the `AliTRDCalDCS` instances and can be accessed directly.

A.4 Monitoring

Two means for data monitoring have been implemented: An XML transformation via XSL (see Section A.3.1) and a ROOT macro which analyzes the final OCDB object.

The XSL file comes with the fxsproxy's RPM package. Such style sheets are used to perform transitions; either again to XML, i. e., as a digest of the data or to other formats such as plain text, HTML or even PDF[6]. Here it is used to perform a transition to HTML which can be displayed with any standard web browser. As depicted in Fig. A.5, where such a digest of the data is shown, a summary of the most important informations is given on top—such as the number of replies from the TRD FEE and whether or not the whole TRD has the same configuration. If the front end electronics of a TRD chamber exhibits different MCM states it is necessary to find out why this happened. In such a case the corresponding cell of the table shown in Fig. A.5 will read "MIXED" and be a hyperlink. The XSL style sheet of the fxsproxy's software package shows the problematic channel of that chamber with a click on that link, see Fig. A.6. In that example screenshot the MCM number 7 of the third readout board is in a state (*tracklet sending*) different from that of the other MCMs (*wait for pretrigger*).
This data monitoring method is intended for fast quasi-online quality assurance and debugging. Since local XML file copies are read this tool is mainly used locally at the ALICE control room. Furthermore, because the storage of the local XML files is not guaranteed, this method is predominantly intended for monitoring recent runs.

The second possibility for data monitoring is realized with a ROOT macro that has been named `AliTRDcheckConfig.C`. In contrast to the XSL style sheet discussed above the final OCDB object is read out instead of the XML file. This tool can be used from wherever there

[6] **P**ortable **D**ocument **F**ormat

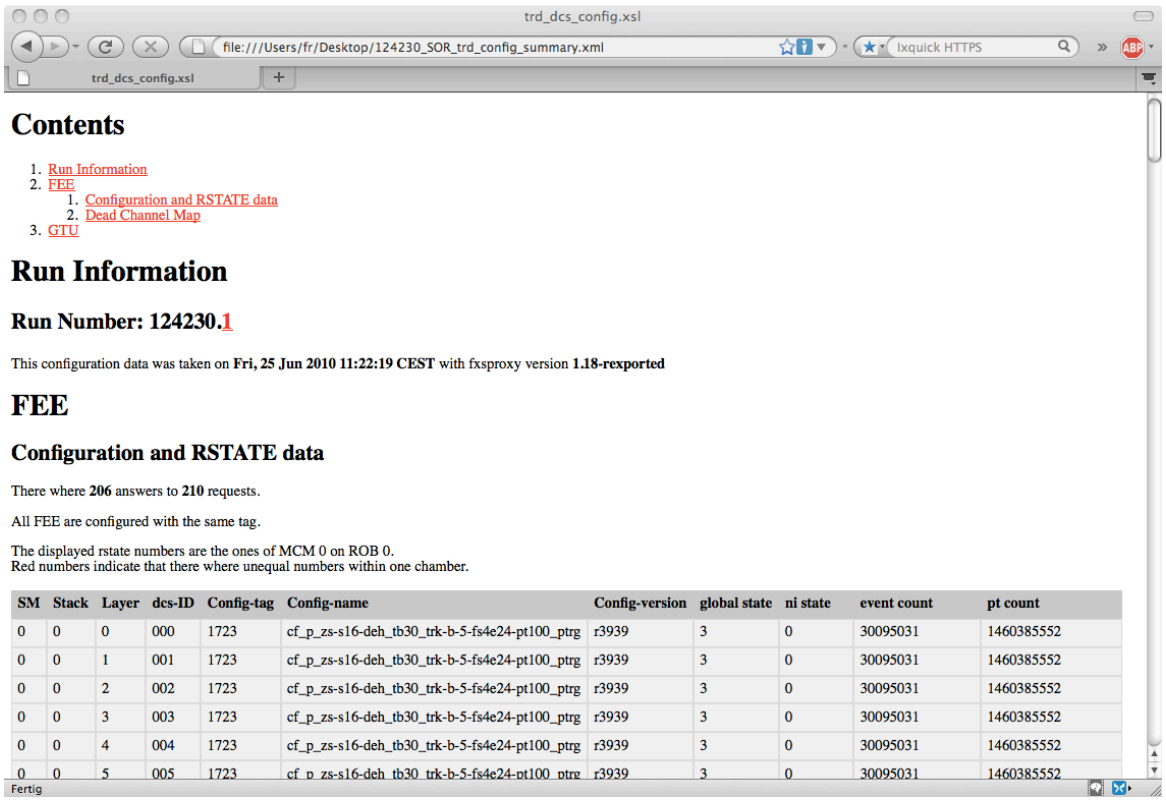

Figure A.5: The local copies of the output XML files can be monitored and analyzed with XSL-T. Shown is a screenshot of the output of a transition to HTML that can be browsed through using any standard web browser. The table shows a digest of the configuration information for each TRD chamber's FEE.

is a local AliRoot [233] installation with access to alien [181, 234]. It has been included in the AliRoot framework and can be found at `$ALICE_ROOT/TRD/Macros`. The run number must be given as argument upon execution. After the corresponding OCDB root file is downloaded from the grid via the alien interface it is being analyzed. All global parameters are printed out, possible error codes listed and a summary of the counter readings and states is given. This tool has mainly been developed for a quick access to the stored data. The OCDB files are not deleted, in contrast to the above method the information of all runs taken with the TRD is accessible.

A.5 Additional Programs of the Package

The fxsproxy package includes several additional executable programs. These are mainly provided for debugging and testing by an expert and are shortly introduced in the following.

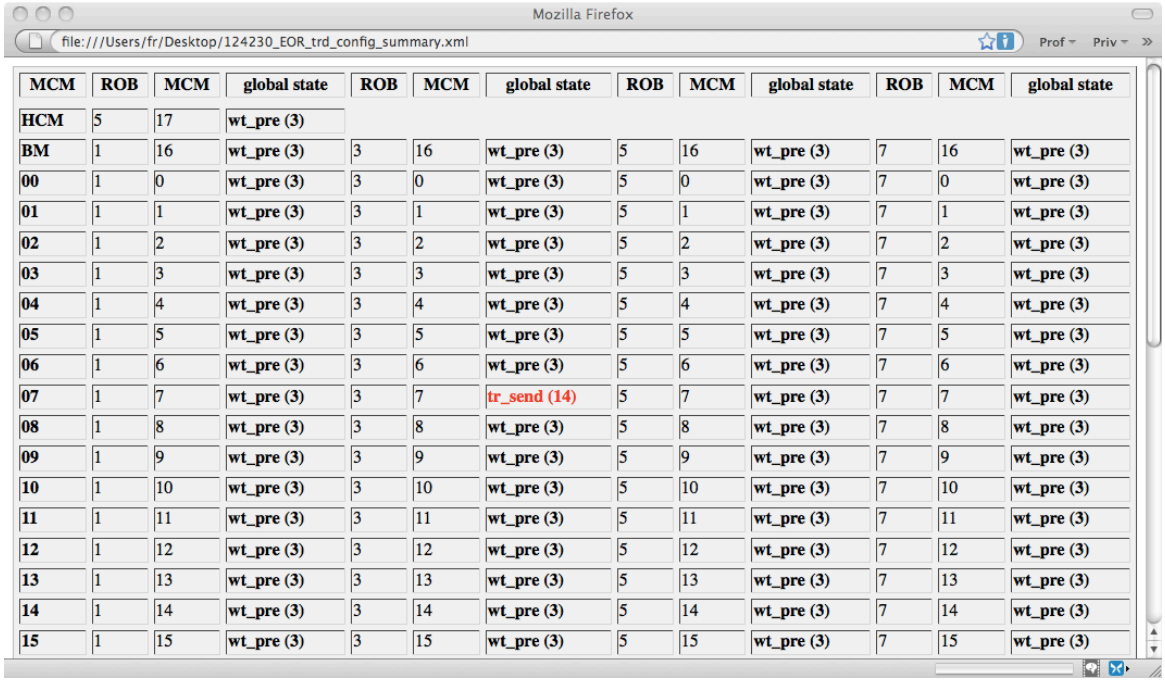

MCM	ROB	MCM	global state	ROB	MCM	global state	ROB	MCM	global state	ROB	MCM	global state
HCM	5	17	wt_pre (3)									
BM	1	16	wt_pre (3)	3	16	wt_pre (3)	5	16	wt_pre (3)	7	16	wt_pre (3)
00	1	0	wt_pre (3)	3	0	wt_pre (3)	5	0	wt_pre (3)	7	0	wt_pre (3)
01	1	1	wt_pre (3)	3	1	wt_pre (3)	5	1	wt_pre (3)	7	1	wt_pre (3)
02	1	2	wt_pre (3)	3	2	wt_pre (3)	5	2	wt_pre (3)	7	2	wt_pre (3)
03	1	3	wt_pre (3)	3	3	wt_pre (3)	5	3	wt_pre (3)	7	3	wt_pre (3)
04	1	4	wt_pre (3)	3	4	wt_pre (3)	5	4	wt_pre (3)	7	4	wt_pre (3)
05	1	5	wt_pre (3)	3	5	wt_pre (3)	5	5	wt_pre (3)	7	5	wt_pre (3)
06	1	6	wt_pre (3)	3	6	wt_pre (3)	5	6	wt_pre (3)	7	6	wt_pre (3)
07	1	7	wt_pre (3)	3	7	tr_send (14)	5	7	wt_pre (3)	7	7	wt_pre (3)
08	1	8	wt_pre (3)	3	8	wt_pre (3)	5	8	wt_pre (3)	7	8	wt_pre (3)
09	1	9	wt_pre (3)	3	9	wt_pre (3)	5	9	wt_pre (3)	7	9	wt_pre (3)
10	1	10	wt_pre (3)	3	10	wt_pre (3)	5	10	wt_pre (3)	7	10	wt_pre (3)
11	1	11	wt_pre (3)	3	11	wt_pre (3)	5	11	wt_pre (3)	7	11	wt_pre (3)
12	1	12	wt_pre (3)	3	12	wt_pre (3)	5	12	wt_pre (3)	7	12	wt_pre (3)
13	1	13	wt_pre (3)	3	13	wt_pre (3)	5	13	wt_pre (3)	7	13	wt_pre (3)
14	1	14	wt_pre (3)	3	14	wt_pre (3)	5	14	wt_pre (3)	7	14	wt_pre (3)
15	1	15	wt_pre (3)	3	15	wt_pre (3)	5	15	wt_pre (3)	7	15	wt_pre (3)

Figure A.6: If the front end electronics of a TRD chamber exhibits different MCM states it is necessary to find out why this happened. The XSL style sheet of the fxsproxy's software package shows the problematic channel of that chamber with one click. The table shows the states, translated to their names, of all MCMs on the given chamber. In this case one MCM is in another state than all others what can happen due to a bit flip in a data marker or a problematic channel.

fxsproxy_config_reload The only purpose of this program is to send the fxsproxy the signal to reload its configuration file. By this means there is no need to restart the fxsproxy if settings are to be changed. During such a restart the fxsproxy is switched off for a short time during which it is not able to receive triggers and what causes alarm messages in the DCS alarm panel. This is to be avoided during data taking periods.

fxsproxy_fee_replied A good way to detect problems in the readout process is to monitor the percentage of good replies from the the DCS boards. This can be done either via the PVSS control software or by this small program, e. g., remotely. The option -f continually prints the number after each readout cycle.

fxsproxy_status The fxsproxy keeps track of its own state. Currently three different states are defined: *ready*, *busy* and *error*. Also this information can be monitored both by the PVSS control system and a simple stand-alone text line program. The option -f continually prints the status as it changes.

fxsproxy_testclient Whenever the readout process must be tested or it is necessary to gather the actual configuration information without the overhead of starting a run just for this purpose this small program offers the possibility to trigger the fxsproxy. The program takes two arguments. First, the run number where 1 should be used for all testing purposes, and second, SOR or EOR to indicate whether the data is corresponding to the start or end of a run. For testing purposes the latter argument must be given for technical reasons but is not further used.

A.6 Outlook

The framework is in a very good shape, all main parts are implemented and running smoothly. The only major part that is still missing is the incorporation of the pretrigger system. This is currently being worked on and expected to be worked out in the near future.
Since the XSL-transformed XML output turned out to be a very useful tool for quick checks it is planned to implement an automatic procedure that appends the HTML digest to the entry in the electronic logbook for each run.
Apart from that of course all new output that might be added at some point needs to be included in the XML handler and the corresponding container class.

Appendix B

N_{trk} Correction Procedure

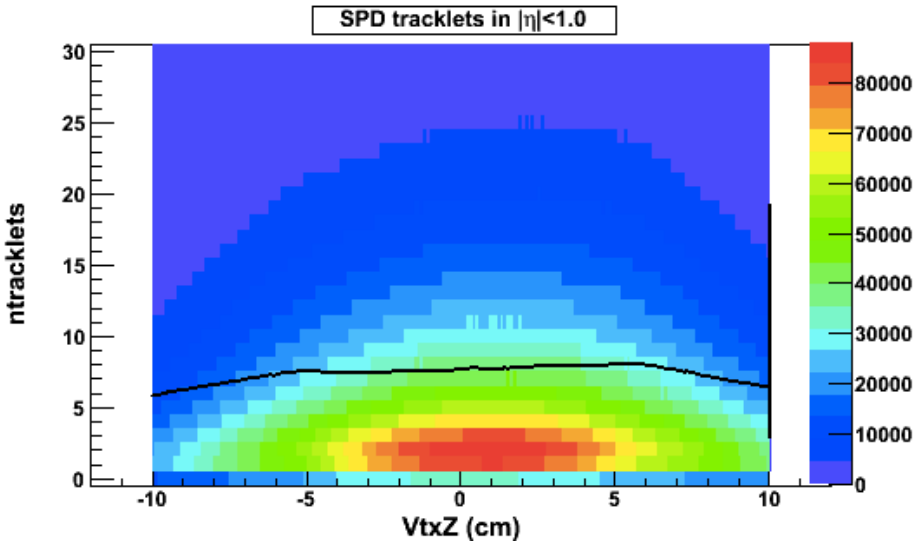

Figure B.1: The $N_{\mathrm{trk}}^{\mathrm{raw}}$ distribution (of LHC10d, as an example) against the z_{vtx} position in the colored 2D histogram as well as the mean $\langle N_{\mathrm{trk}} \rangle$ at each z_{vtx} position as a black line [208].

Figure B.1 shows the $N_{\mathrm{trk}}^{\mathrm{raw}}$ distribution (of LHC10d, as an example) against the z_{vtx} position in the colored 2D histogram as well as the mean $\langle N_{\mathrm{trk}} \rangle$ at each z_{vtx} position as a black line. The region of $z_{\mathrm{vtx}} \approx 3.0$ cm of the period LHC10b is used as a reference since there the highest efficiency was found. The choice of the reference is arbitrary due to the subsequent translation of the measured multiplicity into a physical charged-particle density. These mean values $\langle N_{\mathrm{trk}} \rangle_{z_{vtx}=3\ \mathrm{cm}}^{\mathrm{LHC10b}}$ are then used, on an event-by-event basis, to correct the measured number

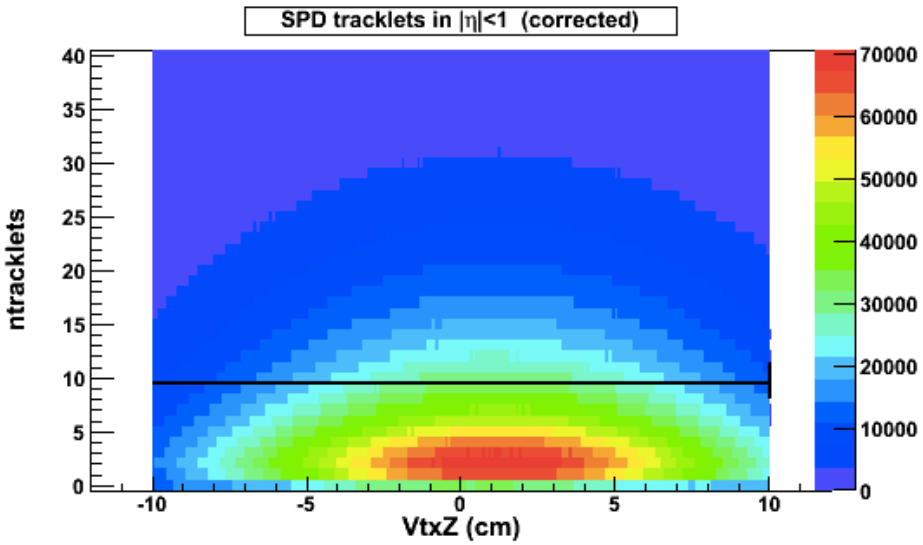

Figure B.2: As Fig. B.1, after the correction procedure [208].

of tracklets:

$$N_{\mathrm{trk}} = N_{\mathrm{trk}}^{\mathrm{raw}} \frac{\langle N_{\mathrm{trk}} \rangle_{\mathrm{z}_{vtx}=3\ \mathrm{cm}}^{\mathrm{LHC10b}}}{\langle N_{\mathrm{trk}} \rangle}. \tag{B.1}$$

Figure B.2 shows the same information as Fig. B.1, just after the correction procedure. Since by this, the population of bins is shifted by a fixed number, strong fluctuations would be introduced. To overcome this, the correction factor $\langle N_{\mathrm{trk}} \rangle_{\mathrm{z}_{vtx}=3\ \mathrm{cm}}^{\mathrm{LHC10b}} / \langle N_{\mathrm{trk}} \rangle$ is distributed by a poissonian with the mean at its fixed value. By this, the data of all beam priods can be summed together for the analysis.

Appendix C

Relativistic Kinematics

Units in High-Energy Physics

The basic units in physics are the seven SI[1] units summarized in Table C.1. Those are not very appropriate in high-energy physics where times, lengths and masses are exremely small. Table C.2 lists the units commonly used in high-energy physics. The unit of length is fm, the *femtometer* or *fermi*. Areas are often given in units of *barn* b where one b is defined as 100 fm^2. The unit of energy is the GeV, that of mass GeV/c^2. The speed of light is either written next to the unit or set to one using the convention $\hbar = c = 1$.

Symbol	Name	Measure
m	meter	length
kg	kilogram	mass
s	second	time
A	ampere	electric current
K	kelvin	temperature
mol	mole	amount of substance
cd	candela	luminous intensity

Table C.1: The seven basic SI units in physics.

[1] **S**ystème **I**nternational d'unités, International System of Units

High Energy Unit	Value in SI Units	Measure
1 fm	10^{-15} m	length
1 GeV/c^2	$1.783 \cdot 10^{27}$ kg	mass, E/c^2
1 fm/c	$3.336 \cdot 10^{-39}$ s^{-1}	time

Table C.2: The basic units in high energy physics.

Energies of Particle Kollisions

The basic relativistic relation between the total energy E, the momentum vector $\vec{p}$ and the mass m of a free particle is:

$$E^2 = \vec{p}^2 c^2 + m^2 c^4. \tag{C.1}$$

The four components $p_\mathrm{x}, p_\mathrm{y}, p_\mathrm{z}, E$ can be written as an energy-momentum 4-vector $\mathbf{P}$. The energy available in a collision of two particles A and B is calculated out of the 4-vectors $\mathbf{P} = (E, \vec{p})$ of the particles using the Mandelstam variable $s = (\mathbf{P}_\mathrm{A} + \mathbf{P}_\mathrm{B})^2$:

$$E_\mathrm{CM} = \sqrt{s} = \sqrt{(E_\mathrm{A} + E_\mathrm{B})^2 - |\vec{p}_\mathrm{A} + \vec{p}_\mathrm{B}|^2}. \tag{C.2}$$

In heavy-ion collisions rather than the total nucleus-nucleus collision energy the relevant measure is the energy of each individual nucleon-nucleon collision $\sqrt{s_\mathrm{NN}}$ because this is the amount of energy available for physics processes. The index NN indicates that the value corresponds to this quantity.

In a fixed target experiment the beam of one accelerator is focussed on a target in rest. When both collision systems A and B are of the same mass, i. e., the same isotopes, the collision energy becomes $\sqrt{s_\mathrm{NN,ft}} = \sqrt{2E_A m_\mathrm{A,B} + 2m_\mathrm{A,B}^2}$. Since $p_\mathrm{A} \gg m_\mathrm{A,B}$ it follows: $\sqrt{s_\mathrm{NN,ft}} = \sqrt{2p_\mathrm{A} m_\mathrm{A,B}}$. In a colliding-beam experiment, on the other hand, the center-of-mass energy of the colliding nucleons is: $\sqrt{s_\mathrm{NN,co}} = 2E$. Obviously, therefore, collider machines are used to access the highest possible collision energies.

Kinematical Variables

Following from Eq. (C.1) the total energy of a free particle A is:

$$E = \sqrt{|\vec{p}|^2 + m_\mathrm{A}^2}. \tag{C.3}$$

The kinematics of a particle is entirely descibed by its mass and 3-momentum. More practical variables for the experiment are the transverse momentum p_{t} and rapidity y, together with the azimuthal angle ϕ. The rapidity, defined as:

$$y = \frac{1}{2}\ln\left(\frac{E + p_{\mathrm{z}}}{E - p_{\mathrm{z}}}\right), \tag{C.4}$$

has the advantage of becoming only linearly shifted under lorentz transformations, the spectral form of rapidity distributions does not change. To calculate the energy of a particle its mass—its identity—must be known. This is not always the case and especially only with uncertainties. Consequently, a similar variable is commonly used, the pseudo-rapidity:

$$\eta = \frac{1}{2}\ln\left(\frac{|\vec{p}| + p_{\mathrm{z}}}{|\vec{p}| - p_{\mathrm{z}}}\right) = -\ln\left[\tan\left(\frac{\theta}{2}\right)\right]. \tag{C.5}$$

This quantity is only depending on quantities directly measured in high energy physics experiments. Both variables, rapidity and pseudo-rapidity, are almost the same; a disadvantage of the latter is its slight deformation under lorentz transformations.

Parton Distribution Functions

The partonic structure of nucleons can be probed in deep inelastic lepton scattering (DIS) experiments. Angular-dependent scattering cross sections lead to the determination of their structure functions $F_{\mathrm{j}}(x)$. While j corresponds to neutral- or charged-current processes (see [36] for details), x, i. e., *Bjorken-x*, is a very common Lorentz-invariant variable:

$$x = \frac{Q^2}{2M\nu}. \tag{C.6}$$

Therein Q^2 is the squared 4-momentum transfer in the scattering, M the mass of the nucleon and $\nu = E - E'$ the lepton's energy loss in the nucleon's rest frame. In the parton model, x is the fraction of the total momentum of the nucleon, carried by the scattered parton. For $Q^2 \gg M^2$, the structure functions are a convolution of the distribution functions $f_i(x, Q^2)$ of the different partons $i = \mathrm{g}, \mathrm{u_v}, \mathrm{d_v}, \bar{\mathrm{u}}, ...$ (PDFs). Figure C.1 shows a NNLO parameterization [235] of the PDFs of the valence quarks ($\mathrm{u_v}$, $\mathrm{d_v}$), gluons and the sea quarks. Note the logarithmic scale on the horizontal axis.

From this picture it becomes clear why at very high (RHIC, LHC) proton-proton collision energies mainly processes of two gluons play a role in $Q\bar{Q}$ production: the parton momentum fraction x_{i}, necessary to produce a heavy quark pair with a mass of a couple of GeV/c^2 is at a region where the gluons stongly dominate.

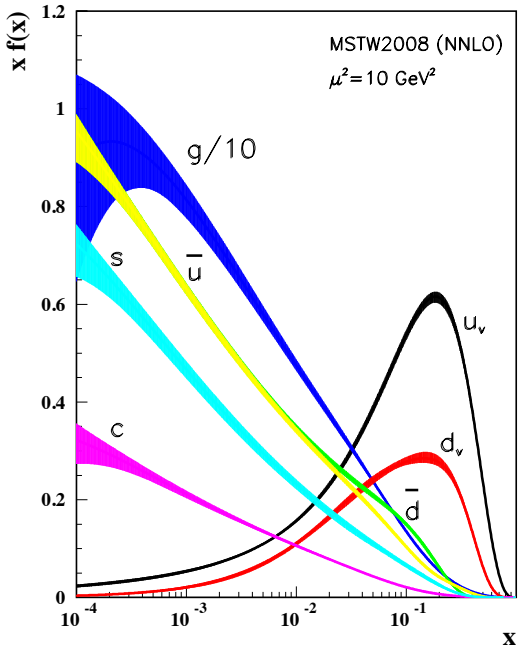

Figure C.1: Distribution of x times the parton distribution functions $f(x)$ of an unpolarized proton using the NNLO MSTW2008 parameterization [235] at a scale of $Q^2 = 10$ GeV^2 (here noted as μ^2). Picture taken from [36].

Calculation of the Invariant Mass

The invariant mass of the mother particle of any two-body decay process:

$$A \to B + C \tag{C.7}$$

can be calculated out of the kinematics of the daughter particles B and C. From Eq. (C.3) it follows for the invariant mass:

$$m_{0,\mathrm{A}} = \sqrt{(E_\mathrm{B} + E_\mathrm{C})^2 - |\vec{p_\mathrm{B}} + \vec{p_\mathrm{C}}|^2}. \tag{C.8}$$

After separation of the momentum components in longitudinal and transverse parts and using the definition of the rapidity, Eq. (C.4), one can make use of the symmetries of sinh and cosh and put in the scalar product of the transverse momentum vectors of B and C. In case of the $\mathrm{J}/\psi \to \mathrm{e}^+\mathrm{e}^-$ decay, one can neglect the electron mass which is small compared to the J/ψ one. Then the equation resolves to:

$$m_{0,\mathrm{J}/\psi} = \sqrt{2 \cdot p_{\mathrm{t,B}} \cdot p_{\mathrm{t,C}} \left(\cosh(\Delta\eta) - \cos(\Delta\phi)\right)}, \tag{C.9}$$

used in this analysis.

Appendix D

Additional Figures

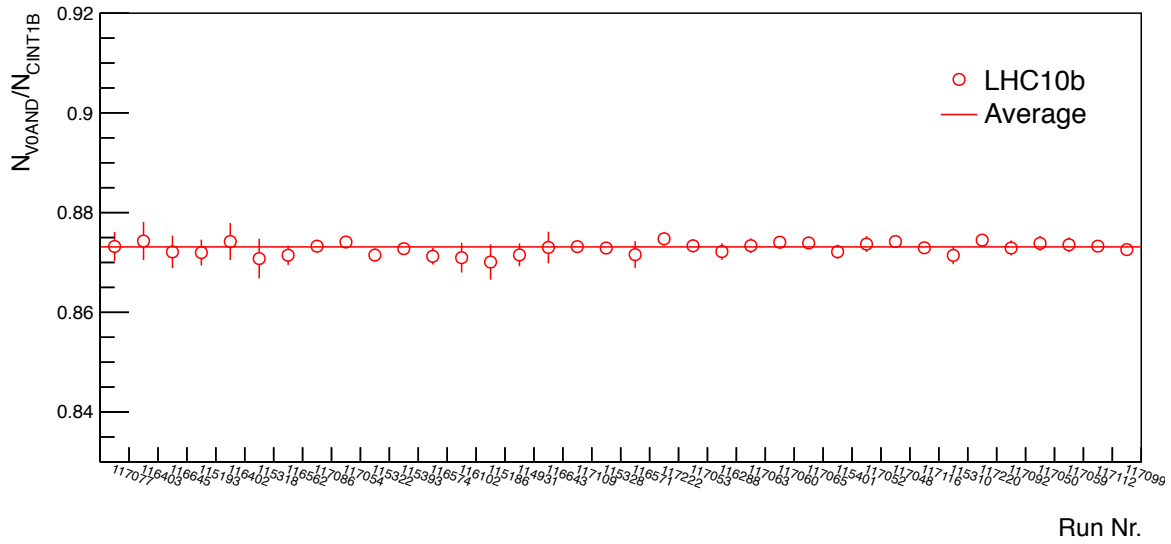

Figure D.1: The ratio of $N_{\mathrm{V0AND}}/N_{\mathrm{CINT1B}}$ triggered events for all analyzed runs in the beam period LHC10b.

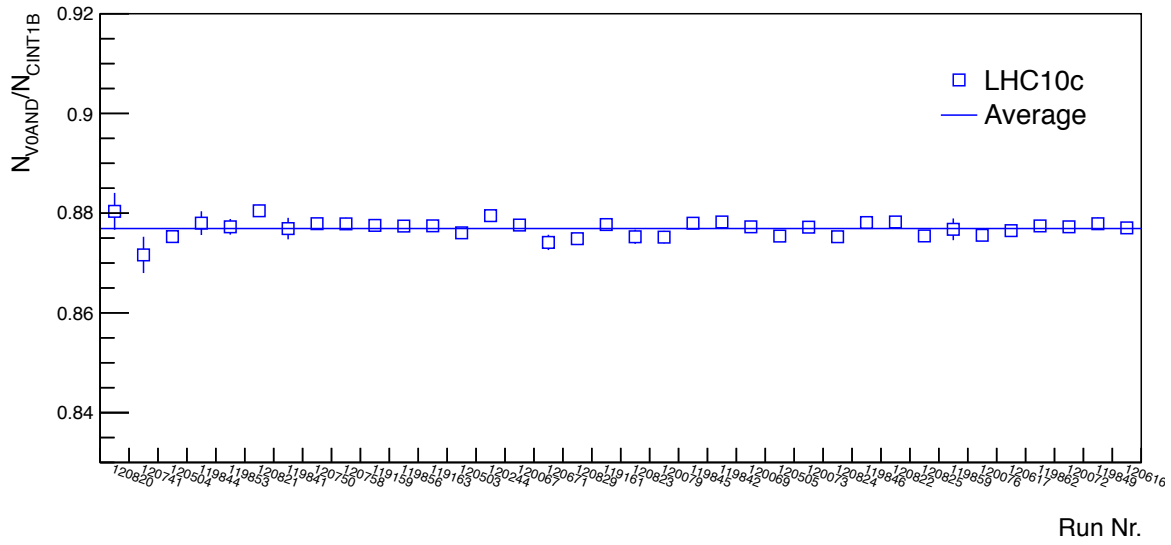

Figure D.2: The ratio of $N_{\mathrm{V0AND}}/N_{\mathrm{CINT1B}}$ triggered events for all analyzed runs in the beam period LHC10c.

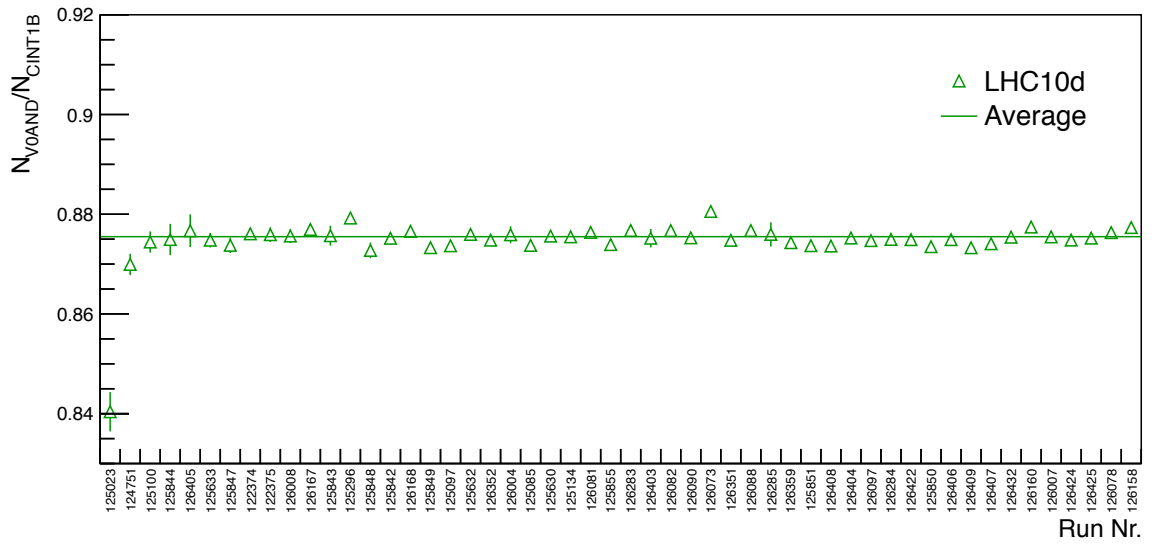

Figure D.3: The ratio of $N_{\mathrm{V0AND}}/N_{\mathrm{CINT1B}}$ triggered events for all analyzed runs in the beam period LHC10d.

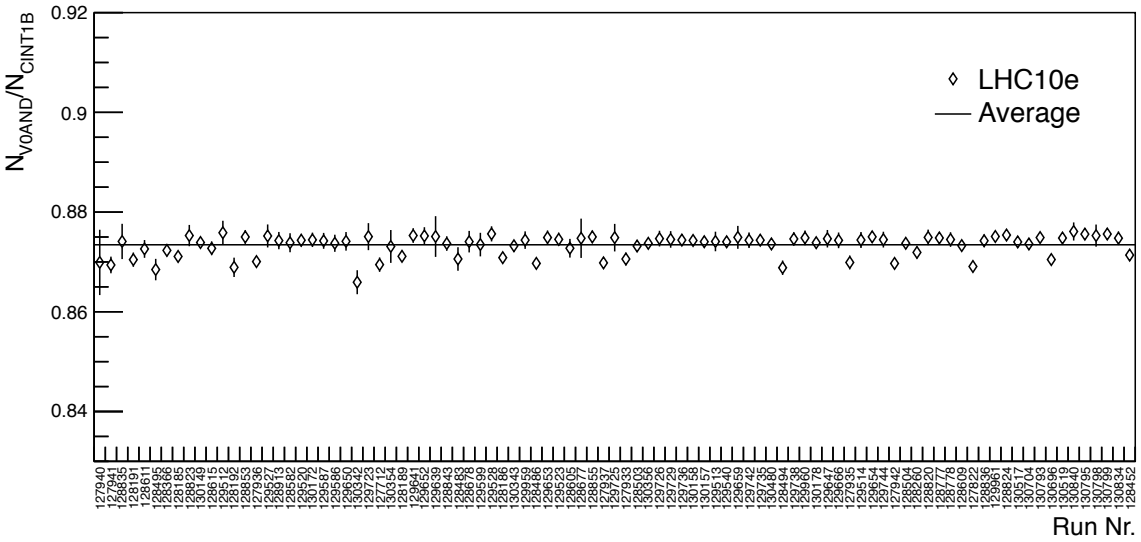

Figure D.4: The ratio of $N_{\mathrm{V0AND}}/N_{\mathrm{CINT1B}}$ triggered events for all analyzed runs in the beam period LHC10e.

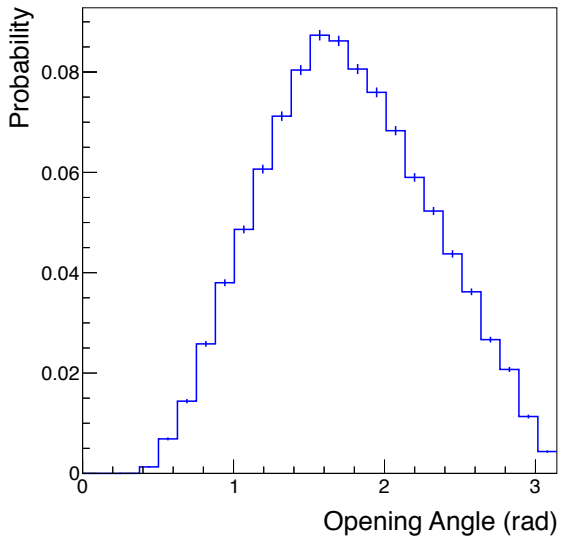

Figure D.5: The distribution of the opening angle of the J/ψ decay electrons according to the MC data set LHC10f7a. The mean value is 1.75 rad.

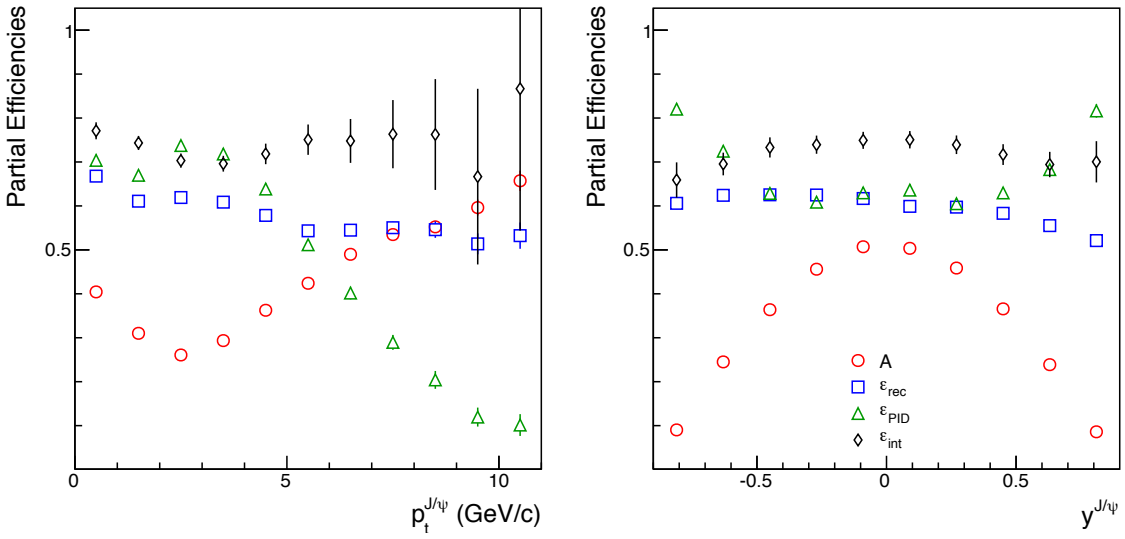

Figure D.6: As Fig. 4.15 for MC data set LHC10f7a_b.

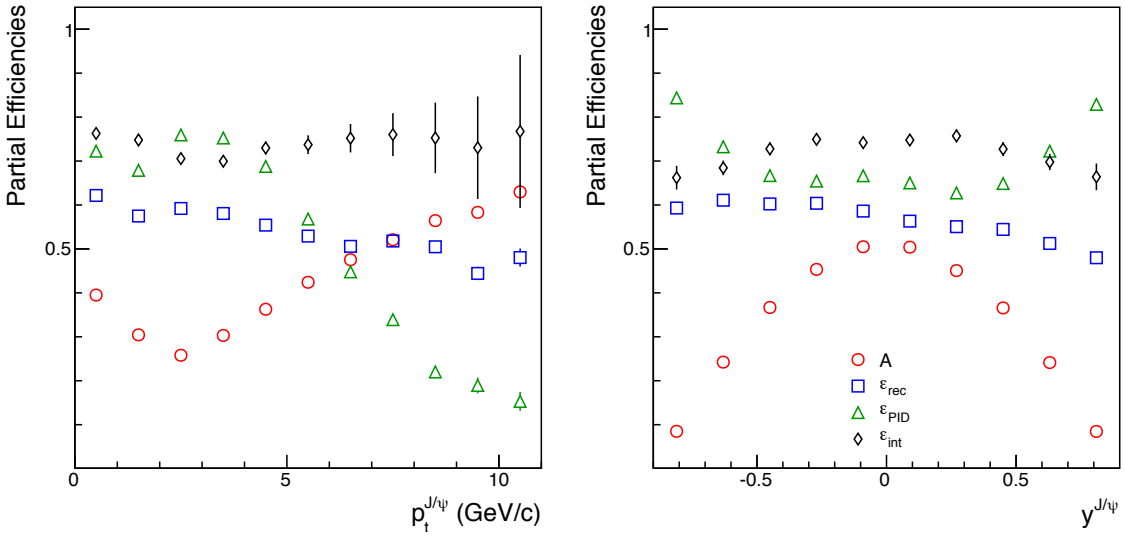

Figure D.7: As Fig. 4.15 for MC data set LHC10f7a_c.

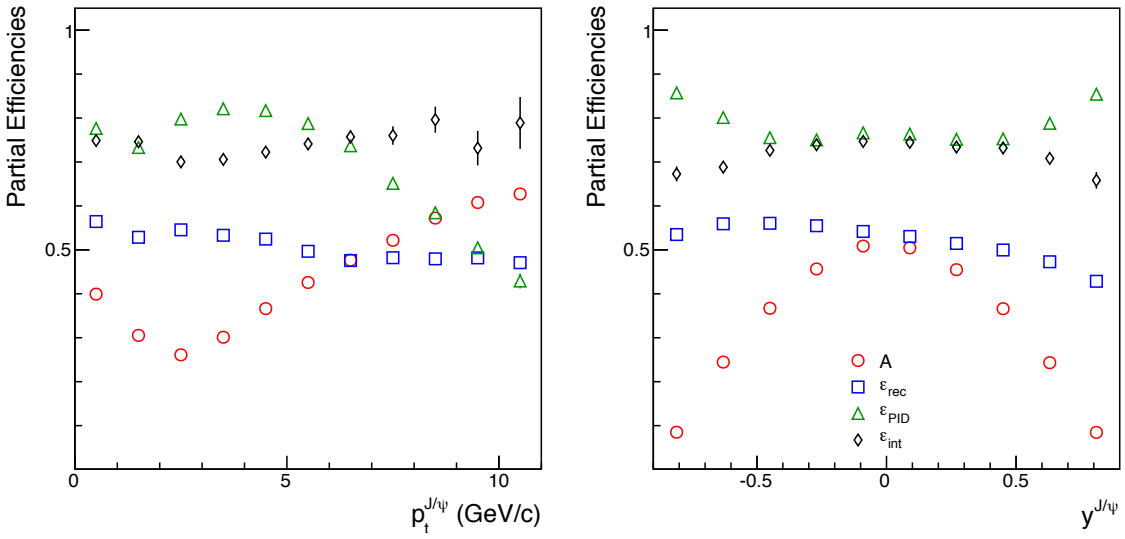

Figure D.8: As Fig. 4.15 for MC data set LHC10f7a_e.

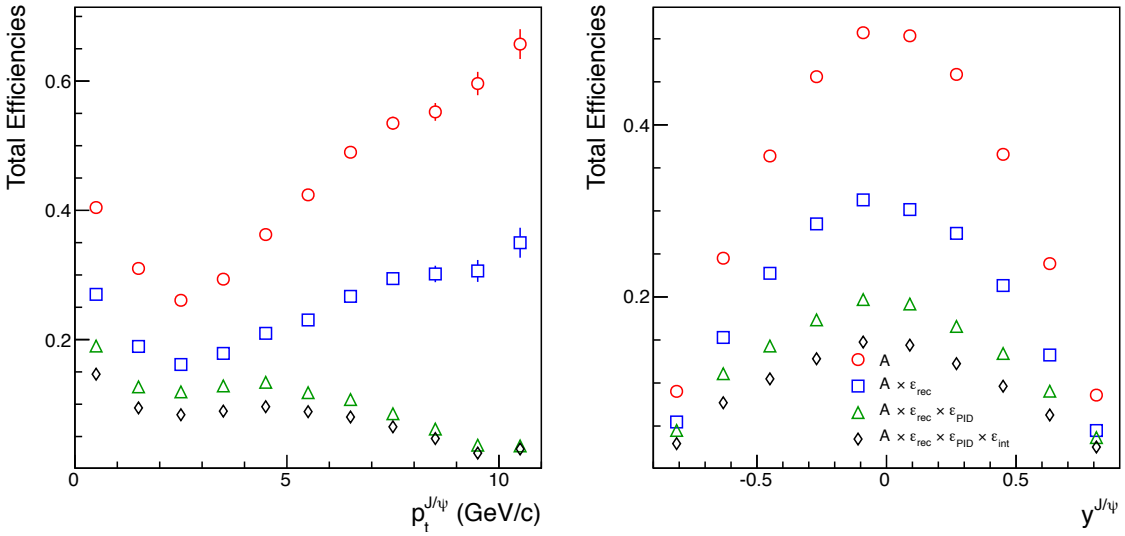

Figure D.9: As Fig. 4.16 for MC data set LHC10f7a_b.

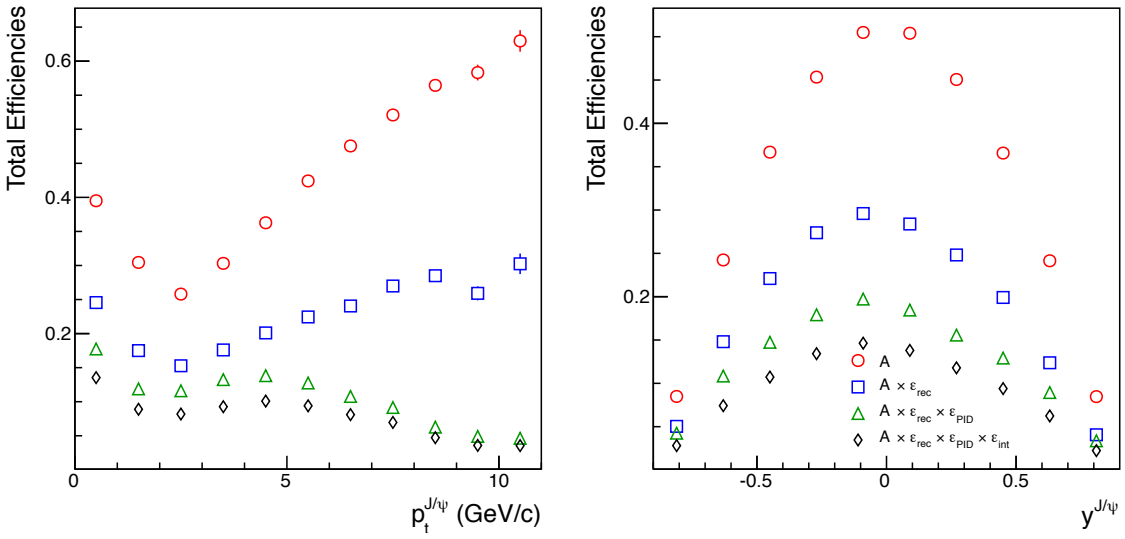

Figure D.10: As Fig. 4.16 for MC data set LHC10f7a_c.

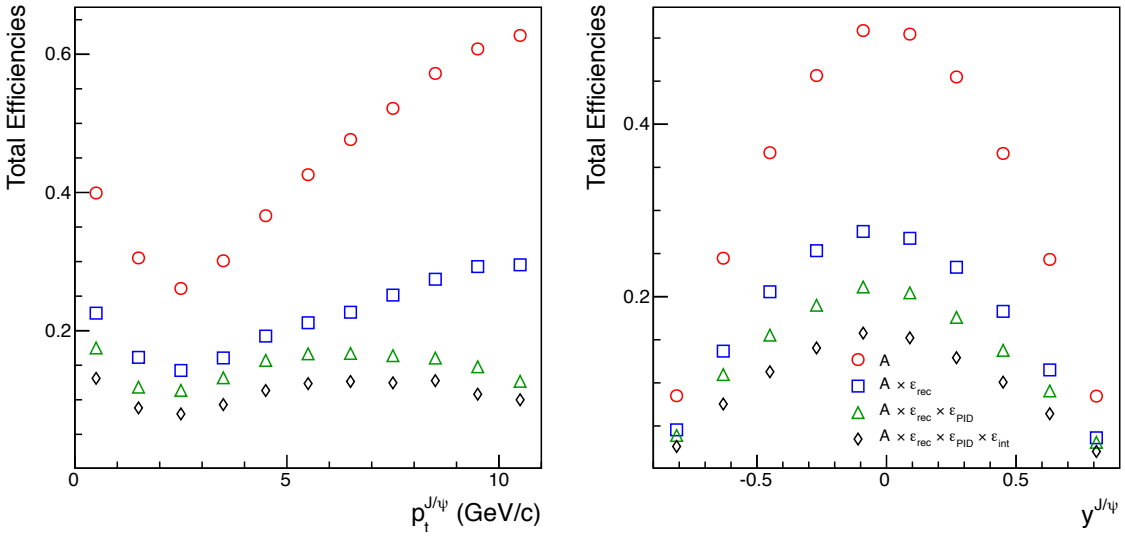

Figure D.11: As Fig. 4.16 for MC data set LHC10f7a_e.

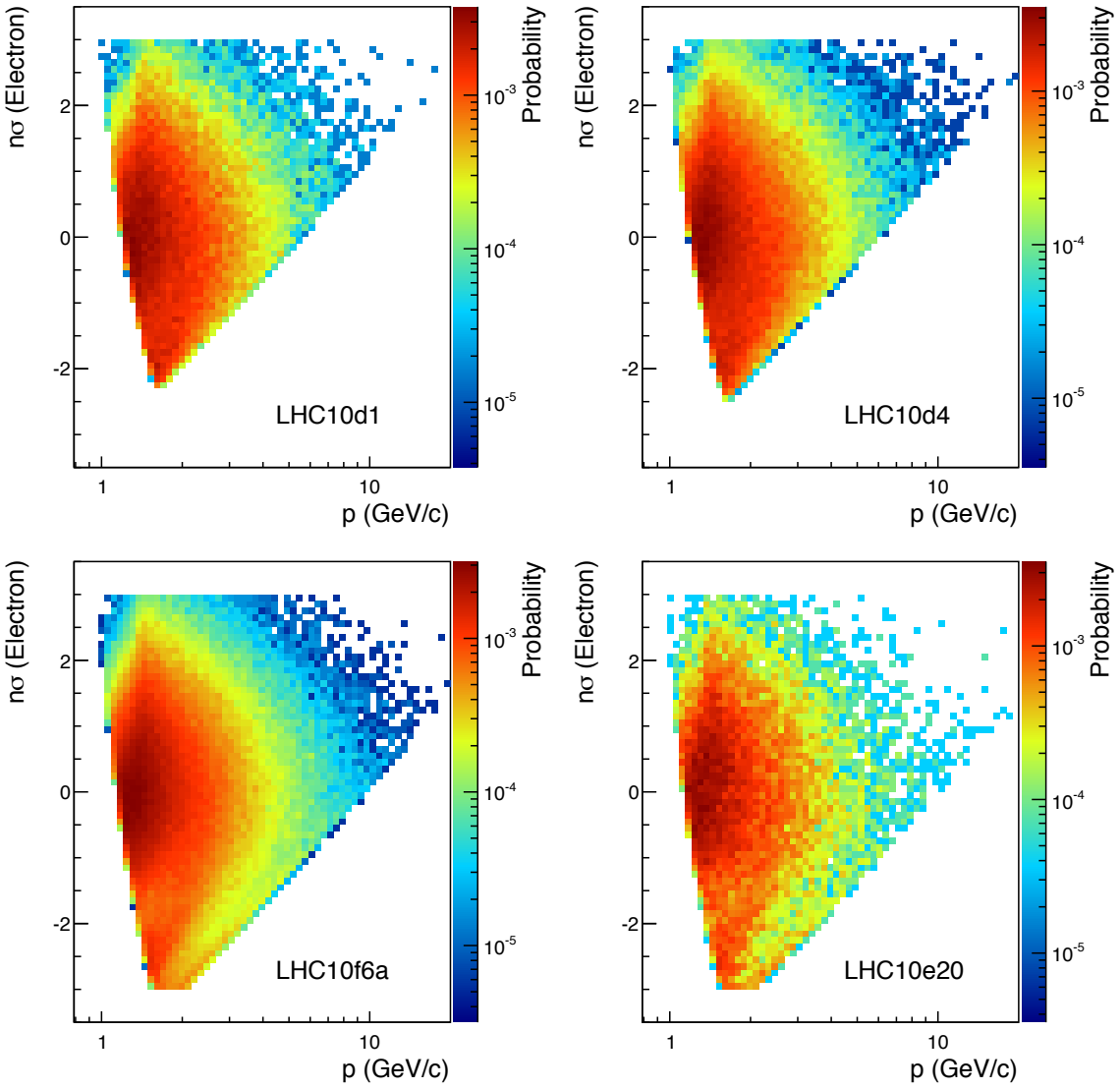

Figure D.12: The $n\sigma$ vs. p distributions of the MB MC data sets, after the PID cuts, tuned for MC as described in Section 4.4.3.

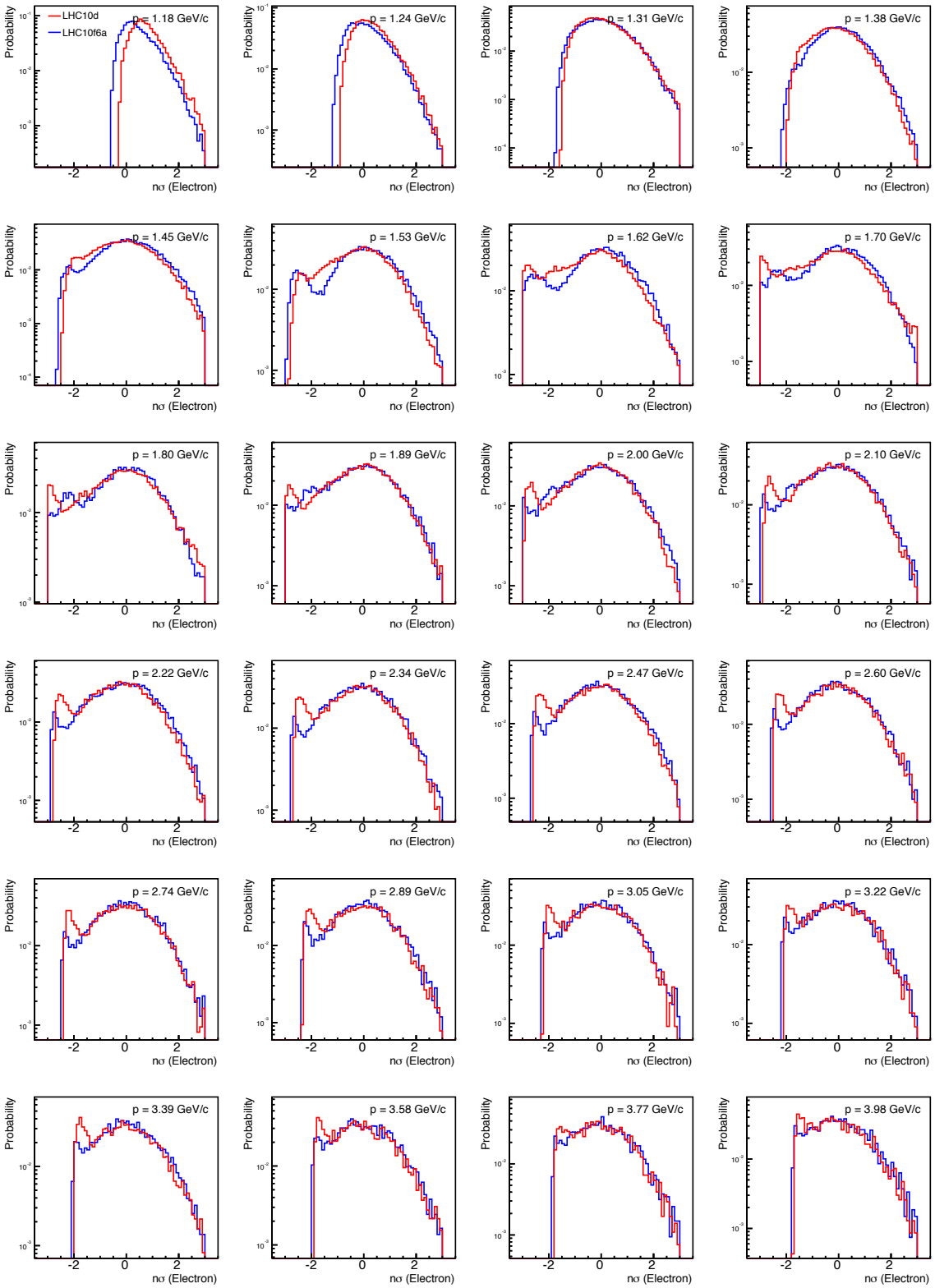

Figure D.13: Comparison of $n\sigma$ distributions in data (LHC10d) and in MC (LHC10f6a) for various slices in momentum. Continued in Fig. D.14.

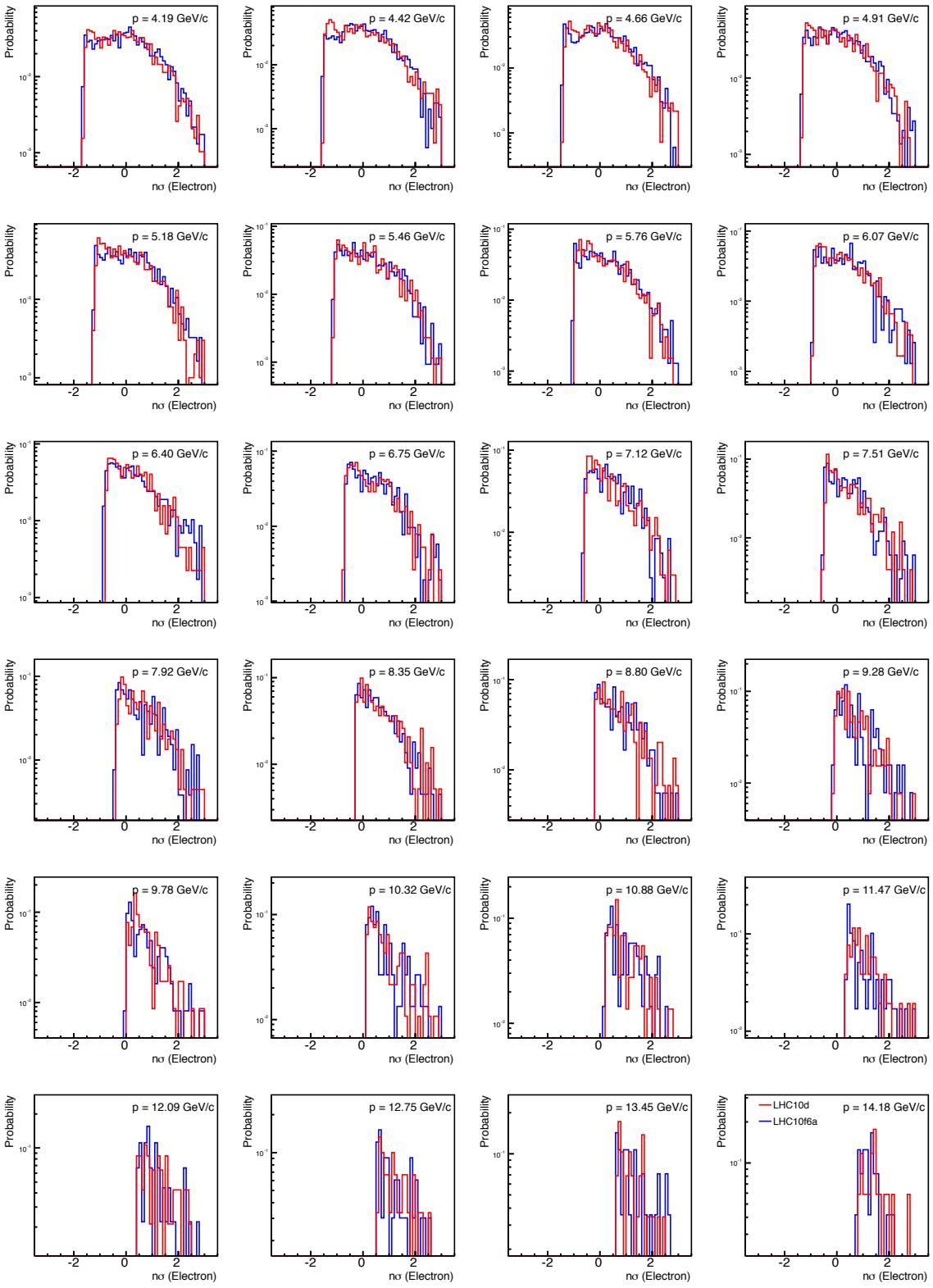

Figure D.14: Continuation of Fig. D.13 for higher momenta.

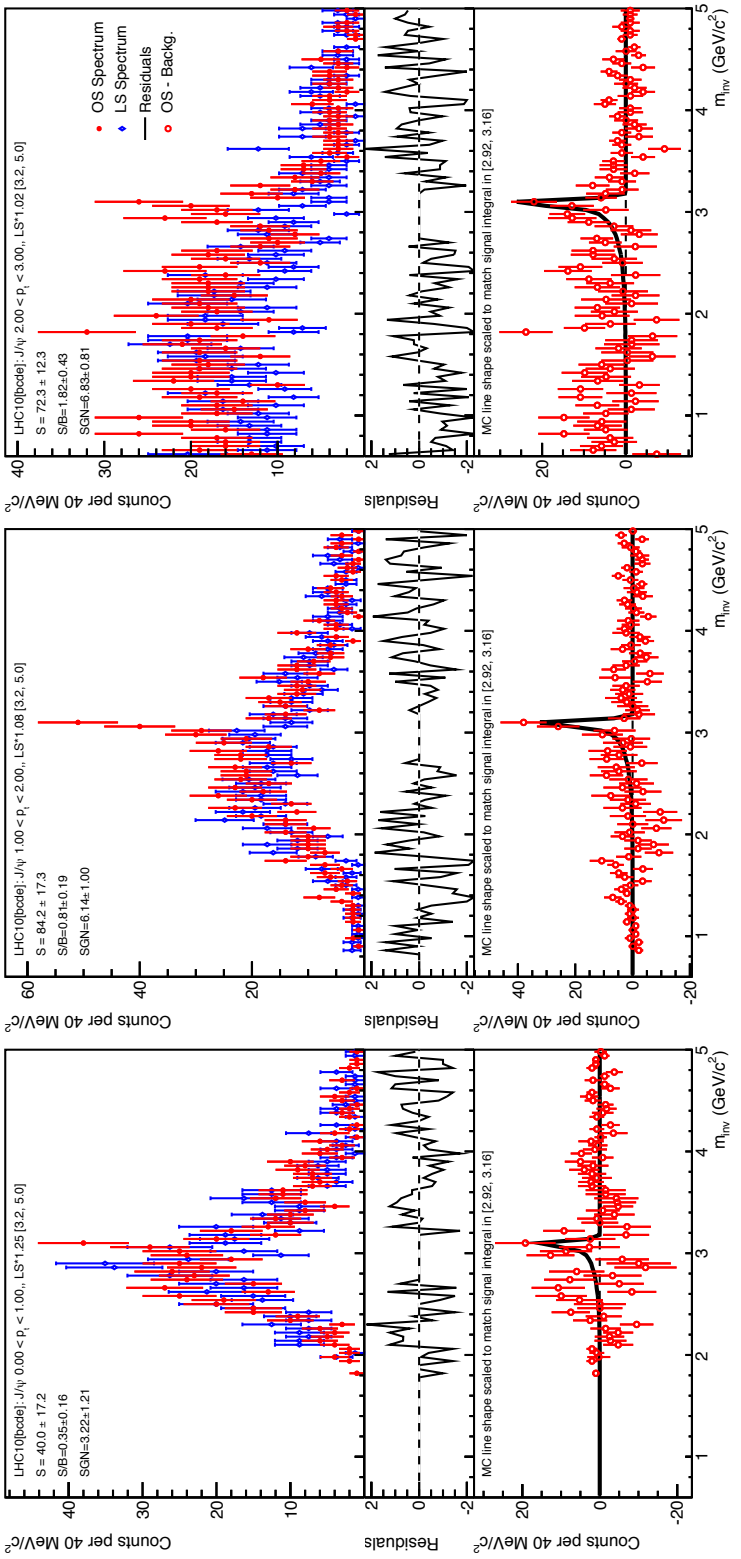

Figure D.15: The invariant mass spectra for the p_{t} intervals 0 to 1 GeV/c, 1 to 2 GeV/c and 2 to 3 GeV/c for the LS background subtraction procedure. For details, see Fig. 4.8 and Table 4.4.

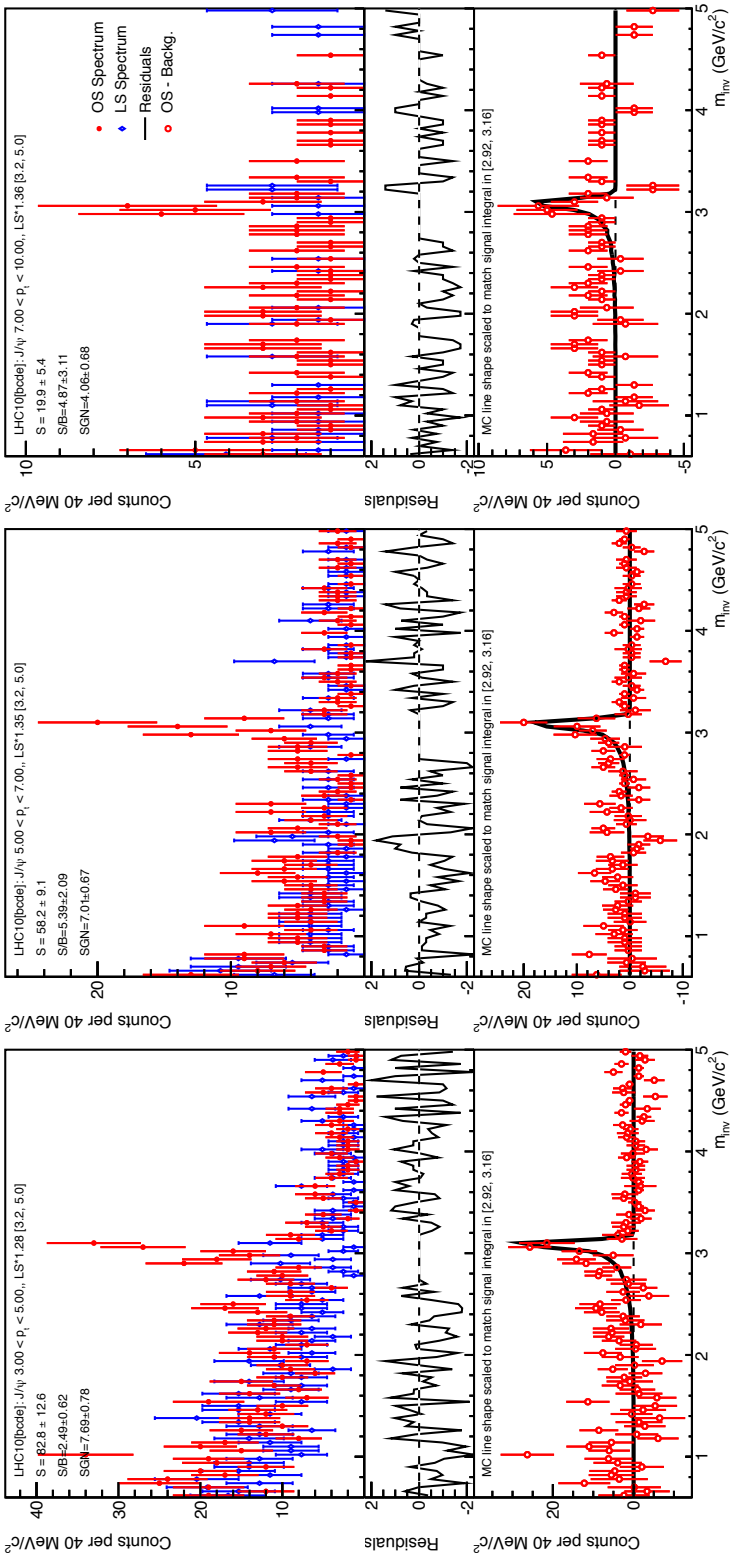

Figure D.16: The invariant mass spectra for the p_{t} intervals 3 to 4 GeV/c, 4 to 6 GeV/c and 7 to 10 GeV/c for the LS background subtraction procedure. For details, see Fig. 4.8 and Table 4.4.

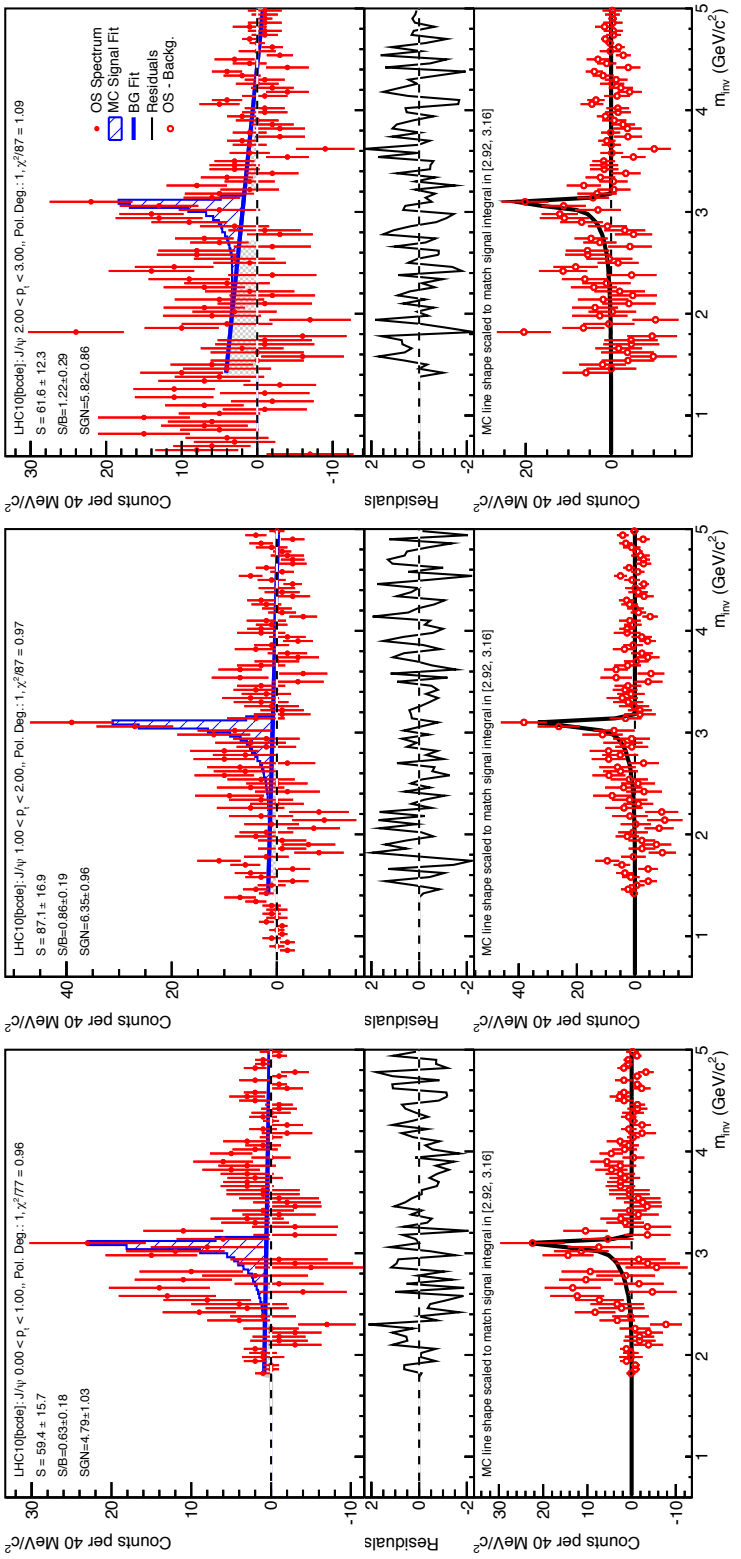

Figure D.17: The invariant mass spectra for the p_{t} intervals 0 to 1 GeV/c, 1 to 2 GeV/c and 2 to 3 GeV/c for the combined LS and fit background subtraction procedure. For details, see Fig. 4.8 and Table 4.4.

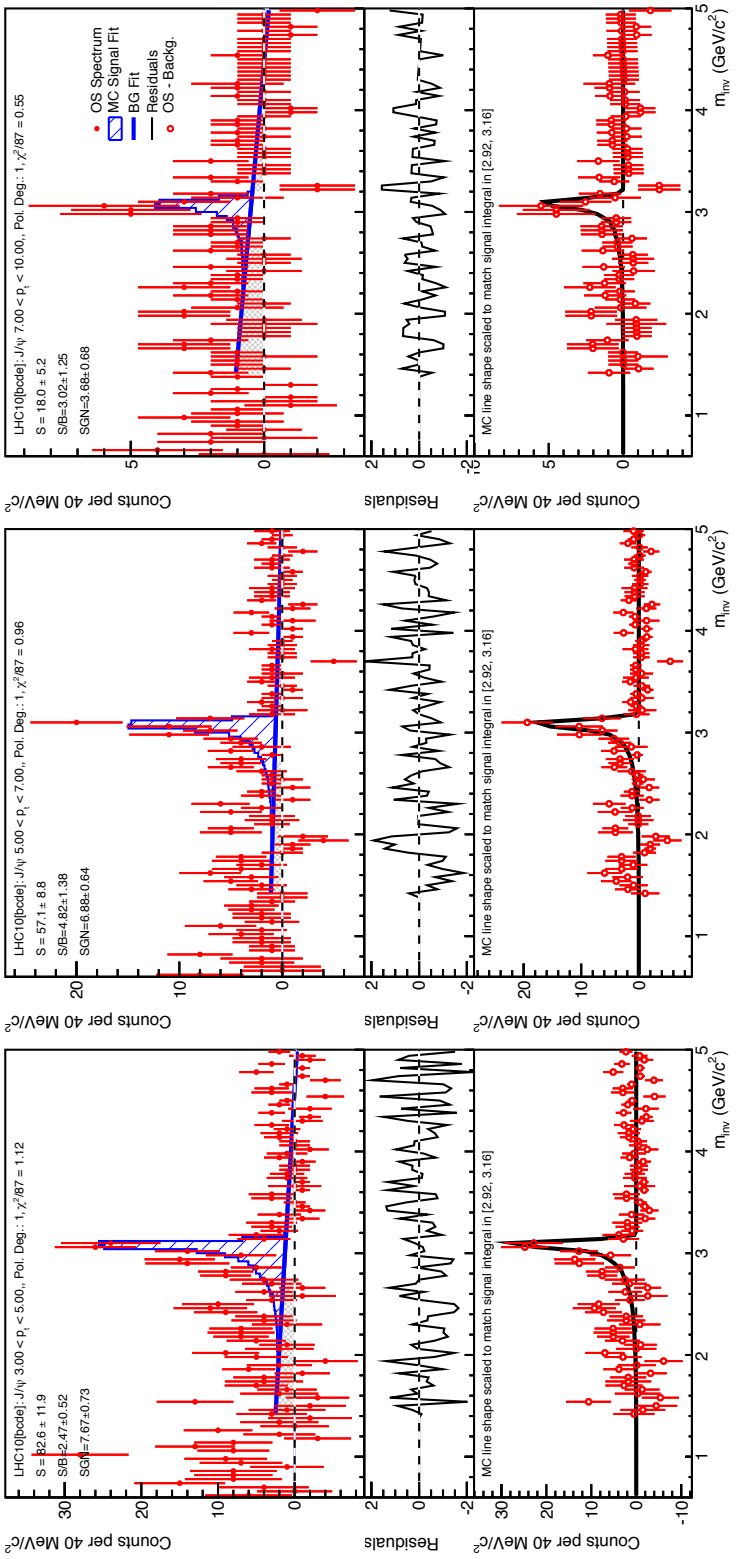

Figure D.18: The invariant mass spectra for the p_{t} intervals 0 to 1 GeV/c, 1 to 2 GeV/c and 2 to 3 GeV/c for the combined LS and fit background subtraction procedure. For details, see Fig. 4.8 and Table 4.4.

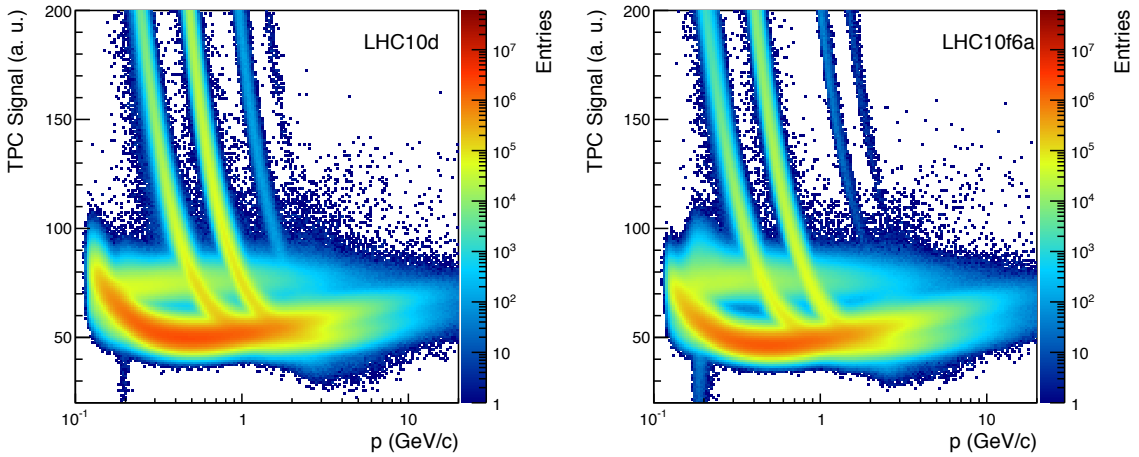

Figure D.19: Comparison of the dE/dx spectra from data (LHC10d, left panel) and MC (LHC10f6a, right panel).

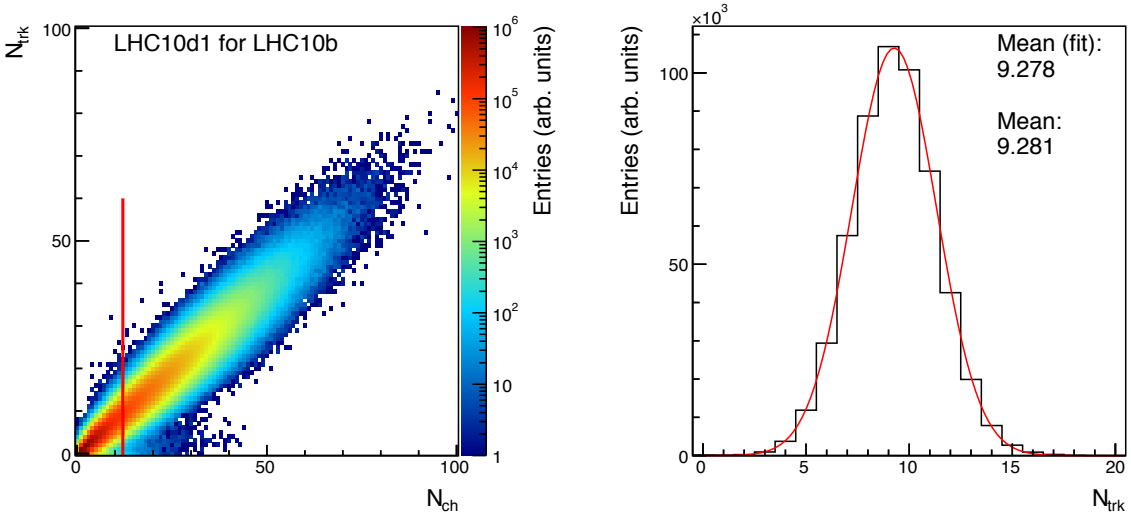

Figure D.20: As Fig. 5.4 for beam period LHC10b.

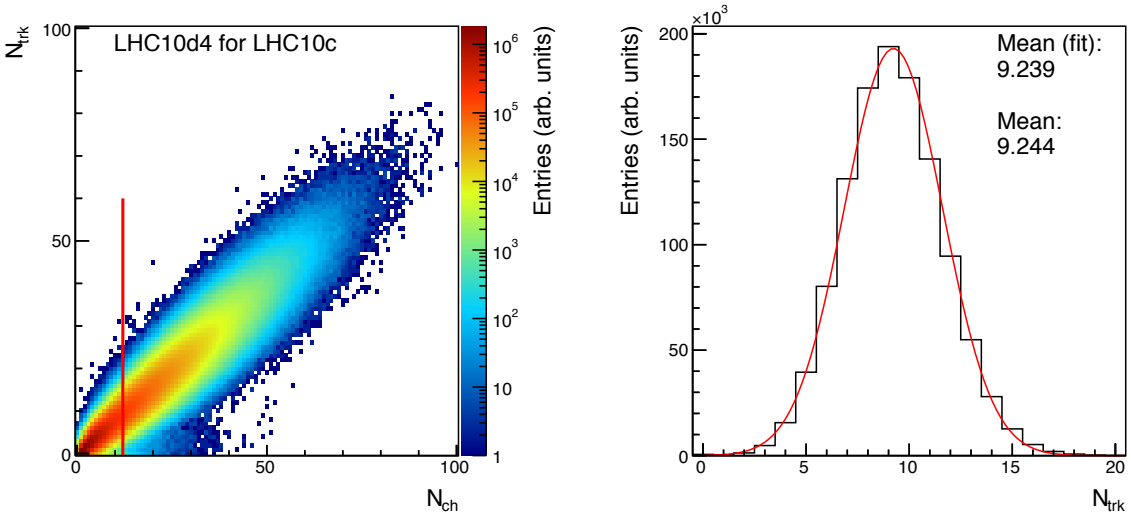

Figure D.21: As Fig. 5.4 for beam period LHC10c.

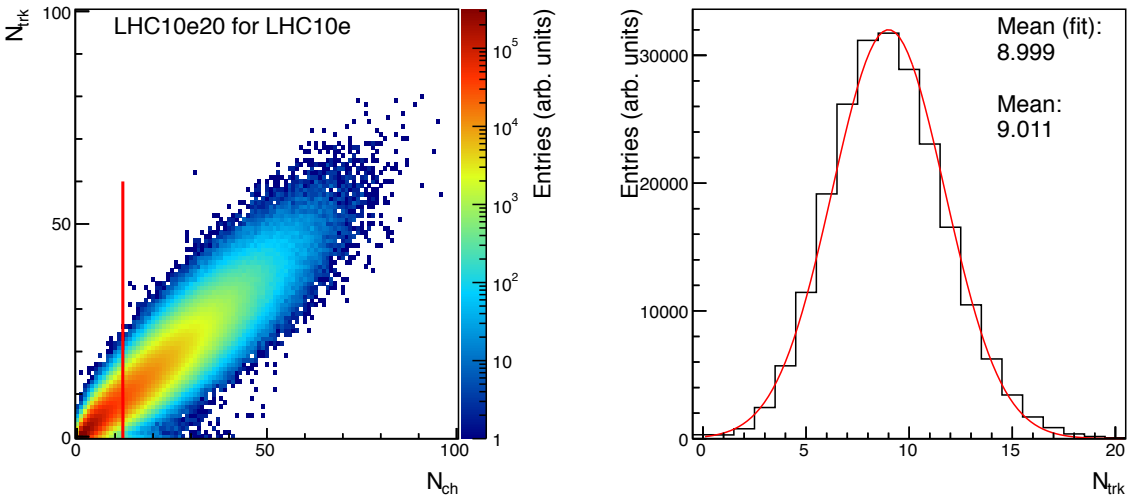

Figure D.22: As Fig. 5.4 for beam period LHC10e.

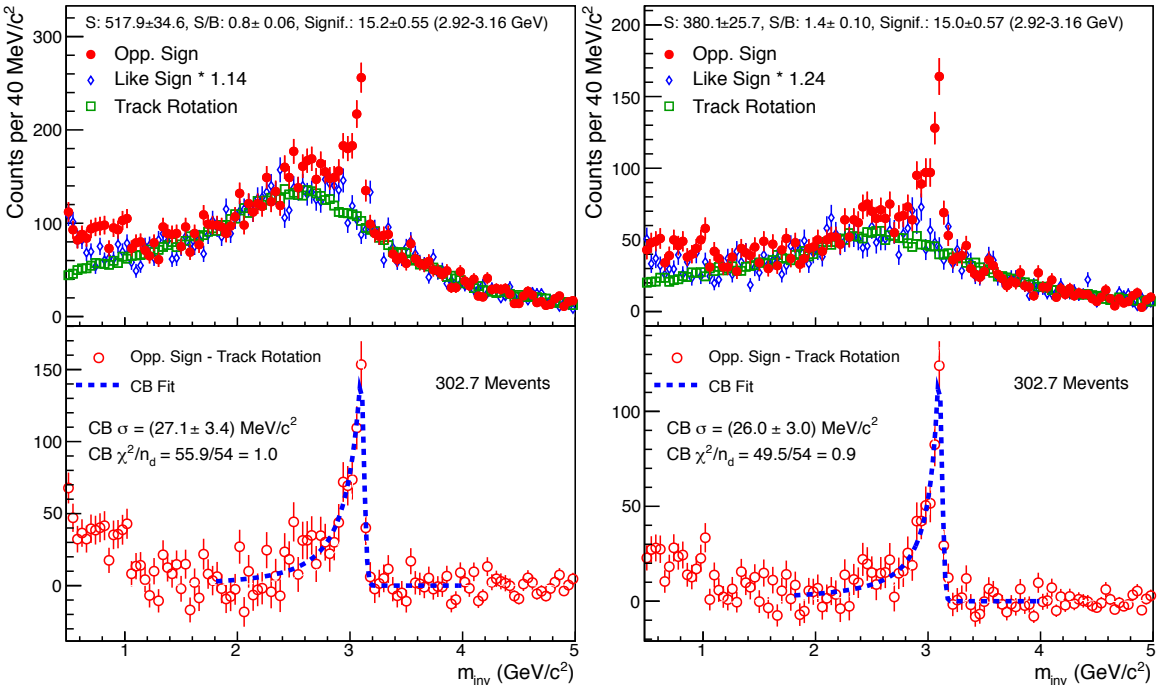

Figure D.23: As Fig. 5.6, just with a Crystal Ball Fit to the invariant mass spectrum after background subtraction.

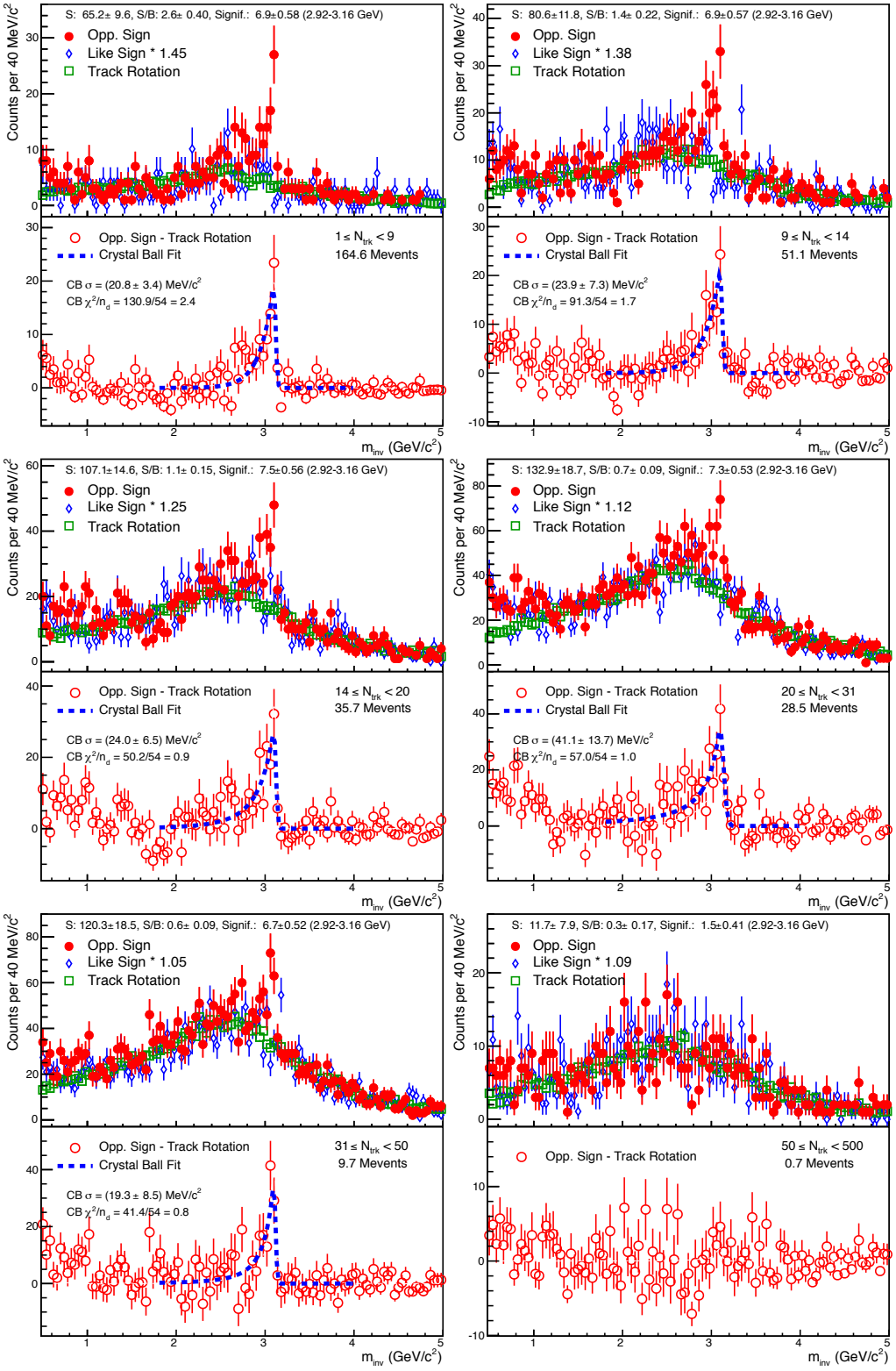

Figure D.24: As Fig. 5.7, just with a Crystal Ball Fit to the invariant mass spectrum after background subtraction.

Appendix E

Statistics

Statistical Errors in Histogrammed Data

When an event, a track, a pair of tracks or any other item is investigated during the data analysis, its properties are evaluated, e. g., the transverse momentum of a track or the invariant mass of a electron-positron pair is reconstructed. The result is then filled in a histogram with defined binning. Each investigation of such an item, for a given bin in one of these histograms, is equal to a Bernoulli process: the bin is either filled or not. Repeating a Bernoulli process many times for an experiment with a rare success rate, the probability distribution of the number of successes k is the Poisson distribution:

$$P(k) = \frac{\mu^{\mathrm{k}} \mathrm{e}^{-\mu}}{k!}. \tag{E.1}$$

It has only one single parameter, μ, which is also the first moment[1] of the Poisson distribution, its mean. The second moment, the variance of the distribution, turns out to be $\sigma^2 = \mu$; the width is $\sigma = \sqrt{\mu}$.

So for each bin in a given histogram the data analysis, i. e., the series of Bernoulli processes, yields as the result a number of successes, e. g., number of particles with a p_{t} falling in that bin. This value is taken as the mean μ in the bin and as the position where to plot the data point, the standard deviation $\sqrt{\mu}$ is given as the statistical uncertainty of the measurement.

[1] Probability distributions can be characterized by their moments: the jth moment of the random variable x about a fixed point x_0 is defined as the expectation value $E[X] = \int XP(X)d\mathrm{x}$ of $(x - x_0)^{\mathrm{j}}$ [236]. The first moment about zero, $E[x]$, is the mean of the distibution, the second moment about the mean, $E[(x - x_0)^2]$, is the variance σ^2.

Goodness-of-Fit Tests

After performing a fit procedure of a hypothesis function to the data it is necessary to quantify the quality of the fit. A common way to do this is to calculate the sum of the squared differences of the n measurements x_i and the expectation values μ_i, divided by the squared variance σ_i:

$$\chi^2 = \sum_{i=1}^{n} \frac{(x_\mathrm{i} - \mu_\mathrm{i})^2}{\sigma_\mathrm{i}^2}. \tag{E.2}$$

For a histogrammed data fit these independent measurements are the n bins of the histogram. A common method used in fit procedures to estimate the parameters is to search for the set with minimal χ^2. As discussed above, the histogrammed data is a vector of Poisson distributed numbers; hence, Eq. (E.2) becomes Pearson's χ^2 statistic [36]:

$$\chi^2 = \sum_{i=1}^{n} \frac{(x_\mathrm{i} - \mu_\mathrm{i})^2}{\mu_\mathrm{i}}. \tag{E.3}$$

If the hypothesis function is correct or at least a good description of the data, the χ^2 statistic will follow the χ^2 probability density function [36]. The first moment of the χ^2 PDF [237]

$$f(x) = \frac{\frac{1}{2}\left(\frac{x}{2}\right)^{\frac{n_\mathrm{d}}{2}-1} e^{-\frac{x}{2}}}{\Gamma\left(\frac{n_\mathrm{d}}{2}\right)}, \tag{E.4}$$

i. e. its mean, equals its single parameter n_d which is the number (positive integer) of degrees of freedom. Thus, χ^2/n_d, often refered to as reduced χ^2, should be equal to one for a good description of the data. In case of histogrammed data, n_d equals the number of independent data points minus the number of parameters of the fit function.

The Crystal Ball Function

The Crystal Ball function (named fter the Crystal Ball Collaboration) is a probability density function composed of a Gaussian core and a power-law tail at its lower end. Its definition is:

$$f(m) = N \cdot \begin{cases} e^{-\frac{t^2}{2}}, & \text{for} \quad t \geq -|\alpha| \\ \left(\frac{n}{|\alpha|}\right)^n e^{-\frac{\alpha^2}{2}} \left(\frac{n}{|\alpha|} - |\alpha| - t\right)^{-n}, & \text{for} \quad t < -|\alpha| \end{cases} \tag{E.5}$$

With $t = (m - m_0)/\sigma$ and where m is the mass, N the norm and m_0, σ, n and α the parameters of the function. Out of these, m_0 and σ are the mean and the standard deviation of the Gaussian, n is the exponent of the power law; α controls the transition of the two parts of the function. The Crystal Ball function is continous and has a continous first derivative [117].

Appendix F

List of Run Numbers

Below, the numbers of all analyzed runs are listed:

LHC10b:
117077, 116403, 116645, 115193, 116402, 115318, 116562, 117086, 117054, 115322, 115393, 116574, 116102, 115186, 114931, 116643, 117109, 115328, 116571, 117222, 117053, 116288, 117063, 117060, 117065, 115401, 117052, 117048, 117116, 115310, 117220, 117092, 117050, 117059, 117112, 117099

LHC10c:
120820, 120741, 120504, 119844, 119853, 120821, 119841, 120750, 120758, 119159, 119856, 119163, 120503, 120244, 120067, 120671, 120829, 119161, 120823, 120079, 119845, 119842, 120069, 120505, 120073, 120824, 119846, 120822, 120825, 119859, 120076, 120617, 119862, 120072, 119849, 120616

LHC10d:
125023, 124751, 125100, 125844, 126405, 125633, 125847, 122374, 122375, 126008, 126167, 125843, 125296, 125848, 125842, 126168, 125849, 125097, 125632, 126352, 126004, 125085, 125630, 125134, 126081, 125855, 126283, 126403, 126082, 126090, 126073, 126351, 126088, 126285, 126359, 125851, 126408, 126404, 126097, 126284, 126422, 125850, 126406, 126409, 126407, 126432, 126160, 126007, 126424, 126425, 126078, 126158

LHC10e:
127940, 127941, 128835, 128191, 128611, 128495, 128366, 128185, 128823, 130149, 128615, 129512, 128192, 128853, 127936, 129527, 128913, 128582, 129520, 130172, 129587, 129586, 129650, 130342, 129723, 127712, 130354, 128189, 129641, 129652, 129639, 128843, 128483,

128678, 129599, 129528, 128186, 130343, 129959, 128486, 129653, 129523, 128605, 128677, 128855, 127937, 129725, 127933, 128503, 130356, 129726, 129729, 129736, 130158, 130157, 129513, 129540, 129659, 129742, 129735, 130480, 128494, 129738, 129960, 130178, 129647, 129666, 127935, 129514, 129654, 129744, 127942, 128504, 128260, 128820, 128777, 128778, 128609, 127822, 128836, 129961, 128824, 130517, 130704, 130793, 130696, 130519, 130840, 130795, 130798, 130799, 130834, 128452

Bibliography

[1] M. Gell-Mann: A schematic model of baryons and mesons, Phys. Lett. **8(3)** (1964) 214.

[2] G. Zweig: An SU_3 model for strong interaction symmetry and its breaking. Part I, CERN-TH-401 (1964) 24.

[3] W. Nolting: Statistische Physik, Springer (2005).

[4] P. Dirac: The Quantum Theory of the Electron, Proc. R. Soc. Lond. **A(117)** (1928) 610.

[5] D. H. Perkins: Introduction to High Energy Physics, Cambridge University Press (2000).

[6] K. Bethge et al.: Elementarteilchen, Wissenschaftliche Buchgesellschaft, Darmstadt (1986).

[7] B. Povh et al.: Teilchen und Kerne, Springer (2004).

[8] M. E. Peskin et al.: An Introduction to Quantum Field Theory, Advanced Book Program, Westview Press, Boulder (Colorado), USA (1995).

[9] E. V. Shuryak: Quark-gluon plasma and hadronic production of leptons, photons and psions, Phys. Lett. **B78(1)** (1978) 150.

[10] Z. Fodor et al.: Critical point of QCD at finite T and mu, lattice results for physical quark masses, JHEP **04** (2004) 050, arXiv:hep-lat/0402006.

[11] M. A. Stephanov: QCD phase diagram: An overview, PoS **LAT2006** (2006) 024, arXiv:hep-lat/0701002.

[12] C.-Y. Wong: Introduction to High-Energy Heavy-Ion Collisions, World Scientific (1994).

[13] F. Becattini et al.: Energy and system size dependence of chemical freeze-out in relativistic nuclear collisions, Phys. Rev. **C73** (2006) 044905, arXiv:hep-ph/0511092.

[14] J. Cleymans et al.: Centrality dependence of thermal parameters deduced from hadron multiplicities in $Au + Au$ collisions at $\sqrt{s_{\mathrm{NN}}} = 130$ GeV, Phys. Rev. **C71(5)** (2005) 054901.

[15] P. Petreczky: QCD at non-zero temperature: Bulk properties and heavy quarks, Mod. Phys. Lett. **A25** (2010) 3081, arXiv:1009.5935.

[16] Y. Aoki et al.: The QCD transition temperature: results with physical masses in the continuum limit, Phys. Lett. **B643(1)** (2006) 46.

[17] Y. Aoki et al.: The QCD transition temperature: results with physical masses in the continuum limit II., JHEP **0906** (2009) 088, arXiv:0903.4155.

[18] P. Petreczky: Recent progress in lattice QCD at finite temperature, arXiv:0906.0502.

[19] J. C. Mather et al.: Calibrator Design for the COBE Far Infrared Absolute Spectrophotometer (FIRAS), The Astrophysical Journal **512(2)** (1999) 511.

[20] Particle Data Group: Particle Adventure (2008), URL `particleadventure.org`.

[21] P. V. Ruuskanen: Transverse Hydrodynamics with a First Order Phase Transition in Very High Energy Nuclear Collisions, Acta Physica Polonica **B18(6)** (1987) 551.

[22] F. Cooper et al.: Single-particle distribution in the hydrodynamic and statistical thermodynamic models of multiparticle production, Phys. Rev. **D10(1)** (1974) 186.

[23] J. Adams et al. (STAR Collaboration): Distributions of Charged Hadrons Associated with High Transverse Momentum Particles in pp and $Au + Au$ Collisions at $\sqrt{s_{\mathrm{NN}}} = 200$ GeV, Phys. Rev. Lett. **95(15)** (2005) 152301.

[24] S. S. Adler et al. (PHENIX Collaboration): Dense-Medium Modifications to Jet-Induced Hadron Pair Distributions in $Au + Au$ Collisions at $\sqrt{s_{\mathrm{NN}}} = 200$ GeV, Phys. Rev. Lett. **97(5)** (2006) 052301.

[25] K. Yagi et al.: Quark-Gluon Plasma, Cambridge University Press (2005).

[26] V. Koch: Aspects of chiral symmetry, Int. J. Mod. Phys. **E6** (1997) 203, arXiv:nucl-th/9706075.

[27] G. Agakishiev et al. (STAR Collaboration): System size and energy dependence of near-side di-hadron correlations, arXiv:1110.5800.

[28] M. Hauer: Statistical Fluctuations and Correlations in Hadronic Equilibrium Systems, Ph.D. thesis, University of Frankfurt, Germany (2010).

[29] S. Jeon et al.: Charged Particle Ratio Fluctuation as a Signal for Quark-Gluon Plasma, Phys. Rev. Lett. **85(10)** (2000) 2076.

[30] M. Stephanov et al.: Event-by-event fluctuations in heavy ion collisions and the QCD critical point, Phys. Rev. **D60(11)** (1999) 114028.

[31] S. Jacobs et al.: Comparing the Schrödinger and spinless Salpeter equations for heavy-quark bound states, Phys. Rev. **D33** (1986) 3338.

[32] S. L. Glashow et al.: Weak Interactions with Lepton-Hadron Symmetry, Phys. Rev. **D2(7)** (1970) 1285.

[33] M. K. Gaillard et al.: Rare decay modes of the K mesons in gauge theories, Phys. Rev. D **10** (1974) 897.

[34] J. J. Aubert et al.: Experimental Observation of a Heavy Particle J, Phys. Rev. Lett. **33(23)** (1974) 1404.

[35] J. E. Augustin et al.: Discovery of a Narrow Resonance in e^+e^- Annihilation, Phys. Rev. Lett. **33(23)** (1974) 1406.

[36] C. Amsler et al. (Particle Data Group): The Review of Particle Physics, Phys. Lett. **B667** (2008) 1.

[37] S. W. Herb et al.: Observation of a Dimuon Resonance at 9.5 GeV in 400-GeV Proton-Nucleus Collisions, Phys. Rev. Lett. **39(5)** (1977) 252.

[38] D. B. Lichtenberg et al.: Interpretation of the $\Upsilon(9.5)$ as Evidence for Another Quark, Phys. Rev. Lett. **39(25)** (1977) 1592.

[39] W. R. Innes et al.: Observation of Structure in the Υ Region, Phys. Rev. Lett. **39(20)** (1977) 1240.

[40] F. Abe et al.: Identification of top quarks using kinematic variables, Phys. Rev. **D52(5)** (1995) R2605.

[41] A. Quadt: Top quark physics at hadron colliders, Eur. Phys. J. **C48(3)** (2006) 835.

[42] I. Bigi et al.: Production and decay properties of ultra-heavy quarks, Phys. Lett. **B181(1-2)** (1986) 157.

[43] H. Satz: Charm and beauty in a hot environment, arXiv:hep-ph/0602245.

[44] G. T. Bodwin: Inclusive quarkonium production and the NRQCD factorization approach, J. Korean Phys. Soc. **45** (2004) S306, arXiv:hep-ph/0312173.

[45] J. C. Collins et al.: Factorization of Hard Processes in QCD, Adv. Ser. Direct. High Energy Phys. **5** (1988) 1, arXiv:hep-ph/0409313.

[46] C. Brenner Mariotto et al.: Soft and hard QCD dynamics in hadroproduction of charmonium, Eur. Phys. J. **C23** (2002) 527, arXiv:hep-ph/0111379.

[47] J. P. Lansberg: J/ψ, ψ' and Υ production at hadron colliders: A Review, Int. J. Mod. Phys. **A21** (2006) 3857, arXiv:hep-ph/0602091.

[48] S. S. Adler et al. (PHENIX Collaboration): J/ψ Production from Proton-Proton Collisions at $\sqrt{s} = 200$ GeV, Phys. Rev. Lett. **92(5)** (2004) 051802.

[49] J. P. Lansberg: On the mechanisms of heavy-quarkonium hadroproduction, Eur. Phys. J. **C61** (2009) 693, arXiv:0811.4005.

[50] E. L. Berger et al.: Inelastic photoproduction of J/ψ and Υ by gluons, Phys. Rev. **D23(7)** (1981) 1521.

[51] J. F. Amundson et al.: Quantitative tests of color evaporation: Charmonium production, Phys. Lett. **B390** (1997) 323, arXiv:hep-ph/9605295.

[52] G. T. Bodwin et al.: Rigorous QCD analysis of inclusive annihilation and production of heavy quarkonium, Phys. Rev. **D51** (1995) 1125, arXiv:hep-ph/9407339.

[53] E. Braaten et al.: Production of Heavy Quarkonium in High-Energy Colliders, Annual Review of Nuclear and Particle Science **46(1)** (1996) 197.

[54] T. Kuhr (CDF Collaboration): Upsilon polarization measurement at CDF, PoS (DIS 2010) 159 (2010).

[55] F.Abe et al. (CDF Collaboration): J/ψ and $\psi(2S)$ Production in pp Collisions at $\sqrt{s} =$ 1.8 TeV, Phys. Rev. Lett. **79(4)** (1997) 572.

[56] E. Braaten et al.: Fragmentation production of J/ψ and ψ' at the Tevatron, Phys. Lett. **B333** (1994) 548, arXiv:hep-ph/9405407.

[57] H. Haberzettl et al.: Possible solution of the J/ψ production puzzle, Phys. Rev. Lett. **100** (2008) 032006, arXiv:0709.3471.

[58] P. Artoisenet et al.: Υ Production at Fermilab Tevatron and LHC Energies, Phys. Rev. Lett. **101** (2008) 152001, arXiv:0806.3282.

[59] J. C. Collins et al.: Angular distribution of dileptons in high-energy hadron collisions, Phys. Rev. **D16(7)** (1977) 2219.

[60] J. P. Lansberg: QCD corrections to J/ψ polarisation in pp collisions at RHIC, arXiv:1003.4319.

[61] P. Faccioli et al.: New approach to quarkonium polarization studies, Phys. Rev. **D81(11)** (2010) 111502.

[62] The ALICE Collaboration: ALICE: Physics Performance Report, Volume II, J. Phys. **G32(10)** (2006) 1295.

[63] M. Kramer: Quarkonium production at high-energy colliders, Prog. Part. Nucl. Phys. **47** (2001) 141, arXiv:hep-ph/0106120.

[64] V. A. Khoze et al.: Inelastic J/ψ and Υ hadroproduction, Eur. Phys. J. **C39** (2005) 163, arXiv:hep-ph/0410020.

[65] M. Butenschoen et al.: World data of J/ψ production consolidate NRQCD factorization at NLO, Phys.Rev. **D84** (2011) 051501, arXiv:1105.0820.

[66] M. Butenschoen et al.: J/ψ production in NRQCD: A global analysis of yield and polarization, 11 pages, 49 figures, to appear in the proceedings of the 'Ringberg Workshop: New Trends in HERA Physics 2011', Ringberg Castle, Germany, 25-28 September, 2011, arXiv:1201.3862.

[67] A. Abulencia et al. (CDF Collaboration): Polarizations of J/ψ and $\psi(2S)$ Mesons Produced in $p\bar{p}$ Collisions at $\sqrt{s} = 1.96$ TeV, Phys. Rev. Lett. **99(13)** (2007) 132001.

[68] B. Abelev et al. (ALICE Collaboration Collaboration): J/ψ Polarization in pp Collisions at $\sqrt{s}$=7 TeV, Phys. Rev. Lett. **108** (2012) 082001, arXiv:1111.1630.

[69] T. Sjöstrand et al.: A multiple-interaction model for the event structure in hadron collisions, Phys. Rev. **D36** (1987) 2019.

[70] T. Sjöstrand et al.: High-energy-physics event generation with PYTHIA 6.1, Comp. Phys. Comm. **135(2)** (2001) 238.

[71] T. Sjostrand et al.: PYTHIA 6.4 Physics and Manual, JHEP **0605** (2006) 026, arXiv:hep-ph/0603175.

[72] T. Åkesson et al.: Double parton scattering in pp collisions at $\sqrt{s}$=63 GeV, Z. Phys. C **34** (1987) 163, 10.1007/BF01566757.

[73] T. Aaltonen et al. (CDF Collaboration): Measurement of particle production and inclusive differential cross sections in $p\bar{p}$ collisions at $\sqrt{s} = 1.96$ TeV, Phys. Rev. **D79** (2009) 112005.

[74] P. Bartalini et al.: Multiple partonic interactions at the LHC. Proceedings, 1st International Workshop, MPI'08, Perugia, Italy, October 27-31, 2008, arXiv:1003.4220.

[75] S. Porteboeuf et al.: J/ψ yield vs. multiplicity in proton-proton collisions at the LHC, Nucl. Phys. Proc. Suppl. **214** (2011) 181, arXiv:1012.0719.

[76] M. Aguilar-Benitez et al. (LEBC-EHS Collaboration): Comparative Properties of 400 GeV/c Proton - Proton Interactions With and Without Charm Production, Z. Phys. **C41** (1988) 191.

[77] C. Kom et al.: Pair production of J/ψ as a probe of double parton scattering at LHCb, Phys. Rev. Lett. **107** (2011) 082002, arXiv:1105.4186.

[78] G. Aad et al. (ATLAS Collaboration): Measurement of the differential cross-sections of inclusive, prompt and non-prompt J/ψ production in proton-proton collisions at $\sqrt{s} = 7$ TeV, Nucl.Phys. **B850** (2011) 387, arXiv:1104.3038.

[79] V. Khachatryan et al. (CMS Collaboration): Prompt and non-prompt J/ψ production in pp collisions at $\sqrt{s} = 7$ TeV, Eur. Phys. J. **C71** (2011) 1575, arXiv:1011.4193.

[80] D. Acosta et al. (CDF Collaboration): Measurement of the J/ψ meson and b-hadron production cross sections in pp collisions at $\sqrt{s} = 1960$ GeV, Phys. Rev. **D71(3)** (2005) 032001.

[81] N. Brambilla et al.: Heavy quarkonium: progress, puzzles, and opportunities, arXiv:1010.5827.

[82] R. Aaij et al. (LHCb Collaboration): Measurement of J/ψ production in pp collisions at $\sqrt{s}$=7 TeV, Eur.Phys.J. **C71** (2011) 1645, arXiv:1103.0423.

[83] D. de Florian et al.: Nuclear parton distributions at next to leading order, Phys. Rev. **D69** (2004) 074028.

[84] K. Eskola et al.: The scale dependent nuclear effects in parton distributions for practical applications, Eur. Phys. J. **C9** (1999) 61.

[85] M. Hirai et al.: Determination of nuclear parton distribution functions and their uncertainties at next-to-leading order, Phys. Rev. **C76** (2007) 065207, arXiv:0709.3038.

[86] K. J. Eskola et al.: An improved global analysis of nuclear parton distribution functions including RHIC data, JHEP **2008(07)** (2008) 102.

[87] C. Lourenco et al.: Energy dependence of J/ψ absorption in proton-nucleus collisions, JHEP **02** (2009) 014, arXiv:0901.3054.

[88] R. Arnaldi et al. (NA60 Collaboration): J/ψ production in proton-nucleus collisions at 158 and 400 GeV, arXiv:1004.5523.

[89] R. Arnaldi (NA60 Collaboration): J/ψ production in p-A and A-A collisions at fixed target experiments, Nucl. Phys. **A830** (2009) 345c, arXiv:0907.5004.

[90] N. Armesto et al.: Charmonium suppression in lead lead collisions: Is there a break in the J/ψ cross-section?, Phys. Rev. **C59** (1999) 395, arXiv:hep-ph/9807258.

[91] A. Capella et al.: J/ψ suppression at $\sqrt{s} = 200$ GeV in the comovers interaction model, Eur. Phys. J. **C42** (2005) 419, arXiv:hep-ph/0505032.

[92] A. Capella et al.: Charmonium dissociation and recombination at RHIC and LHC, Eur. Phys. J. **C58** (2008) 437, arXiv:0712.4331.

[93] E. G. Ferreiro: Charmonium Dissociation and Recombination: Cold Effects, arXiv:0805.2753.

[94] T. Lang: Charmonium dynamics in the UrQMD transport model, Poster 531 at Quark Matter 2011, Annecy, France, May 26, 2011 (2011).

[95] T. Lang: Private Communication, (18.7.2011).

[96] T. Matsui et al.: J/ψ Suppression by Quark-Gluon Plasma Formation, Phys. Lett. **B178** (1986) 416.

[97] M. Asakawa et al.: J/ψ and η_c in the Deconfined Plasma from Lattice QCD, Phys. Rev. Lett. **92** (2004) 012001.

[98] P. Braun-Munzinger et al.: Charmonium from Statistical Hadronization of Heavy Quarks – a Probe for Deconfinement in the Quark-Gluon Plasma, arXiv:0901.2500.

[99] P. Braun-Munzinger et al.: (Non)thermal aspects of charmonium production and a new look at J/ψ suppression, Phys. Lett. **B490** (2000) 196, arXiv:nucl-th/0007059.

[100] S. S. Adler et al. (PHENIX Collaboration): Centrality dependence of charm production from single electrons measurement in Au + Au collisions at $\sqrt{s_{\rm NN}} = 200$ GeV, Phys. Rev. Lett. **94** (2005) 082301, arXiv:nucl-ex/0409028.

[101] A. Andronic et al.: Statistical hadronization of charm in heavy-ion collisions at SPS, RHIC and LHC, Phys. Lett. **B571** (2003) 36, arXiv:nucl-th/0303036.

[102] R. L. Thews: In-medium formation of quarkonium, J. Phys. **G32** (2006) S401, arXiv:hep-ph/0605322.

[103] R. L. Thews: Quarkonium formation in statistical and kinetic models, Eur. Phys. J. **C43** (2005) 97, arXiv:hep-ph/0504226.

[104] R. L. Thews et al.: Momentum spectra of charmonium produced in a quark-gluon plasma, Phys. Rev. **C73** (2006) 014904, arXiv:nucl-th/0505055.

[105] D. d'Enterria (CMS Collaboration): High-density QCD with CMS at the LHC, J. Phys. **G35(10)** (2008) 104039.

[106] N. Armesto: Predictions for the heavy-ion programme at the Large Hadron Collider, arXiv:0903.1330.

[107] J. Uphoff et al.: Production and elliptic flow of heavy quarks at RHIC and LHC within a partonic transport model, J. Phys. **230(1)** (2010) 012004.

[108] J. Uphoff et al.: Heavy quark production at RHIC and LHC within a partonic transport model, Phys. Rev. **C82** (2010) 044906, arXiv:1003.4200.

[109] P. Levai et al.: Thermal charm production by massive gluons and quarks, Phys. Rev. **C56** (1997) 2707, arXiv:hep-ph/9704360.

[110] M. C. Aberu et al.: NA50 Proposal, CERN/SPSLC 91-55, SPSLC-P265-Rev. (1991).

[111] A. Baldit et al.: NA60 Proposal, CERN/SPSC 2000-010, SPSC-P316 (2000).

[112] R. J. Glauber et al.: High-Energy Scattering of Protons by Nuclei, Nucl. Phys. **B21(1)** (1970) 135.

[113] R. Arnaldi et al. (NA60 Collaboration): J/ψ Production in Indium-Indium Collisions at 158 *GeV/Nucleon*, Phys. Rev. Lett. **99(13)** (2007) 132302.

[114] K. Adcox et al.: PHENIX detector overview, Nucl. Instr. Meth. **A499(2-3)** (2003) 469, the Relativistic Heavy Ion Collider Project: RHIC and its Detectors.

[115] A. Adare et al. (PHENIX Collaboration): J/ψ production vs centrality, transverse momentum, and rapidity in Au+Au collisions at $\sqrt{s_{\rm NN}}$ = 200 GeV, Phys. Rev. Lett. **98** (2007) 232301, arXiv:nucl-ex/0611020.

[116] S. Chatrchyan et al. (CMS Collaboration): Indications of suppression of excited Υ states in PbPb collisions at $\sqrt{s_{\rm NN}}$ = 2.76 TeV, Phys. Rev. Lett. **107** (2011) 052302, arXiv:1105.4894.

[117] J. E. Gaiser: Charmonium Spectroscopy from Radiative Decays of the J/ψ and ψ', Ph.D. thesis, SLAC-0255, Stanford University, USA (1982).

[118] B. Abelev et al. (ALICE Collaboration): J/ψ production at low transverse momentum in Pb-Pb collisions at $\sqrt{s_{\rm NN}}$ = 2.76 TeV, Submitted to Phys. Rev. Lett., arXiv:1202.1383.

[119] S. Chatrchyan et al. (CMS Collaboration): Suppression of non-prompt J/ψ, prompt J/ψ, and Y(1S) in PbPb collisions at $\sqrt{s_{\rm NN}}$ = 2.76 TeV, arXiv:1201.5069.

[120] A. Andronic et al.: The thermal model on the verge of the ultimate test: particle production in Pb-Pb collisions at the LHC, J.Phys.G **G38** (2011) 124081, arXiv:1106.6321.

[121] X. Zhao et al.: Medium Modifications and Production of Charmonia at LHC, Nucl. Phys. **A859** (2011) 114, arXiv:1102.2194.

[122] Y.-p. Liu et al.: J/ψ Transverse Momentum Distribution in High Energy Nuclear Collisions at RHIC, Phys. Lett. **B678** (2009) 72, arXiv:0901.2757.

[123] CERN Document Server: URL `cdsweb.cern.ch`.

[124] L. Evans et al.: LHC Machine, Journal of Instrumentation **3(08)** (2008) S08001.

[125] D. G. d'Enterria: Hard scattering cross sections at LHC in the Glauber approach: From p p to p A and A A collisions, arXiv:nucl-ex/0302016.

[126] M. G. Poghosyan et al. (ALICE Collaboration): Diffraction dissociation in proton-proton collisions at $\sqrt{s}$ = 0.9 TeV, 2.76 TeV and 7 TeV with ALICE at the LHC, arXiv:1109.4510.

[127] CERN LHC LHC Programme Coordination Web Pages: URL `http://lpc.web.cern.ch/lpc`.

[128] K. Aamodt et al.: The ALICE experiment at the CERN LHC , J. Inst. **3** (2008) S08002.

[129] The ALICE Collaboration: First proton-proton collisions at the LHC as observed with the ALICE detector: measurement of the charged-particle pseudorapidity density at $\sqrt{s} = 900$ GeV, Eur. Phys. J. **C65(1-2)** (2010) 111.

[130] G. Aad (ATLAS Collaboration): The ATLAS Experiment at the CERN Large Hadron Collider, JINST **3** (2008) S08003.

[131] C. Amsler et al. (CMS Collaboration): Mechanical design and material budget of the CMS barrel pixel detector, JINST **4** (2009) P05003.

[132] A. A. J. Augusto et al. (LHCb Collaboration): The LHCb Detector at the LHC, JINST **3(08)** (2008) S08005.

[133] L. Betev et al.: Definition of the ALICE Coordinate System and Basic Rules for Subdetector Components Numbering, ALICE-INT **038**.

[134] J. Wiechula: Commisioning and Calibration of the ALICE-TPC, Ph.D. thesis, University of Frankfurt, Germany (2008).

[135] The ALICE Collaboration: Dimuon Forward Spectrometer Technical Design Report, CERN/LHCC 99-22 (1999).

[136] The ALICE Collaboration: Dimuon Forward Spectrometer Technical Design Report Addendum, CERN/LHCC 2000-046 (2000).

[137] P. Giubellino: Heavy Ion Physics at the LHC, arXiv:nucl-ex/0809.1062.

[138] The ALICE Collaboration: ITS Technical Design Report, CERN/LHCC 99-12 (1999).

[139] The ALICE Collaboration: TPC Technical Design Report, CERN/LHCC 2000-001 (2000).

[140] The ALICE Collaboration: ALICE Time Projection Chamber, CERN-Poster-2002-045 (2002).

[141] R. E. Bosch et al.: The ALTRO chip: a 16-channel A/D converter and digital processor for gas detectors, IEEE Trans. Nucl. Sci. **50** (2003) 2460.

[142] The ALICE Collaboration: TRD Technical Design Report, CERN/LHCC 2001-021 (2001).

[143] A. Andronic: Electron identification performance with ALICE TRD prototypes, Nucl. Instr. Meth. **A522** (2004) 40, arXiv:physics/0402131v1.

[144] The ALICE Collaboration: Trigger, Data Acquisition, High-Level Trigger and Control System Technical Design Report, CERN/LHCC 2003-062 (2004).

[145] F. Ragusa et al.: Tracking at LHC, New Journal of Physics **9(9)** (2007) 336.

[146] V. L. Ginzburg et al.: The Radiation of an Uniformly Moving Electron Passing the Interface Between two Media, Zh. Eksp. Teor. Fiz. **16** (1946) 150.

[147] P. Goldsmith et al.: Optical Transition Radiation from Protons Entering Metal Surfaces, Phil. Mag. **4** (1959) 836.

[148] M. L. Cherry et al.: Transition radiation from relativistic electrons in periodic radiators, Phys. Rev. **D10(11)** (1974) 3594.

[149] B. Dolgoshein: Transition Radiation Detectors, Nucl. Inst. Meth. **A326(3)** (1993) 434.

[150] H. Bethe et al.: On the Stopping of Fast Particles and on the Creation of Positive Electrons, Proc. R. Soc. Lond. A 1 **146(856)** (1934) 83.

[151] W. Heitler: The Quantum Theory of Radiation, Oxford University Press (1954).

[152] W. Adam et al.: RESEARCH NOTE FROM COLLABORATION: Reconstruction of electrons with the Gaussian-sum filter in the CMS tracker at the LHC, J. Phys. **G31** (2005) 9, arXiv:physics/0306087.

[153] R. E. Kalman: A New Approach to Linear Filtering and Prediction Problems, Transactions of the ASME–Journal of Basic Engineering **82(D)** (1960) 35.

[154] G. Welch et al.: An Introduction to the Kalman Filter, TR 95-041 (2006).

[155] P. Billoir: Track Fitting with Multiple Scattering: A New Method, Nucl. Instr. Meth. **225** (1984) 352.

[156] R. Frühwirth: Application of Kalman Filtering to Track and Vertex Fitting, Nucl. Instr. Meth. **A262** (1987) 444.

[157] B. Hippolyte: Bulk matter physics and its future at the Large Hadron Collider, Eur. Phys. J. **C62** (2009) 237, arXiv:0901.3176.

[158] E. Bouhova-Thacker et al.: Electron bremsstrahlung recovery in ATLAS tracking using Dynamic Noise Adjustment, PoS (ACAT) 046 (2007).

[159] R. Frühwirth: Track fitting with non-Gaussian noise, Comp. Phys. Comm. **100(1-2)** (1997) 1.

[160] R. Frühwirth: A Gaussian-mixture approximation of the Bethe-Heitler model of†electron energy loss by bremsstrahlung, Comp. Phys. Comm. **154(2)** (2003) 131.

[161] T. M. Atkinson: Electron Reconstruction with the ATLAS Inner Detector, Ph.D. thesis, University of Melbourne, Australia (2006).

[162] W. Adam et al.: Reconstruction of Electrons with the Gaussian-Sum Filter in the CMS Tracker at the LHC, CMS NOTE 2005/001 (2005).

[163] The ATLAS Collaboration: Expected performance of the ATLAS experiment: detector, trigger and physics, CERN, Geneva, Swizerland (2009).

[164] The ATLAS Collaboration: Technical Design Report, CERN/LHCC 99-14 (1999).

[165] The CMS Collaboration: Technical Proposal, CERN/LHCC 94-38 (1994).

[166] T. Cornelissen et al.: The new ATLAS track reconstruction (NEWT), J. Phys. **119(3)** (2008) 032014.

[167] V. Kartvelishvili: Electron bremsstrahlung recovery in ATLAS, Nucl. Phys. **B172** (2007) 208, proceedings of the 10th Topical Seminar on Innovative Particle and Radiation Detectors.

[168] H. Gjersdal: Invariant mass determination using the output from a specialized electron track reconstruction alorithm, Master's thesis, University of Melbourne (2008).

[169] S. Baffioni et al.: Electron Reconstruction in CMS, CMS NOTE 2006/40 (2006).

[170] V. Kartvelishvili: Private Communication, (12.8.2010).

[171] S. A. Tampe: Optimierung der Rekonstruktionsparameter zur Messung von Quarkonia im zentralen ALICE Detektor, Master's thesis, University of Frankfurt (2011).

[172] W. Sommer et al.: Quarkonia Measurements with the Central Detectors of ALICE, IJMPE **16(7-8)** (2007) 2484, arXiv:nucl-ex/0702045v1.

[173] K. Aamodt et al. (ALICE Collaboration): Rapidity and transverse momentum dependence of inclusive J/ψ production in pp collisions at $\sqrt{s} = 7$ TeV, Phys. Lett. **B704** (2011) 442, arXiv:1105.0380.

[174] ROOT Website: URL `root.cern.ch`.

[175] The ALICE Collaboration: Computing Technical Design Report, CERN/LHCC 2005-18 (2005).

[176] The ALICE Collaboration: ALICE: Physics Performance Report, Volume I, J. Phys. **G30(11)** (2004) 1517.

[177] M. Gyulassy et al.: HIJING 1.0: A Monte Carlo program for parton and particle production in high-energy hadronic and nuclear collisions, Comput. Phys. Commun. **83** (1994) 307, arXiv:nucl-th/9502021.

[178] CERN Computing and Networks Division: GEANT – Detector description and simulation tool, CERN Program Library Long Write-up W5013 (1993).

[179] S. Agostinelli et al.: G4–a simulation toolkit, Nucl. Instr. Meth. **A506(3)** (2003) 250.

[180] A. Fassò et al.: The FLUKA code: present applications and future developments, Proc. of Computing in High Energy and Nuclear Physics, La Jolla, California (2003).

[181] S. Bagnasco et al.: AliEn: ALICE environment on the GRID, J. Phys. **119(6)** (2008) 062012.

[182] P. Z. Skands: Tuning Monte Carlo Generators: The Perugia Tunes, Phys. Rev. **D82** (2010) 074018, arXiv:1005.3457.

[183] D. Stocco and others: Quarkonia detection with the ALICE Muon Spectrometer in pp collisions at $\sqrt{s}$ =14 TeV, ALICE-INT **029**.

[184] K. Aamodt et al. (ALICE Collaboration): Charged-Particle Multiplicity Measurement in Proton-Proton Collisions at $\sqrt{s} = 0.9$ and 2.36 TeV with ALICE at LHC, Eur. Phys. J. **C68** (2010) 89.

[185] B. Abelev et al. (ALICE Collaboration): Measurement of Inelastic, Single and Double Diffraction Cross Sections in Proton-Proton Collisions at LHC with ALICE, paper in preparation .

[186] K. Oyama (ALICE Collaboration): Cross section normalization in proton-proton collisions at $\sqrt{s} = 2.76$ TeV and 7 TeV, with ALICE at LHC, arXiv:1107.0692.

[187] M. Gagliardi (ALICE Collaboration): Measurement of reference cross sections in pp and Pb-Pb collisions at the LHC in van der Meer scans with the ALICE detector, arXiv:1109.5369.

[188] S. van der Meer: Calibration of the effective beam height in the ISR, Technical Report CERN-ISR-PO-68-31., CERN, Geneva (1968), URL `http://cdsweb.cern.ch/record/296752`.

[189] A. Bernhard: Effizienz-Studie zur Messung von J/ψ mit den zentralen ALICE-Detektoren, Master's thesis, University of Frankfurt (2011).

[190] F. Kramer: Studie zur Messung von Quarkonia mit dem ALICE-TRD und Aufbau eines Teststandes für seine Auslesekammern, Master's thesis, University of Frankfurt (2006).

[191] J. Book: Zentralitätsabhängigkeit der K^0_s-Produktion in relativistischen Schwerionenkollisionen, Master's thesis, University of Frankfurt (2009).

[192] B. Abelev et al. (ALICE Collaboration): J/ψ Production as a Function of Charged Particle Multiplicity in pp Collisions at $\sqrt{s} = 7$ TeV, Submitted to Phys. Lett. B (2012), arXiv:1202.2816.

[193] R. Vogt: Cold nuclear matter effects on J/ψ and Υ production at energies available at the CERN Large Hadron Collider (LHC), Phys. Rev. C **81** (2010) 044903.

[194] R. Vogt: Private Communication, (23.2.2012).

[195] J. Lansberg: Total J/ψ and Upsilon production cross section at the LHC: theory vs. experiment, PoS **ICHEP2010** (2010) 206, arXiv:1012.2815.

[196] S. J. Brodsky et al.: Heavy-quarkonium production in high energy proton-proton collisions at RHIC, Phys. Rev. D **81** (2010) 051502.

[197] J. Lansberg: Private Communication, (2.3.2012).

[198] A. Adare et al. (PHENIX Collaboration): J/ψ Production versus Transverse Momentum and Rapidity in $p+p$ Collisions at $\sqrt{s} = 200$ GeV, Phys. Rev. Lett. **98** (2007) 232002.

[199] F. Abe et al. (CDF Collaboration): Production of J/ψ Mesons from χ_c Meson Decays in $p\bar{p}$ Collisions at $\sqrt{s} = 1.8$ TeV, Phys. Rev. Lett. **79** (1997) 578.

[200] B. Abelev et al. (ALICE Collaboration): Measurements of prompt and non-prompt J/ψ production cross sections at mid-rapidity in pp collisions at $\sqrt{s}$=7 TeV, paper in preparation .

[201] J. P. Lansberg: J/ψ production at $\sqrt{s}$=1.96 and 7 TeV: colour-singlet model, NNLO* and polarization, J. Phys. G **38(12)** (2011) 124110.

[202] M. Butenschoen: Private Communication, (4.1.2012).

[203] P. Gonzalez et al. (ALICE Collaboration): Simulation Study of $\chi_c \to J/\psi + \gamma$ Detection with $J/\psi \to e^+e^-$ in pp Collisions in the ALICE Experiment at LHC, Eur. Phys. J. **C61** (2009) 899, arXiv:hep-ex/0811.1592.

[204] P. Gonzalez et al. (ALICE Collaboration): Simulation Study of $\chi_c \to J/\psi + \gamma$ Detection with $J/\psi \to e^+e^-$ in pp Collisions in the ALICE Experiment at LHC, Eur. Phys. J. Erratum **C61** (2009) 915.

[205] F. Bossu et al.: Phenomenological extrapolation of the inclusive J/ψ cross section to proton-proton collisions at 2.76 TeV and 5.5 TeV, arXiv:1103.2394.

[206] B. Abelev et al. (ALICE Collaboration Collaboration): Inclusive J/ψ production in pp collisions at $\sqrt{s} = 2.76$ TeV, arXiv:1203.3641.

[207] K. Aamodt et al. (ALICE Collaboration): Charged-particle multiplicity measurement in proton–proton collisions at $\sqrt{s} = 7$ TeV with ALICE at LHC, Eur. Phys. J. **C68** (2010) 345.

[208] I. Arsene: Private Communication, (10.10.2011).

[209] A. Breakstone et al. (Ames-Bologna-CERN-Dortmund-Heidelberg-Warsaw Collaboration): Charged multiplicity distribution in pp interactions at CERN ISR energies, Phys. Rev. **D30** (1984) 528.

[210] K. Aamodt et al. (ALICE Collaboration): Centrality Dependence of the Charged-Particle Multiplicity Density at Midrapidity in Pb-Pb Collisions at $\sqrt{s_{\rm NN}} = 2.76$ TeV, Phys. Rev. Lett. **106** (2011) 032301.

[211] M. Lenhard: Etude du taux de production des J/ψ et muons simples en collisions proton-proton à l'aide du spectromètre à muons de l'expérience ALICE au LHC, Ph.D. thesis, University of Nantes, France (2011).

[212] R. Barlow: Systematic errors: Facts and fictions, arXiv:hep-ex/0207026.

[213] M. Strikman: Transverse structure of the nucleon and multiparton interactions, Prog. Theor. Phys. Suppl. **187** (2011) 289.

[214] L. Frankfurt et al.: Transverse nucleon structure and diagnostics of hard parton-parton processes at LHC, Phys.Rev. **D83** (2011) 054012, arXiv:1009.2559.

[215] M. Strikman: Transverse nucleon structure and multiparton interactions, Acta Phys.Polon. **B42** (2011) 2607, arXiv:1112.3834.

[216] L. Frankfurt et al.: Color Fluctuations in the Nucleon in High-Energy Scattering, Phys. Rev. Lett. **101** (2008) 202003.

[217] M. Strikman: Remarks on the observation of high multiplicity events at the LHC, Phys. Rev. **D84** (2011) 011501.

[218] V. Khachatryan et al.: Observation of long-range, near-side angular correlations in proton-proton collisions at the LHC, JHEP **2010** (2010) 1.

[219] B. Alver et al. (PHOBOS Collaboration): High transverse momentum triggered correlations over a large pseudorapidity acceptance in Au+Au collisions at $\sqrt{s_{\mathrm{NN}}} = 200$ GeV, Phys. Rev. Lett. **104** (2010) 062301, arXiv:0903.2811.

[220] S. Porteboeuf-Houssais: Private Communication, (7.11.2011).

[221] H. Jung: The CCFM Monte Carlo generator CASCADE, Comput.Phys.Commun. **143** (2002) 100, arXiv:hep-ph/0109102.

[222] T. Sjostrand et al.: A Brief Introduction to PYTHIA 8.1, Comput.Phys.Commun. **178** (2008) 852, arXiv:0710.3820.

[223] J. F. Grosse-Oetringhaus et al. (ALICE Collaboration): The ALICE online-offline framework for the extraction of conditions data, J. Phys. **219(2)** (2010) 022010.

[224] A. Colla et al.: The Shuttle Framework – A system for automatic readout and processing of conditions data, ALICE-INT **011**.

[225] C. Gaspar et al.: DIM, a Portable, Light Weight Package for Information Publishing, Data Transfer and Inter-process Communication, International Conference on Computing in High Energy Nuclear Physics (Padova, Italy) (Feb 1st-11th 2000).

[226] GNU Build System: URL `http://gnu.org/`.

[227] RPM Package Manager: URL `http://rpm.org/`.

[228] R. Brun et al.: ROOT: An object oriented data analysis framework, Nucl. Instr. Meth. **389(1-2)** (1997) 81.

[229] The LHC Computing Grid: URL `http://lcg.web.cern.ch/LCG/public/`.

[230] Extensible Markup Language (XML): URL `http://www.w3.org/XML/`.

[231] American Standard Code for Information Interchange (ASCII): URL `http://wps.com/projects/codes/X3.4-1963/index.html`.

[232] Hypertext Markup Language (HTML): URL `http://www.w3.org/History/1989/proposal.html`.

[233] ALICE Offline Website: URL `aliceinfo.cern.ch/Offline`.

[234] P. Saiz et al.: AliEn–ALICE environment on the GRID, Nucl. Instr. Meth. **A502(2-3)** (2003) 437, proceedings of the VIII International Workshop on Advanced Computing and Analysis Techniques in Physics Research.

[235] A. D. Martin et al.: Parton distributions for the LHC, Eur. Phys. J. **C63** (2009) 189, arXiv:0901.0002.

[236] W. R. Leo: Techniques for Nuclear and Particle Physics Experiments, Springer (1994).

[237] Frederick James: Statistical Methods in Experimental Physics, World Scientific, Singapore (2006).

Danksagung

Insbesondere meinem Doktorvater Christoph Blume möchte ich vielmals für seine großartige Unterstützung danken. Besonders hervorzuheben ist auch, dass er mir einen halbjährigen Forschungsaufenthalt am CERN ermöglicht hat, der mir interessante und tiefe Einblicke in das Experiment brachte. Darüber hinaus möchte ich ihm für seine hervorragende Arbeit als Vorsitzender unseres Publikationskomitees danken. Reinhard Stock war es, der mich ursprünglich von der Hochenergiephysik begeistert hat. Dafür möchte ich ihm danken, wie auch für seine ansteckende Begeisterung für die fundamentalen Fragen der Physik. Ihm und Dirk Rischke möchte ich gemeinsam dafür danken, dass sie mein H-QM-PhD-Komitee gebildet haben. Die Treffen dieses Komitees waren sehr hilfreich um hin und wieder den Blick für das Ganze zu schärfen. Direkt im Anschluss gilt mein Dank auch den Graduiertenschulen, deren Mitglied ich sein durfte: H-QM, HGS-HIRe und GRADE. Deren Angebot von Vorlesungswochen, Softskill-Seminaren, Reisemittel für Konferenzen und auch ein kleines Stipendium für den CERN-Aufenthalt war außerordentlich hilfreich. Diese Graduiertenschulen sind nicht zu nennen ohne Henner Büsching für seine Hingabe bei deren Aufbau zu danken. Danken möchte ich auch allen Mitgliedern der $J/\psi \to e^+e^-$-Analysegruppe für die gute Zusammenarbeit und die vielen interessanten Diskussionen, insbesondere Anton Andronic, Jens Wiechula und Ionut Arsene. Letzterem sowie Matthieu Lenhard möchte ich für die erfolgreiche Zusammenarbeit beim Bestimmen der Multiplizität danken sowie Gines Martinez für sein Engagement unsere Daten zur Publikation zu bringen. Vielen herzlichen Dank auch an Mark Strickman, Thomas Lang, Jean-Philippe Lansberg, Mathias Butenschön, Ramona Vogt und Sarah Porteboeuf dafür, dass sie mir ihre theoretischen Vorhersagen zur Verfügung stellten, sowie für Erleuterungen zu den Details der Modelle und spannende Diskussionen. Das gleiche gilt für Vakhtang Kartvelishvili im Bezug auf seine Methoden zur Bremsstrahlungs-Rekonstruktion. Namentlich nennen möchte ich insbesondere meine Bürokollegen Tim Schuster und Julian Book, herzlich danken möchte ich aber allen Mitgliedern des IKF für die schöne Zeit, interessante Diskussionen und gegenseitige Hilfe bei Problemen oder Fragen.
Herzlichst bedanken möchte ich mich auch bei den mir nahestehenden für ihre großartige Unterstützung und ihr Interesse an meiner Arbeit und ihrem Fortschritt.